



Gradient Delivery of Bioactive Molecules across Porous Hydrogels

Hoda Maher Mohamed Amin Eltaher, MSc

Thesis submitted to the University of Nottingham
for the degree of Doctor of Philosophy

January 2016

Everything we hear is an opinion, not a fact. Everything we see is a perspective, not the truth.

Marcus Aurelius
26 April 121 -17 March 180

This thesis is dedicated to the loving memory of Maher M. Eltaher.
1944 - 2000

Abstract

Tissue regeneration approaches involve the recreation of biochemical and mechanical cues dictating tissue fate. Gradients of chemical cues are common in the natural microenvironment and are usually accompanied with gradual changes in cellular responses. Consequently, thorough understanding of biomolecule gradient development, their effective concentrations and the corresponding cellular responses as a function of time and space are essential for efficient design of scaffolds for biomedical applications.

Here, we developed a compartmental diffusion model to study the development and measurement of biomolecule gradients. The model was validated to ensure effective spatiotemporal measurements of diffusing species within three-dimensional (3D) hydrogels. Results confirmed that the factors regulating the diffusing molecules' behaviour in hydrogel matrices were dependant on the size of the diffusing species and the interaction with the matrix. The source compartment was subsequently replaced by polymeric particulate depots with tuneable characteristics to maintain structural protein stability and provide controlled temporal release of proteins and the diffusion through the hydrogel compartment was accordingly monitored.

Glycosaminoglycan enhanced transduction (GET) technology was employed to study 3D gradient transduction of reporter protein in cell-laden hydrogels and to examine the effect of cells on the diffusion of biomolecules. Results demonstrated that cellular uptake of GET proteins altered the diffusion pattern as compared to acellular scaffolds and cells themselves acted as a sink that maintained steep GET protein gradients over the 5 mm wide scaffold. Furthermore, the synergistic combination of poly-arginine cell penetrating peptide (CPP) together with the cell membrane binding peptide using the GET technology demonstrated significant intracellular transduction in a gradient fashion in comparison to CPP alone. Employing GET technology and the compartmental diffusion model in the gradient delivery of the transcription factor MyoD to cell-laden hydrogels, resulted in directing the cells towards myogenic differentiation. However, the gradient pattern of differentiation was not clearly observed due to the limited number of genes examined. In conclusion, the model can be employed for the effective spatiotemporal gradient delivery of functional proteins to achieve the tissue complexity observed in the native tissues.

Publications and Presentations

The following publications and presentations have resulted from the work presented in this thesis:

Publications in Peer-Reviewed Journals:

Christopher D.J. Parmenter, Michael W. Fay, Cheryl Hartfield, & Hoda M. Eltaher “Making the practically impossible ‘merely difficult’ – Cryogenic FIB Lift- out for ‘damage free’ soft matter imaging”. Microscopy Research and Technique, DOI 10.1002/jemt.22630, 2016.

Oral presentations:

- “Three-dimensional gradient delivery of novel highly efficient GAG-binding enhanced transduction proteins for directing cell fate” H. Eltaher, J. Yang, J. Dixon & K. Shakesheff
WCRM, 21-23 October 2015, Leipzig, Germany
Published abstract: Regenerative Medicine 10 (7), 26-27 (2015)
- “Characterization of proteins concentration gradients for directed stem cell differentiation” H. Eltaher, J. Yang, J. Dixon & K. Shakesheff
UKPharmSci, 7-10 September 2014, Hatfield, United Kingdom
- “Proteins concentration gradients in compartmental diffusion model” H. Eltaher, J. Yang, J. Dixon & K. Shakesheff
CBS symposium, 29th May 2014, Nottingham, United Kingdom

Poster presentations:

- “Biomimetic three-dimensional gradient of GAG-binding Enhanced Transduction Proteins for stem cell differentiation” HM Eltaher, J Yang, JE Dixon & KM Shakesheff
TERMIS, 8-11 September 2015 Boston, USA
Published abstract: TISSUE ENGINEERING PART A 21, S97 (2015)

- “Assessment of the gradient delivery of bioactive molecules to hydrogel-encapsulated cells using flow cytometric analysis” HM Eltaher, J Yang, JE Dixon & KM Shakesheff
TCES, 19-21 July 2015, Southampton, United Kingdom
Published abstract: European Cells and Materials 29 (3), 48 (2015).
- “Three dimensional printing of hydrogels, growth factors and mammalian cells to create a biomimetic environment for nervous tissue formation in vitro” OA Hamid, J Yang, HM Eltaher & KM Shakesheff
TCES, 19-21 July 2015, Southampton, United Kingdom
Published abstract: European Cells and Materials 29 (3), 63 (2015).
- “Intracellular transduction of GET proteins in 3D gradients” Hoda M. Eltaher, Jing Yang, James E. Dixon & Kevin M. Shakesheff
TCES, 2-4 July 2014, Newcastle, United Kingdom
Published abstract: European Cells and Materials 28 (4), 84 (2014).
- “Spatial and temporal control of protein release from microspheres-hydrogel composite scaffolds” Hoda M. Eltaher, Jing Yang, Lee Buttery & Kevin M. Shakesheff
UKICRS held at Cork, Ireland 9-10th April 2014

Acknowledgments

First and foremost, I am thankful to my supervisor, Professor Kevin Shakesheff who has supported me throughout the thesis journey with advice, insights and guidance whilst allowing the room for self-dependence and development. I am, as well, grateful to Dr. James Dixon for the training, advice and support he provided throughout my PhD. Moreover, I would like to thank Dr. Jing Yang, Professor Phil Williams, Dr. Glen Kirkham, Dr. Michael Sawkins, Dr. Omar Qutachi, Dr. Hassan Rashidi and Dr. Helen Cox for training and discussions on various techniques during different stages of my PhD.

I am vastly thankful to the staff and members of the tissue engineering group in the school of pharmacy, University of Nottingham. Throughout 4 years in Nottingham, these colleagues were like a second family to me. Outside the tissue engineering group, I am grateful to Dr. Christopher Parmenter, Dr. Michael Fay, Mrs Nicola Weston, Mr Bryan Morris and Dr. David Onion from different research groups across the University of Nottingham for the technical support and help offered.

I am highly indebted to my home university and the Ministry of Higher Education of Egypt for the PhD scholarship awarded. This PhD was a great opportunity to discover myself and explore different research groups and ideas. I have learnt a lot during the journey and I hope to implement fruitful research ideas in my research group; Department of pharmaceuticals, Alexandria University. From this point, I would like to express my deepest gratitude to my Master thesis' supervision panel. They provided a continuous source of help and support that extended beyond the Master degree to my personal and academic life.

Last, but not least, my words won't suffice the gratitude I have towards my **Mother** who has always been a fountain of support, enthusiasm, inspiration and motivation that kept me going during the rocky journey. This gratitude expands to include my loving, supporting **husband** who has always believed in my potentials and given up many opportunities for the sake of my career development. My academic achievements would mean nothing without him on my side. Finally, I am heartily thankful for my biggest blessing ever; my child "**Malek**". He is the reason I woke up every morning with a new hope!

Hoda M. Eltaker

List of Abbreviations

Abbreviation	Term
2D	Two dimensional
3D	Three dimensional
AB/AM	Antibiotic/Antimycotic
AFM	Atomic force microscopy
BCA	Bicinchoninic Acid
BMP	Bone morphogenetic protein
BSA	Bovine Serum albumin
cAMP	Cyclic adenosine monophosphate
CMC-TYR	Carboxymethyl cellulose tyramine
CNTF	Ciliary neurotrophic factor
CPP	Cell penetrating peptide
CS	Chitosan
DCM	Dichloromethane
DMEM	Dulbecco's Modified Eagle Medium
DMSO	Dimethyl sulphoxide
Dpp	Decapentaplegic
DRG	Chick dorsal root ganglia
DTT	Dithiothreitol
ECM	Extracellular matrix
EDTA	Ethylenediaminetetraacetic acid
EGF	Epidermal growth factor
ELL	Endothelial-lined lumen
ESCs	Embryonic stem cells
FBS	Foetal bovine serum
FDA	US Food and Drug Administration
FGF	Fibroblast growth factor
FIB	Focused ion beam
FITC-BSA	Albumin-fluorescein isothiocyanate
fMLP	Formyl-Met-Leu-Phe
FRAP	Fluorescent Recovery After Photobleaching
GAG	Glycosaminoglycan
GET	Glycosaminoglycan enhanced transduction
GTN-HPA	Gelatin hydroxyphenylpropionic acid
HA	Hydroxyapatite
HBD	Heparin binding domain
HB-EGF	Heparin binding epidermal growth factor
HEK 293T	Human embryonic kidney cells 293T

Abbreviation	Term
10 mM HEPES	(4-(2-hydroxyethyl)-1-piperazineethanesulfonic acid)
HIFs	Hypoxia inducible factors
HIV	Human immunodeficiency virus
hMSCs	Human mesenchymal stem cells
HPLC	High performance liquid chromatography
HS	Heparan sulphate
HUVECs	Human umbilical vein endothelial cells
IL8	Interleukin-8
IPTG	β -D-1-thiogalactopyranoside
LB	Luria Broth
LN-1	Laminin
LTB4	leukotriene B4
MRF	Myogenic regulatory factors
mRFP-1	Red fluorescent protein
Mwt	Molecular weight
NGF	Nerve growth factor
NMR	Nuclear magnetic resonance
NT-3	Neurotrophin-3
O.C.T	Optimal Cutting Temperature
OCT4	Octamer-binding transcription factor 4
OD	Optical density
PAAM	Polyacrylamide
Pax7	Paired Box 7
PBS	Phosphate buffer saline
PC12	Phaechromocytoma
PCL	Polycaprolactone
PDGF-BB	Platelet derived growth factor
PDL	Poly-d-lysine
PDMS	Polydimethyl siloxane
PEG	Polyethylene glycol
PEGDA	Poly (ethylene glycol)-diacrylate
PFA	Paraformaldehyde
pHEMA	Polyhydroxyethylmethacrylate
PLGA	Poly (DL-lactic-co-glycolic acid)
PTD	Protein transduction domain
PTFE	Polytetrafluoroethylene
PVA	Poly vinyl alcohol
RGDS	Arg-gly-asp-ser
rhIGF-I	Insulin-like growth factor

Abbreviation	Term
RT-PCR	Real Time-Polymerase chain reaction
SCs	Satellite stem cells
SD	Standard deviation
SDF-1	Stromal cell-derived factor 1
SDS	Sodium dodecyl sulphate
SEM	Scanning electron microscope
SHH	Sonic Hedgehog
SOC	Super optimal growth media
TEM	Transmission electron microscope
TGF-β	Transforming growth factor- β
TG-L1Ig6	Immunoglobulin-like domain of cell adhesion molecule L1
Triblock	PLGA-PEG-PLGA triblock copolymer
TRITC-BSA	Tetramethylrhodamine isothiocyanate bovine serum albumin
TRITC-Dextran	Tetramethylrhodamine isothiocyanate–Dextran
UV	Ultraviolet
VEGF	Vascular endothelial growth factor
Wnt	Wingless Int
α-SMA	Smooth muscle actin
β-TCP	β -tricalcium phosphate

Table of contents

Abstract	i
Publications and Presentations	ii
Acknowledgments	iv
List of Abbreviations	v
Table of contents	viii
List of Figures	xii
List of Tables	xxiii
Chapter 1: Introduction	1
1.1. Background	1
1.2. Gradients in biology	3
1.2.1. Physical gradients	4
1.2.2. Mechanical gradients	4
1.2.3. Oxygen gradients	5
1.2.4. Chemical gradients	9
1.3. Cellular responses to gradients	11
1.4. Biomimetic gradient scaffolds	12
1.4.1. Hydrogel Matrices	15
1.4.2. Non hydrogel matrices	18
1.5. Methods of generation of chemical gradients	18
1.5.1. Cell culture systems	18
1.5.2. 3D systems	22
1.6. Challenges and future considerations	32
1.6.1. <i>In vivo</i> correlation and integrated techniques	32
1.6.2. Technical concerns	33
1.6.3. Biomimicry and clinical translation concerns	34
1.7. Thesis aims	36
Chapter 2: Materials and methods	37
2.1. Materials	37
2.2. Methods	39
2.2.1. General Cell Culture	39
2.2.2. Cryopreservation	39
2.2.3. Plain and protein loaded PLGA microspheres	40
2.2.4. Expression and Purification of Recombinant glycosaminoglycans (GAG-binding enhanced transduction) GET proteins	41
2.2.5. Hydrogels fabrication	45
2.2.6. Estimation of hydrogel pore size and internal structure	45

2.2.7.	Cell viability & proliferation	47
2.2.8.	Compartmentalized diffusion chamber.....	48
2.2.9.	Intracellular transduction gradients assessment.....	53
2.2.10.	Gene expression and real time polymerase chain reaction (RT-PCR).....	55
Chapter 3: Diffusion gradients in compartmentalized diffusion model; Model optimization and validation		58
3.1.	Introduction.....	58
3.2.	Aims & objectives.....	59
3.2.1.	Aim	59
3.2.2.	Objectives	59
3.3.	Materials and methods	59
3.3.1.	Hydrogel fabrication.....	59
3.3.2.	Development of compartmental diffusion model.....	59
3.3.3.	Diffusion studies in compartmentalized diffusion model.....	60
3.3.4.	Evaluation of diffusion gradients in hydrogel membranes	60
3.3.5.	Imaging of diffusion gradient across hydrogel scaffolds	60
3.3.6.	Model validation.....	60
3.3.7.	Determination of hydrogel pore size using microscopic techniques	62
3.4.	Results.....	62
3.4.1.	Validation of diffusion model.....	62
3.4.2.	Determination of proteins diffusion coefficients	74
3.4.3.	Determination of hydrogel structure.....	74
3.4.4.	Effect of nature of diffusing species	85
3.5.	Discussion	85
3.5.1.	Model validation.....	85
3.5.2.	Effect of hydrogel composition on diffusivity.....	92
3.5.3.	Effect of nature of diffusing species	96
3.6.	Conclusions	97
Chapter 4: Spatial and temporal control of protein release from microspheres/hydrogel composite scaffolds		98
4.1.	Introduction.....	98
4.2.	Aims & objectives.....	99
4.2.1.	Aim	99
4.2.2.	Objectives	99
4.3.	Materials and methods	100
4.3.1.	Fabrication of plain and protein loaded PLGA microspheres	100
4.3.2.	Microspheres-hydrogel composite layered scaffolds	102

4.4.	Results	103
4.4.1.	Characterization of PLGA microspheres	103
4.4.2.	Development of layered hydrogel scaffolds	104
4.4.3.	Evaluation of FITC-BSA diffusion gradients	104
4.5.	Discussion	113
4.6.	Conclusions	117
Chapter 5: Intracellular transduction of proteins in three dimensional gradients system		118
5.1.	Introduction.....	118
5.2.	Aims & objectives.....	119
5.2.1.	Aim	119
5.2.2.	Objectives	120
5.3.	Materials and methods	120
5.3.1.	GET proteins.....	120
5.3.2.	Cellular viability and proliferation in 3D hydrogels.....	121
5.3.3.	Compartmentalized diffusion	121
5.3.4.	Evaluation of proteins diffusion gradients.....	121
5.3.5.	Temporal imaging of scaffolds	121
5.3.6.	3D Intracellular transduction across cellular hydrogels	121
5.4.	Results	123
5.4.1.	GET proteins characterization	123
5.4.2.	2D intracellular transduction	123
5.4.3.	Cellular viability and proliferation in 3D hydrogels.....	124
5.4.4.	Compartmental diffusion model.....	125
5.4.5.	Gradient intracellular transduction	139
5.5.	Discussion	141
5.5.1.	2D intracellular transduction	141
5.5.2.	Cellular health in 3D hydrogel systems	154
5.5.3.	Gradient 3D protein Delivery Gradient	156
5.5.4.	3D intracellular transduction	158
5.6.	Conclusions	159
Chapter 6: Induction of myogenic differentiation using GAG-enhanced transduction proteins in 3D model		160
6.1.	Introduction.....	160
6.2.	Aims & objectives.....	161
6.2.1.	Aim	161
6.2.2.	Objectives	161

6.3. Materials and methods	162
6.3.1. GET protein synthesis.....	162
6.3.2. 2D intracellular transduction	162
6.3.3. 2D myogenic differentiation.....	162
6.3.4. Cellular viability and proliferation	162
6.3.5. Cell-laden compartmentalized diffusion chamber	162
6.3.6. Evaluation of temporal protein diffusion gradients	162
6.3.7. Imaging of temporal protein diffusion gradients	162
6.3.8. 3D Intracellular transduction across cellular hydrogels	162
6.3.9. 3D gradient myogenic differentiation across hydrogel scaffold.....	163
6.4. Results	163
6.4.1. NIH 3T3 mouse fibroblasts	163
6.4.2. BJ6 human dermal fibroblasts	163
6.4.3. Human embryonic kidney cells HEK 293T cell line	165
6.5. Discussion	181
6.5.1. NIH 3T3 mouse fibroblasts	181
6.5.2. BJ6 human dermal fibroblasts	189
6.5.3. Human embryonic kidney cell line	191
6.6. Conclusions	192
Chapter 7: General discussion & Future work	193
7.1. General discussion & conclusions	193
7.1.1. Model validation.....	193
7.1.2. Localized release depots	194
7.1.3. Gradient delivery of GET proteins	195
7.1.4. Model application in induced myogenic differentiation.....	195
7.2. Future directions	196
Chapter 8: References	199
Appendix I: Supporting information	219
Appendix II: Validating the use of infinite [®] 200 pro microplate reader to measure diffusion gradients of protein drugs across hydrogel based scaffolds	231
I. Introduction.....	231
II. Methods	231
III. Results & discussion	234
IV. Conclusion	238
Appendix III: Fluorescence recovery after photobleaching (FRAP).....	239

List of Figures

Figure 1: Microenvironmental factors controlling cell behaviours spatiotemporally. Reproduced from [1].	2
Figure 2: Substrate stiffness directs mesenchymal stem cells differentiation. (A) Stiffness of variable body organs in terms of elastic modulus. (B) Hydrogel system with controlled variable elastic moduli directing naïve mesenchymal cells towards specific lineages. Scale bar is 20 μm . Reproduced from [35].	6
Figure 3: Stem cell niches within human body are exposed to variable oxygen tensions. Reproduced from [36].	7
Figure 4: Oxygen gradients in the developing human placentas showing the differentiation pathway taken by cytotrophoblast stem cells in human uterus. Reproduced from [37].	8
Figure 5: Cellular responses towards <i>in-vivo</i> physicochemical gradients. A: cell migration, cell elongation, and cell differentiation in response to chemical gradients. B: Ran-GTP gradient guide the mitotic spindle during mitosis. C: Morphology as a function of gradient steepness. D: Mesenchymal stem cells differentiate into osteoids or calcified bone cells in response to signals of mechanical gradients in the ECM. Reproduced from [12].	14
Figure 6: <i>In vitro</i> cell culture assays used to generate bioactive molecules gradients to study cell responses along the direction of the developed gradients. Modified from [2].	21
Figure 7: Chamber designs of different microfluidics-based systems utilized to generate chemical gradients in cell-laden hydrogels. Modified from [97, 99, 100]	25
Figure 8: Spatial localization of BSA loaded PLGA microspheres in layered PEGDA hydrogel a. schematic presentation of the layered scaffolds b. bright field image c. Fluorescence micrographs (pseudocolor images) of hydrogels containing depots loaded with Rhodamine-BSA, Rhodamine-BSA-loaded PLG microspheres, blank PLGA microspheres and non-diffusive fluorophore loaded polystyrene beads. Modified from [18].	28
Figure 9: Developing bFGF gradient fibrous scaffolds by graded distribution of bFGF-PLGA microspheres with gradient bFGF loading using a simultaneous electrospaying/electrospinning process. Reproduced from [103].	30
Figure 10: Schematic presentation of the growth factors immobilized gradients in PCL scaffolds prepared by centrifugation/surface immobilization. Gradients of growth factors (BMP-7, TGF- β (2) or VEGF (165)) were formed by the centrifugation and the subsequent immobilization via heparin binding through hydrogen bonding to PCL fibres and ionic interactions to growth factors. Reproduced from [106].	31
Figure 11: Compartmentalized diffusion chamber showing mould design. a. Top schematic view of acetal mould with PTFE spacer fitted inside. b. Side schematic view of the mould design showing mould dimensions. c. Top schematic view of the mould showing sink (Si), source (So) and gel (G) compartments with their relevant dimensions.	50

Figure 12: Top view of compartmentalized diffusion chamber showing a: mould design with equal sizes PTFE blocks to create 3 compartments of source-gel-sink & b: 2 different sizes PTFE spacers fitted inside to create a depot compartment of hydrogel with FITC-BSA loaded microspheres dispersed in.52

Figure 13: Schematic diagram showing the process of evaluation of the developed gradients. Hydrogel scaffold after the diffusion process was removed from the mould, stored in the mounting medium at -80 °C and then sliced A. using a Leica CM1100 cryostat at -20°C i. Perpendicular to the direction of the protein diffusion to establish quantitative diffusion profiles or ii. Parallel to the direction of the protein diffusion to image the gradient across the scaffold width or B. manually sliced to 1 mm slices, subjected to gel digestion protocol that involved heat and enzymatic treatment and samples were then analysed using a MoFlo™ DP (DAKO) Flow Cytometer.54

Figure 14: Top view of compartmentalized diffusion chamber showing hydrogel membranes of 15×5×6.6 mm (Length × Width × Height) dimensions cast in the middle of the chamber.63

Figure 15: Calibration curve of FITC-BSA per 20 µm thick slices retrieved from cryosectioning of homogenously dispersed increasing concentrations of FITC-BSA in 1% agarose hydrogel scaffolds of 15×5×6.6 mm (Length × Width × Height) dimensions. Each concentration point was evaluated from 2 different scaffolds each with 8 different slices retrieved from random positions of the scaffold. Slices were dissolved in PBS and analysed for protein concentrations using a TECAN infinite 200PRO multimode reader (excitation: 490 nm; emission: 525 nm).65

Figure 16: Confocal microscope images of 20 µm thick 1% agarose hydrogel slices sliced parallel to the direction of the flow of FITC-BSA diffusing from the source compartment of the compartmental diffusion chamber after 14.5 hours using Leica TCS SPE Confocal a. Macroscopic featuring green fluorescent channel, b. overlay of fluorescent and bright field channels and c. Diffusion pattern of 1 mg/mL FITC-BSA across 1% agarose hydrogel scaffolds of 15×5×6.6 mm (Length × Width × Height) dimensions after 14.5 hours. Each time point was evaluated from triplicate scaffolds through which 1 mg/mL FITC-BSA diffused.66

Figure 17: a. Representative images of compartmentalized diffusion chamber featuring diffusion of 32.15 µg/mL Fluorescein in 1% agarose hydrogel scaffolds of 15×5×6.6 mm Length × Width × Height) dimensions with Fluorescein diffusing from the source compartment to the left of the hydrogel scaffold at zero, 2, 5, 16 and 24 hours and b. the corresponding concentration profiles.67

Figure 18: Diffusion pattern of FITC-BSA across 1% agarose hydrogel scaffolds of 15×5×6.6 mm (Length × Width × Height) dimensions. Each time point was evaluated from triplicate scaffolds through which a: 0.5 mg/mL or b: 1 mg/mL FITC-BSA diffused over days 1, 2 & 3.69

Figure 19: A: Representative image of compartmentalized diffusion chamber at day 3 featuring 1% agarose hydrogel scaffolds of 15×5×6.6 mm Length × Width × Height) dimensions with TRITC & FITC-BSA diffusing from different sides of the scaffold. B-D: Fluorescence microscopy images of 20 µm thick 1% agarose hydrogel slices sliced parallel to the direction of the flow of double opposing diffusing TRITC & FITC-BSA from either sides of the hydrogel scaffold at day 1 using Nikon stereomicroscope SMZ 1500 featuring b: red channel, c: green channel & d: overlay of both channels. Scale bar is 1 mm.70

Figure 20: Diffusion pattern of opposing diffusion of TRITC (left) and FITC (right) labelled BSA across 1% agarose hydrogel scaffolds of 15×5×6.6 mm (Length × Width × Height) dimensions. Each time point was evaluated from triplicate scaffolds through which 0.5 mg/mL TRITC & FITC-BSA diffused from either side of the gel membrane respectively. 71

Figure 21: Monitoring TRITC & FITC-BSA concentrations (mg/mL) in left and right compartments next to 1% agarose hydrogel scaffold in the compartmentalized diffusion chamber following diffusion of 0.5 mg/mL TRITC-BSA from the left compartment and 0.5 mg/mL FITC-BSA from the right compartment. a. representative image of compartmentalized diffusion chamber & b. quantitative evaluation of source and sink concentrations 72

Figure 22: Diffusion pattern of FITC-BSA across 2% agarose hydrogel scaffolds of 15×5×6.6 mm (Length × Width × Height) dimensions. Each time point was evaluated from triplicate scaffolds through which a: 0.5 mg/mL or b: 1 mg/mL FITC-BSA diffused over days 1, 2 & 3. 73

Figure 23: Diffusion pattern of FITC-BSA across 1% agarose-1% gelatin hydrogel scaffolds of 15×5×6.6 mm (Length × Width × Height) dimensions. Each time point was evaluated from triplicate scaffolds through which a: 0.5 mg/mL or b: 1 mg/mL FITC-BSA diffused over days 1, 2 & 3. 75

Figure 24: A. One phase decay curve describing the kinetics of diffusion of FITC-BSA across 2% & 1% agarose and 1% agarose-1% gelatin hydrogel scaffolds. The goodness of fit in terms of correlation coefficient (r^2) of the non-linear regression fitting is calculated to be 0.9360, 0.9247 & 0.9320 for 2% & 1% agarose and 1% agarose-1% gelatin hydrogel scaffolds respectively. 77

Figure 25: Comparative diffusion patterns of 0.5 & 1 mg/mL FITC-BSA across a: 1%, b: 2% agarose & c: 1% agarose-1% gelatin hydrogel scaffolds of 15×5×6.6 mm (Length × Width × Height) dimensions at day 3. 78

Figure 26: Determination of the diffusion coefficient of FITC-BSA in agarose hydrogels using membrane permeation model utilizing acellular scaffolds of 15×5×6.6 mm (Length × Width × Height) dimensions as gel membranes. Each time point was evaluated from 3 different scaffolds through which 500 µg/mL FITC-BSA diffused. a: Real time data points of amount of FITC-BSA measured in the sink compartments at the relevant time points. b: Linear regression for the same set of data after 24 hours, from which the diffusion coefficient of FITC-BSA in 1% agarose is evaluated to be $5.20 \times 10^{-7} \text{ cm}^2/\text{s}$ 79

Figure 27: Determination of the diffusion coefficient of FITC-BSA in 2% agarose hydrogels using membrane permeation model utilizing acellular scaffolds of 15×5×6.6 mm (Length × Width × Height) dimensions as gel membranes. Each time point was evaluated from 3 different scaffolds through which 500 µg/mL FITC-BSA diffused. Linear regression for real time data points of FITC-BSA diffusion in 2% agarose after 36 hours, from which the diffusion coefficient is evaluated to be $3.24 \times 10^{-7} \text{ cm}^2/\text{s}$ 80

Figure 28: Cryo scanning electron micrographs of a: 1% agarose, b: 2% agarose, c: 1% agarose-1% gelatin & d: 1 day hydrated 1% agarose-1% gelatin as viewed under JEOL JSM-6060LV scanning electron micrograph under cryogenic conditions. 81

Figure 29: Cryo scanning electron micrographs of a: 1% agarose-1% gelatin, b: region in hydrogel cut using focused ion beam and c: thinned section following focused ion beam thinning viewed under scanning electron micrograph under cryogenic conditions & d: thin hydrogel section as viewed under transmission electron microscope.	82
Figure 30: Transmission electron micrographs of a: 1% agarose following ultra-thin sectioning viewed under TEM, b: higher magnification, c: annotated pores from which the average pore size is calculated to be 273 ± 141 nm.	83
Figure 31: Transmission electron micrographs of a: 1% agarose-1% gelatin following ultra-thin sectioning viewed under TEM, b: higher magnification, c: annotated pores from which the average pore size is calculated to be 198 ± 8 nm.	84
Figure 32: Diffusion pattern of TRITC-Dextran 65000 across 1% agarose hydrogel scaffolds of $15\times 5\times 6.6$ mm (Length \times Width \times Height) dimensions. Each time point was evaluated from triplicate scaffolds through which a: 0.5 mg/mL or b: 1 mg/mL FITC-BSA diffused over days 1, 2 & 3.	86
Figure 33: Monitoring TRITC-Dextran 65000 concentrations (mg/mL) in source and sink compartments next to 1% agarose hydrogel scaffold in the compartmentalized diffusion chamber following diffusion of a: 0.5 mg/mL & b: 1 mg/mL TRITC-Dextran 65000 at different time points.	87
Figure 34: Diffusion pattern of TRITC-Dextran 4400 across 1% agarose hydrogel scaffolds of $15\times 5\times 6.6$ mm (Length \times Width \times Height) dimensions. Each time point was evaluated from triplicate scaffolds through which a: 0.5 mg/mL or b: 1 mg/mL FITC-BSA diffused over 13.5 hours & days 1, 2 & 3.	88
Figure 35: Monitoring TRITC-Dextran 4400 concentrations (mg/mL) in source and sink compartments next to 1% agarose hydrogel scaffold in the compartmentalized diffusion chamber following diffusion of a: 0.5 mg/mL & b: 1 mg/mL TRITC-Dextran 4400 at different time points.	89
Figure 36: Diffusion pattern of TRITC-Dextran 65000 vs TRITC-Dextran 4400 across 1% agarose hydrogel scaffolds of $15\times 5\times 6.6$ mm (Length \times Width \times Height) dimensions at day 1.	90
Figure 37: Size distribution (% volume) of microspheres prepared by double emulsion method. Plots show representative sample from each batch (Bn01- Bn04) PLGA 50:50 plain (Bn01), BSA loaded (Bn02), Plain with 10% Triblock (Bn03) or BSA loaded with 10% Triblock (Bn04)	105
Figure 38: Scanning electron micrographs of PLGA 50:50 microspheres showing the size distribution of batches 1-4 over images A, C, E and G respectively and a close up to the microspheres' shape and surface characteristics over images B, D, F and H respectively.	106
Figure 39: Bright field image (A) and fluorescence microscopy image (B) showing the entrapment of the fluorescent BSA inside the PLGA 50:50 microspheres (Bn02). Scale bar is 10 μ m.	107
Figure 40: Release profiles of FITC-BSA (μ g) in 3 mL Phosphate Buffer Saline from 40 mg Bn02 (a) or Bn04 (b) quantified using BCA assay kit and measuring absorbance at 562 nm using a TECAN infinite 200PRO multimode reader.	108

Figure 41: a: % FITC-BSA released in 3 mL Phosphate Buffer Saline from 40 mg Bn02 and Bn04 quantified using BCA assay kit and measuring absorbance at 562 nm using a TECAN infinite 200PRO multimode reader. b: close-up on data collected until day 3 109

Figure 42: A. Representative image of microspheres-hydrogel composite scaffold in the three compartmental diffusion chamber. 300 μ L of gelatin-agarose hydrogels with suspended 12.9 mg PLGA (50:50) microspheres (Bn01-Bn04) (15 \times 7.5 \times 6.6 mm) were cast next to the plain hydrogel membrane (15 \times 5 \times 6.6 mm). B: Bn04 in GIA layered scaffolds on day 3 using Nikon SMZ1500 dissection microscope i: bright field & ii: green fluorescence channel 110

Figure 43: 20 μ m thick transverse section of the microspheres-hydrogel composite scaffold showing the plain hydrogel layer adjacent to the microspheres hydrogel layer with 21.5 mg PLGA (50:50) microspheres viewed under Nikon SMZ1500 dissection microscope at different magnifications. Scaffolds were subject to sucrose dehydration steps prior to preservation in OCT, freezing at -80 $^{\circ}$ C and sectioning using Leica CM1100 cryostat. 111

Figure 44: Scanning electron micrographs of the microspheres-hydrogel composite scaffold showing a: the plain hydrogel layer & b: the microspheres/hydrogel composite layer as viewed under Jeol JSM 6060LV. 111

Figure 45: 20 μ m thick longitudinal section of the microspheres-hydrogel composite scaffold showing the microspheres hydrogel layer with suspended 13.9 mg PLGA (50:50) microspheres (Bn04) viewed under Nikon SMZ1500 dissection microscope in a: bright field and b: fluorescent modes. Close up images at higher magnification are shown at the bottom row i: bright field, ii: fluorescence microscopy images & iii: an overlay of bright field and fluorescence channels. Scaffolds were directly preserved in OCT, frozen at -80 $^{\circ}$ C and then sectioned using Leica CM1100 cryostat. 112

Figure 46: Diffusion gradient patterns of FITC-BSA released from FITC-BSA loaded microspheres in the microspheres-hydrogel layer to the plain 1% gelatin-1% agarose hydrogel layer on days a. 1 & b. 3. 114

Figure 47: Cumulative amounts of FITC-BSA released to the sink compartment in the three compartmentalized diffusion chamber model following diffusion through 1% gelatin-1% agarose scaffolds of 15 \times 5 \times 6.6 mm (Length \times Width \times Height) dimensions. 115

Figure 48: Schematic diagram of the test proteins; mRFP-1 is the reporter red fluorescent protein, mR-8R is the cell penetrating 8 arginine peptide linked to mRFP-1 while P21-mR is mRFP-1 with an *N*-terminal fusion of the P21 domain of heparin binding EGF (HB-EGF). P21-mR-8R is mRFP-1 with *N*-terminal fusion of P21 and C-terminal fusion of 8R. Reproduced from [118]. 126

Figure 49: Determination of the protein molecular weight of mRFP-1, P21-mR-8R, mR-8R and P21-mR using SDS-PAGE using a SeeBlue[®] protein standard. 126

Figure 50: Determination of the hydrodynamic radii R_h (nm) of A: mRFP-1, B: P21-mR-8R, C: P21-mR, D: mR-8R, E: P21-mR-MyoD-8R, F: FITC-BSA, G: Standard Divinyl benzene Polymer microspheres & H: collective proteins in 10 mM HEPES buffer at 37 $^{\circ}$ C using Zeta sizer Nano ZS 127

Figure 51: Intracellular transduction of P21-mR-8R versus mRFP-1 in NIH 3T3 mouse fibroblasts cultured in monolayer on tissue culture plastic. Mean fluorescence intensity inside cells was quantified using flow cytometric analysis using MoFlo™ DP (DAKO) Flow Cytometer. Data were normalized to the mean fluorescence intensity per monolayer of cells (1×10^6) exposed to 50 $\mu\text{g}/\text{mL}$ mRFP-1 for 2 hours. Data are represented as the mean ($n=3$) \pm standard deviation. 129

Figure 52: Fluorescence microscopy images of NIH 3T3 mouse fibroblasts exposed to culture medium or 50 $\mu\text{g}/\text{mL}$ mRFP-1 or P21-mR-8R at different time points imaged using Leica DM IRB microscope. Cells were detached using Trypsin-EDTA and the mean fluorescence intensity per cells was quantified using MoFlo™ DP (DAKO) Flow Cytometer and samples of cell solutions were subsequently imaged. Scale bar is 100 μm 130

Figure 53: A: Intracellular transduction of P21-mR-8R versus mRFP-1, P21-mR & mR-8R in NIH 3T3 mouse fibroblasts cultured in monolayer on tissue culture plastic. Mean fluorescence intensity inside cells was quantified using flow cytometric analysis using MoFlo™ DP (DAKO) Flow Cytometer. Data were normalized to the mean fluorescence intensity per monolayer of cells (1×10^6) exposed to 50 $\mu\text{g}/\text{mL}$ mRFP-1 for 2 hours. Data are represented as the mean ($n=3$) \pm standard deviation. B: Fluorescence microscopy images of NIH 3T3 mouse fibroblasts exposed to culture medium or 50 $\mu\text{g}/\text{mL}$ mRFP-1, P21-mR, mR-8R or P21-mR-8R at different time points imaged using microscope. 131

Figure 54: a: Viability of NIH 3T3 mouse fibroblasts cultured in monolayer on tissue culture plastic versus viability of cells encapsulated in 1% agarose, 2% agarose & 1% agarose-1% gelatin hydrogel at different time points using Live/Dead® Viability/Cytotoxicity Kit. b: representative images of viable (green), dead (red) cells and overlay of both for cells encapsulated in 1% agarose-1% gelatin hydrogel at day 3. Data is expressed as % of viable cells compared to total live and dead cells. Cells were counted using ImageJ software. Each data point is an average of 3 different samples and each sample was assessed from 3 different fields of views. 132

Figure 55: Metabolic activity of NIH 3T3 mouse fibroblasts cultured in monolayer on tissue culture plastic versus to results of cells encapsulated in 1% agarose, 2% agarose & 1% agarose-1% gelatin hydrogel at different time points using Prestoblue® proliferation assay. Data is normalized to the relevant fluorescence intensity of hydrogel systems at day zero. Each time point is an average of triplicate samples. 133

Figure 56: Proliferation assay of NIH 3T3 mouse fibroblasts cultured in monolayer on tissue culture plastic versus cells encapsulated in 1% agarose-1% gelatin hydrogel at different time points using CyQuant® NF proliferation assay. Data is normalized to the relevant fluorescence intensity at day zero. Each time point is an average of triplicate samples. 133

Figure 57: Calibration curve of mRFP-1 per 20 μm thick slices retrieved from cryosectioning of homogenously dispersed increasing concentrations of mRFP-1 in cellular (2×10^6 NIH 3T3 mouse fibroblasts cells/mL) or acellular 1% agarose – 1% gelatin hydrogel scaffolds of $15 \times 5 \times 6.6$ mm (Length \times Width \times Height) dimensions. Each concentration point was evaluated from 2 different scaffolds each with 8 different slices retrieved from random positions of the scaffold. Slices were dissolved in PBS and analysed for protein concentrations using a TECAN infinite 200PRO multimode reader (excitation: 584 nm; emission: 620 nm). 134

Figure 58: Diffusion gradients of 50 $\mu\text{g}/\text{mL}$ mRFP-1 across (a) acellular and (b) cellular (NIH 3T3 mouse fibroblasts, $2 \times 10^6/\text{mL}$) 1% agarose-1% gelatin hydrogels at 1, 2, 6, 24 and 72 hours (n=3).	135
Figure 59: Diffusion gradients of 50 $\mu\text{g}/\text{mL}$ P21-mR-8R across (a) acellular and (b) cellular (NIH 3T3 mouse fibroblasts, $2 \times 10^6/\text{mL}$) 1% agarose-1% gelatin hydrogels at 1, 2, 6, 24 and 72 hours (n=3).	136
Figure 60: Concentration of proteins in the source and sink compartments next to cellular scaffolds (NIH 3T3 mouse fibroblasts; 2 M/mL) at 24 and 72 hours.	137
Figure 61: Fluorescence microscope images of cross sections of the cellular hydrogels sliced parallel to the direction of the protein flow: non-transducing mRFP-1 (left) and cell penetrating P21-mR-8R (right). Red dots represent transduced cells. Dashed lines represent the border between the hydrogel scaffold and the protein source (scale bar=0.5 mm).	138
Figure 62: Flow cytometric analysis (dot plot) of monolayer of NIH 3T3 mouse fibroblasts cells exposed to 50 $\mu\text{g}/\text{mL}$ mRFP-1 or P21-mR-8R for 1 day with or without Hoechst 33342 staining.	142
Figure 63: % Gated cells (upper right quadrant; double stained for red (mRFP-1) and blue (Hoechst 33342) fluorescence) from total cells examined per slice using flow cytometric analysis following diffusion of control culture media, non-transducing mRFP-1 and P21-mR-8R through cellular (NIH 3T3 mouse fibroblasts, $2 \times 10^6/\text{mL}$) gelatin/agarose hydrogels at days 1 & 3. Data shown are representative of a single independent experiment and are represented as the mean (n=2) \pm standard deviation.	143
Figure 64: Flow cytometric analysis (dot plot) of cells retrieved from digested gel slices as a function of distance away from source protein following 1 day of protein diffusion. A: levelled minimal red fluorescent intensities (upper right quadrants) in slices comprising control scaffold (upper panel). B: mRFP-1 scaffold showing levelled fluorescent intensities for the last 4 slices with the first slice slightly higher. C: P21-mR-8R scaffold (lower panel) showing gradient cellular uptake of the red fluorescent protein across the hydrogel width. Dot plots shown are representative of a single set of scaffolds of a duplicate experiment.	144
Figure 65: Flow cytometric analysis (histogram) of cells retrieved from digested gel slices as a function of distance away from source protein following 1 day of protein diffusion showing frequencies of number of gated cells in slices comprising A: control culture medium scaffold. B: mRFP-1 scaffold C: P21-mR-8R scaffold. Histograms shown are representative of a single set of scaffolds of a duplicate experiment.	145
Figure 66: Intracellular fluorescent gradient profiles following control media, non-transducing mRFP-1 and P21-mR-8R diffusion through cellular (NIH 3T3 mouse fibroblasts, $2 \times 10^6/\text{mL}$) gelatin/agarose hydrogels using flow cytometry analysis: (a) 24 hours and (b) 72 hours. Data were normalized to the mean fluorescence intensity per monolayer of cells (1×10^6) exposed to 50 $\mu\text{g}/\text{mL}$ mRFP-1 for 24 hours. Data are represented as the mean of three independent experiments (n=3) \pm standard deviation.	146

Figure 67: Representative fluorescence microscopy images of digested hydrogel slices retrieved from cellular scaffolds (NIH 3T3 mouse fibroblasts, 2×10^6 /mL) exposed to media, mRFP-1 or P21-mR-8R respectively on day 1. Hoechst 33342; blue (left) and red fluorescent protein; red (right), scale bar = 100 μ m. A: crude images & B: enhanced contrast images using ImageJ software. 147

Figure 68: Representative fluorescence microscopy images of digested gel slices retrieved from cellular scaffolds (NIH 3T3 mouse fibroblasts, 2M/mL) exposed to media, mRFP-1 or P21-mR-8R respectively on day 3. Hoechst 33342; blue and red fluorescent protein; red, scale bar = 100 μ m. A: crude images & B: enhanced contrast images using ImageJ software. 148

Figure 69: Image analysis of the fluorescence intensity of the liquefied gels retrieved as a function of distance away from source proteins using ImageJ software. Representative image analysis of liquefied hydrogels exposed to mRFP-1 or P21-mR-8R (50 μ g/mL) for A: 24 hours or B: 72 hours showing the mean red fluorescence intensity per image (upper row) and the standard deviation of the mean red fluorescence intensity per image (lower row). 149

Figure 70: % Gated cells (upper right quadrant; double stained for red (mRFP-1) and blue (Hoechst 33342) fluorescence) from total cells examined per slice using flow cytometric analysis following diffusion of non-transducing mRFP-1, P21-mR, mR-8R and P21-mR-8R through cellular (NIH 3T3 mouse fibroblasts, 2×10^6 /mL) gelatin/agarose hydrogels at days 1 & 3. Data shown are representative of a single independent experiment and are represented as the mean (n=2) \pm standard deviation. 150

Figure 71: Intracellular fluorescent gradient profiles following control media, non-transducing mRFP-1, P21-mR, mR-8R and P21-mR-8R diffusion through cellular (NIH 3T3 mouse fibroblasts, 2×10^6 /mL) gelatin/agarose hydrogels using flow cytometry analysis: (a) 24 hours and (b) 72 hours. Data were normalized to the mean fluorescence intensity per monolayer of cells (1×10^6) exposed to 50 μ g/mL mRFP-1 for 24 hours. Data are represented as the mean (n=3) \pm standard deviation. 151

Figure 72: Representative fluorescence microscopy images of digested gel slices retrieved from cellular scaffolds (NIH 3T3 mouse fibroblasts, 2M/mL) exposed to media, mRFP-1, P21-mR, mR-8R or P21-mR-8R respectively on day 1. Hoechst 33342; blue and red fluorescent protein; red, scale bar = 100 μ m. 152

Figure 73: Representative fluorescence microscopy images of digested gel slices retrieved from cellular scaffolds (NIH 3T3 mouse fibroblasts, 2M/mL) exposed to media, mRFP-1, P21-mR, mR-8R or P21-mR-8R respectively on day 3. Hoechst 33342; blue and red fluorescent protein; red, scale bar = 100 μ m. 153

Figure 74: Intracellular transduction of P21-mR-MyoD-8R versus mRFP-1 in NIH 3T3 mouse fibroblasts cultured in monolayer on tissue culture plastic. Mean fluorescence intensity inside cells was quantified using flow cytometric analysis using MoFlo™ DP (DAKO) Flow Cytometer. Data were normalized to the mean fluorescence intensity per monolayer of cells (1×10^6) exposed to 50 μ g/mL mRFP-1 for 2 hours. Data are represented as the mean (n=3) \pm standard deviation. 166

Figure 75: Fluorescence microscopy images of NIH 3T3 mouse fibroblasts exposed to culture medium or 50 µg/mL mRFP-1 or 100 µg/mL P21-mR-MyoD-8R at different time points imaged using Leica DM IRB microscope. Cells were detached using Trypsin-EDTA and the mean fluorescence intensity per cells was quantified using MoFlo™ DP (DAKO) Flow Cytometer and samples of cell solutions were subsequently imaged. Scale bar is 100 µm. 167

Figure 76: Diffusion gradients of 60 µg/mL P21-mR-MyoD-8R across (a) acellular and (b) cellular (NIH 3T3 mouse fibroblasts, 2x10⁶/mL) 1% agarose-1% gelatin hydrogels at 6, 24, 72 and 96 hours (n=3). 168

Figure 77: Bright and fluorescence microscopy images of cross sections of the cellular (NIH 3T3 mouse fibroblasts 2M/mL) hydrogels sliced parallel to the direction of the P21-mR-MyoD-8R at 72 hours. Red dots represent transduced cells (scale bar=0.5 mm). 169

Figure 78: Fluorescence microscopy images of monolayer of 50,000 BJ6 dermal fibroblasts exposed to culture medium or 20 µg/mL P21-mR-MyoD-8R at different time points imaged using Leica DM IRB microscope. Scale bar is 100 µm. 170

Figure 79: a: Intracellular transduction of P21-mR-MyoD-8R versus mRFP-1 in BJ6 dermal fibroblasts cultured in monolayer on tissue culture plastic. b: Intracellular transduction of lower doses of P21-mR-MyoD-8R in BJ6 dermal fibroblasts cultured in monolayer on tissue culture plastic. Mean fluorescence intensity inside cells was quantified using flow cytometric analysis using MoFlo™ DP (DAKO) Flow Cytometer. Data were normalized to the mean fluorescence intensity per monolayer of cells (0.5x10⁶) exposed to 7.5 µg/mL mRFP-1 for 1 day. Data are represented as the mean (n=3) ± standard deviation. 171

Figure 80: Fluorescence microscopy images of BJ6 dermal fibroblasts exposed to 7.5 µg/mL or 15 µg/mL P21-mR-MyoD-8R at different time points imaged using Leica DM IRB microscope. Cells were detached using Trypsin-EDTA and the mean fluorescence intensity per cells was quantified using MoFlo™ DP (DAKO) Flow Cytometer and samples of cell solutions were subsequently imaged. Scale bar is 100 µm. 172

Figure 81: Viability of BJ6 dermal fibroblasts cultured in monolayer on tissue culture plastics versus viability in 1% agarose-1% gelatin hydrogel at different time points using Live/Dead® Viability/Cytotoxicity Kit. Data is expressed as % of viable cells compared to total live and dead cells. Cells were counted using ImageJ software. Each data point is an average of 3 different samples and each sample was assessed from 3 different fields of views. 173

Figure 82: Proliferation assay of BJ6 human dermal fibroblasts cultured in monolayer on tissue culture plastic versus cells encapsulated in 1% agarose-1% gelatin hydrogel at different time points using CyQuant® NF proliferation assay. Data is normalized to the relevant fluorescence intensity at day zero. Each time point is an average of triplicate samples. 173

Figure 83: Diffusion gradients of 60 µg/mL P21-mR-MyoD-8R across cellular (BJ6 dermal fibroblasts, 1x10⁶/mL) 1% agarose-1% gelatin hydrogels at 2, 6, 24 and 72 hours (n=3). 174

Figure 84: Concentration of P21-mR-MyoD-8R in the source and sink compartments next to cellular scaffolds (BJ6 dermal fibroblasts; 1 M/mL) at different time points. 174

Figure 85: Intracellular fluorescent gradient profiles following diffusion of control culture medium, 30 µg/mL mRFP-1 and 60 µg/mL P21-mR-MyoD-8R diffusion through cellular (BJ6 dermal fibroblasts 1×10^6 /mL) gelatin/agarose hydrogels using flow cytometry analysis: (a) 24 hours and (b) 72 hours. Data were normalized to the mean fluorescence intensity per monolayer of cells (0.5×10^6) exposed to 30 µg/mL mRFP-1 for 24 hours. Data are represented as the mean (n=3) ± standard deviation. 175

Figure 86: The effect of exposure of monolayer of BJ6 dermal fibroblasts 0.5 M cultured on tissue culture plastics to P21-mR-MyoD-8R (60 µg/mL) at different time points. Myogenic differentiation is evaluated based on the fold increase in hMYF5 and hMyoD-1 gene expression compared to control untreated cells with the use of β-actin as the house keeping gene using real time quantitative PCR. Data is expressed as mean ± SD. Table insert shows RNA concentrations (ng/µL) of test samples as quantified using NanoDrop® ND-1000 Spectrophotometer. 176

Figure 87: The effect of 3-days exposure of monolayer of BJ6 dermal fibroblasts 0.5 M cultured on tissue culture plastics to 30 µg/mL mRFP-1 or increasing concentrations of P21-mR-MyoD-8R. Myogenic differentiation is evaluated based on the fold increase in hMYF5 and hMyoD-1 gene expression compared to control untreated cells with the use of β-actin as the house keeping gene using real time quantitative PCR. Data is expressed as mean ± SD. 178

Figure 87: Proliferation assay of HEK 293T human embryonic stem cells cultured in monolayer on tissue culture plastic versus cells encapsulated in 1% agarose-1% gelatin hydrogel at different time points using CyQuant® NF proliferation assay. Data is normalized to the relevant fluorescence intensity at day zero. Each time point is an average of triplicate samples. 180

Figure 89: Intracellular fluorescent gradient profiles following diffusion of control culture medium, 30 µg/mL mRFP-1 and 60 µg/mL P21-mR-MyoD-8R diffusion through cellular (Human embryonic kidney cells HEK293T 2×10^6 /mL) gelatin/agarose hydrogels using flow cytometry analysis: (a) 24 hours and (b) 72 hours. Data were normalized to the mean fluorescence intensity per monolayer of cells (1×10^6) exposed to 30 µg/mL mRFP-1 for 24 hours. Data are represented as the mean (n=3) ± standard deviation. 182

Figure 90: Representative fluorescence microscopy images of digested gel slices retrieved from cellular scaffolds (HEK293T human embryonic kidney cells, 2M/mL) exposed to control culture media, mRFP-1 or P21-mR-MyoD-8R respectively on day 1. Hoechst 33342; blue and red fluorescent protein; red, scale bar = 100 µm. 183

Figure 91: Representative fluorescence microscopy images of digested gel slices retrieved from cellular scaffolds (HEK293T human embryonic kidney cells, 2M/mL) exposed to control culture media, mRFP-1 or P21-mR-MyoD-8R respectively on day 3. Hoechst 33342; blue and red fluorescent protein; red, scale bar = 100 µm. 184

Figure 92: The effect of 3-days exposure of monolayer of Human embryonic kidney cells HEK293T (1 M) cultured on tissue culture plastics to increasing concentrations of P21-mR-MyoD-8R. Myogenic differentiation is evaluated based on the fold increase in hMyoD-1 gene expression compared to control untreated cells with the use of β -actin as the house keeping gene using real time quantitative PCR. Data is expressed as mean \pm SD 186

Figure 93: Relative myogenic gene expression as a function of distance away from source following diffusion of 60 μ g/mL P21-mR-MyoD-8R across cellular HEK293T (2 M/mL) 1% agarose-1% gelatin hydrogel scaffolds of 15 \times 5 \times 6.6 mm (Length \times Width \times Height) dimensions. Myogenic differentiation is evaluated based on the fold increase in hMyoD-1 gene expression compared to control cells recovered from 5 different slices of a scaffold through which control culture medium diffused with the use of β -actin as the house keeping gene using real time quantitative PCR. Data is expressed as mean (n=5) \pm SD. 188

List of Tables

Table 1: Summary of various physical and chemical stimuli affecting cellular migration, modified from [59].	13
Table 2: Selected examples from literature showing biomimetic physical and chemical gradient scaffolds and the key findings of each system	35
Table 3: list of TaqMan [®] Gene Expression Assays used in the rT-qPCR analysis	57
Table 4: List of diffusing species diffusing through the compartmentalized diffusion chamber and their respective experimental conditions	61
Table 5: Linear and exponential fit of the diffusion profiles of various diffusing species in different hydrogel systems in the compartmental diffusion model	76
Table 6: One phase decay equation fit of the diffusion profiles of FITC-BSA in different hydrogel systems in the compartmental diffusion model	77
Table 7: Exact composition of batches formed using double emulsion/solvent evaporation method	101
Table 8: Size distribution characteristics for representative samples of PLGA microspheres (Bn01-Bn04) as determined by laser diffraction using a LS230 Beckmann Coulter	105
Table 9: Content and encapsulation efficiency of FITC-BSA in PLGA microspheres (Bn02 & Bn04) as determined by bicinchoninic acid assay, theoretical FITC-BSA content per 40 mg microspheres is 400 μ g.	107
Table 10: list of reporter fluorescent protein & recombinant proteins produced via GAG enhanced binding transduction technology, their amino acid sequences and their expected molecular weights & isoelectric points as calculated from [216]	122
Table 11: Determination of the hydrodynamic radius (nm) of various test samples in different dispersants using Zeta sizer Nano ZS at 37°C	128
Table 12: Determination of the Zeta potential of various test samples in 10 mM HEPES buffer using Zeta sizer Nano ZS at 37°C	128
Table 13: List of RNA concentrations extracted from different monolayers of BJ6 dermal fibroblasts (0.5M) exposed to variable concentrations of P21-mR-MyoD-8R or 30 μ g/mL mRFP-1 for 3 days. RNA was extracted using RNAeasy spin columns and quantified using NanoDrop [®] ND-1000 Spectrophotometer. Data is expressed as mean (n=3) \pm SD.	177

Table 14: List of RNA concentrations extracted from BJ6 dermal fibroblasts loaded hydrogel slices (5×15×1 mm, 1M/mL) as a function of distance away from source of 60 µg/mL P21-mR-MyoD-8R or control culture media for 3 days. RNA was extracted using RNeasy spin columns and quantified using NanoDrop® ND-1000 Spectrophotometer. 179

Table 15: List of RNA concentrations extracted from different monolayers of HEK293T cells (1M) exposed to variable concentrations of P21-mR-MyoD-8R for 3 days. RNA was extracted using RNeasy spin columns and quantified using NanoDrop® ND-1000 Spectrophotometer. Data is expressed as mean (n=3) ± SD. 185

Table 16: List of RNA concentrations extracted from HEK293T loaded hydrogel slices (6.6×15×1 mm, 2M/mL) as a function of distance away from source of 60 µg/mL P21-mR-MyoD-8R or control culture media for 3 days. RNA was extracted using RNeasy spin columns and quantified using NanoDrop® ND-1000 Spectrophotometer. Data is expressed as mean (n=5 scaffolds) ± SD. Control scaffold is the average of 3 different slices retrieved from the same scaffold. 187

Chapter 1: Introduction

1.1. Background

Biological processes occurring within the dynamic, three dimensional (3D) microenvironments of living tissues are governed by a series of physical, mechanical and chemical cues [1]. Gradients of these cues (Figure 1) represent the signalling mechanisms essential for guiding cell growth, migration and differentiation. They are, as well, involved in many crucial physiological phenomena like inflammation, immune response, wound healing, cancer and nerve regeneration [2]. These kinds of processes are usually triggered by a nearby tissue producing dictating signals that function as directional cues.

Historically, Wolpert proposed that gradients formed by the diffusion of bioactive molecules named morphogens from sources to sinks dictate positional information to cells to adopt different fates depending on the positional values assigned [3]. This happens in a two-step process that is initiated with informing cells of their position and is followed with interpretation of this positional information to form the final structure. Different concentration-dependant instructions result in turning on or off the genes across the pattern of this diffusion and eventually elicit gradual cellular responses. This was summoned up by the ‘French flag model’ discussed in Wolpert’s original paper [3]. The model is a conceptual definition representing the effect of a morphogen on cell differentiation. Cellular states resulting from graded morphogen concentrations are represented by the colours comprising the French flag. High concentrations of the morphogen activate the blue gene; lower concentrations activate the white gene, whilst the red represents the default state of cells below morphogen concentration threshold [3].

Wolpert’s model was preceded by the discussion of the chemical basis of morphogenesis established by Turing [4]. Morphogenesis is defined as the controlled dynamic change in tissues leading to the development of mature organs and the overall body plan. The concept of morphogenesis was studied from a mathematical point of view to be applied on biological phenomena [4]. Theoretical work in the form of numerical simulations was continued from Turing’s earlier work to reveal mechanisms describing the influence of two morphogens and their subsequent patterns of activity [5, 6]. Such theories contributed hugely to the development of developmental biology. However, their impact was not fully realised except after mid 1990s after thorough studies on the *Drosophila* development were published [7].

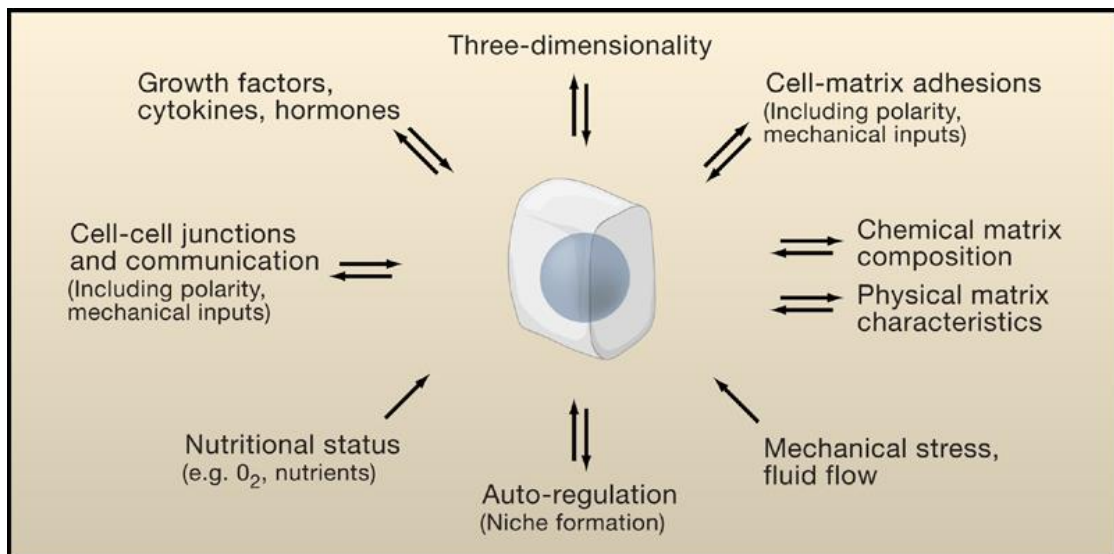


Figure 1: Microenvironmental factors controlling cell behaviours spatiotemporally. Reproduced from [1].

These studies demonstrated the role of bicoid; an intracellular morphogen and Decapentaplegic (Dpp); an extracellular morphogen on the development of *Drosophila* [8, 9]. Since then, continuous research featuring variable morphogens have been published [7].

In the process of tissue regeneration, it is crucial to build up an *in vivo* microenvironment or a niche that can recruit neighbouring cells to provide spatio-temporal signals guiding repair, proliferation and differentiation mechanisms [10]. Biomimetic approaches adopted to restore faulty organs functions or regenerate failing tissues (reviewed in [2, 11-18]) involve recreation of the cellular microenvironments by incorporating physical, chemical, temporal, and spatial gradients within engineered 3D scaffolds. The efficient design of such biomimetic scaffolds is subject to thorough understanding of the underlying directional cues.

1.2. Gradients in biology

The extracellular matrix (ECM) represents a 3D complex network providing mechanical support to versatile types of cells present in specific tissues. It serves as a barrier between different cell types and accommodates guidance cues essential for development, wound healing or tissue repair [11, 12]. It possesses hydrogel-like structure with a high degree of hydration and viscoelasticity [12] with the ability to resist compressive and shear forces present within the cellular microenvironment [11]. Nevertheless, it permits the diffusion of nutrients and metabolites between the tissue microvasculature and the cells.

The ECM is composed of various types of proteoglycans, collagen fibres, glycoproteins such as elastin and various adhesion peptides. Signalling macromolecules are assembled into the ECM in close vicinity to the cells that secrete them. These chemically different macromolecules such as growth factors, cytokines and hormones, have the potential to alter cell polarity, manipulate cell adhesion, induce or inhibit cell migration and control receptor-mediated apoptosis [19]. In addition, the ECM is a dynamic structure that is constantly remodelled by the cellular activity. Matrix metalloproteinases are proteolytic enzymes that have the ability to degrade the ECM permitting cell migration and exposure to various cell binding sites [20]. Alongside with the molecular composition of the ECM, its physical & mechanical properties are involved in the regulation of cellular responses. Such features allow the ECM to be a functional environment hosting different cues dictating cell responses and deciding on tissue fate. Gradients in cellular–

extracellular architecture exist in the distinctive organs comprising the human body, especially at tissue interfaces, to satisfy the spatially diverse specific functional needs of each tissue [15].

1.2.1. Physical gradients

The natural microenvironment of cells exhibits gradual changes of physical properties like stiffness, porosity, and topology [12]. Stiffness is a physical property that has been described as compliance, rigidity, elasticity, or pliability [1]. Stiffness as measured by the elastic modulus of the substrate contributes to cellular differentiation, regeneration, and plays important roles in disease progression [21]. Stiffness in the cellular microenvironment is often recognised at the interface between loose and dense tissues or temporally between stages of early and late wound healing [1]. Accordingly, physical gradients often take place at tissue boundaries where there is a gradual change in the tissue texture and composition [22]. Gradients existing at the tissue interface include the ligament–bone interface of the articular cartilage and the muscle-tendon interface [23].

Other examples of tissues' natural physical gradients include gradient porosity of bone tissues [24] and gradient collagen fibre orientation in the heart tissues [25]. Bone is a complex tissue that possesses various compositions of organic and inorganic materials affecting the overall stiffness and strength in a gradient manner [26]. A change in the topology and the orientation of collagen fibres have been observed from the epicardium to the endocardium. Such stiffness gradient functions in ventricular wall thickness adaptations during heart contraction cycles [25]. Substrate stiffness was, as well, proven to be an effective cue for cell recruitment during early neuronal differentiation [27].

1.2.2. Mechanical gradients

Biomechanics influences various biological processes; such as morphological and structural adaptations, tissue development and homeostasis. For instance, compressive and tensile stresses are involved in muscle and bone tissues development [28]. During cardiac morphogenesis, the heart beats resulting in shear forces and transmural pressures required for heart development [29]. Branching morphogenesis as studied in mouse embryonic lung is, as well, regulated by mechanical tensions gradients which guide the patterns of budding [30]. The repeated stretching of lungs during foetal breath movements occurring at the third trimester is essential for cell proliferation and lung growth [31].

Mechanical cues can direct basic cellular processes of cell survival [32], proliferation[33] and epithelial-mesenchymal transition critical for the embryonic development [34]. Substrate stiffness has the potential to direct human mesenchymal stem cells towards specific lineages during developmental differentiation as shown in Figure 2 [35].

1.2.3. Oxygen gradients

During cellular respiration, oxygen plays a crucial role functioning as the ultimate electron acceptor for oxidative phosphorylation and energy metabolism. Oxygen tension in human body organs is highly variable from tissue to tissue as shown in Figure 3. Concentration gradients of oxygen act as signals regulating cell fate [36]. In this regard, the decrease in the oxygen availability in cellular microenvironment, below 5%, results in production of hypoxia inducible factors (HIFs). These factors are involved in the differentiation of progenitor cells in Notch, β -catenin, Wnt (Wingless/int), OCT4 (octamer-binding transcription factor 4) and c-MYC [37].

Mammalian development occurs in a relatively low O₂ microenvironment <3%. For instance, O₂ tension is involved in controlling mammalian cell fate during human placental cytotrophoblast development [38]. The surface of the uterus during the early stage of pregnancy is exposed to low oxygen level around 2.5%. In order to generate the utero-placental circulation, cytotrophoblasts of the embryo enter the maternal arterioles achieving connections with the maternal vasculature as shown in Figure 4. The process of differentiation of the proliferating cytotrophoblasts is dependent on the oxygen tension. Cells migrate towards the maternal spiral arteries with higher oxygen tension of value around 8.6% [37].

In bone marrow, as blood flows from central arteries into arterioles and down into sinusoids, progressive drop in the blood velocity and oxygenation is observed creating oxygen tension gradients [39]. Haematopoietic stem cells are exposed to oxygen gradient in which oxygen tension ranges from below 1% in the deeper peri-sinusoidal regions up to 6% near the blood vessels. Haematopoietic stem cells capable of differentiation into all blood lineages tend to reside in niches with little or no perfusion. In such way oxygen gradients assist the differentiation of haematopoietic cells through hypoxic molecular mechanisms [36].

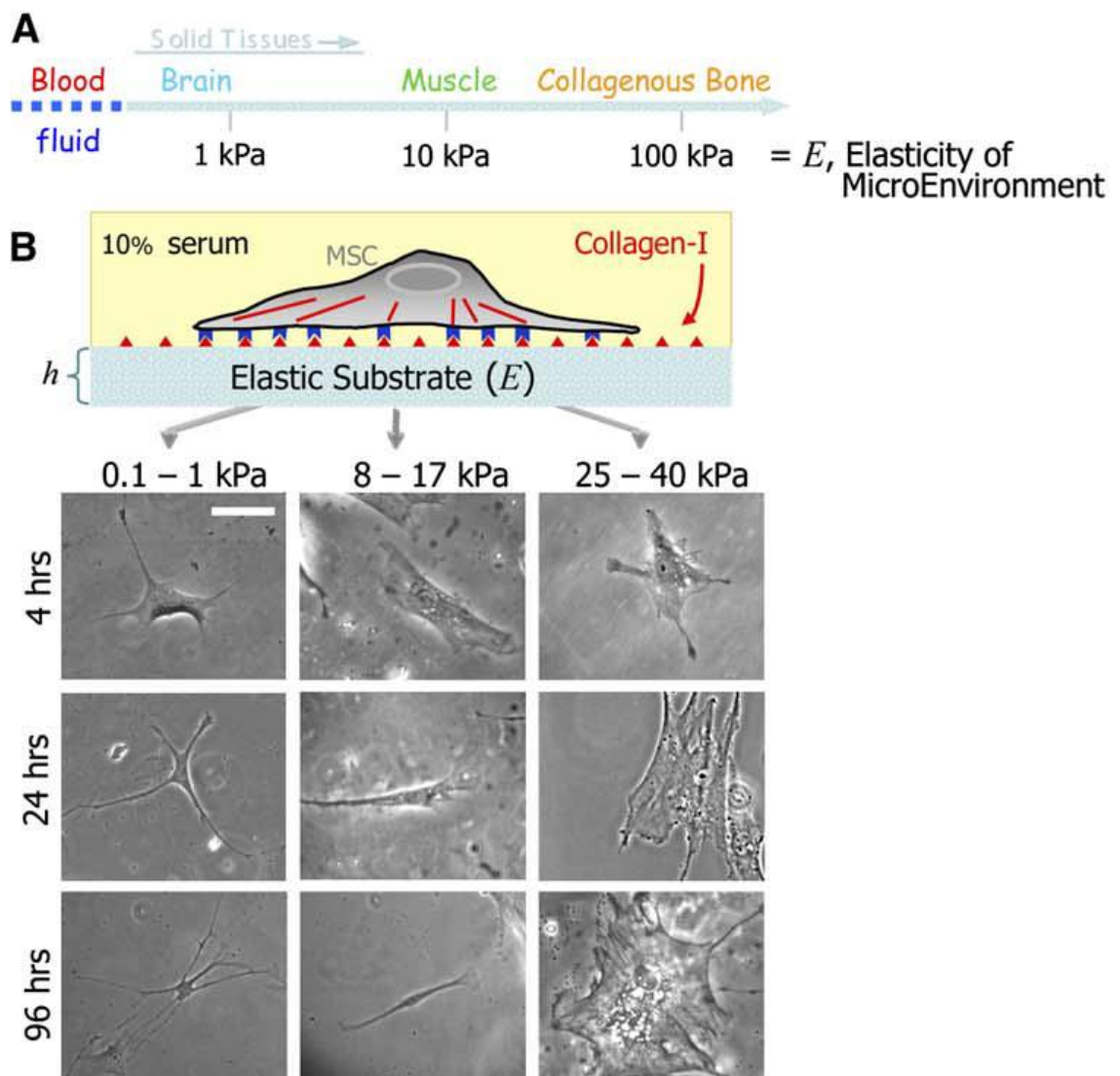


Figure 2: Substrate stiffness directs mesenchymal stem cells differentiation. (A) Stiffness of variable body organs in terms of elastic modulus. (B) Hydrogel system with controlled variable elastic moduli directing naïve mesenchymal cells towards specific lineages. Scale bar is 20 μm . Reproduced from [35].

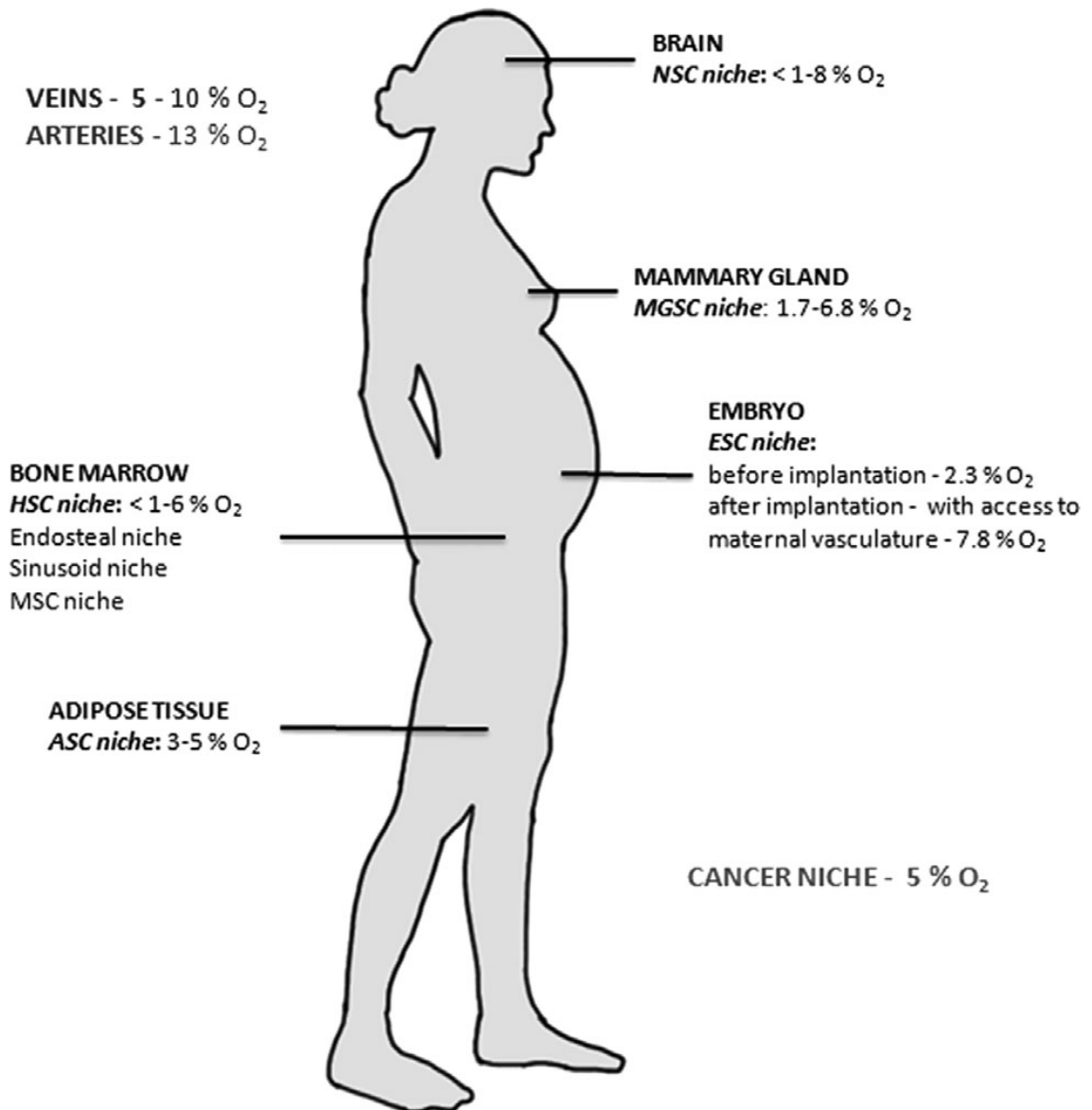


Figure 3: Stem cell niches within human body are exposed to variable oxygen tensions. Reproduced from [36].

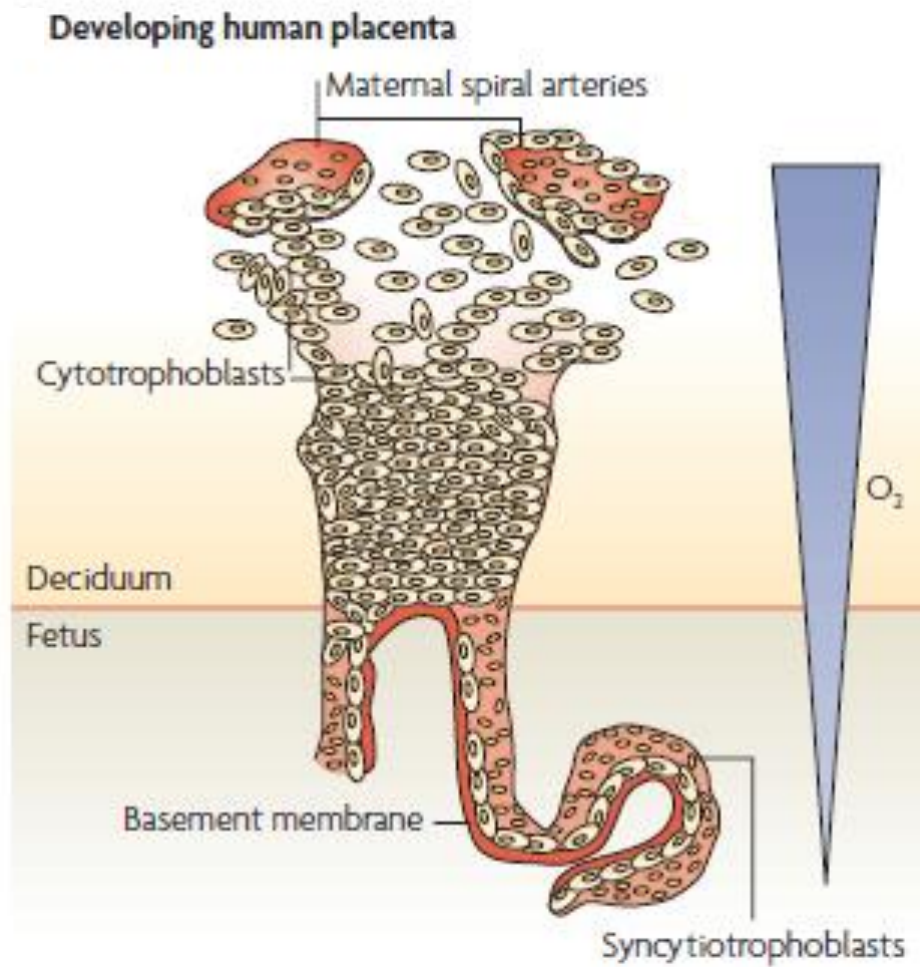


Figure 4: Oxygen gradients in the developing human placentas showing the differentiation pathway taken by cytotrophoblast stem cells in human uterus. Reproduced from [37].

1.2.4. Chemical gradients

1.2.4.1. Morphogenesis & developmental gradients

Cellular rearrangements in tissue morphogenesis take place during embryonic development. Cellular movements do not suffice as such for building functional tissues architectures; they have to take place at the correct location and time [40]. In this regard, gradients of morphogens can guide cell behaviours spatially to assist cellular movement to form new tissues [3, 41].

Signals secreted at a defined location form a concentration gradient as it extends through tissues [3]. Subsequently, cellular responses vary along these developed concentration gradients as a function of the cell position & the threshold concentration. In this context, morphogenesis is regulated by the shape of the gradient which is initially controlled via the geometry of the source cell population secreting the morphogen and the geometry of the surrounding tissue representing the sink [40].

1.2.4.1.1. *Embryogenesis*

Various morphogen gradients including hedgehog (SHH), Wnts, bone morphogenetic protein (BMP), transforming growth factor- β (TGF- β), and fibroblast growth factors (FGFs) have been reported to be involved in the patterning of mammalian embryos [42]. SHH gradient is involved in the anterior-posterior patterning of the distal part of the vertebrate limb [43]. It acts as a long-range morphogen directing the pattern of neurogenesis in the ventral region of spinal cord through positional information dictated to the ventral neural progenitors [44]. During development, outgrowth of axons establishes neuronal connections to the nervous system and peripheral tissues through defined pathways that are controlled by cues of chemoattractant or chemorepulsive gradients. Nerve growth factor (NGF); a member of the neurotrophin family, possesses a trophic effect on sensory and sympathetic neurons. It is secreted from preinnervational tissues, forming a gradient capable of attracting growing axons toward the correct target in mouse embryo [45]. Other examples involved in the embryonic development include the opposing gradients of BMP and nodal TGF- β which act as morphogens inducing molecular mechanisms organizing the uncommitted cells of zebrafish into a well-developed embryo [46].

1.2.4.1.2. *Organogenesis*

During organ formation from tissues; organogenesis, morphogen gradients play an important role giving instructions essential for branching morphogenesis [40]. This

process is responsible for shaping the complicated branching architecture of various organs [47]. An example for branching morphogenesis is the fibroblast growth factor (FGF) family secreted from mesenchymal tissues which provide positional information essential for mammalian lung morphogenesis. The developed gradient acts as a chemoattractant for the growing epithelial branches comprising the lung tissues [48]. BMP4 is, as well, involved in the lung bud morphogenesis, yet in an opposing direction. Lung organogenesis is dependent on the geometries of FGF10 and BMP4 opposing signalling gradients where the size and the position of the gradients matter to the branching morphogenesis of the lung [49].

Differential binding of bioactive molecules to the ECM and its receptors is capable of production of spatial concentration gradients. An example for this is the ability of members of the fibroblast growth factors to bind to heparan sulphate present in the ECM. There is a preferential binding of heparan sulphate to the FGF10 over FGF7. This creates steep gradients of FGF10 near cell sources producing it and in contrast, FGF7 diffuses readily creating longer gradients. This is concomitant with the different roles played by each growth factor in the process of branching morphogenesis in which cell elongation occurs in response of steep gradient of FGF10 whilst branching of salivary glands is triggered by long mild gradient of FGF7 [42].

1.2.4.1.3. Growth and functionality

Morphogenesis elicits continuous change of the tissue shape and thus usually happens in parallel with corresponding change in mass and growth [40]. Gradients of Ran-GTP–importin- β secreted from the chromosomes provide positional signals organising the mitotic spindle during mitosis. Regions close to the source chromosome maintain microtubule nucleation whilst stabilisation occurs at greater distances away from the origin [50]. Similarly, the efficient functioning of variable body organs such as bones and the heart are also regulated via bioactive molecule gradients [23]. For instance, the endocrine system utilizes soluble molecules gradients to guide different functions in the body [51].

1.2.4.2. Immune response

The critical role played by the biomolecule gradients in the process of immune response involves guiding the body's immune cells with directional cues to migrate towards the infection sites. Chemotaxis is regulated via natural chemical gradients of various chemoattractants, along which cells migrate. The process is triggered via recognition of

the pathogen by the phagocytic immune cells; macrophages. After identification of the pathogen with the macrophages, they start secreting signalling proteins, called cytokines, in a gradient manner [2]. Cytokines (CXCL-8 & TNF- α) gradients and bacterial peptides originating from the site of infection stimulate the endothelial cells lining the region's blood vessel to express cell adhesion molecules and variable adhesive proteoglycans. The process is of chemoattractant-induced activation of spatially localised signals which provoke the circulating immune cells; neutrophils to take a polarized morphology along the direction of the cytokine gradient [52]. The process is complemented by the movement of fibroblasts towards the wound space. The overall process of chemotaxis initiates directed migration of variable immune cells; leukocytes, towards the site of infection to destroy the infecting pathogen [53].

1.2.4.3. Cancer

The development of metastatic cancer was found to be implicated with biomolecules gradients [54]. Cells escaping from the original tumour site start to invade new tissue alongside gradients of proteins that induce chemotaxis. Thereafter, migrating cancer cells recruit endothelial cells to create new vasculature in the new cancer site [54]. Once more, angiogenesis is promoted via the developed proteins' gradients[55]. CXCL-8; a cytokine recruited by neutrophils in the immune response process during inflammation, is as well involved in cancerous cell proliferation [56]. Common tissues subject to metastasis include lymph nodes, lungs, liver, and bone marrow. Such tissues express relatively large quantities of cytokines that can trigger the chemotaxis and angiogenesis processes resulting in metastasis [54].

1.3. Cellular responses to gradients

In response to biological gradients, cells adhere to three sequential steps including directional sensing followed by cellular motility and polarization [57]. The process of cell motility can be in response to various physical and chemical stimuli. Chemoattractant-induced directional cues for cell migration are not restricted to the process of immune response but also play important roles in morphogenesis, homeostasis and cancer metastasis [58]. Cells migrate in response to chemoattractants stimuli gradients in a process known as chemotaxis. The process is named haptotaxis when cell migration occurs in response to surface-attached molecules. On the other hand, mechanotaxis or durotaxis describe the cellular migration in guidance of biophysical cues. Other forms of cellular migration include galvanotaxis which occur

in response to gradients of electrostatic potential, phototaxis, geotaxis and tensotaxis in response to light intensity, gravitational potential or extracellular tension respectively [59]. A summary of different forms of cell migration is listed in Table 1.

Other forms of cellular responses towards biological physicochemical gradients are summarized in Figure 5. Examples include changes in cell morphology as a function of the steepness of FGF10 & FGF7 gradients as observed in fibroblasts [42]. Equally, the morphology of fibroblasts is subject to the orientation and nature of substrate[60]. The ability of ventral progenitor cells to differentiate into different neuronal subtypes in response to graded concentrations of SHH demonstrates cellular response towards chemical gradients [44]. Likewise, directing naïve mesenchymal cells towards specific lineages cells in response to stiffness gradients has been reported [35].

1.4. Biomimetic gradient scaffolds

Bioactive molecules diffuse isotropically with no restrictions in free solution. Consequently, frequent supply and removal of known volumes of the molecules at specific locations are required to maintain bioactive molecule gradients [2]. From these perspectives and to achieve anisotropic concentrations along which different responses could be elicited, tissue engineering approaches can be utilized to generate gradient biomimetic three dimensional scaffolds. Such systems represent growth environments for cells provided that optimal oxygen and nutrient conditions are maintained. In ideal conditions, the scaffolds permit self-assembly of cells into tissues after cells deposit ECM forming 3D biomimetic architecture of optimum integrity after the scaffolds degrade [13].

Hydrogels are highly hydrated ECM-like viscoelastic networks that possess diffusive transport characteristics tuneable based on their chemical and physical characteristics. They provide 3D microenvironments that mimic the natural ECM in many aspects and thus the development of gradient hydrogels offers suitable models to facilitate graded tissue formation [14]. Hydrogels made from natural or synthetic biomaterials were used to establish biomolecule gradients. However, the use of hydrogels is subject to variability in the placement of cells and bioactive molecules. The inability to determine the exact bioactive gradient to which individual cells are exposed to hinders the correlation of observed cellular responses to spatiotemporal profiles of the bioactive molecules gradients.

Table 1: Summary of various physical and chemical stimuli affecting cellular migration, modified from [59].

Gradient		Cell migration	<i>In vitro</i> assessment		Reference
Type	Stimuli		Cell type	Stimuli example	
Chemical	Soluble factors	Chemotaxis	PC12 cell neurites	Nerve growth factor NGF	[61]
	Surface-attached molecules	Haptotaxis	Human melanoma cell line	Substrate bound vitronectin	[62]
Physical	Substrate rigidity	Durotaxis/ Mechanotaxis	NIH 3T3 mouse fibroblasts	Polyacrylamide gel with type I collagen with variable stiffness	[59]
	Electrostatic potential	Galvanotaxis	pRNS-1-1 & PNT2 Prostate cells	Electric field	[63]
	Light intensity	Phototaxis	<i>D. discoideum</i> strain AX2 and GRP125-null mutants	Light	[64]
	Gravitational potential	Geotaxis	Balancer cells/cilia Of <i>M. leidyi</i> or <i>B. infundibulum</i> statocysts	Angle of orientation of microscopic slides	[65]
	Tension	Tensiotaxis	Chick forebrain neurons	Mechanical tension of 2 glass needles	[66]

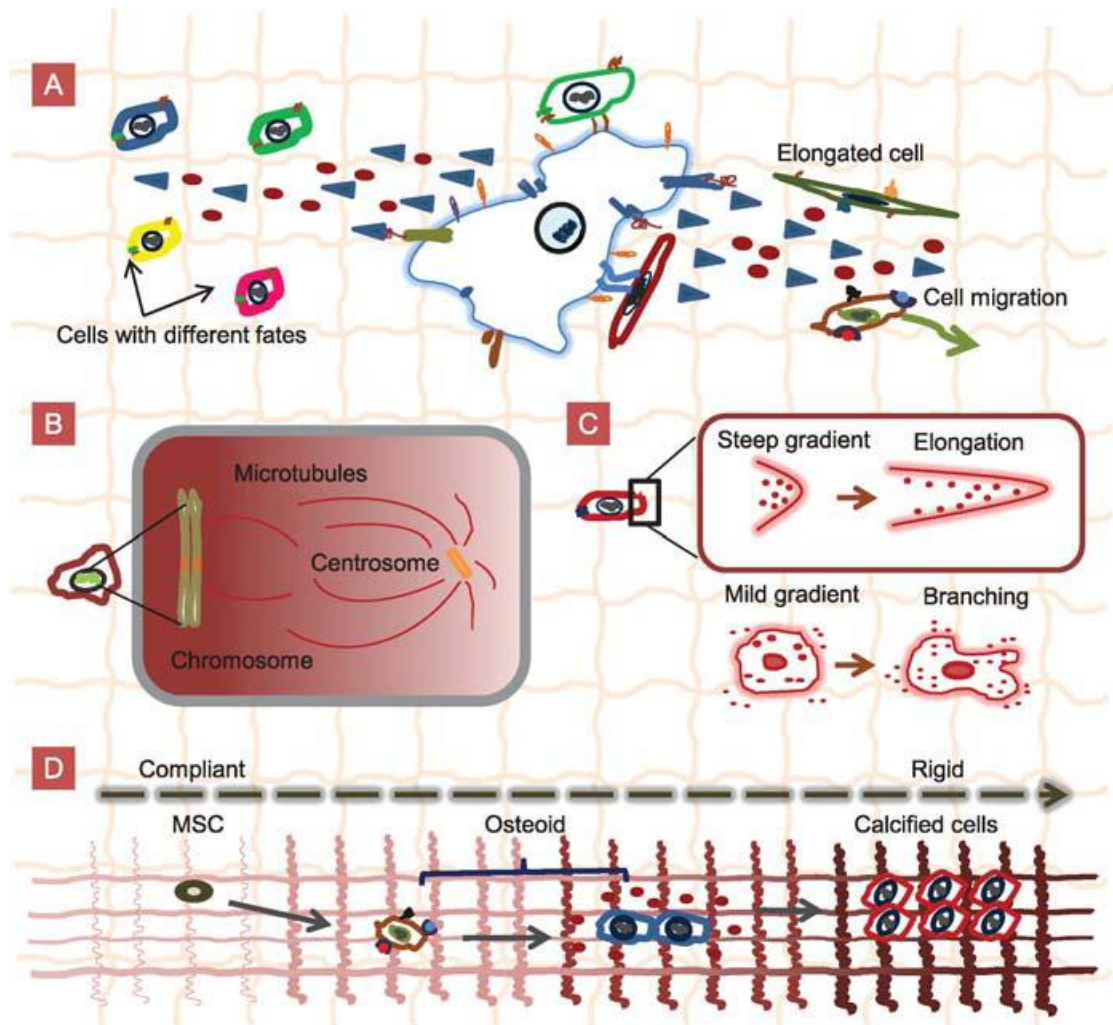


Figure 5: Cellular responses towards *in-vivo* physicochemical gradients. A: cell migration, cell elongation, and cell differentiation in response to chemical gradients. B: Ran-GTP gradient guide the mitotic spindle during mitosis. C: Morphology as a function of gradient steepness. D: Mesenchymal stem cells differentiate into osteoids or calcified bone cells in response to signals of mechanical gradients in the ECM. Reproduced from [12].

Moreover, it is difficult to observe individual cell responses due to the optical properties of the 3D structure of some hydrogels [2].

1.4.1. Hydrogel Matrices

1.4.1.1. Chemical gradients hydrogels

1.4.1.1.1. Soluble chemical gradients

3D collagen scaffolds with gradient of angiogenic vascular endothelial growth factor (VEGF) have been fabricated to follow endothelial cell migration. The cells encapsulated within VEGF gradient collagen hydrogels demonstrated “sprouting” structures as compared to limited migration of endothelial cells in control scaffolds. This demonstrates that biomimetic approaches adopted to replicate the cellular microenvironments have managed to promote vascularization [67].

Other examples include gradients of BMP and insulin-like growth factor (rhIGF-I) loaded microspheres within alginate and silk scaffolds. Temporal release of growth factors has created gradients in the hydrogel scaffolds and have been used to study the differentiation of mesenchymal stem cells towards the osteo-chondrogenic lineages. The gradients range and slope in silk hydrogel were capable of inducing human mesenchymal stem cells (hMSCs) towards osteogenic and chondrogenic differentiation along BMP gradients and cross-gradients of BMP/rhIGF-I. However, this was not the situation within alginate scaffolds because of the rapid diffusion of growth factors [68]. Equally, the orientation of pheochromocytoma (PC12) cell neurites in response to stable NGF concentration gradients across agarose hydrogels has been studied. PC12 cells have been plated underneath the agarose scaffold cast in a compartmental diffusion chamber. A minimum concentration gradient value of 133 ng/ml per mm was required to achieve effective guidance of neurite growth [61].

On the other hand, poly-acrylamide-hydrogels have been generated with gradients of FGF-2, ciliary neurotrophic factor (CNTF) or foetal bovine serum (FBS) inkjet printed on top of them. Primary foetal neural stem cells were seeded on top of the printed gradients. Differentiation towards the glial fibrillary acid protein-positive phenotype or smooth muscle cells were found to occur along CNTF or FBS gradients respectively. No differentiation was observed along FGF-2 gradients [69].

1.4.1.1.2. Immobilized chemical gradients

Gradient immobilisation of growth factors and adhesion peptides in hydrogel scaffolds have been implemented to study cellular behaviour in response to the developed

gradients. Ligand adhesion peptides Arg-Gly-Asp-Ser (RGDS) have been immobilized in poly (ethylene glycol)-diacrylate (PEGDA) hydrogels in a gradient manner to test the response of endothelial cells. Cellular attachment and spreading has been found to occur along the areas with the lower PEGDA concentration as compared to spread morphology in the regions with higher concentrations [70]. Moore *et al.* immobilized NGF and neurotrophin-3 (NT-3) in a gradient manner in polyhydroxyethylmethacrylate (pHEMA) hydrogel to study the chick dorsal root ganglia (DRG) responses. Receptors for these growth factors have been shown to be co-localized on DRG cells. A NGF concentration gradient of 200 ng/mL/mm has been shown to guide DRG neurite growth when a synergistic NT-3 concentration gradient of 200 ng/mL/mm existed [71]. Covalent linkages involved in immobilizing signalling molecules can affect the cellular uptake signalling pathways. This can result in hindering of the replication of the natural microenvironment and hence soluble protein gradients are employed to overcome these drawbacks [12].

1.4.1.2. Physical gradients

1.4.1.2.1. Stiffness gradients

Gradient hydrogels with gradual change in the elastic modulus have been fabricated to study the effect of material stiffness on cells. Gradient in elastic modulus in polyacrylamide (PAAM) hydrogels ranging from 140 to 300 kDyn/cm² has been found to affect fibroblasts durotaxis. Cell residence or migration towards the stiffer regions has been observed [59]. Similar durotactic effects towards stiffer substrates have been observed with vascular smooth muscle cells [72] and macrophages [73] in gradient elastic modulus PAAM or PEGDA hydrogels respectively.

Combined chemical and physical gradients in polyethylene glycol (PEG) hydrogels have resulted in directing fibroblasts alignment, migration, and attachment as a response to material stiffness together with proliferation along the developed chemical nutrient gradient [74]. In a different study, photodegradable PEG hydrogels demonstrating elasticity gradients in the range of 7–32 kPa have been found to manipulate the differentiation of valvular interstitial cells seeded on top of them. Smooth muscle actin (α -SMA) stress fibres were observed towards the higher elasticity regions following 3 days of culture designating myogenic differentiation [75]. Equally substrate stiffness can influence the processes of cell spreading and proliferation. Methacrylated hyaluronic acid scaffolds exhibiting 15 mm long gradient of elastic modulus from \sim 3

to ~90 kPa were shown to affect the proliferation of hMSCs. Cellular spreading and proliferation were found to be optimal in regions possessing elastic modulus higher than 25 kPa [76].

1.4.1.2.2. Topographical gradients

Topographical features such as wells, grooves, pores, and fibres attribute to the scaffold architecture and are involved in the directing cues dictating cell fate. Murine embryonic cortical neurons were cultured on top of Poly-D-Lysine (PDL) and MatrigelTM-patterned Polydimethyl siloxane (PDMS) substrates of variable groove heights ranging from 2.5 to 69 μm . The depth of the groove was found to have a significant effect on the growing axon. The axons growth followed the straightest permissible path in the PDL substrate suggesting that topographical and biochemical cues have significant roles in axon turning. Deep grooves larger than 22 μm permitted axon growth inside the groove while in shallow ones smaller than 4.6 μm , axons continued to extend into or outside of them [77]. Similarly, topographical features have been proven to direct rat hippocampal neurons on silicon oxide surfaces [78] or fibroblasts alignment on nanogrooved patterns [79]. The morphological differences between fibroblasts cultured on smooth and nanogrooved substrates ranging from 5-350 nm deep substrata have been assessed. Fibroblasts alignment occurred as a function of the groove depth with random spread over smooth substrata [79].

1.4.1.2.3. Porosity and pore size gradients

Porosity and pore size affect cell viability through regulation of cellular binding, movement, intercellular communications, and nutrients and metabolites transport [12]. Porosity gradient scaffolds can be either in form of continuous change in porosity; gradient nature or step-wise change; graded nature[80]. Tuneable porosity gradients have been fabricated in gelatin hydroxyphenylpropionic acid (GTN-HPA) hydrogels with biocompatible carboxymethyl cellulose tyramine (CMC-TYR) polymer to study the chemotactic effect of HT1080 human fibrosarcoma cells. The study demonstrated that cellular migration occurs along the pore size gradient in the absence of chemoattractant. Synergistic effect was observed when chemoattractant; FBS gradient is opposite to the porosity gradient. In such way, fibrosarcoma cells were migrating to the chemoattractant in one direction and towards large pores in the opposite direction, resulting in a region of high cell density in the middle of the chamber [81]. Similarly, PEGDA hydrogels with gradients of porosity have been generated using freeze drying

technique alongside RGDS chemical gradient to investigate the porosity effects on the endothelial cells spreading and proliferation [70].

1.4.2. Non hydrogel matrices

The gradient biomimetic approach is not limited to hydrogel based scaffolds. Biomimetic poly caprolactone (PCL) scaffolds with pore size and porosity gradients have been fabricated using a centrifugation method and have shown that osteoblasts tend to grow faster within regions with pores ranging in size from 380 to 405 μm . However, the actual formation of bone takes place in regions with 290–310 μm pore size [82]. Similarly, hydroxyapatite (HA) ceramic scaffolds with gradient channel structures have been prepared using modified freeze-casting technique. The scaffolds showed interconnected gradient channels mimicking the porous network of bone. The scaffold supported self-seeding of cells via capillary flow through the gradient channel structures [83].

In order to mimic the nanofibrous protein structure present in the ECM, polymer or composite nanofibers from natural or synthetic materials have been developed. Tuneable physical and chemical properties of nanofibers can be utilized to manipulate cell growth and tissue fate. A gradient heparinized nanofibrous scaffold was developed using co-electrospinning of chitosan/poly ϵ -caprolactone (CS/PCL) with various ratios to support endothelial cells alignment on the blood vessel lumen to prevent thrombosis. Heparinization and immobilization of VEGF was subsequently achieved within the gradient CS/PCL in a way that the quantity of heparinized chitosan nanofibers increased gradually towards the lumen surfaces of the tissue engineered vessel. Human umbilical vein endothelial cells (HUVECs) proliferated to form a monolayer on the top of the gradient scaffold creating small-diameter blood vessel grafts replicating the mammalian vessels [84].

1.5. Methods of generation of chemical gradients

1.5.1. Cell culture systems

Generally, to produce gradients on two dimensional planar surfaces, two categories of manufacture could be employed including bottom-up and top-down technologies. Top-down technologies rely on the use of external sources of ultra violet (UV) light, etching solutions, plasma, corona or chemical degradation. On the other hand, the bottom-up technologies depend on the introduction of different building blocks of silane, thiol or macromolecules on the surface without interruption of the bulk properties. The process

of introducing the building blocks can be performed via infusion, diffusion, microcontact printing, microfluidic or electrochemical methods [16]. A range of cell culture systems employing the bottom-up technologies can be used to generate gradients of bioactive molecules on a single focal plane to study single cell responses [2]. A detailed description of each system, its advantages and limitations can be found in the critical review written by Keenan and Folch [2].

1.5.1.1. Micropipette-generated gradients

Steep gradients of cyclic adenosine monophosphate (cAMP) and epidermal growth factor (EGF) have been generated via pneumatic ejection through micropipette positioned at a known distance away from the cells in the extracellular space using a manipulator and microscope [85, 86]. The system is shown in Figure 6a. The developed gradient is controlled via the ejected “puffs” volume and frequency of ejections. However, micropipette assays do not result in reproducible or controllable gradients. The shape of micropipette tips, hydrodynamic properties of the micropipette and vibrations, thermal imbalances or evaporation during the experiments contribute to the factors altering the gradient during the experiment [2].

1.5.1.2. Boyden Chamber

The generation of chemoattractant gradients using Boyden chamber or transwell assay depends on placing a chemoattractant solution in the lower compartment of the culture chamber. The upper compartment is composed of a porous membrane and is seeded with cells. This compartment is placed over the bottom compartment and thus the chemoattractant diffuses through the membrane up to the cell compartment as shown in Figure 6b. Subsequently, the generated gradient stimulates cell migration through the transmembrane towards the chemoattractant solution. However, the inability to control the generated gradients because of the fluid level imbalance between the upper and lower compartments represents one limitation to the usage of Boyden chambers in chemotaxis assays. Furthermore, the quantification of the developed gradient is often complicated by the presence of the non-transparent membrane [2]. However, this could be overcome using confocal microscopy or fluorescent dyes. Endothelial cell migration in response to the chemotactic gradients of VEGF-A165 was studied in a modified Boyden chamber to study mechanisms of angiogenesis [87].

1.5.1.3. Zigmond Chamber

The Zigmond chamber represents another system used to study the chemotactic effect of different molecules on cell migration as introduced by Sally Zigmond in 1977 [88]. The chamber is composed of two parallel channels fitted within a glass slide. A glass ridge is situated below a glass coverslip on which cells were seeded. A thin gap between the coverslip and the glass ridge ranging from 3 to 10 mm tall and 1 mm wide was created between equal volumes of the sink and source channels as shown in Figure 6c. The developed gradient can be reproduced via the fine control over the geometry of the system and the subsequent cellular responses in terms of cell migration or differentiation is visualized using microscopy. The polarization of differentiated human neutrophil-like HL-60 cells were studied in response to N-formyl-Met-Leu-Phe (fMLP) gradient generated in the Zigmond chamber under hypoxia (<3% O₂). Extensive suppression of polarization was observed along the direction of the fMLP gradient [89]. The system is capable of generation of rapid short term gradients; however, it is unable to maintain steady gradients over long period of time. Furthermore, the system is susceptible to evaporation resulting in variability of concentrations of the bioactive agents over longer periods of time. The system is also restricted to simple gradient generation because of the limited geometry and thus unable to study cellular responses towards complex multi-factor gradients [2].

1.5.1.4. Dunn Chamber

A modified Zigmond chamber with less susceptibility to evaporation was introduced by Graham Dunn [90]. The system is composed of concentric source and sink' chambers covered with an inverted glass coverslip seeded with cells (Figure 6d). The modification resulted in generation of gradients less susceptible to evaporation [2].

Boyden and Dunn chambers were utilized to follow neural stem/progenitor cells migration to compare the transfilter migration rate and single-cell migration speed. The results demonstrated that each differentiation stage owns different migratory capacity in response to stromal cell-derived factor 1 (SDF-1) [91]. Once more, and like the aforementioned systems, the gradients are short lived, develop along a single axis and are only controlled by the geometry of the system and cannot be changed once set up [2].

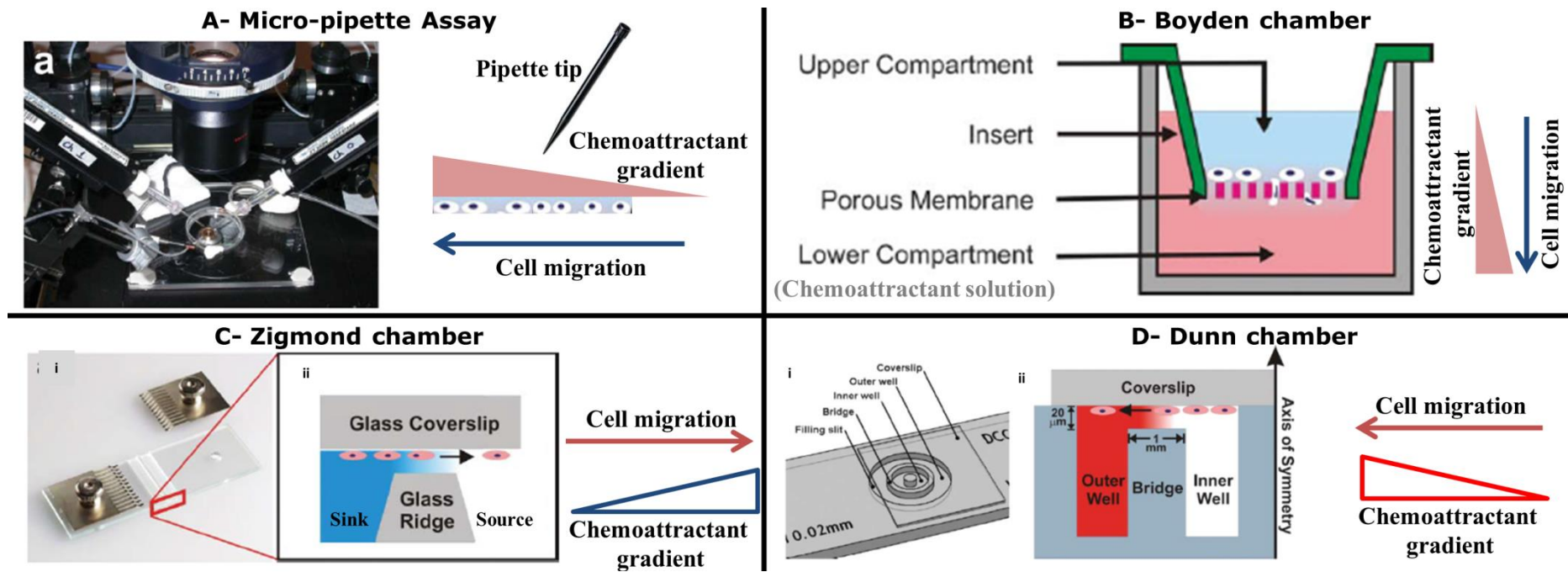


Figure 6: *In vitro* cell culture assays used to generate bioactive molecules gradients to study cell responses along the direction of the developed gradients. Modified from [2].

1.5.2. 3D systems

In the human body, cellular niches are complex 3D microenvironments that permit cellular growth and communications in guidance of variable soluble factors, ECM topographies and compositions. Tissue engineering approaches aim at production of cell-laden 3D scaffolds to study mechanisms of cell growth and differentiation. These 3D systems have the potential to expose the cells to conditions similar to their natural microenvironments and thus will be better representatives than two-dimensional (2D) cell culture systems in following gradient driven cellular responses[13]. The misrepresentation upon using 2D models arises from inconsistencies in morphologies, cell-cell and cell-matrix interactions, and differentiation potentials as compared to 3D counterparts. A range of methods can be employed to generate gradients of physical and chemical factors in 3D scaffolds. Some of these methods are used concomitantly to generate the desired gradients with different properties. Here, we briefly list the broad categories employed in generating chemical gradients highlighting the advantages and limitations of each method.

1.5.2.1. Microfluidic Systems

Microfluidics refers to the fine control over the flow of minute amounts of liquids in micrometre range channels [14]. Flow-based microfluidic platforms were utilized to generate 2D bioactive molecules gradients [92]. Equally, the approach has been utilized to create gradient hydrogels in microfluidic devices [14]. In comparison to 2D bioactive molecules gradients, 3D systems reduce the shear stress applied on cells as induced by liquid perfusion [14]. Furthermore, 3D matrices encapsulating cells offer maintenance of the signals in a way that mimics the restricted extracellular diffusion observed in natural microenvironments. Conversely, 3D systems do not account for the complex multicellular nature of tissues and usually fail to mimic tissue vasculature. Recently, microfluidic techniques applied in 3D cell culture are driven by the ability of multiple cells co-culture, production of and tuning of stable bioactive molecules gradients and finally the incorporation of perfusion systems to mimic tissue vasculature [93]. Applying microfluidics approaches, the spatial and temporal delivery of bioactive molecule and the gradient slope are tuneable via adjustment of the flow rates of the inlets and outlets together with the channel geometry. Microfluidics platforms represent excellent *in vitro* tools for studying the function of soluble morphogen gradients. However, such systems are not suitable to reflect on *in vivo* usage or potential clinical applications [17]. Based on the device employed to generate the flow of the liquid, three

main categories are recognized to establish gradients using microfluidics. Detailed description of microfluidics gradient generators systems can be found in Keenan and Folch [2].

1.5.2.1.1. Laminar Flow systems

Laminar flow gradient generators are systems in which two or more solutions are brought into the microchannel networks simultaneously. As fluids go through these connected networks, they diffuse from one compartment to the other and pass through multiple micromixers to create the desired gradients [94]. Such systems maintain soluble biomolecules concentrations in inlet source and outlet sink channels and consequently the gradients can be sustained for long periods of time [17]. On the other hand, the convective flow can wipe away the signalling factors secreted by cells and generate asymmetrical mass transport [95]. Furthermore, it induces shear stresses that affect cell behaviours like anisotropic migration and complex the process of studying gradients driven cellular responses [96]. As an approach to overcome such drawbacks, flow barriers; capillary channels or thin films of polymers with nanoscale pores, have been utilized to introduce the signalling bioactive molecule to the system via diffusion [17]. Amadi *et al.* introduced a microfluidic device employing a parallel arrangement of wells and channels to reduce convective flow. Low resistance channels in parallel with the gel channel, resulted in degeneration of pressure gradients between the source and sink wells thus minimizing the convection of solute in this region. The device generated gradients of platelet derived growth factor (PDGF-BB), SDF-1 or VEGF, in vascular smooth muscle cells, Jurkat T-lymphocytes or bovine aortic endothelial cells loaded collagen gels respectively. The subsequent cell migration was evaluated in guidance of the developed chemical gradients irrespective of the interstitial flow between the two wells [97].

1.5.2.1.2. Pneumatic Valve Systems

Pneumatic valve systems equally generate chemical gradients with extra control over the timing of gradient formation[98]. This occurs via integration of pneumatic actuated valve; a thin elastomeric membrane separating the fluidic layer from pneumatic control microchannels network [2]. This results in creation of more complex experimental conditions resembling signalling in physiological microenvironment [98]. Alongside the temporal control of initiation of the gradients, the relatively small reagent volumes utilized allow the accumulation of cell signals essential for many biological processes

unlike the observed loss of these signals upon usage of convective-based signals. Limitations include minimal subsequent control over the developed gradient that is limited to opening and closure of the valve [2]. Lii *et. al.* utilized the pneumatically actuated microvalves principle to achieve dynamic control over the 3D system encapsulating embryonic stem cells (ESCs) and studied chamber-to-chamber communication of diffusible factors. Cell tracker dye incorporated in a PEGDA hydrogel in the neighbouring chamber was allowed to diffuse between chamber through the pneumatic valve into the MatrigelTM to gradually stain the ESCs [99].

1.5.2.1.3. Microfluidics without Pumps or Tubes

Alternative platforms to laminar flow systems and valve controlled systems are the tubeless systems. They permit gradient generation depending on passive pumping, or surface-energy driven fluid flow without the need for complex flow channels or complicated pumping tools. Furthermore, they allow multiple gradient generation with possible automation [17]. Angiogenic sprouting in response to VEGF gradients was assessed using tubeless microfluidic device to develop 3D endothelial-lined lumens using HUVECs loaded Collagen I/MatrigelTM. Co-cultured 10T1/2 mouse smooth muscle cells in the connecting side channels of the triple microchannel system that contains the patterned endothelial-lined lumen (ELL) in the central channel reduced the number and size of endothelial sprouts as compared to ELL in response VEGF gradient alone [100]. A schematic presentation of microfluidics systems discussed in the three categories of fluid flow in the microfluidic channel is shown in Figure 7.

1.5.2.2. Molecular diffusion

The source-sink model of diffusion is the underlying mechanism explaining the morphogen concentration gradients in the complex multicellular tissues and during embryonic development [41, 101]. In this environmental source-sink diffusion model, morphogens are secreted from source cells, diffuse in target tissues and are subsequently degraded. A relatively simpler way of creating gradients of soluble agents across hydrogel scaffold is to allow diffusion of signalling agent between source and sink compartments [12, 14]. The method relies on passive diffusion of soluble molecules from source compartment without the need of pumping or controlled flow tools employed in microfluidics.

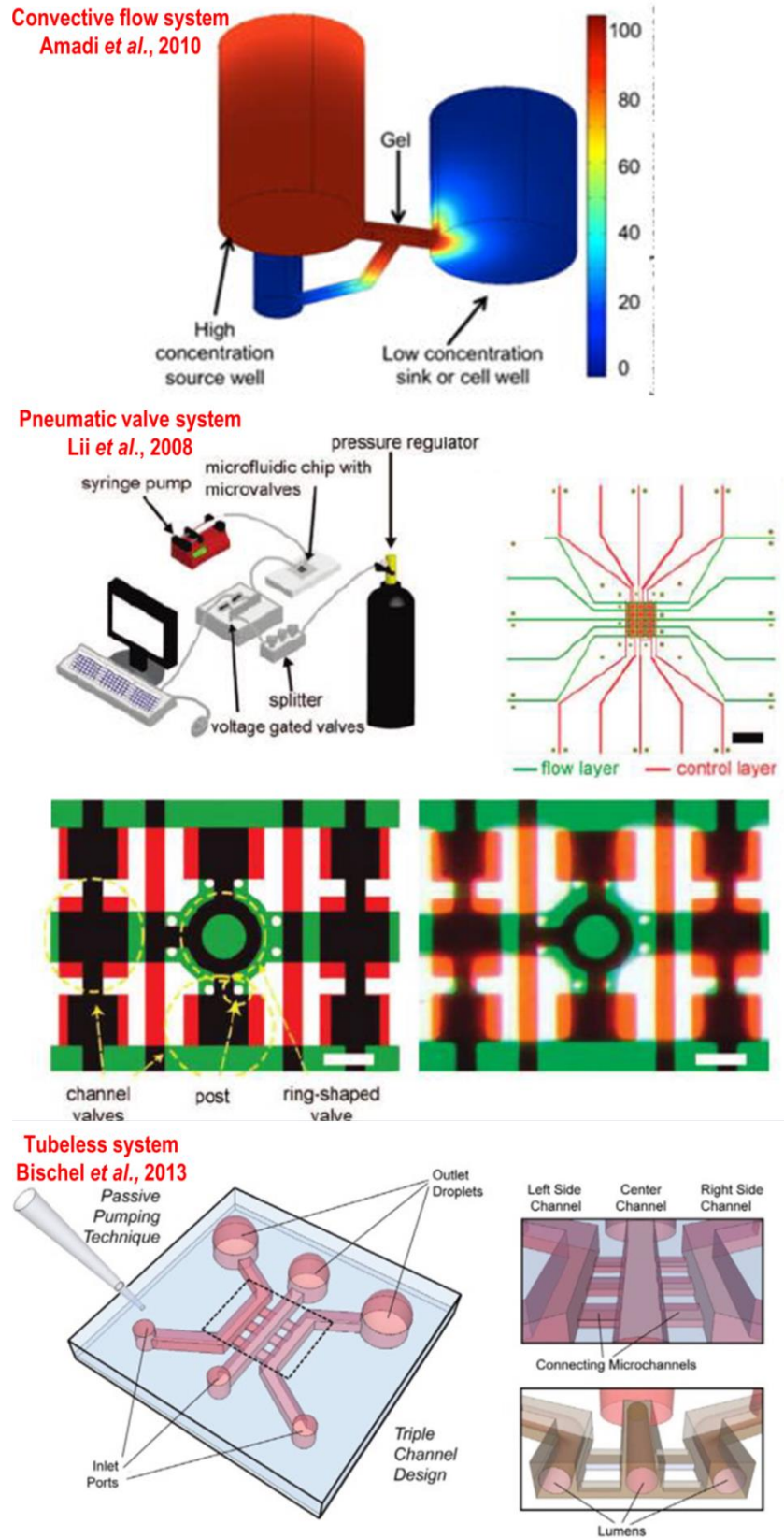


Figure 7: Chamber designs of different microfluidics-based systems utilized to generate chemical gradients in cell-laden hydrogels. Modified from [97, 99, 100]

In this context, the encapsulated cells within the scaffold matrix are not exposed to shear stresses and asymmetric mass transport generated in convection-based methods [95]. However, molecular diffusion methods are time consuming and require continuous replenishment of source/sink compartments to maintain stable linear gradients over days [12, 61]. Furthermore, the method is liable to evaporation of the liquid compartments affecting the concentrations of the signalling molecules with time. Cao & Shoichet [61] managed to create stable linear concentration gradient profiles of nerve growth factor NGF across 3D agarose membranes based on the molecular diffusion approach. Based on the kinetics of diffusion of NGF across agarose hydrogels, source and sink compartments were regularly changed every 6 hours to achieve steady-state diffusion and maintain stable concentration gradients for axonal guidance studies. Furthermore, they defined the minimum and the maximum distance required for guidance of neurite growth of PC12 cell line plated underneath the hydrogel membrane. Neurite outgrowth was subsequently assessed by phase contrast microscopy as a function of distance away from the NGF source compartment [61].

1.5.2.3. Localized Controlled Release

An alternative approach to create gradients of soluble factors is using drug delivery systems that act as depot for temporal release of biomolecules encapsulated within depot biomaterials. Fine tuning of the gradient characteristics can be controlled via combination of biomaterials release/degradation properties and spatial localization of depot. Such approach mimics the natural signalling process, in which temporal morphogen release from a specific cell source affects the nearby cells in a concentration-dependant manner [17].

Employing drug delivery approaches in developing biomimetic gradient scaffolds can be by one of two approaches. One approach involves spatial localization of biomolecules depots and counting on the release characteristics of the system to create gradients of released bioactive agents. The other depends on accurate spatial distribution of the biomolecules depots within the scaffold in a gradient manner to create the desired bioactive molecule gradients.

1.5.2.3.1. Release depots in biomaterials

As an example to show the ability of biomaterials and drug delivery approaches to create gradients of bioactive agents, Suciati *et al.* fabricated layered scaffolds via heat sintering method of recombinant human bone morphogenetic protein-2 (rhBMP-2) loaded and

blank Poly (D, L-lactide) (PLA) microparticles. C2C12 mouse myoblasts were subsequently seeded in the interconnected porous scaffold and the zonal release created a gradient of the diffused rhBMP-2 that induced site-specific osteogenic differentiation [102]. In another example, spatial positioning of protein-releasing depots within layered hydrogel networks shown in Figure 8 resulted in the formation of soluble rhodamine-labelled bovine serum albumin (BSA) concentration gradients across the PEGDA hydrogels [18]. This system coupled the use of controlled release depots together with diffusion-based methods for gradient generation.

1.5.2.3.2. Graded distribution of depots

As an example for utilizing a drug delivery approach to create gradient biomimetic scaffolds with graded distribution of bioactive molecule reservoirs, 3D fibrous polycaprolactone scaffolds were fabricated by simultaneous electrospinning and electro spraying process. Guo *et al.* created graded distribution of bFGF loaded PLGA microspheres prepared by coaxial electro spraying via gradual increase of the injection rate of the bFGF solution with constant injection rate of the PLGA solution. The final outcome was similar microspheres density at different distances within the PCL fibrous mat electro spun simultaneously but with gradient loading of bFGF [103]. Cell migration from the top of the scaffolds where mouse dermal fibroblasts were seeded, was observed along the bFGF gradients. Furthermore, angiogenesis as a function of bFGF gradient was followed after subcutaneous implantation of the scaffold in mouse model. High density of sprouting was observed in the constructs and was increasing concomitantly with the increased steepness of the bFGF gradient suggesting high potential of development of vascularized tissues in biomimicry situation [103]. Similarly, β -tricalcium phosphate (β -TCP) nanoparticles in PCL scaffolds were prepared using extrusion/electrospinning to create gradients of β -TCP. The subsequent osteogenesis response of preosteoblasts along the gradient direction was subsequently assessed [104].

1.5.2.4. Immobilization of protein gradients

Gradients in biology are not restricted to the soluble signalling molecules and a range of substrate bound signals are present in the natural microenvironment in a graded manner.

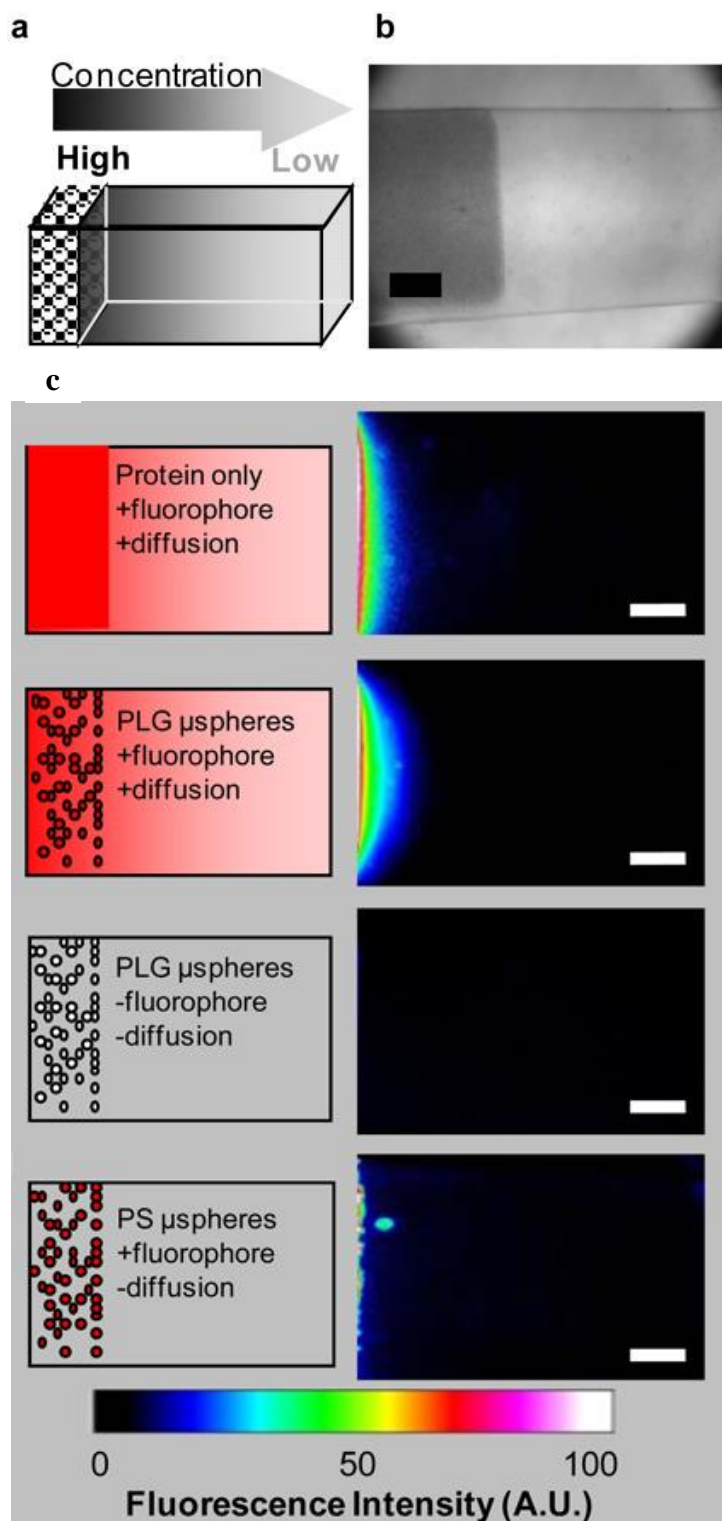


Figure 8: Spatial localization of BSA loaded PLGA microspheres in layered PEGDA hydrogel a. schematic presentation of the layered scaffolds b. bright field image c. Fluorescence micrographs (pseudocolor images) of hydrogels containing depots loaded with Rhodamine-BSA, Rhodamine-BSA-loaded PLG microspheres, blank PLGA microspheres and non-diffusive fluorophore loaded polystyrene beads. Modified from [18].

Examples of substrate bound adhesion peptides are fibronectin and laminin (LN-1) in the ECM which regulate the communications and adhesion of cells [16]. From this perspective, growth factors and adhesion peptides were as well immobilized in gradient scaffolds and the corresponding cellular responses in the form of alignment, attachment, migration and neurite extension were subsequently assessed [12]. The benefits of immobilization include maintenance of stable gradients over long periods of time or biomimicry to physiological processes. Limitations to covalently immobilised proteins methods for generating biomolecules gradients include variation of covalent bonds strength required to ensure immobilization. Additionally, the immobilization process may render the proteins not accessible to the cells or affecting cellular uptake and eventually compromising their role in the studied processes [18].

Lühmann *et al.* created linear immobilized gradients of the immunoglobulin-like domain of cell adhesion molecule L1 (TG-L1Ig6) via covalent bonding within fibrin matrices with fibroblasts seeded on top or dispersed within the system. The system demonstrated stability of the immobilized gradient for 24 hours in comparison to soluble gradients which totally disappeared. An observed alignment of the fibroblasts along the gradients was noticed for both systems. However, the number of aligned cells significantly decreased by 30% in case of cells encapsulated within the matrix compared to cells seeded on top of the gradient matrix [105]. Similarly, cylindrical PCL/Pluronic F127 scaffolds (Figure 10) with gradients of growth factors (BMP-7, TGF- β (2) or VEGF(165)) were formed by centrifugation and subsequent immobilization via heparin binding to produce scaffolds [106]. Combinations of above listed methods were as well used to generate immobilized gradients of LN-1 using molecular diffusion [107] or microfluidics [108, 109].

The generation and stabilization of immobilized biomolecules gradients can be achieved by photopolymerization technique via ultraviolet and temperature crosslinking of prepolymer solutions [14]. Burdick *et al.* gradually introduced two initiator solutions into a microfluidic channel system creating a prepolymer gradient. This gradient of RGDS was subsequently photopolymerized within PEGDA hydrogel matrix via UV light exposure. The fabrication of adhesive ligand gradients modulated the spatial distribution of HUEVCs towards RGDS rich areas and gradients of cross-linking densities resulted in with spatially dependent swelling and accordingly mesh sizes [109].

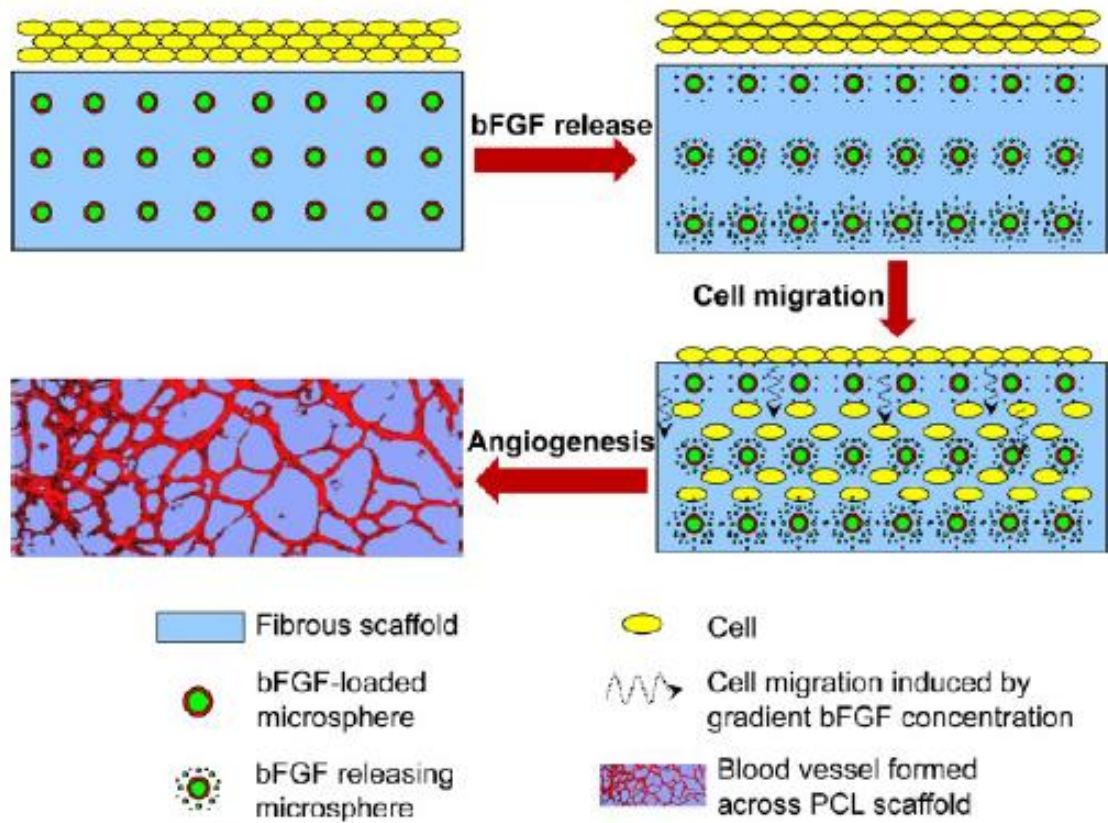


Figure 9: Developing bFGF gradient fibrous scaffolds by graded distribution of bFGF-PLGA microspheres with gradient bFGF loading using a simultaneous electrospaying/electrospinning process. Reproduced from [103].

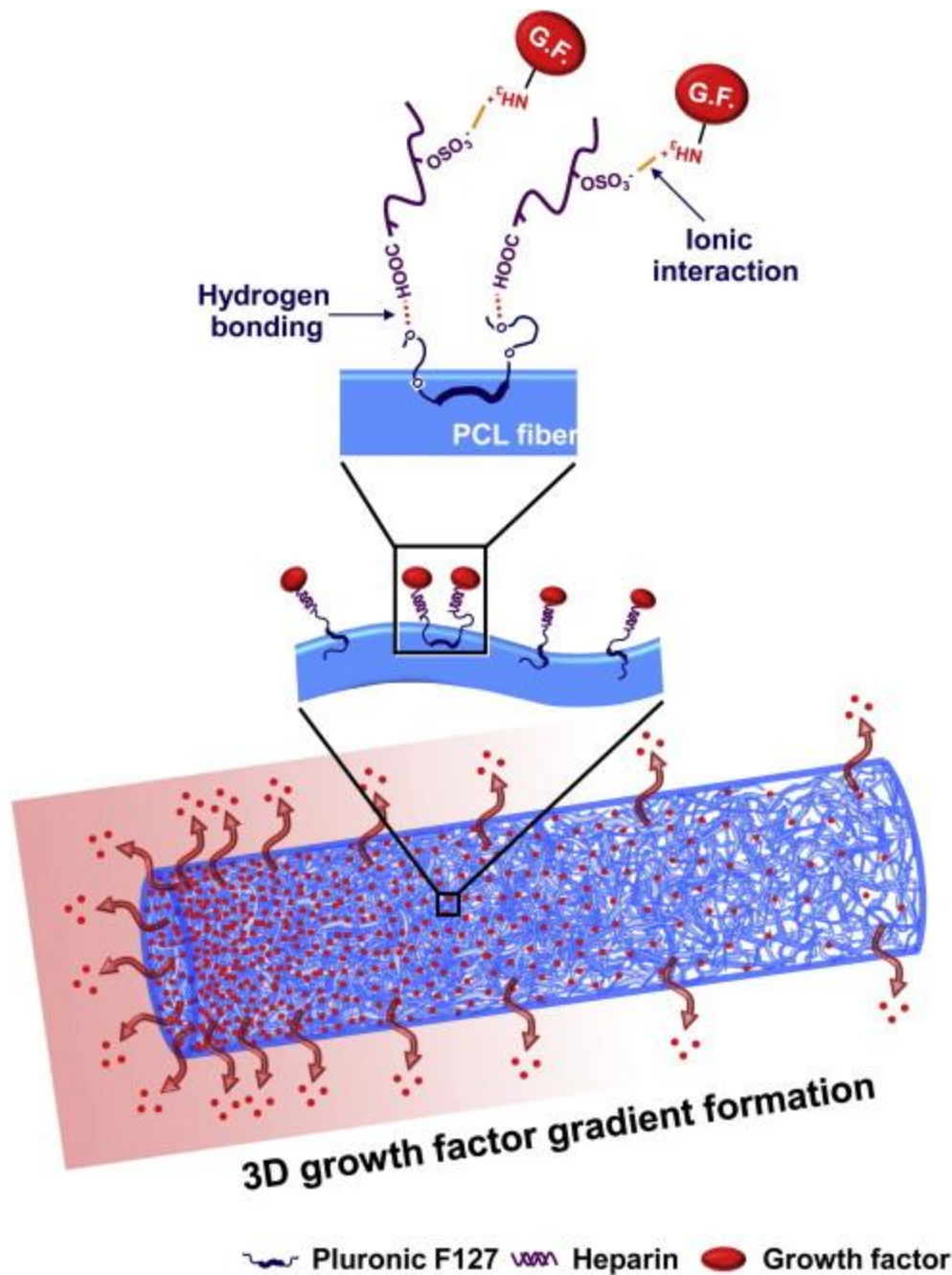


Figure 10: Schematic presentation of the growth factors immobilized gradients in PCL scaffolds prepared by centrifugation/surface immobilization. Gradients of growth factors (BMP-7, TGF- β (2) or VEGF (165)) were formed by the centrifugation and the subsequent immobilization via heparin binding through hydrogen bonding to PCL fibres and ionic interactions to growth factors. Reproduced from [106].

1.5.2.5. Micro-patterned gradients

Microstamping was equally used to create adsorbed biomolecule gradients in 3D systems. The method employs a microfabricated elastomeric stamp for printing proteins on a cell culture substrate. Fine tuning of the developed gradients in terms of slope and concentration ranges can be achieved via control of the space and density of the stamp patterns. The ease of generation of micro-patterned gradients without the need for complicated machinery to maintain the developed gradients together with the control over the pattern and concentrations come along the advantages of the technique. On the other hand, the developed gradients cannot be changed dynamically once patterned. Furthermore, the technique is limited to signalling biomolecules that are not compromised by adsorption or chemical coupling to surfaces. Additionally, the stability of the patterned gradient is compromised by the presence of other proteins in the system that might degrade or displace the molecule of interest [2]. Kunze *et al.* developed 3D gradient system composed of micro-patterned hydrogel layers. The micro-patterned layers encapsulated dissociated cortical neurons in laminar cell layers with NGF and B27 gradients and the linear chemical gradients were maintained for two weeks using the microfluidic device. Spatial distribution of synapses was subsequently assessed to monitor synaptic densities as a function of synergistic NGF/B27 gradients [110].

Table 2 shows examples of physical and chemical gradient biomimetic scaffolds, the method used in gradient development and measurement and the key findings of each system.

1.6. Challenges and future considerations

1.6.1. *In vivo* correlation and integrated techniques

The discussed *in vitro* methods for generating gradients represent invaluable tools for identification of bioactive agents eliciting concentration-dependent cell responses. Moreover, they help reveal the underlying mechanisms regulating such cellular responses [7]. Combinations of the aforementioned methods were reported to be helpful in unravelling the cellular responses towards concentration-dependant signalling biomolecules making use of the advantages of each method and overcoming the limitations of the other [107-109]. However, the actual quantitation of the *in vivo* bioactive molecule gradients responsible for morphogenesis is still not clear [2]. Similarly, in immune and cancer metastasis, the exact mapping of soluble factor concentrations is particularly challenging [111]. Furthermore, the *in vivo* gradient

profile of bioactive molecules is not defined solely by the biomolecule's diffusive characteristics, but spans to include its binding kinetics to the components of the dynamic cellular microenvironment. Thus, the ability to generate complex gradient settings of physical, chemical and biological cues would enable precise quantitative estimation of multiple gradient signals contributing to cell growth, polarization, migration, and differentiation [7].

The embryonic development, immunocytochemistry methods and *in situ* hybridization assisted the understanding of biomolecules expression and tissue distribution in the tissue at different stages. However, these methods are not capable of providing quantitative information sufficient to understand the exact profiles required to induce specific cellular responses [2]. Additionally, further optimization of the developed gradient slopes is to be investigated to direct cell behaviour in the desired way in the *in vitro* and *in vivo* settings. Other techniques such as gene therapy and intracellular protein delivery could be integrated together to generate gradients of genetic information or functional proteins that activate autocrine and paracrine cell signalling mechanisms in a concentration dependant manner [14].

1.6.2. Technical concerns

The process of generation and evaluation of chemical gradients of signalling molecules is technically challenging in terms of the stability of the developed gradient and the feasibility, ease and validation of the analysis tool. The involvement of localized release delivery systems allows the temporal resemblance to the natural mechanisms of production of signalling factors in the native tissues and provides stability to the short half-lived biologically active agents. The quantitative measurement of chemical gradients can be in form of fluorescence microscopy of fluorescently labelled biomolecules within the scaffolds coupled with data analysis software [18, 97, 103]. Such techniques provide thorough real time monitoring of the evolving gradients without the need of multiple test scaffolds for temporal evaluation of the gradient. However, accurate validation of image analysis software and fluorescent labelling is required prior to the quantification process. Other limitations include the ability of microscopy to visualize and collect fluorescent signals in the 3D structure [2]. However, this was overcome using confocal microscopy. Furthermore, the effect of fluorescent labelling on the functionality of the active biomolecules has to be assessed so as not to compromise their biological activities. Alternatively, sacrificial methods of quantitative

analysis can be done on sectioned scaffolds as a function of position along the gradient [61, 112]. Such methods permit the analysis of different biomolecules and do not limit the analysis to fluorescent-labelled test molecules. Other assay methods included immunosorbent assays [61] and radioactivity [112]. Furthermore, these methods ensure the quantification of the concentration profiles down to micron range distances. On the other hand, the quantitative potential is limited by the sensitivity of the assay employed to detect the minute concentrations down to the ng/mL range and yet capable of eliciting cellular responses. Other drawbacks to such quantitative techniques involve the requirements to develop multiple test scaffolds to evaluate the gradients at each time points during the generation and decay of the gradients. This would be time and cost ineffective and might induce high variability in test results due to different environmental factors to which different scaffolds are exposed to.

1.6.3. Biomimicry and clinical translation concerns

Finally, the fabrication of biomimicry environments with optimum porosities, vasculature and mechanical properties relevant to the native tissues to be replicated is required for more accurate cellular proliferation, migration and differentiation studies in response to chemical or physical gradients. Other challenges to be addressed in clinical translation of gradient biomaterials include methods for long-term storage without compromising the key characteristics. This is particularly needed to reduce the waiting time prior to transplantation of engineered grafts [14].

Table 2: Selected examples from literature showing biomimetic physical and chemical gradient scaffolds and the key findings of each system

Gradient Type	3D system	Cell(s) type	Cells position	Method of gradient generation	Method of gradient analysis	Finding(s)	Rn.	
Physical gradients	Stiffness	PAAM hydrogel sheets coated with type I collagen with gradient in elastic modulus.	NIH 3T3 mouse Fibroblasts	On top of coated sheets	Gradient mixing	Young's Modulus measurement	Durotaxis towards the stiffer regions as measured by time lapse microscope	[59]
	Topography	PDL and Matrigel™-patterned PDMS substrates of variable groove heights	Murine embryonic cortical neurons	On top of substrates	Photolithography	Confocal microscopy	Deep grooves permitted axon growth while in shallow ones, axons continued to extend into or outside of them	[77]
	Porosity	GTN-HPA hydrogels with CMC-TYR polymer with pore size & chemoattractant; FBS gradients	HT1080 human fibrosarcoma cells	Within scaffolds	Microfluidics with gradient diffusion of cellulase enzyme or FBS	Confocal microscopy coupled with software analysis of fluorescence or pore size	Synergistic chemotaxis when FBS gradient is opposite to the porosity gradient	[81]
Chemical gradients		Collagen I/Matrigel™ with VEGF gradients	HUVECs/ 10T1/2 mouse smooth muscle cells	Endothelial-lined lumens	Tubeless Microfluidics device	Fluorescence microscopy coupled with software analysis	Angiogenesis in endothelial-lined lumen in response VEGF gradient alone	[100]
		Agarose hydrogel with linear NGF gradient	PC12 cell neurites	Underneath scaffold	Molecular diffusion	Cryosectioning/ ELISA	Definition of the minimum and the maximum distance required for guidance of neurite growth	[61]
		PCL fibrous mat with graded distribution of bFGF-PLGA microspheres	Mouse dermal fibroblasts	On top of scaffolds	Electrospraying/ Electrospinning	Fluorescence microscopy coupled with software analysis	Increased cellular migration and angiogenesis along steep bFGF gradient	[103]
		Fibrin gels with immobilized gradients of TG-L1Ig6	Human foreskin fibroblasts and HUVECs	On top or within system	Piston-driven gradient mixer	Confocal microscopy coupled with software analysis of fluorescence	Alignment of the fibroblasts along TG-L1Ig6 gradients for both systems with decreased for encapsulated cells	[105]
		Micro-patterned hydrogel layers with NGF and B27 gradients	Cortical neurons	Within system	Micropatterning/ Microfluidics	Fluorescence microscopy coupled with software analysis	Spatial distribution of synapses as a function of synergistic NGF/B27 gradients	[110]

1.7. Thesis aims

The general aim of this thesis is to develop a validated quantitative method to generate and measure 3D chemical gradients in cell-laden hydrogel systems. This is to understand cellular responses towards gradients of biologically active proteins and to be used as an effective tool for accurate design of gradient biomimetic scaffolds for biomedical applications.

To achieve this broad aim, specific objectives included:

1. Development and validation of a robust, reliable compartmental diffusion model that could generate and monitor diffusion gradients of different molecular weights species across 3D hydrogel membranes.
2. Fabrication of controlled release protein depots to replace the source compartment in the Source-Gel-Sink compartmental diffusion model for optimum protein delivery.
3. Development of a cell-laden hydrogel system to study gradient delivery of model novel high efficiency transduction protein via the validated compartmental diffusion model.
4. Application of the compartmental diffusion model in the gradient delivery of enhanced transduction myogenic transcription factor MyoD to a cell-laden hydrogel system and monitoring of the subsequent gene expression as a function of distance away from source protein.

Chapter 2: Materials and methods

2.1. Materials

- 0.2 μm pore size filter (Minisart, Sigma Aldrich, UK)
- Agarose – catalogue number A2576, Sigma-Aldrich (Poole, UK)
- Albumin, Tetramethylrhodamine isothiocyanate bovine, lyophilized powder, TRITC BSA, catalogue number A2289
- Albumin–fluorescein isothiocyanate conjugate, albumin bovine (FITC-BSA) Molecular weight of albumin: 66 kDa, Molecular weight of FITC: 389.4, λ_{max} : 495 nm (product number: A9771) (Sigma-Aldrich)
- Antibiotic/Antimycotic (AB/AM) – catalogue number 30-004-CI, Mediatech (Manassas, VA, USA)
- Cryogenic vials (Nunc[®] CryoTube[®] Vials, Denmark)
- Cyquant[®] NF cell proliferation, part number C35007, (Fisher Scientific, UK)
- Dichloromethane DCM (HPLC grade, Sigma-Aldrich, UK)
- Dimethyl sulphoxide DMSO (Sigma-Aldrich, UK)
- Dulbecco's Modified Eagle Medium (DMEM) catalogue number 42430-025, Life Technologies (Paisley, UK)
- Fluorescein, Catalogue number 470108-580, (VWR Ltd, Leicester, UK)
- Foetal Bovine Serum (FBS) – catalogue number 900-108, Gemini Bio-Products (West Sacramento, CA, USA) or catalogue number F9665, Sigma-Aldrich (Poole, UK)
- Gelatin from bovine skin, Type B, powder, BioReagent, suitable for cell culture, catalogue number G9391, Sigma-Aldrich (Poole, UK)
- Glutathione-Sepharose resin (GE Healthcare)
- Hoechst 33342, part number 4082S, New England Biolabs (UK)
- L-Glutamine – catalogue number G7513, Sigma-Aldrich (Poole, UK)
- Live/Dead Viability/Cytotoxicity Kit – catalogue number L-3224, Life Technologies (Paisley, UK)
- Micro BCA Bicinchoninic Acid Kit for Protein Determination– catalogue number 23235, Fisher Scientific (Loughborough, UK)
- Nalgene 'Mr. Frosty' (Fisher Scientific, Loughborough, UK)
- Novex[®] 10% Tris-Glycine mini protein gel (1 mm, 10 wells, 8*8 cm), (Catalog number: EC6075BOX), Life Technologies (Paisley, UK)
- Novex[®] Tris-Glycine SDS Running Buffer (10X), (Catalogue number: LC2675), Life Technologies (Paisley, UK)

Materials and Methods

- Novex® Tris-Glycine SDS Sample Buffer (2X), (Catalogue number: LC2676), Life Technologies (Paisley, UK)
- O.C.T. COMPOUND, part number 361603E, (VWR Ltd, Leicester, UK)
- Para-formaldehyde (PFA) (Sigma-Aldrich, UK)
- Poly (vinyl alcohol) (PVA) (Mwt. 23000, 87-89% hydrolysed, Sigma-Aldrich)
- Poly (lactic-co-glycolic acid) (PLGA) – various products (Lakeshore Biomaterials, Evonik Industries, UK)
- PreScission™ Protease cleavage (GE healthcare)
- PrestoBlue® Cell Viability Reagent – catalogue number A-13262, Life Technologies (Paisley, UK)
- QIAshredder, part number QIA79654, (Sigma Aldrich, UK)
- Rapid GST inclusion body solubilisation and renaturation kit (AKR-110; Cell Biolabs, Inc., San Diego, CA)
- RNAeasy spin column, part number QIA74104, (Sigma Aldrich, UK)
- RNase-Free DNase Set Catalogue number 79254, (QIAGEN, UK)
- SeeBlue® Plus2 Pre-Stained Protein Standard (Catalogue number:LC5925), Life Technologies (Paisley, UK)
- Sodium dodecyl sulphate (SDS), (Sigma Aldrich, UK)
- Standard Divinyl benzene Polymer microspheres, 0.057µm diameter (Bangs Laboratories, Inc.)
- SuperScript™ III Reverse Transcriptase Catalogue number 18080-044 10,000 units, concentration: 200 U/µl, Life Technologies (Paisley, UK)
- Tetramethylrhodamine isothiocyanate–Dextran, average mol wt 4,400, TRITC Dextran 4400, catalogue number T1037, Sigma-Aldrich (Poole, UK)
- Tetramethylrhodamine isothiocyanate–Dextran, average mol wt 65,000-85,000, TRITC Dextran 66000, catalogue number T1162, Sigma-Aldrich (Poole, UK)
- Trypsin/EDTA – catalogue number 25-053-CI, Mediatech (Manassas, VA, USA)
- XCell SureLock™ Mini-Cell Electrophoresis System, Life Technologies (Paisley, UK)
- β-Agarase I, part number M0392S, (New England Biolabs, UK)
- β-D-1-thiogalactopyranoside (IPTG), part number A1008.0025, (VWR Ltd, UK)
- β-Mercaptoethanol, part number 97622, (Sigma Aldrich, UK)
- Unless otherwise specified all other reagents are of analytical reagent grade and purchased from Sigma-Aldrich (Poole, UK).

2.2. Methods

2.2.1. General Cell Culture

2.2.1.1. NIH 3T3 Murine Fibroblast Cell Line

3T3 cells (catalogue number ATCC-CRL-1658, LGC Standards, Teddington, UK) were cultured in culture medium that is composed of DMEM (Life Technologies) supplemented with 10% (v/v) FBS (Sigma-Aldrich), 1% (v/v) L-glutamine and 1% Antibiotic/Antimycotic. Monolayer cultures were maintained on tissue culture treated plastics at 37°C and 5% (v/v) CO₂. Cells were passaged by trypsinisation after 80% confluency and reseeded at 1/10th of the cell density into a new flask. Routine cell passaging was performed by aspiration of culture medium from the flask and the cell monolayer washed with PBS. After aspiration of the PBS, 4 mL of trypsin/EDTA was added to T175 flask and left to be incubated at 37°C until all cells had detached. The trypsin was deactivated by the addition of 6 mL of culture medium and the cell suspension was centrifuged at 200 g for 5 minutes using a SIGMA 1-14 Microfuge. The cell pellet was collected after aspiration of the supernatant and then resuspended in fresh culture medium for the desired seeding ratios.

2.2.1.2. BJ6 human dermal fibroblasts

Human dermal fibroblasts were provided by Dr. James Dixon, received at passage 16, expanded and cryopreserved at passages 16-19 and used at passages 20-22. Composition of culture medium was similar to that described for mouse fibroblasts in section 2.2.1.1. Routine cell passaging was done as previously described in section 2.2.1.1 except for seeding density which was 1/5th instead of 1/10th.

2.2.1.3. Human embryonic kidney cells HEK 293T cell line

Human embryonic kidney cells were provided by of Dr. James Dixon, received at passage 13, expanded and cryopreserved at passages 13-16 and used at passages 17-19. Composition of culture medium was similar to that described for mouse fibroblasts in section 2.2.1.1. Routine cell passaging was done as previously described in section 2.2.1.1 except for centrifugation of the cell suspension which was usually performed at 300 g for 5 minutes.

2.2.2. Cryopreservation

Cells were cryopreserved in liquid phase nitrogen for later usage and to prevent possible risk of phenotypic changes upon extended subculture. The cryopreservation medium was composed of FBS supplemented with 10% (v/v) DMSO as a cryoprotectant. Cryopreservation process involved resuspension of cell pellets, recovered from normal

trypsinisation process, in cryopreservation medium. 1 mL of cell suspensions kept at 1 M/mL were stored in cryogenic vials and then transferred into a Nalgene 'Mr. Frosty' and placed in a -80°C freezer for 48 hours prior to liquid nitrogen storage. This was to guarantee a cooling rate of approximately 1°C per min to ensure effective cell cryopreservation.

For cell resuscitation, cryogenic vials containing frozen cell suspension were removed from vapour phase liquid nitrogen and then thawed by placing them into a water bath set to 37°C. Cell suspensions were diluted in pre-warmed culture medium and centrifuged as appropriate to the cell type. Cell pellets were then resuspended in pre-warmed culture medium and subsequently cultured at the appropriate seeding density.

2.2.3. Plain and protein loaded PLGA microspheres

2.2.3.1. Microspheres manufacture

FITC-BSA loaded Poly (DL-lactic-co-glycolic acid) (PLGA 50:50, Mwt. 58 kDa) microspheres with or without 10% PLGA-PEG-PLGA triblock copolymer (prepared in house using ring opening polymerisation of DL-Lactide and glycolide onto poly(ethylene glycol) in the presence of stannous octoate catalyst under dry nitrogen atmosphere [113]) were prepared using double emulsion technique followed by solvent evaporation [114].

2.2.3.2. Characterisation of the microspheres

2.2.3.2.1. Size Analysis using Laser Diffraction

Microparticles were sized by laser diffraction using a Coulter LS230 (Beckmann Coulter). Microspheres samples were suspended in double deionised water and added to the Coulter glass cell. 30 second runs were done in triplicate. Values of the mean, median and the mode were monitored to evaluate the size distribution of the formed batches.

2.2.3.2.2. Microscopy

2.2.3.2.2.1. Scanning Electron microscopy (SEM)

Microspheres of different batches prepared as detailed in section 2.2.3.1 were mounted on SEM stubs (Agar, G301) and adhered using adhesive carbon tabs (Agar, G3347N). Samples were sputter coated using a Balzers SCD 030 gold sputter coater (Balzers Union Ltd., Leichtenstein) and then imaged using a Jeol JSM 6060LV variable pressure scanning electron microscope (Jeol Ltd., UK) with an accelerating voltage of 10-25 kV.

2.2.3.2.2.2. Fluorescence microscopy

Microspheres were mounted on a microscope glass slide and imaged using Leica DM IRB microscope (Leica Microsystems (UK), Milton Keynes, UK) to check for the entrapment of the fluorescent FITC-BSA inside the microspheres using a blue filter cube that includes an

excitation filter of excitation range 450-490, dichromatic mirror and an emission filter nm to detect the green fluorescence of FITC.

2.2.1.1.1 Estimation of the protein encapsulation efficiency

Encapsulation efficiency of FITC-BSA within PLGA microspheres was assessed using Bicinchoninic Acid (BCA) assay kit [115].

2.2.1.1.2 Protein release from the microspheres

In vitro protein release from protein loaded microspheres was assessed in 3 mL Phosphate buffer saline (PBS) and the released protein was quantified using a BCA assay kit [116].

2.2.4. Expression and Purification of Recombinant glycosaminoglycans (GAG-binding enhanced transduction) GET proteins

A series of recombinant proteins was prepared by cloning of plasmid cDNA in *Escherichia coli* grown on agar/luria broth (LB) plates supplemented with 100 µg/mL penicillin. 50 µL of bacteria was thawed, added to 1 µL plasmid and left on ice for 20 minutes then heated for 45 seconds at 42°C in a water bath. This was followed by storage for 5 minutes on ice. 300 µL of super optimal broth (SOB) was added to recover bacteria after heat shock and were shaken at 220 rpm in a controlled temperature incubator shaker (Innova™ 4200, New Brunswick Scientific, Edison, NJ, USA) at 32°C for 1 hour. 200 µL of the mixture was spread over the top of the agar/LB plates. For each target protein, one colony was picked using a sterile 20 µL pipette tip to be placed in 5 mL LB supplemented with 50 µg/mL ampicillin. Tubes were placed and left overnight in the incubator shaker at 32°C at 220 rpm until colonies started to grow as determined by an increase in the optical density $OD_{600} = 0.6$. The plasmids DNA from bacteria cultures were isolated using QIAprep® Spin Miniprep Kit (OIA GEN, Valencia, CA) following the manufacturer's protocol. Enough amounts of the growing bacteria were spun at 9000 rpm for 1 minute to get a bacterial pellet that was then suspended in 250 µL of P1 resuspension buffer. The solution was then mixed with 250 µL of P2 alkaline buffer with SDS. 500 µL of N3 buffer were added and the whole mixture was spun for 5 minutes at 16000 rpm. The pellet was discarded and the supernatant that contained the circular plasmid DNA was kept for subsequent purification step using QIAprep spin mini columns designed to keep DNA and purify them and elute RNA. QIAprep spin columns were centrifuged for 10 seconds at 16000 rpm. The flow through was discarded and the columns were washed twice using 500 µL of PE buffer with centrifugation step for 30 seconds and an extra spin to get the membrane dry. The columns were then placed in fresh collection tubes and 500 µL of molecular grade water were added, left to stand for 1 minute and spun again to collect the flow through purified plasmids.

The constructed plasmids were transformed into BL21-DE3 *Escherichia coli* cells onto Ampicillin (50 µg/ml) and Chloramphenicol (34 µg/ml) plates. cDNA for mRFP-1 as a kind gift from Prof. R. Y. Tsien (University of California, USA)[117]. 8R and MYOD cDNAs were provided by Dr. James Dixon and were synthesized *de novo* (Eurofins MWG Operon) [118]. cDNAs were cloned into the pGEX6-P1 expression vector (Novagen) to create in-frame fusions and expressed proteins in BL21 (DE21) pLysS *Escherichia coli* (Novagen). For each target protein, one colony was picked using a sterile 20 µL pipette tip to be placed in 10 mL LB supplemented with Ampicillin (50 µg/mL) and chloramphenicol (34 µg/mL). Tubes were placed and left overnight in the incubator shaker at 32°C at 220 rpm until colonies started to grow as determined by an increase in the optical density OD₆₀₀= 0.8 then transferred to larger to 100 mL LB media supplemented with ampicillin in a sterile area. 100 mL content are then transferred to 300 mL medium using aseptic technique in the incubator shaker at 37°C at 220 rpm until confluent.

Exponentially growing LB cultures (OD₆₀₀ = 0.6) shaken at 220 rpm at 37°C were induced using 1 mM isopropyl β-D-1-thiogalactopyranoside (IPTG) for 24 hours at 25°C. This was followed by 20 minutes' centrifugation at 8000G at 4°C using Eppendorf 5415R centrifuge (Hamburg, Germany). Bacterial pellets were stored in -80°C freezer for subsequent lysis steps which included sonication (7 amplitudes, 1 minute, 5 times) of bacterial pellets in 1X STE extraction buffer (50 mM Tris, pH 7.5, 150 mM NaCl, 1 mM EDTA containing 1mM DTT, 0.2 mg/ml lysozyme, and 1X protease inhibitor cocktail). This was done to keep the protein in the reduced state for the ease of binding to the purification beads and the lysozyme was added to destroy the bacterial cell walls.

Insoluble protein was retrieved using the Rapid GST inclusion body solubilisation and renaturation kit (AKR-110; Cell Biolabs, Inc., San Diego, CA). The beads were suspended in STE buffer after 3 successive washing steps with diluted STE buffer (1:10). Recombinant proteins were purified by affinity chromatography using Glutathione-Sepharose resin and the mixture was incubated overnight at 4°C to block non-specific protein binding. Protein pellets were collected by centrifugation of the protein-beads suspension at 4200 rpm for 5 minutes and were subsequently washed three times with 1X phosphate-buffered saline (PBS) rotating at 4°C for an hour. GST-tags were removed and eluted from resin by 150 µL PreScissionTM Protease cleavage in 1X 5550 µL cleavage buffer (50 mM Tris-HCl pH 7.0, 150 mM NaCl, 1 mM EDTA and 1 mM DTT). Beads were incubated in the buffer overnight

at 4°C to ensure maximal recovery of renatured proteins. The eluted proteins were aliquoted and stored at -80°C for further characterization.

2.2.4.1. Determination of proteins molecular weight using sodium dodecyl sulphate-polyacrylamide gel electrophoresis SDS-PAGE

In order to determine the molecular weights of the recombinant proteins produced via GET technology, SDS-PAGE was used to discriminate between proteins based on their net charges, sizes and shapes. An inert matrix of highly cross-linked polyacrylamide gel; Novex® 10% Tris-Glycine mini protein gel was used as a medium through which test proteins migrated. The first and the last wells of the polyacrylamide gel were loaded with 10 µL SeeBlue® plus2 pre-stained protein standard containing 10 different polypeptides in the range of 4–250 kDa. Aliquots equivalent to 5 µg of each test protein were diluted using the 2X Novex® Tris-Glycine SDS sample buffer to obtain a final volume of 25 µL. To denature sample proteins, diluted samples were heated at 60°C for 5 minutes and then samples were centrifuged at 14800 rpm for 5 minutes to remove debris. Samples were loaded separately to different wells leaving a well gap (filled with 25 µL loading buffer) from the standard and then run in Novex® Tris-Glycine SDS running buffer (diluted 1:10 using deionized water) in XCell SureLock™ Mini-Cell Electrophoresis System at 125V, 35 mAmp & 50W for 90 minutes using Fisher Scientific power 608 power supply. After electrophoresis, the apparatus was disassembled and the gel was washed off the glass plates with 500 mL of the gel-fixing solution composed of 50% (v/v) ethanol in water with 10% (v/v) acetic acid and left soaking in that solution for 1 hour. The gel-fixing solution was then aspirated and 500mL of the gel-washing solution (50% (v/v) methanol in water with 10% (v/v) acetic acid) was added to the gel and left overnight at room temperature with gentle agitation.

After the removal of the gel-washing solution, the gel was immersed in the Coomassie stain solution (0.1% (w/v) Coomassie blue R350, 20% (v/v) methanol, and 10% (v/v) acetic acid) at room temperature for 4 hours with gentle agitation. The Coomassie stain solution was then removed and 250 mL of the destain solution (50% (v/v) methanol in water with 10% (v/v) acetic acid) were added with continuous change of the destain solution until the protein bands were seen without background staining of the gel. The gel was then left in the storage solution (5% (v/v) acetic acid in water) for 1 hour to restore its original dimensions. Photos of gel were then taken by Fujifilm LAS-3000 imaging system.

2.2.4.2. Determination of hydrodynamic radius of proteins using Zeta Sizer Nano

The hydrodynamic radii of the recombinant proteins produced via GET technology explained in section 2.2.4 were determined in 10 mM HEPES buffer (pH 7.4), PBS (pH 7.2) and HPLC grade water using Zetasizer Nano ZS (Malvern Instruments Ltd, UK). Measurements of pH were done using Mettler Toledo pH meter. Particle size analysis was measured using dynamic light scattering as the basic principle of operation [119]. A series of test proteins including mRFP-1, mR-8R, P21-mR, P21-mR-8R and P21-mR-MyoD-8R together with FITC-BSA were tested at 37 °C. All dispersants were double filtered through 0.2 µm pore size filter (Minisart, Sigma Aldrich, UK) prior to dispersion of proteins within. A standard reference of known size; Standard Divinyl benzene Polymer microspheres, 0.057µm diameter (Bangs Laboratories, Inc.) were used to validate the measurement method.

2.2.4.3. Determination of the zeta potential of the protein solutions using Zeta Sizer Nano ZS

The electrostatic charge on each protein solution was evaluated in 10 mM HEPES buffer using Zetasizer Nano ZS (Malvern Instruments Ltd, UK). Zeta potential estimation was estimated using Doppler electrophoresis as the basic principle of operation.

2.2.4.4. Intracellular transduction in monolayer of cells

The intracellular transduction potential of the developed proteins in comparison to the reporter mRFP-1 on different cell types was evaluated over time using monolayer of cells cultured in 12 well tissue culture treated plate. To each well, 0.5 mL of test proteins (50 µg/mL) was added to the cells (0.5×10^6 BJ6 human dermal fibroblasts or 1×10^6 NIH 3T3 mouse fibroblasts).

2.2.4.4.1. Imaging

At different time points, protein solutions were aspirated and the cells were washed twice with PBS and then imaged using Leica DM IRB microscope to check for the red fluorescence inside the cells.

2.2.4.4.2. Flow cytometry

Following the double washing procedure using PBS, Trypsin/EDTA was used to detach cells from the well plates and the collected cell pellets were resuspended in 500 µL PBS. Samples were then analysed using a MoFlo™ DP (DAKO) Flow Cytometer using the green (561 nm) lasers to detect staining for red fluorescent proteins. A total of 50,000 events were utilized to analyse data. Mean red fluorescence per cell was used to compare transduction

power of test proteins with background from unlabelled cells being subtracted and values taken as ratios to the control monolayer of NIH mouse fibroblasts (1×10^6 cells) or Human embryonic kidney cells (1×10^6 cells) or BJ6 dermal fibroblasts (0.5×10^6 cells) exposed to an equivalent concentration of mRFP-1 for 2 hours.

2.2.5. Hydrogels fabrication

2.2.1.2 Agarose hydrogels

1-2% w/v Type IX, ultra-low gelling temperature agarose was dissolved in PBS upon heating to 60°C for 30 minutes, sterilized by exposure to pressurized saturated steam at 121°C for 20 minutes using Prestige medical autoclave (model number 21002, England) and then kept at 37°C in humidified incubator ready for usage.

2.2.1.3 Agarose-gelatin hydrogels

1% w/v Type IX, ultra-low gelling temperature agarose -1% w/v gelatin from bovine skin dissolved in either PBS solution or culture medium previously described in section 2.2.1.1 were heated to 60°C for 30 minutes, sterilized by exposure to UV lamp for 20 minutes and then kept at 37°C in humidified incubator ready for usage.

2.2.1.4 Cell-laden hydrogels preparation

In order to prepare cellular scaffolds, the appropriate cell pellets collected after trypsinisation process previously described in 2.2.1.1 were suspended in the liquid agarose-gelation hydrogels described in 2.2.1.3 at $1-2 \times 10^6$ /mL cell density based on cell type.

2.2.6. Estimation of hydrogel pore size and internal structure

2.2.1.5 Cryo scanning electron microscope (CryoSEM)

Fresh and one-day hydrated hydrogel samples were mounted onto an appropriate holder and securely attached to the vacuum transfer device into a cryo-station filled with liquid nitrogen. The samples were placed in the cryo-chamber at -210 °C, fractured at a temperature of -130 °C and sublimed for 1 minute at -80 °C. After sublimation, the samples were sputter coated with gold for 4 minutes and transferred into the JEOL JSM-6060LV electron microscope fitted with an Oxford CT 1500 cryo-preparation chamber. Images were acquired using an electron beam of 7–22 kV.

2.2.1.6 Cryo scanning electron microscope/focused ion beam coupled with transmission electron microscopy CryoSEM/FIB/TEM

1% agarose-1% gelatin hydrogel sample was rapidly cooled, plunge frozen into a slush of liquid nitrogen and transferred under liquid nitrogen to the cold stage of the FEI Quanta 200 3D Dual Beam FIB-SEM (Portland, OR, USA) equipped with a Quorum PPT 2000 (Quorum scientific, Loughton, UK) cryostage and an in-house custom-built sledge. Images of hydrogel samples were acquired at 15 kV accelerating voltage. Ion beam images were acquired at 30 kV and current of 30 pA.

For the hydrogel lamella preparation using focused ion beam (FIB), cryo sample was first sputter-coated with a platinum light dusting in the Quorum on-column preparation chamber. It was further coated with the organometallic platinum precursor in the FIB/SEM chamber. Milling of the cryo sample was performed using current values ranging between 0.1-1 nA to yield a lamella of approximately 2 μm . This was cut using a cooled tip to remove the lamella. Lift-out manipulator with a re-engineered OmniProbe 100 needle (Oxford Instruments, High Wycombe, UK) was used. The probe needle was modified to achieve thermal isolation between the needle and manipulator and to maintain the temperature of the cryo sample at -160°C . The lamella was secured to the manipulator tip by cryo-condensation of water vapour via an internal water gas injector. After the cryo lift-out, the lamella was transferred to a standard OmniProbe Cu TEM lift-out support grid. Again, it was stabilized by cryo-condensation of water using the gas injector and the tip was released from the lamella by gentle milling. Images were taken using JEOL 2100F transmission electron microscope using an accelerating voltage of 200 kV using the High Angle Annular Dark Field STEM mode [120].

2.2.1.7 Ultra-thin sectioning coupled with transmission electron microscopy

Hydrogel test samples were infiltrated in 2.3 M sucrose for 24 hours and small hydrogel pieces were mounted on a 2 mm aluminium stub and plunged into liquid nitrogen to freeze before transfer to the cryo chamber of a RMC Powertome Cryoultramicrotome fitted with CR-X cryo-attachment. The Cryoultramicrotomy was operated to cut 80 nm sections at a speed of 0.9 mm/sec at -60°C . Sections were collected with a droplet of 2.3M sucrose and then placed on holey carbon support films in copper grids (HC300-Cu, Electron Microscopy Sciences, UK) of 300 mesh size. Sectioning was performed using a freshly made glass knife for each gel sample. The copper grids were then transferred to the JEOL 2100F transmission

electron microscope equipped with digital STEM detector using an accelerating voltage of 200 kV. The imaging was performed using the High Angle Annular Dark Field STEM mode. Randomly selected pores were used to determine the average pore size and frequency distribution using ImageJ software.

2.2.7. Cell viability & proliferation

2.2.1.8 LIVE/DEAD® Viability/Cytotoxicity assay

A LIVE/DEAD® viability/cytotoxicity kit for mammalian cells was used to estimate cell viability on tissue culture plastics or within hydrogels. The assay relies on the intracellular esterase activity and the integrity of the plasma membrane as characteristics of living cells. The kit simultaneously stains live cells with green-fluorescent calcein-AM due to esterase activity and dead cells with red-fluorescent ethidium homodimer-1 (EH-1) because of the loss of plasma membrane integrity. A working solution of 2 μ M/4 μ M calcein AM/EH-1 in PBS solution was used to stain live cells in green or dead cells in red. Cells grown on tissue culture plastics were incubated with the working solution for 10 minutes. For each time point, triplicate samples were stained and three different fields of views were monitored per sample to assess cell viability. For viability assessment of cells encapsulated within hydrogels, triplicates of hydrogel samples of each time point were immersed in the working solution for 30 minutes. Equally, three different fields of views were taken per hydrogel replicate. Imaging of hydrogel samples were undertaken following removal of the staining solution and pressing samples against glass slides by glass coverslips. Samples were viewed using a Leica DM IRB inverted microscope equipped with QCapture Pro software (QImaging, Surrey, Canada).

2.2.1.9 PrestoBlue® cell proliferation assay

The proliferative cell activity within different hydrogel systems were evaluated as function of time to be utilized together with the viability assay described in section 2.2.1.8 to select the optimum composition of the hydrogel. Different 3D cell laden hydrogel systems were examined for cellular proliferation after 1, 2 and 3 days using Prestoblu® cytotoxicity kit. The assay relies on the reducing power of living cells to resazurin-based solutions to quantitatively measure the proliferation of cells. The reagent contains a blue cell-permeant compound that turns red in colour and becomes highly fluorescent after reduction by living cells. At specific time points, hydrogel systems were culture medium aspirated and washed gently with PBS. Prestoblu® cytotoxicity reagent was added to the hydrogel scaffold and

incubated for 6 hours at 37°C. The working solution was then collected and analysed for the increase in fluorescence intensity at 570 nm using TECAN infinite 200PRO multimode reader.

2.2.1.10 CyQUANT® cell proliferation assay

The cellular proliferation within the selected hydrogel system was evaluated as compared to control monolayer of cells cultured on tissue culture plastics using CyQUANT® NF Cell Proliferation Assay Kit. The assay relies on the DNA content rather than the metabolic activity. Different types of cells encapsulated within 3D cell-laden hydrogel were monitored for the cellular proliferation at days 1 & 3. Samples of cell-laden hydrogels at determined time points were -80 °C frozen until the time of analysis. Hydrogel samples were β -agarase/heat digested for 24 hours and 100 μ L samples of the hydrogel digest were examined using CyQUANT® NF reagent according to the manufacturer's instructions.

2.2.8. Compartmentalized diffusion chamber

500 μ L liquid hydrogel at 37°C with or without cells were cast in custom made moulds to create three compartmentalized assembly of source-gel-sink. The assembly was modified from X. Cao and MS. Shoichet [61] so that custom built acetal resin mould and portable polytetrafluoroethylene (PTFE) fitted blocks were used to create the middle hydrogel compartment separating two compartments of equal dimensions. Figure 11 shows compartmentalized diffusion chamber assembly. After hydrogel solidification by cooling at 4°C for 30 minutes, the PTFE blocks were removed leaving a hydrogel cuboid of 15x5x6.6 mm dimensions in the middle of the mould with two created compartments on either sides of the hydrogel scaffold.

2.2.8.1. Oxygen etching of mould base

Acetal resin moulds were oxygen etched at the base of middle compartment to enhance hydrogel attachment prior to diffusion studies via rendering the surface hydrophilic [121]. The oxygen etching was carried out for 15 minutes in a T-shaped borosilicate chamber closed with stainless steel endplates that were sealed with Viton O-rings at a power of 20 W, under a working pressure of 300 mTorr. This process was done to ensure perfect seal of hydrogel to the mould's base to guarantee the production of three compartments assembly without leakage.

2.2.8.2. Mould sterilization

Prior to cell-laden hydrogel casting, the moulds and PTFE blocks were sterilized in industrialized methylated spirit 70% for 30 minutes, washed twice with sterile PBS, air dried in microbiological safety cabinet and then exposed to UV light for 20 minutes ready for usage. Hydrogels were allowed to cast in moulds for 30 minutes at 4°C then PTFE blocks were removed creating the sink and source compartments. This resulted in scaffolds with the dimension of 15×5×6.6 mm (Length × Width × Height).

2.2.8.3. Microspheres-hydrogel composite layered scaffolds

Plain or FITC-BSA loaded PLGA microspheres with or without triblock copolymer prepared at section 2.2.3.1 were mixed with liquid gelatin/agarose hydrogel. The microspheres/hydrogel mixture were cast next to one side of the solidified hydrogel compartment created in section 2.2.8 using a PTFE block of reduced width relative to the original PTFE block used to create the original 3 compartments model (Figure 12).

2.2.8.4. Diffusion studies in compartmentalized diffusion chamber

Source compartments were loaded with 500 µL of diffusing species dispensed in PBS or in culture medium for cell laden hydrogels. Sink compartments were loaded with 500 µL of plain PBS or culture medium respectively. Diffusion experiments were carried out at 37°C under 5% CO₂ in humidified incubator. At pre-determined time points, the medium in the source and sink compartments were analysed for diffusing species concentrations using a TECAN infinite 200PRO multimode reader.

2.2.8.5. Evaluation of diffusion gradients in the hydrogel membrane

At pre-determined time points, cellular or acellular scaffolds were directly frozen in O.C.T mounting media at -80°C and then serially sectioned perpendicular to the direction of protein diffusion using Leica CM 1100 cryostat at -20°C into 20 µm thick slices. The protein concentration within each slice was then determined using fluorometric analysis. Each time point diffusion study was carried out in triplicate, and the fluorometric analysis to detect protein concentration per slice was performed in triplicate for each hydrogel slice in each diffusion study. Diffusion gradient profiles across the width of the hydrogel scaffolds were constructed by plotting diffusing species concentrations per 20 µm thick slices at different time points as a function of distance in the scaffold away from source.

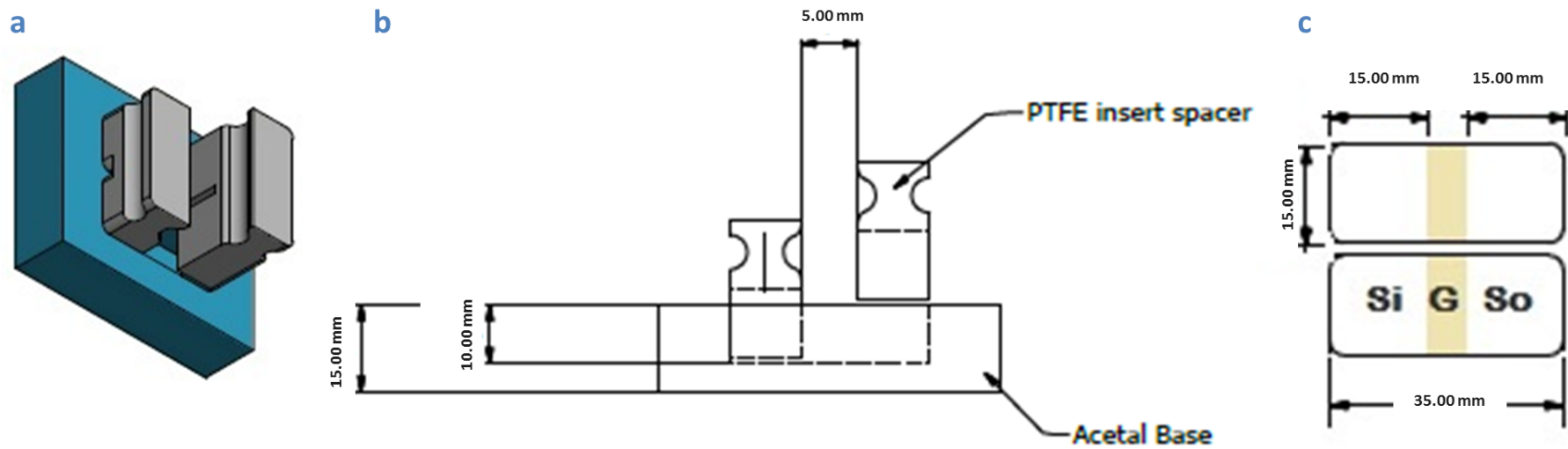


Figure 11: Compartmentalized diffusion chamber showing mould design. a. Top schematic view of acetal mould with PTFE spacer fitted inside. b. Side schematic view of the mould design showing mould dimensions. c. Top schematic view of the mould showing sink (Si), source (So) and gel (G) compartments with their relevant dimensions.

2.2.8.6. Imaging of diffusion gradient across hydrogel scaffolds

2.2.8.6.1. Acellular scaffolds

Hydrogel scaffolds at different time points were frozen in O.C.T mounting media at -80°C and then serially sectioned parallel to the direction of protein diffusion using Leica CM 1100 cryostat at -20°C into 20 µm thick slices. Retrieved gel slices were then viewed in bright field and under fluorescence microscopy image capturing using Nikon stereomicroscope SMZ 1500 & Leica TCS SPE Confocal Macroscope for entire slice imaging.

2.2.8.6.2. Cellular scaffolds

Cell laden hydrogel scaffolds at different time points were exposed to a selective washing protocol by placing cellular scaffolds in the fixing solution composed of 3.7% PFA in PBS for 3 hours followed by 2 hours' immersion in sucrose 15% w/v and finally left overnight in sucrose 30% w/v. Scaffolds were then placed in O.C.T mounting media, frozen in liquid nitrogen cooled isopentane bath then stored at -80°C freezer. Scaffolds were subsequently sectioned parallel to the direction of protein diffusion using Leica CM 1100 cryostat at -20°C into 20 µm thick slices. Retrieved gel slices were then viewed in bright field and under fluorescence microscopy image capturing using Nikon stereomicroscope SMZ 1500 for entire scaffold imaging.

2.2.8.7. Model validation

2.2.8.7.1. Calibration of the quantification method

In order to validate the quantification method applied, a series of homogenous dispersions of variable concentrations of test diffusing species in cellular or acellular hydrogel scaffolds cast to the exact dimensions of the gel compartment were prepared. The scaffolds were then sectioned at random positions of the scaffold into 20 µm thick slices similar to the slicing method described in section 2.2.8.5.

2.2.8.7.2. Effect of the molecular weight of diffusing species on the developed gradient

The ability of the compartmental diffusion chamber to discriminate between different size molecular weights of diffusing species was tested to validate the model and the quantifying methodology.

2.2.8.7.3. Opposing diffusion of TRITC & FITC-BSA in 1% Agarose scaffolds

To confirm the validity of the model to evaluate the diffusion characteristics of the diffusing species irrelevant to the fluorescent tag attached, different fluorescent-tagged BSA were allowed to diffuse in opposite directions across 1% hydrogel scaffolds.

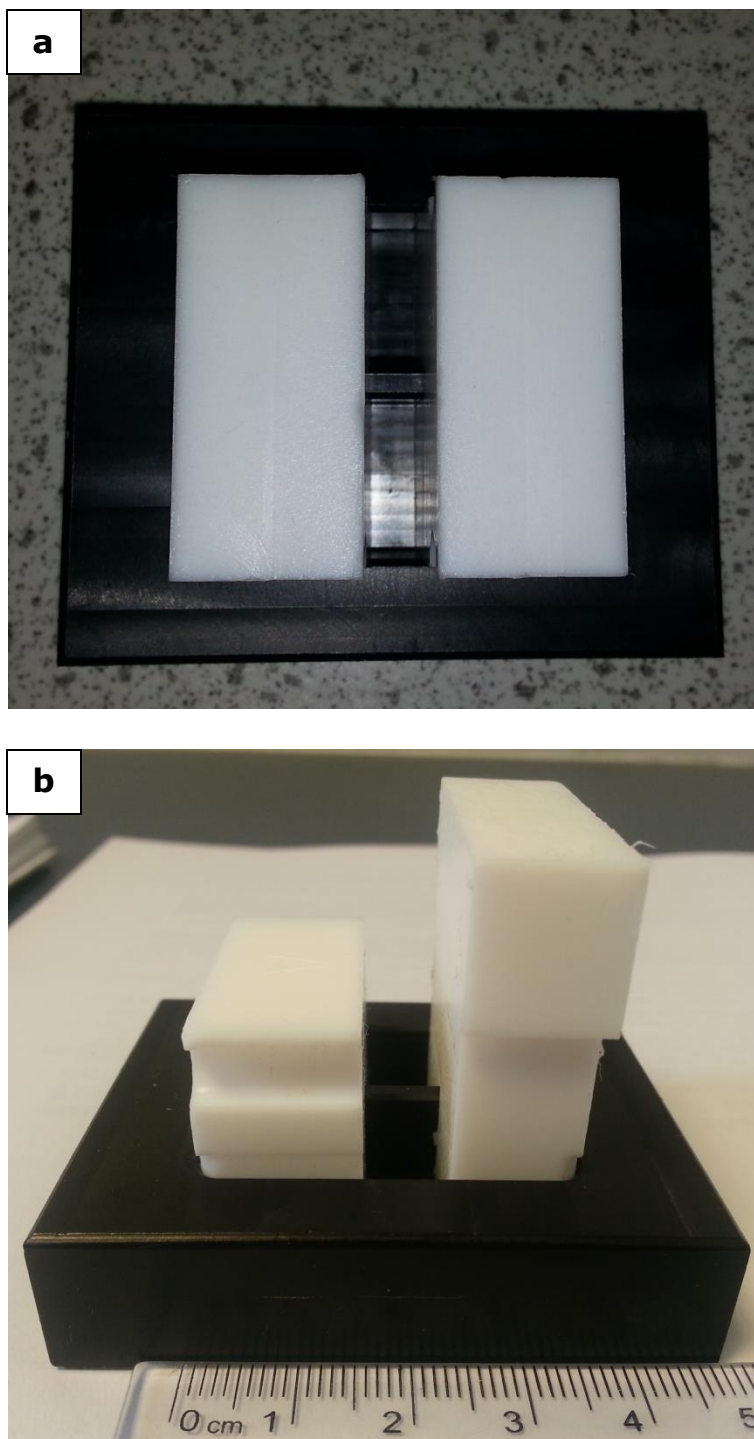


Figure 12: Top view of compartmentalized diffusion chamber showing a: mould design with equal sizes PTFE blocks to create 3 compartments of source-gel-sink & b: 2 different sizes PTFE spacers fitted inside to create a depot compartment of hydrogel with FITC-BSA loaded microspheres dispersed in.

2.2.8.7.4. Determination of diffusion coefficients of diffusing species

To determine the diffusion coefficient of the diffusing species in hydrogels, a model permeation method was employed [61, 122, 123]. Diffusing species were added to the source compartment next to the hydrogel scaffold and the source compartment were filled with blank PBS or culture medium dependant on the dispersion in which the diffusing species were prepared. The cumulative amount of diffusing species that diffused through the hydrogel was used to establish a concentration versus time curve from which the diffusion coefficient can be calculated. Following the establishment of steady state diffusion, Equation 1 can be utilized to solve for the diffusion coefficients of different species where P_i is the permeability of protein in the hydrogel, C_{di} is the initial concentration of the source compartment, L is the thickness of the hydrogel membrane and D_i is the diffusion coefficient of proteins in the hydrogel system.

$$m_i = P_i C_{di} / L \left(t - \frac{L^2}{6D_i} \right)$$

Equation 1: Determination of the diffusion coefficient of protein macromolecules in hydrogel membrane using model permeation method [61, 123].

2.2.9. Intracellular transduction gradients assessment

The 3D intracellular transduction was monitored as a function of distance and time using flow cytometric analysis following hydrogel enzymatic/heat digestion. Samples were then analysed using a MoFlo™ DP (DAKO) Flow Cytometer using the green (561 nm) and violet (405 nm) lasers to detect staining for red fluorescent proteins and Hoechst 33342 respectively. A total of 20,000 events were utilized to analyse data. Mean red fluorescence per cell retrieved from 1 mm thick hydrogel slices was used to compare the transduction power of the used proteins with the background from unlabelled cells being subtracted. Values were taken as ratios to the control monolayer of NIH mouse fibroblasts or HEK 293T cells (1×10^6 cells) or BJ6 dermal fibroblasts (0.5×10^6 cells) exposed to an equivalent concentration of mRFP-1 for 24 hours. 25 μ L samples from liquefied hydrogel slices were placed in 48 tissue culture treated well plates and were subsequently imaged with Leica DM IRB microscope. Figure 13 shows the collective process of evaluation of protein gradients across the width of the hydrogel scaffold.

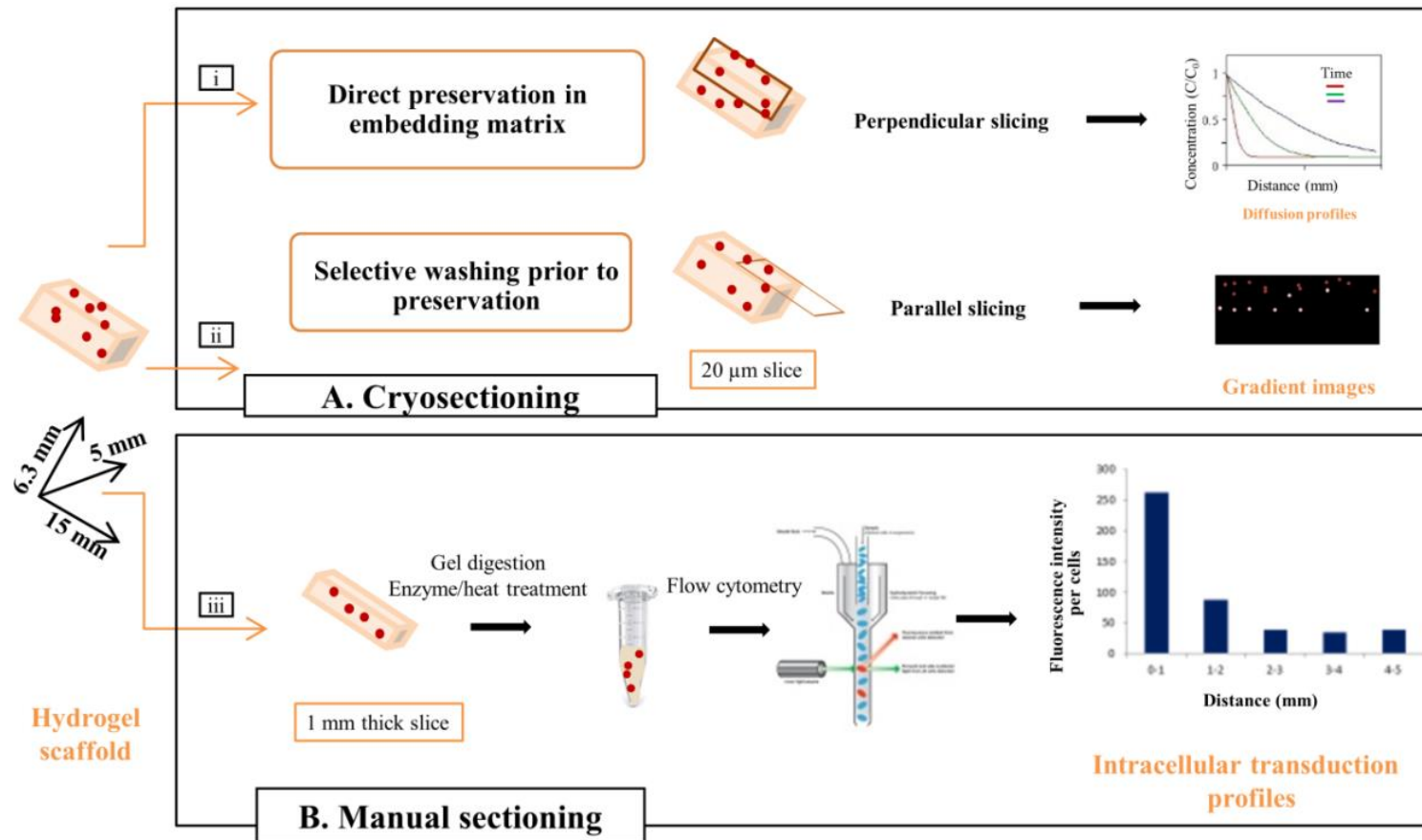


Figure 13: Schematic diagram showing the process of evaluation of the developed gradients. Hydrogel scaffold after the diffusion process was removed from the mould, stored in the mounting medium at -80 °C and then sliced A. using a Leica CM1100 cryostat at -20°C i. Perpendicular to the direction of the protein diffusion to establish quantitative diffusion profiles or ii. Parallel to the direction of the protein diffusion to image the gradient across the scaffold width or B. manually sliced to 1 mm slices, subjected to gel digestion protocol that involved heat and enzymatic treatment and samples were then analysed using a MoFlo™ DP (DAKO) Flow Cytometer.

2.2.10. Gene expression and real time polymerase chain reaction (RT-PCR)

2.2.10.1. RNA extraction

RNA was extracted from cells cultivated in monolayers on tissue culture treated well plates or encapsulated in 3D hydrogel matrix using a Qiagen RNeasy kit following manufacturer's instruction. Cells retrieved from monolayer cultures were washed three times PBS, centrifuged at 300 g using SIGMA 1-14 Microfuge for 5 minutes and the cell pellets were snap frozen and kept at -80°C freezer till the next analysis step. Alternatively, cell-laden hydrogel slices were snap frozen immediately after the manual slicing step and were stored in RNase-Free collection tubes at -80°C freezer.

A lysis step using 350 µL RLT buffer supplemented with 1% β-Mercaptoethanol was subsequently performed. Samples were first vigorously mixed briefly for 10 seconds using vortex-Genie1 touch mixer and then loaded on to Qia-shredder tube (Qiagen, UK) for 2 minutes at 16000g using SIGMA 1-14 Microfuge. 1 volume 70% Ethanol prepared in RNase-free water was then mixed with the lysate and the mixture is transferred to RNA-easy mini column and spun at 8000 g for 15 seconds. The column is subsequently washed with 350 µL RW1 buffer and spun at 8000 g for 15 seconds. Genomic DNA digestion was performed by addition of 80 µL RNase-Free DNase dispensed in RDD buffer followed by an incubation period of 15 minutes at room temperature. This was followed by a repeated washing step using 350 µL RW1 buffer and two washing steps using 500 µL RPE buffer. The column was thereby dried by extended spinning for 2 minutes at 8000 rpm. Finally, the column was placed on RNase-free eppendorf tube and 30 µL of RNase-Free water was added on the membrane and left for 1 minute prior to spinning at 16000 g for 1 minute. The filtrate was then stored at -80°C freezer for further downstream applications.

2.2.10.2. RNA quantification

RNA concentrations were determined using a Nanodrop spectrophotometer (ND-100 Thermo Scientific). 2 µL extracted RNA samples were loaded onto the optical pedestals and concentrations in terms of (ng/µL) were measured at 260 and 280 nm. The ratio of absorbances at these wavelengths was used as a measure of purity of the extracted RNA.

2.2.10.3. Reverse transcription

Following RNA extraction, a step of reverse transcription of the single stranded RNA into the single stranded complementary DNA (cDNA) is performed using SuperScript™ III Reverse Transcriptase enzyme. In 0.2 mL thin walled PCR tube

(STARLAB, UK), a volume equivalent to 500 ng RNA, 1 μ L 10 mM dNTP mix and 1 μ L 10 μ M random hexamers were mixed and the reaction mixture is completed to 13 μ L RNase-free water. The mixture was then heated at 65°C for 5 minutes and incubated on ice for 1 minute using Eppendorf AG PCR thermocycler machine (Hamburg, Germany) to denature RNA. To each 13 μ L sample, 4 μ L 5X First-Strand Buffer, 1 μ L 0.1 M DTT, 1 μ L RNaseOUT™ Recombinant RNase Inhibitor (Cat. no. 10777-019, 40 units/ μ L) and 1 μ L of SuperScript™ III RT (200 units/ μ L) were added.

The final mixture was gently mixed by pipetting and incubated at 25°C for 5 minutes. The reverse transcription was performed by incubation of the reaction mixture at 50°C for 60 minutes followed by enzyme deactivation at 70°C for 15 minutes. The resultant cDNA was stored at -20°C for the succeeding rT-PCR step. Alongside, negative RT samples which contained the entire list of reagents except for the SuperScript™ III Reverse Transcriptase enzyme were prepared to detect any amplification of genomic DNA that had not been degraded upon DNase digestion at the RNA extraction step.

2.2.10.4. Quantitative real time polymerase chain reaction

Following cDNA synthesis, quantification of the target genes expression was performed alongside amplification using rT-qPCR analysis and measurement of the fluorescence intensity of DNA-binding fluorescent dye which binds to double-stranded DNA each time it is created. The reaction mixture was composed of 10 μ L of the 2X Taqman Gene expression master mix (Applied Biosystems, UK), 1 μ L of the test 20X TaqMan® Gene Expression Assay, 7 μ L RNase-free water and 2 μ L cDNA template. TaqMan® Gene Expression Assays that were used in the rT-PCR analysis is listed in Table 3. Samples were prepared in duplicates and loaded into MicroAmp® Optical 96-well reaction plate (Applied Biosystems, UK). The plate was subsequently sealed with MicroAmp® optical adhesive film (Applied Biosystems, UK), briefly centrifuged in Eppendorf 5430R microcentrifuge and then loaded into the real time PCR 7500 (Applied Biosystems, UK). The plate was run under the thermal cycling conditions that started with holding stage at 50 °C for 2 minutes followed by denaturation step at 95°C for 10 minutes. This was followed by 50 thermal cycles that started with initial denaturation for 15 seconds at 95°C followed by annealing and extension step for 1 minute at 60°C. The generated amplification plots showing exponential increase of the amplified PCR product were monitored to quantify the target DNA that was amplified with time. Data was quantified

using the relative quantitation method (Comparative C_T Method ($\Delta\Delta C_T$ Method)) comparing the ΔC_T of the sample to that of the calibrator control.

The amount of amplified target gene normalized to an endogenous reference house-keeping gene and relative to a calibrator sample is given by Equation 2. The method can be used for quantitation provided that the PCR efficiencies between the targets and endogenous controls are relatively equivalent.

Table 3: list of TaqMan[®] Gene Expression Assays used in the rT-qPCR analysis

Gene Name	Assay ID
B-Actin	Hs 99999903-m1
MyF 5	Hs00271574_m1
MyoD1	Hs00159528_m1

$$2^{-\Delta\Delta C_T}$$

Equation 2: Computing the fold difference in target gene expression relative to calibrator reference sample using comparative relative quantitation method ($\Delta\Delta C_T$ Method) where $\Delta\Delta C_T$ is the difference between the ΔC_T of the sample target gene and endogenous house-keeping gene and the ΔC_T of the calibrator reference target gene and endogenous house-keeping gene assuming that TaqMan[®] Gene Expression Assays have amplification efficiencies of 100% ($\pm 10\%$)

Chapter 3: Diffusion gradients in compartmentalized diffusion model; Model optimization and validation

3.1. Introduction

Molecular diffusion between source and sink compartments represents the simplest method of developing soluble molecule gradients. Soluble molecules are allowed to diffuse through hydrogel membranes separating two compartments from the highest to the lowest concentration compartment [14]. This generates a molecular concentration gradient along the hydrogel membrane dependant on the molecule/hydrogel interaction characteristics. This method has been more than once employed to generate protein concentration gradients across various types of hydrogel membranes [61, 107, 112, 124].

Chemotactic “under-agarose” assays widely utilize the principle of molecular diffusion to study cellular migration following diffusion of chemotactic agents across hydrogel matrix [125-127]. Gradients of recombinant human interleukin-8 (IL8) and the regulatory cell-derived lipid leukotriene B4 (LTB4) were developed using the under-agarose assay to provide a combinatorial control over leukocyte chemotaxis [112]. The gradients were quantified based on the radioactivity as a function of distance. Meanwhile, cellular responses in terms of distance of migration were assessed microscopically. The continuous variation in the developed gradients in under-agarose assays with time and position entailed the development of modified models providing stable linear gradients to quantify slight changes of cellular morphology [61]. This drawback was overcome using a modified chemotaxis chamber introduced in Fisher *et al.* [128]. The chamber was comprised of Enka PF296 hollow fibres embedded in the agarose gel. Continuous pumping of the chemoattractant cAMP from the source side was achieved concurrently with pump withdrawal from the sink side. This promoted the development of a stable chemical gradient sufficient to quantify the cellular motility and chemotaxis in *dictyostelium discoideum* [128].

The diffusion approach was as well utilized to fabricate PAAM hydrogels with a concentration gradient of type I collagen; concentration gradient of carboxyl groups, by exposure to gradients of NaOH in a side-by-side diffusion chamber [129]. L929 mouse fibroblasts were then seeded on top of the gradient hydrogel of 5×3×1 mm dimensions and microscopy were utilized to evaluate cellular adhesion.

The molecular diffusion approach was likewise employed in cell encapsulated hydrogel matrices and was not restricted to models where cells were plated underneath or on top of the hydrogels [107, 124]. An example for cell-laden hydrogels subjected to gradients

formed by molecular diffusion was discussed in Dodla and Bellamkonda [107]. The model followed the growth-promoting glycoprotein; LN-1 gradients across chicken dorsal root ganglion neurons (DRG) cell-laden 2.5 mm thick agarose blocks. LN-1 was photochemically coupled to agarose by concurrent diffusion of the cross-linker sulfosuccinimidyl-6-[40-azido-20-nitrophenylamino] hexanoate (SANPAH) conjugate from the source compartment for 6 hours followed by scaffold exposure to UV light for 60 seconds. The model followed the rhodamine-labelled LN-1 gradients via fluorescence microscopy. Neurite extension along the developed gradient was subsequently assessed via microscopy.

3.2. Aims & objectives

3.2.1. Aim

The aim of the work presented in this chapter is to generate and validate a robust, reliable compartmental diffusion model that could monitor diffusion gradients of protein drugs across 3D hydrogel membranes.

3.2.2. Objectives

Research objectives addressed in this chapter included:

1. Design and development of compartmental diffusion chamber with optimized experimental conditions.
2. Design and validation of a quantification protocol to estimate the diffusion gradients as a function of distance away from source compartment across the hydrogel membrane.
3. Investigation of the effect of size & nature of the diffusing species on the diffusion pattern as a function of time and distance.
4. Correlation of the effect of hydrogel concentration and composition on the diffusion pattern of different species.

3.3. Materials and methods

3.3.1. Hydrogel fabrication

Details of fabrication of 1%, 2% agarose and 1% agarose-1% gelatin are explained in section 2.2.5.

3.3.2. Development of compartmental diffusion model

Three-compartments diffusion model of Source-Gel-Sink assembly was developed as detailed in section 2.2.8.

3.3.3. Diffusion studies in compartmentalized diffusion model

The parameters & conditions utilized to conduct diffusion studies using the compartmental diffusion chamber are explained in section 2.2.8.4. Details of diffusing species concentrations, dispensing medium, analysis time points, rate of change of source and sink compartments, hydrogels composition & plate reader excitation and emission maxima are shown in Table 4.

3.3.4. Evaluation of diffusion gradients in hydrogel membranes

In order to evaluate the developed diffusion concentration gradients across the hydrogel membranes, a protocol of slicing (described in section 2.2.8.5) was followed by protein quantification. The protein concentration within each slice dissolved in PBS was then determined using fluorometric analysis using a TECAN infinite 200PRO multimode reader according to relative excitation and emission maxima of fluorescent-labelled diffusing species stated in Table 4.

3.3.5. Imaging of diffusion gradient across hydrogel scaffolds

See section 2.2.8.6.

3.3.6. Model validation

3.3.6.1. Slicing homogeneously dispersed fluorescent species in hydrogel membranes

Different concentrations of homogeneously dispersed fluorescent species across hydrogel scaffolds were prepared. The scaffolds were then sectioned according to protocol of slicing described in section 2.2.8.5 at random position within the scaffolds. The protein concentration within each slice dissolved in PBS was then determined using fluorometric analysis using a TECAN infinite 200PRO multimode reader according to relative excitation and emission maxima of fluorescent-labelled diffusing species stated in Table 4. Each specific test concentration scaffold was prepared in duplicate, and the fluorometric analysis to detect protein concentration per slice was performed on eight randomly sliced scaffolds for each hydrogel scaffold.

3.3.6.2. Effect of the molecular weight of diffusing species on the developed gradient

Fluorescein (32.125 µg/mL), as a small molecular weight fluorescent species, was allowed to diffuse through 1% agarose as described in 2.2.8.4 and the diffusion pattern across the hydrogel membrane was monitored at different time points. This was done in comparison to the diffusion pattern of FITC-BSA across 1% agarose hydrogel membrane.

Table 4: List of diffusing species diffusing through the compartmentalized diffusion chamber and their respective experimental conditions

Diffusing species	Hydrogel composition in PBS	Diffusing species dispensing medium	Source compartment concentration	Rate of change of source/sink compartments	Analysis time points (hours)	Plate reader settings	
						Excitation wave length	Emission wave length
Fluorescein	1% Agarose	PBS	32.125 µg/mL	None	2,5, 16 & 24	460 nm	515 nm
TRITC-BSA			0.5 mg/mL	Every 24 hours	24 & 72	541 nm	572 nm
TRITC-Dextran 65000			0.5 mg/mL		24, 48 & 72		
TRITC-Dextran 4400			0.5 mg/mL		24 & 72		
FITC-BSA			2% Agarose		0.5 mg/mL	24 & 72	490 nm
	1% Gelatin-1% Agarose	0.5 & 1 mg/mL	24, 48 & 72				

3.3.6.3. Opposing diffusion of TRITC & FITC-BSA in 1% Agarose scaffolds

Samples (500 μL) of (0.5 mg/mL) FITC-BSA were added to one compartment next to the cast hydrogel membrane. 500 μL (0.5 mg/mL) TRITC-BSA was added to the other compartment on the other side of the gel. Each compartment was changed every 24 hours with fresh solutions. Following the same quantification procedure, each hydrogel slice was evaluated for each fluorescent tag at the relevant excitation and emission maxima of the fluorescent-labelled BSA as stated in Table 4. The diffusion pattern across the hydrogel membrane was constructed on day 1 and day 3 as a function of distance inside the hydrogel scaffold.

3.3.6.4. Determination of diffusion coefficients of diffusing species

Samples (500 μL) of diffusing species were added to the source compartment next to the hydrogel scaffold and the source compartment was filled with blank PBS. Samples from the sink compartment were not changed during the time span of the experiment and were collected at different time points and analysed using fluorometric analysis using TECAN infinite 200PRO multimode reader according to relative excitation and emission maxima of fluorescent-labelled diffusing species stated in Table 4. Each time point was evaluated from 3 different scaffolds and the cumulative amount of diffusing species that diffused through the hydrogel were used to establish a concentration versus time curve. Equation 1 was used to solve for the diffusion coefficients of different species across agarose-based hydrogels.

3.3.7. Determination of hydrogel pore size using microscopic techniques

See section 2.2.6

3.4. Results

Casting the molten hydrogel between 2 PTFE blocks as described in 2.2.8 resulted in a hydrogel middle compartment of $15 \times 5 \times 6.6$ mm (Length \times Width \times Height) dimensions as shown in Figure 14. This system was utilized for diffusion studies in a source-gel-sink assembly following the removal of PTFE blocks after 30 minutes of cooling and hydrogel cross linking.

3.4.1. Validation of diffusion model

3.4.1.1. Correlation of quantification to qualitative methods

Conducting diffusion studies of FITC-BSA from source to sink compartments across the hydrogel middle membrane as described in 2.2.8.4 showed gradual decrease in fluorescence intensity across the hydrogel width as shown in Figure 16.



Figure 14: Top view of compartmentalized diffusion chamber showing hydrogel membranes of $15 \times 5 \times 6.6$ mm (Length \times Width \times Height) dimensions cast in the middle of the chamber.

This was matching with the quantitative evaluation of the developed FITC-BSA gradient after 14.5 hours (Figure 16) using a calibrated quantitative method. A calibration curve of the fluorescence intensity of hydrogel slices retrieved from homogeneously dispersed FITC-BSA in hydrogels of similar dimensions to that used in the diffusion model was established (Figure 15). Similar calibration curves of different diffusing species-hydrogels combination are shown in Supplementary figure 1-8. Random hydrogel slices from different positions of duplicate scaffolds for each protein concentration were quantified in a manner similar to the method employed to quantify the gradient developed in the diffusion model. Figure 15 shows an increase in fluorescence intensity per slice as a function of the increase of FITC-BSA concentration.

3.4.1.2. Effect of diffusing species molecular weight

To further validate the capability of diffusion model and the quantification method to monitor diffusion of different size species, Fluorescein; 3',6'-dihydroxyspiro[2-benzofuran-3,9'-xanthene]-1-one; $C_{20}H_{12}O_5$; a small molecular weight fluorescent molecule (332.31 g/mol) [130] was allowed to diffuse across the hydrogel membrane. Figure 17 shows digital images of the diffusion chamber at different time points. Progression of the green colour of the sink compartment (right hand side) was observed from zero time till 24 hours. The hydrogel membrane itself started showing a gradient green shade along the direction of fluorescein diffusion. At late time points, the entire membrane and both compartments were evenly shaded suggesting an equilibrium state. Diffusion gradient profiles of fluorescein across 1% agarose hydrogel membrane were established as a function of time as shown in Figure 17. A steep gradient of fluorescein was observed on the first time point at 2 hours that started to be moderate at 5 hours and completely equilibrated at 16 hours. At 24 hours, there was no observed gradient in fluorescence intensity and on contrast almost all positions showed relatively equal values of fluorescence intensities except for the distant 1 mm of the scaffold. However, the values of the fluorescence intensity at each position were higher than corresponding values detected for the 16-hours diffusion.

The diffusion profiles of two different starting concentrations (0.5 & 1 mg/mL) of FITC-BSA across the hydrogel membrane were followed as shown in Figure 18. The concentration gradient was maintained by the frequent change of the source and sink compartments every 24 hours as stated in Table 4.

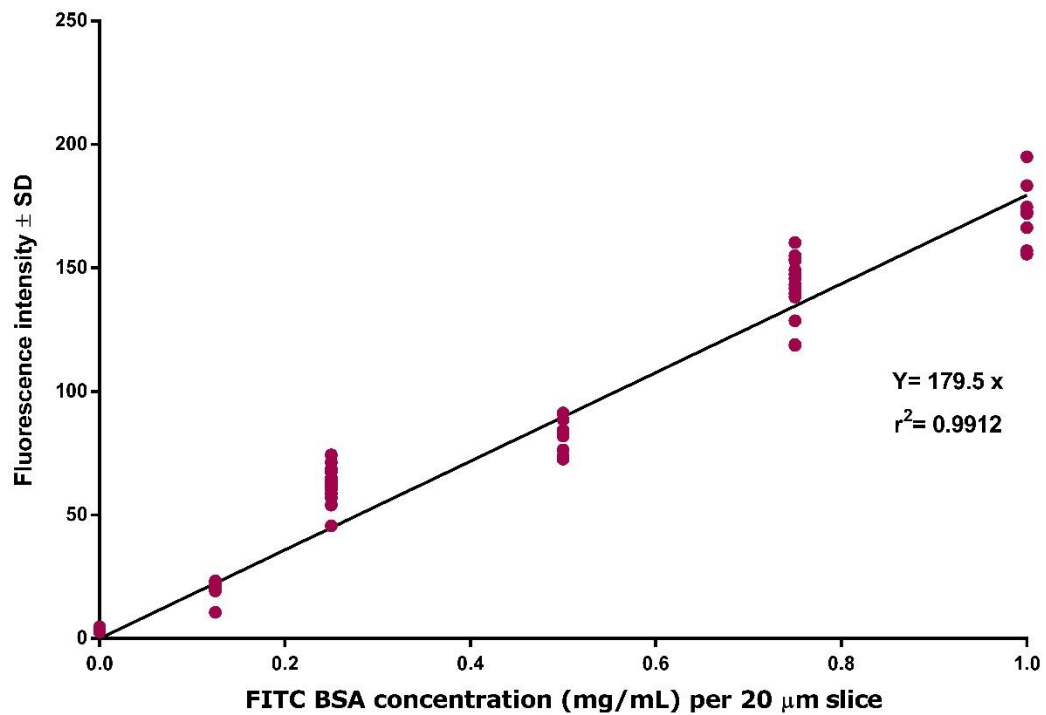


Figure 15: Calibration curve of FITC-BSA per 20 μm thick slices retrieved from cryosectioning of homogenously dispersed increasing concentrations of FITC-BSA in 1% agarose hydrogel scaffolds of 15×5×6.6 mm (Length × Width × Height) dimensions. Each concentration point was evaluated from 2 different scaffolds each with 8 different slices retrieved from random positions of the scaffold. Slices were dissolved in PBS and analysed for protein concentrations using a TECAN infinite 200PRO multimode reader (excitation: 490 nm; emission: 525 nm).

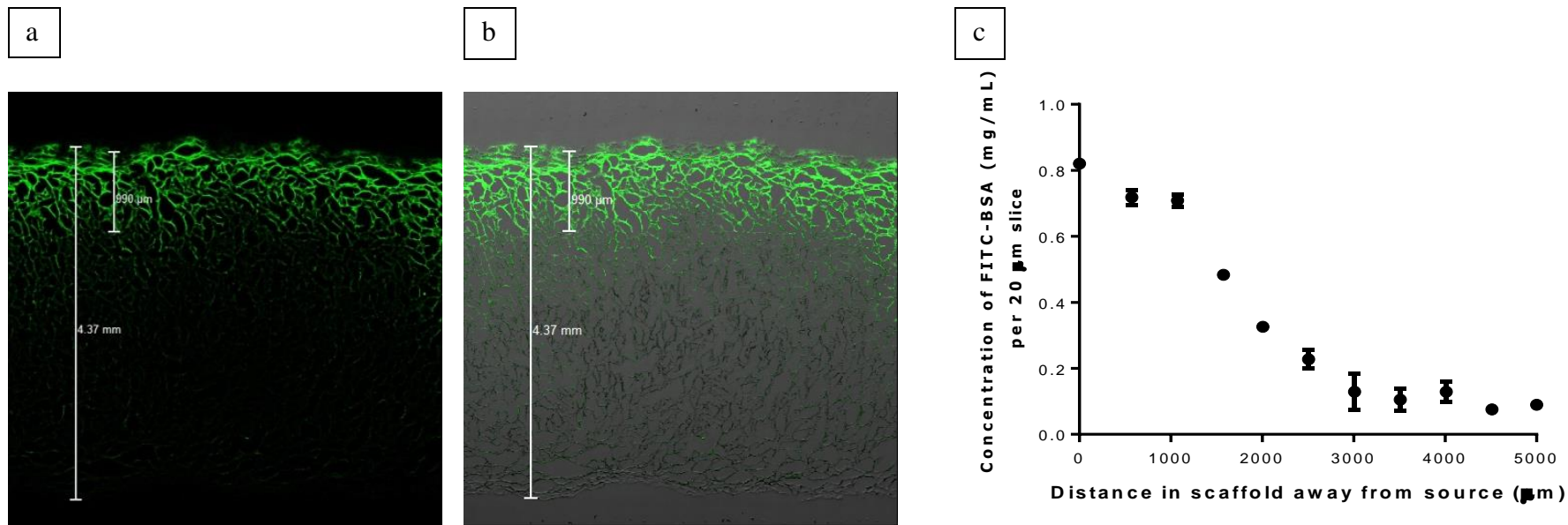


Figure 16: Confocal microscope images of 20 μm thick 1% agarose hydrogel slices sliced parallel to the direction of the flow of FITC-BSA diffusing from the source compartment of the compartmental diffusion chamber after 14.5 hours using Leica TCS SPE Confocal a. Macroscopic featuring green fluorescent channel, b. overlay of fluorescent and bright field channels and c. Diffusion pattern of 1 mg/mL FITC-BSA across 1% agarose hydrogel scaffolds of 15×5×6.6 mm (Length × Width × Height) dimensions after 14.5 hours. Each time point was evaluated from triplicate scaffolds through which 1 mg/mL FITC-BSA diffused.

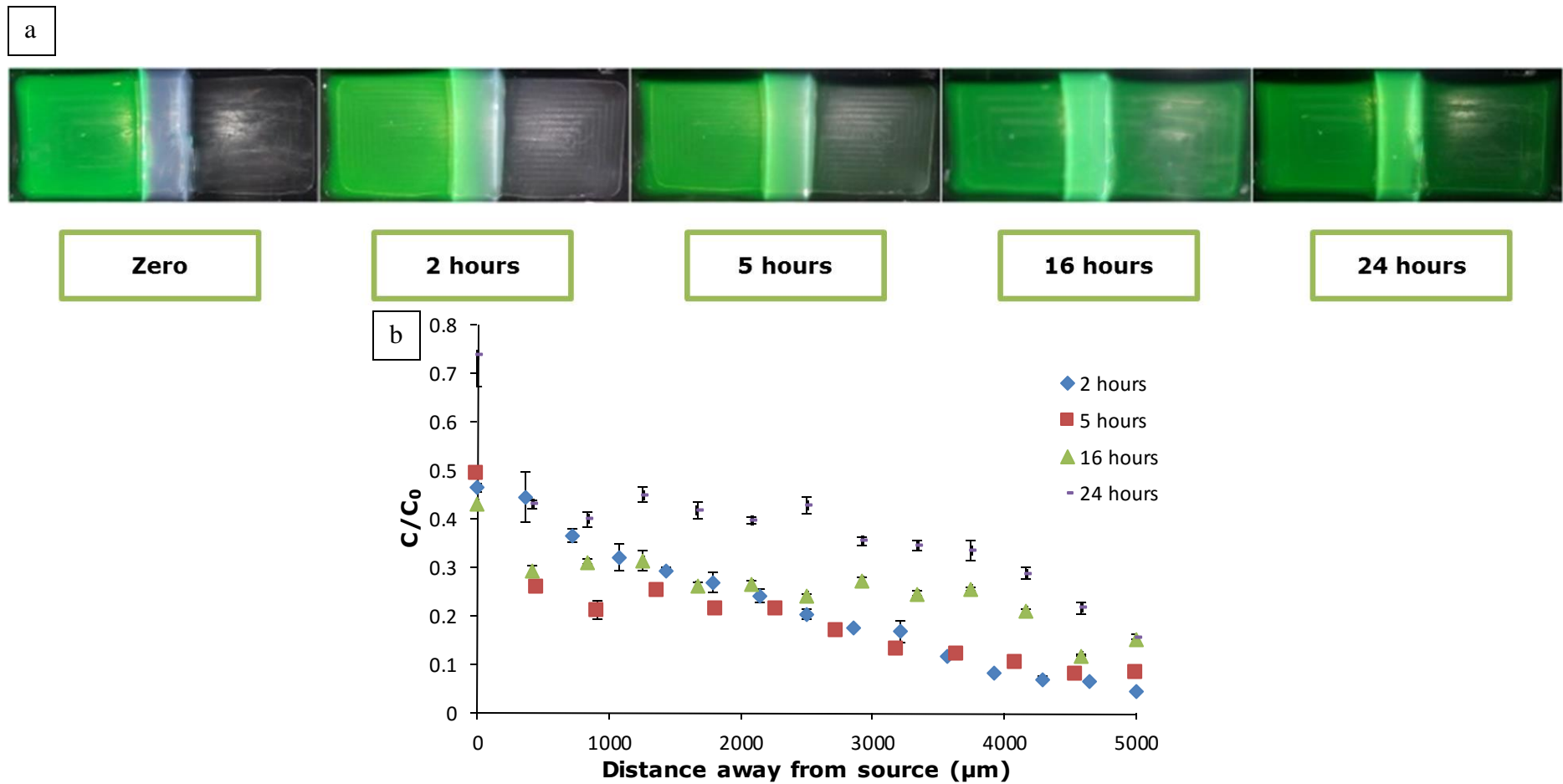


Figure 17: a. Representative images of compartmentalized diffusion chamber featuring diffusion of $32.15 \mu\text{g/mL}$ Fluorescein in 1% agarose hydrogel scaffolds of $15 \times 5 \times 6.6 \text{ mm}$ Length \times Width \times Height) dimensions with Fluorescein diffusing from the source compartment to the left of the hydrogel scaffold at zero, 2, 5, 16 and 24 hours and b. the corresponding concentration profiles.

The diffusion profiles maintained the gradient trend irrespective of the starting source compartment concentration as shown in Figure 18 a & b.

3.4.1.3. Effect of fluorescent tag and diffusion direction

The diffusion model relies on fluorescent tagged molecules for quantification and temporal imaging of the developed gradients. To confirm that the model is capable of following diffusion gradients of variable molecules irrespective of the fluorescent tag neither of the direction of flow the diffusing species, BSA tagged with TRITC was allowed to diffuse from the left compartment opposing to FITC-BSA diffusion from the right compartment. Representative fluorescence microscopy images of double opposing diffusing TRITC & FITC-BSA from either sides of the hydrogel scaffold at day 1 using Nikon stereomicroscope SMZ 1500 are shown in Figure 19. Monitoring the progression of fluorescence intensity as a function of distance using fluorescence microscopy imaging was performed at different time points. Double opposing diffusion gradient profile of TRITC & FITC-BSA at days 1 and 3 is shown in Figure 20. Mirror image diffusion profiles for TRITC & FITC-BSA were observed at each specific time point. As a follow up and further validation of the model, the concentrations of proteins at both compartments were monitored as a function of time. Figure 21 shows an increase in the FITC-BSA concentration in the left compartment from day 1 to day 2 and this was slightly decreased on day 3 (green bars plotted on the left axis). Similarly, the fluorescence intensity of TRITC BSA was increasing in the left compartment with time (rose bars plotted on the left axis). A similar trend was observed in the right compartment for TRITC & FITC-BSA respectively.

3.4.1.4. Effect of hydrogel nature and concentration

The effects of hydrogel concentration and nature were investigated by following the diffusion of FITC-BSA through 2% agarose or 1% agarose-1% gelatin scaffolds together with 1% agarose scaffolds. Figure 22 shows the diffusion of FITC-BSA (0.5 & 1 mg/mL) across 2% agarose. The diffusion profiles maintained the gradient profile irrespective of the starting source compartment concentration as shown in Figure 22 a & b. A similar observation was noticed for FITC-BSA diffusion across 1% agarose-1% gelatin scaffolds as shown in Figure 23 a & b.

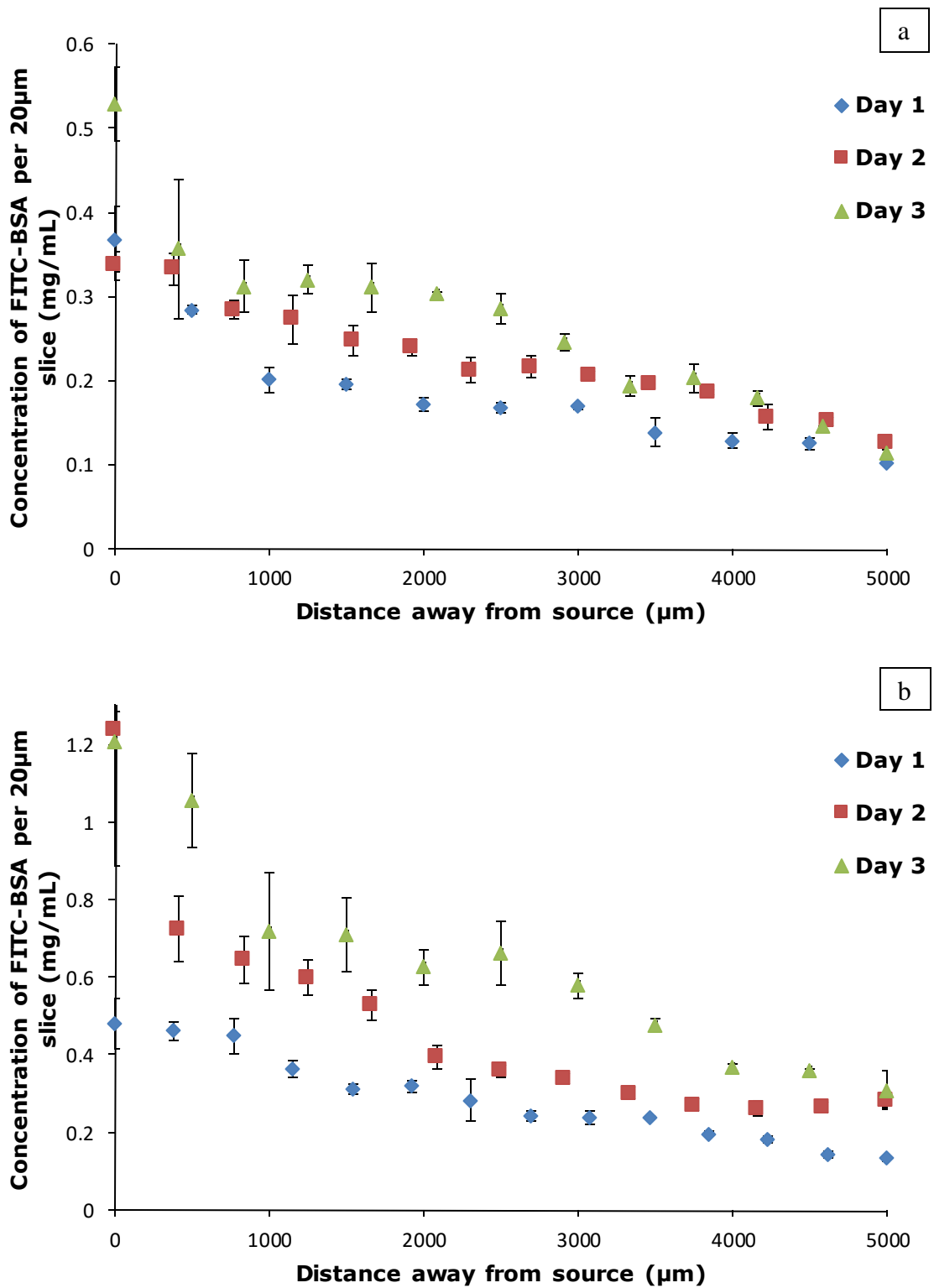


Figure 18: Diffusion pattern of FITC-BSA across 1% agarose hydrogel scaffolds of 15×5×6.6 mm (Length × Width × Height) dimensions. Each time point was evaluated from triplicate scaffolds through which a: 0.5 mg/mL or b: 1 mg/mL FITC-BSA diffused over days 1, 2 & 3.

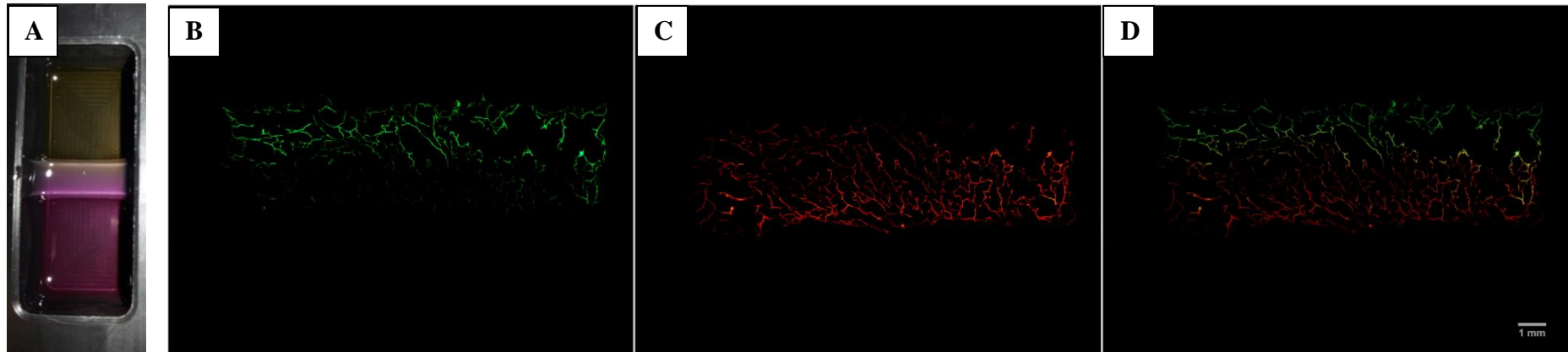


Figure 19: A: Representative image of compartmentalized diffusion chamber at day 3 featuring 1% agarose hydrogel scaffolds of 15×5×6.6 mm (Length × Width × Height) dimensions with TRITC & FITC-BSA diffusing from different sides of the scaffold. B-D: Fluorescence microscopy images of 20 μm thick 1% agarose hydrogel slices sliced parallel to the direction of the flow of double opposing diffusing TRITC & FITC-BSA from either sides of the hydrogel scaffold at day 1 using Nikon stereomicroscope SMZ 1500 featuring b: red channel, c: green channel & d: overlay of both channels. Scale bar is 1mm.

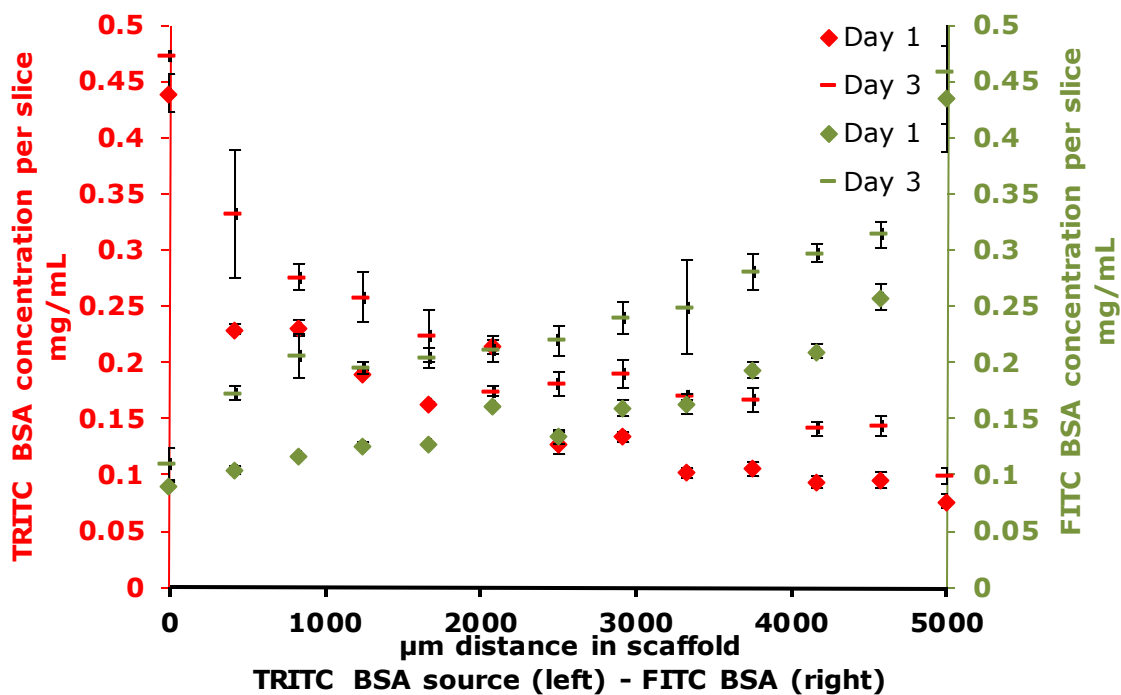


Figure 20: Diffusion pattern of opposing diffusion of TRITC (left) and FITC (right) labelled BSA across 1% agarose hydrogel scaffolds of 15×5×6.6 mm (Length × Width × Height) dimensions. Each time point was evaluated from triplicate scaffolds through which 0.5 mg/mL TRITC & FITC-BSA diffused from either side of the gel membrane respectively.

a



b

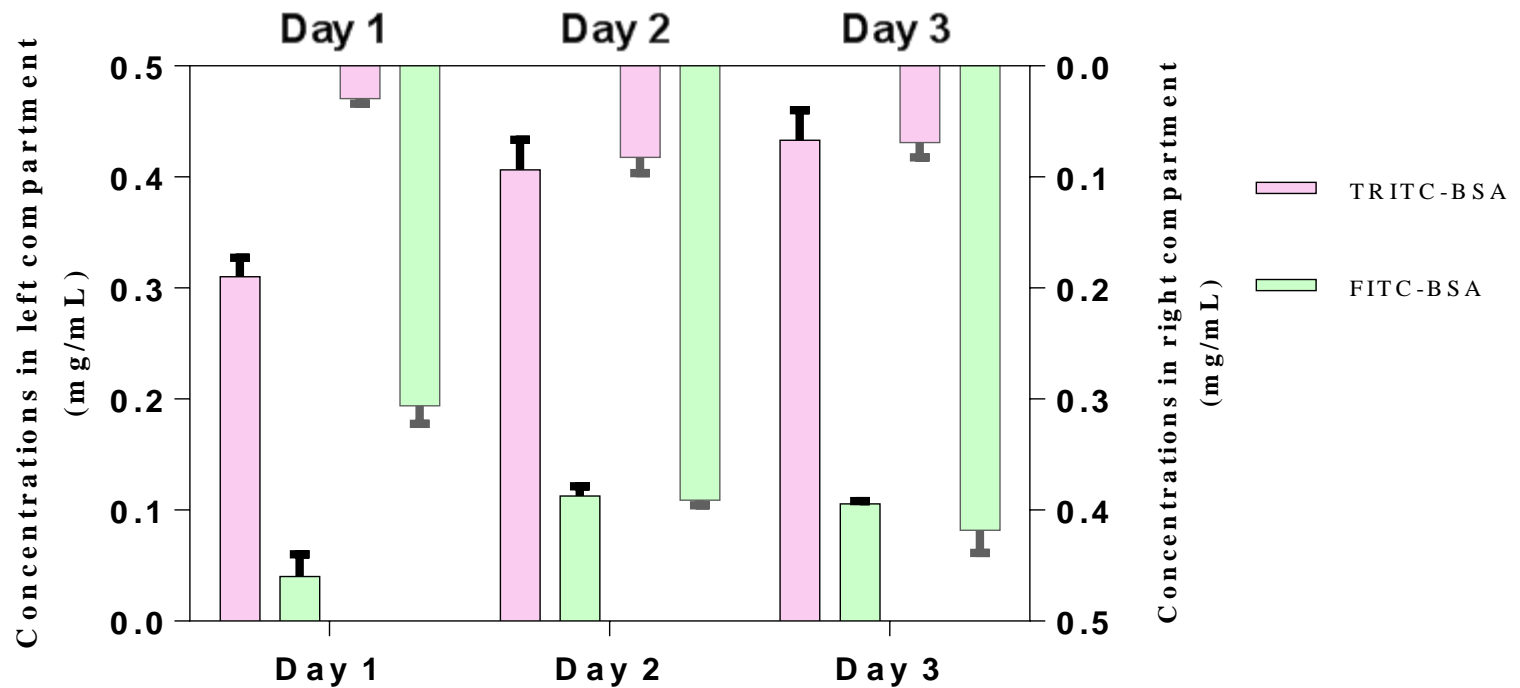


Figure 21: Monitoring TRITC & FITC-BSA concentrations (mg/mL) in left and right compartments next to 1% agarose hydrogel scaffold in the compartmentalized diffusion chamber following diffusion of 0.5 mg/mL TRITC-BSA from the left compartment and 0.5 mg/mL FITC-BSA from the right compartment. a. representative image of compartmentalized diffusion chamber & b. quantitative evaluation of source and sink concentrations

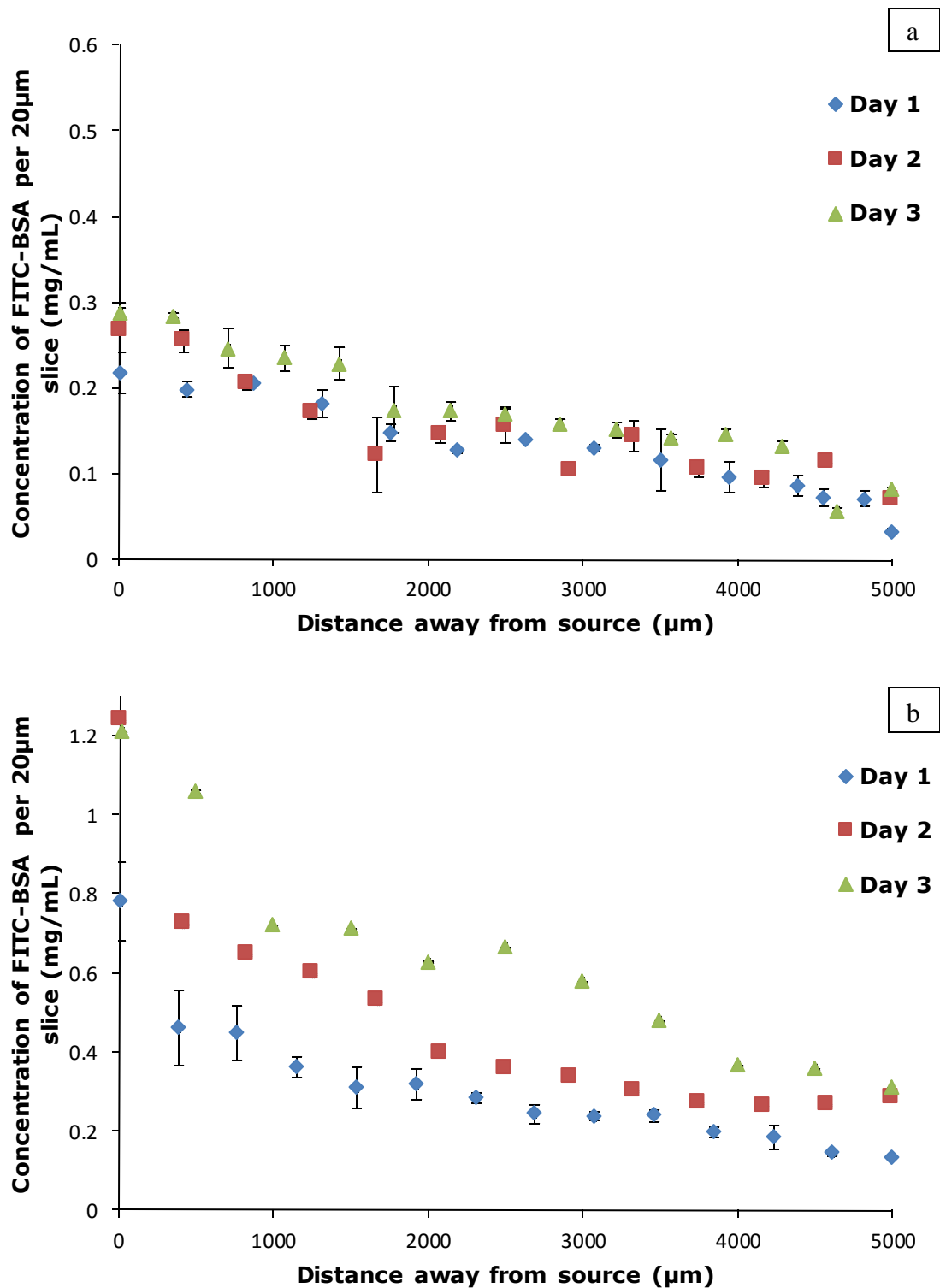


Figure 22: Diffusion pattern of FITC-BSA across 2% agarose hydrogel scaffolds of 15×5×6.6 mm (Length × Width × Height) dimensions. Each time point was evaluated from triplicate scaffolds through which a: 0.5 mg/mL or b: 1 mg/mL FITC-BSA diffused over days 1, 2 & 3.

To compare the different diffusion profiles of FITC-BSA in different hydrogel systems, data of protein diffusion was fitted to the linear and exponential decay models as shown in Table 5. Figure 24 and Table 6 show the exponential decay curve fitting describing the diffusion of FITC-BSA across 1% agarose, 2% agarose and 1% agarose-1% gelatin. Detailed comparative diffusion of FITC-BSA (0.5 & 1 mg/mL) across the three different hydrogel systems is shown in Figure 25. It shows relatively higher values of FITC-BSA in 1% agarose hydrogel slices at all positions as compared to 2% agarose and 1% agarose-1% gelatin hydrogels.

3.4.2. Determination of proteins diffusion coefficients

The model permeation method was employed to compute the diffusion coefficients of FITC-BSA across 1% & 2% agarose cast in the compartmental diffusion chamber. Figure 26a shows the real time monitoring of the FITC-BSA concentrations in the sink compartment at different time points following diffusion across 1% agarose. Fitting the data collected after achievement of steady state concentration using linear regression as shown in Figure 26b resulted in a regression equation that was solved for the slope and intercept from Equation 1. Similarly, FITC-BSA concentrations in the sink compartment following diffusion across 1% agarose were monitored and fitted using linear regression after 24 hours as shown in Figure 27. From both regression equations, the diffusion coefficients of FITC-BSA across 1% and 2% agarose were calculated to be 5.20×10^{-7} & 3.24×10^{-7} cm²/s respectively.

3.4.3. Determination of hydrogel structure

The hydrogel structure was revealed using CryoSEM as shown in Figure 28. Fresh 1%, 2% agarose and 1% agarose-1% gelatin are shown in Figure 28a, b and c respectively. 1 day hydrated 1% agarose-1% gelatin is shown in Figure 28d. The hydrogel morphology of 1% agarose was different from 2% agarose and fresh 1% agarose-1% gelatin hydrogels which looked more or less similar. Hydration of 1% agarose-1% gelatin (Figure 28d) resulted in more plasticized surface rather than fresh sample (Figure 28c). The structure of the hydrogels and the mesh size were further investigated using the CryoSEM coupled with focused ion beam technology. A thin section of 1% agarose-1% gelatin was transferred under cryogenic conditions to the transmission electron microscope to attain a higher magnification image of the mesh size as shown in Figure 29. Figure 30-Figure 31 show TEM images featuring the mesh size of 1% and 1% agarose-1% gelatin following ultra-thin microtomy.

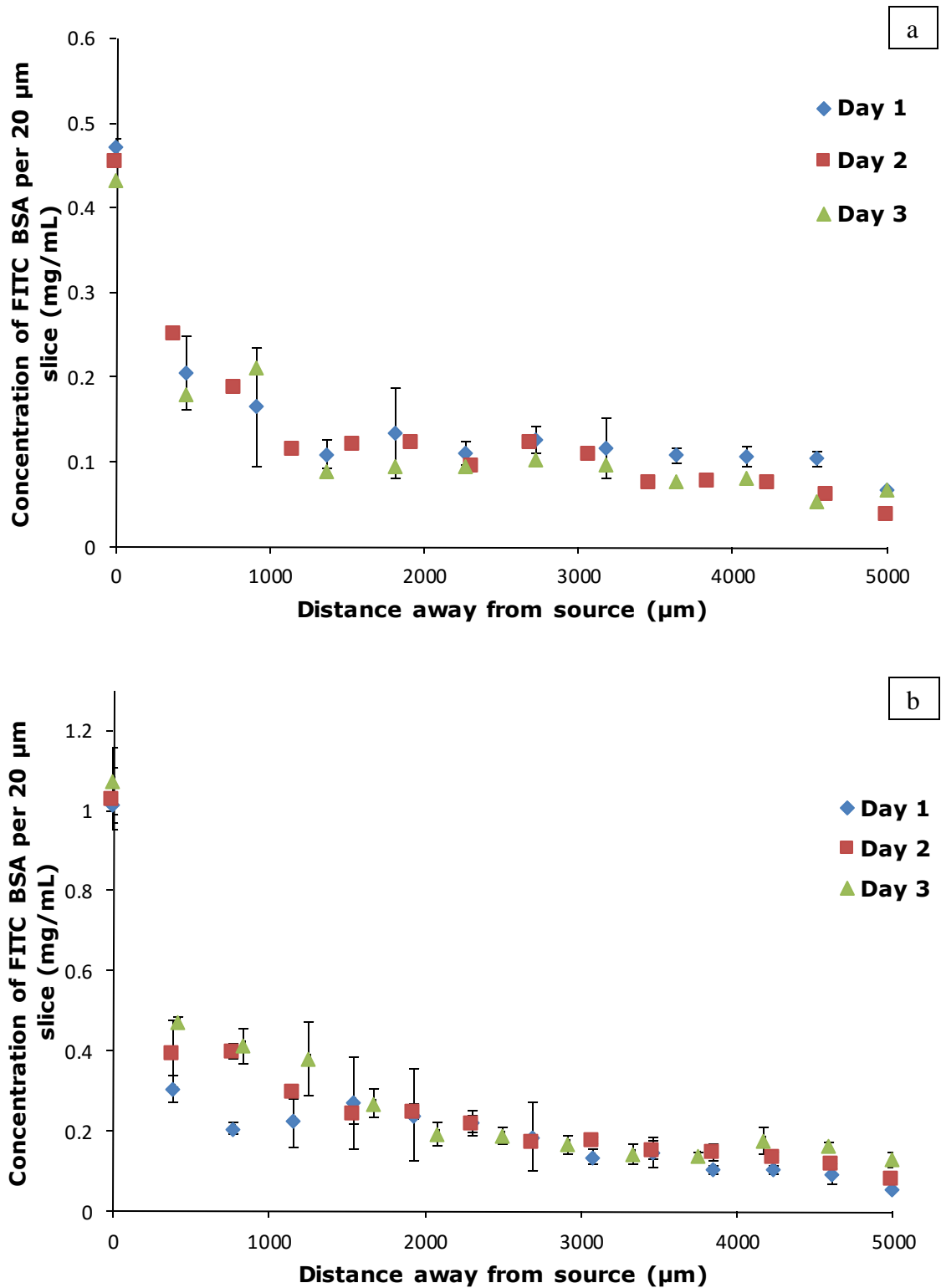


Figure 23: Diffusion pattern of FITC-BSA across 1% agarose-1% gelatin hydrogel scaffolds of 15×5×6.6 mm (Length × Width × Height) dimensions. Each time point was evaluated from triplicate scaffolds through which a: 0.5 mg/mL or b: 1 mg/mL FITC-BSA diffused over days 1, 2 & 3.

Table 5: Linear and exponential fit of the diffusion profiles of various diffusing species in different hydrogel systems in the compartmental diffusion model.

Diffusing species/hydrogel	Linear Regression		Exponential Regression	
	slope $\times 10^{-5}$	intercept	r^2	r^2
Fluorescein in 1% Agarose	-10	0.6949	0.4956	0.702
FITC-BSA in 1% Agarose	-7	0.4626	0.9567	0.9753
FITC-BSA in 1% Agarose-1% Gelatin	-10	0.4871	0.4688	0.8089
FITC-BSA in 2% Agarose	-8	0.3991	0.4581	0.739
TRITC Dextran 4400 in 1% Agarose	-7	0.5202	0.6273	0.7285
TRITC Dextran 65000 in 1% Agarose	-10	0.6675	0.8764	0.9382

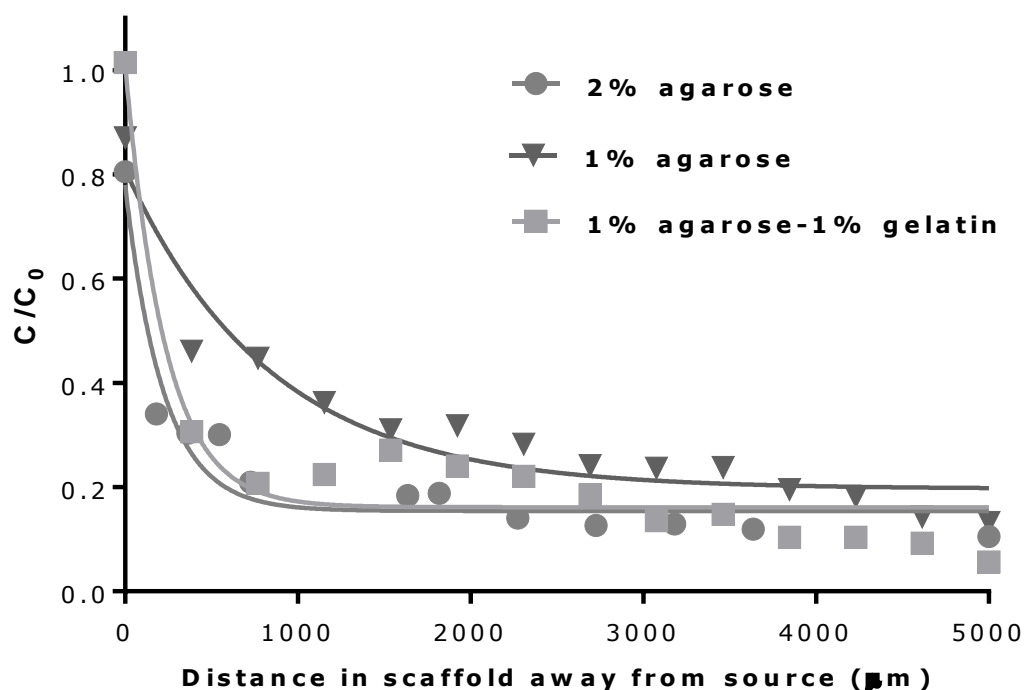


Figure 24: A. One phase decay curve describing the kinetics of diffusion of FITC-BSA across 2% & 1% agarose and 1% agarose-1% gelatin hydrogel scaffolds. The goodness of fit in terms of correlation coefficient (r^2) of the non-linear regression fitting is calculated to be 0.9360, 0.9247 & 0.9320 for 2% & 1% agarose and 1% agarose-1% gelatin hydrogel scaffolds respectively.

Table 6: One phase decay equation fit of the diffusion profiles of FITC-BSA in different hydrogel systems in the compartmental diffusion model.

Hydrogel system	Equation	r^2
2% agarose	$Y=0.03*e^{(-0.001*X)} + 0.02$	0.936
1% agarose	$Y=0.61*e^{(-0.001*X)} + 0.19$	0.925
1% agarose -1% gelatin	$Y=0.85*e^{(-0.004*X)} + 0.16$	0.932

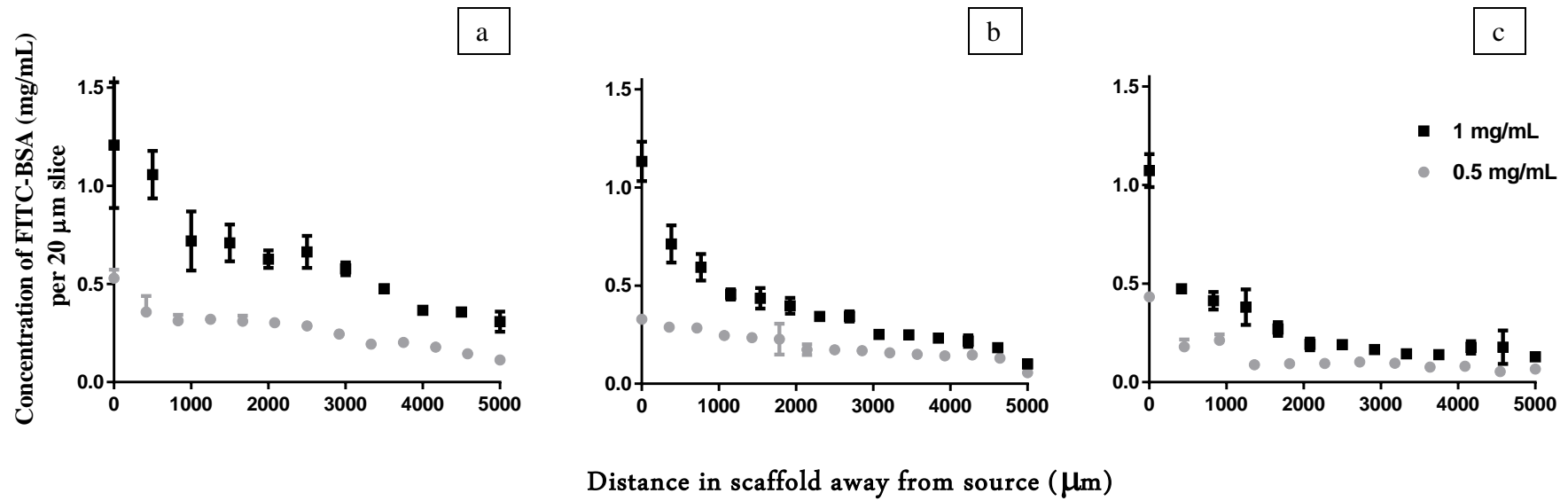


Figure 25: Comparative diffusion patterns of 0.5 & 1 mg/mL FITC-BSA across a: 1%, b: 2% agarose & c: 1% agarose-1% gelatin hydrogel scaffolds of 15×5×6.6 mm (Length × Width × Height) dimensions at day 3.

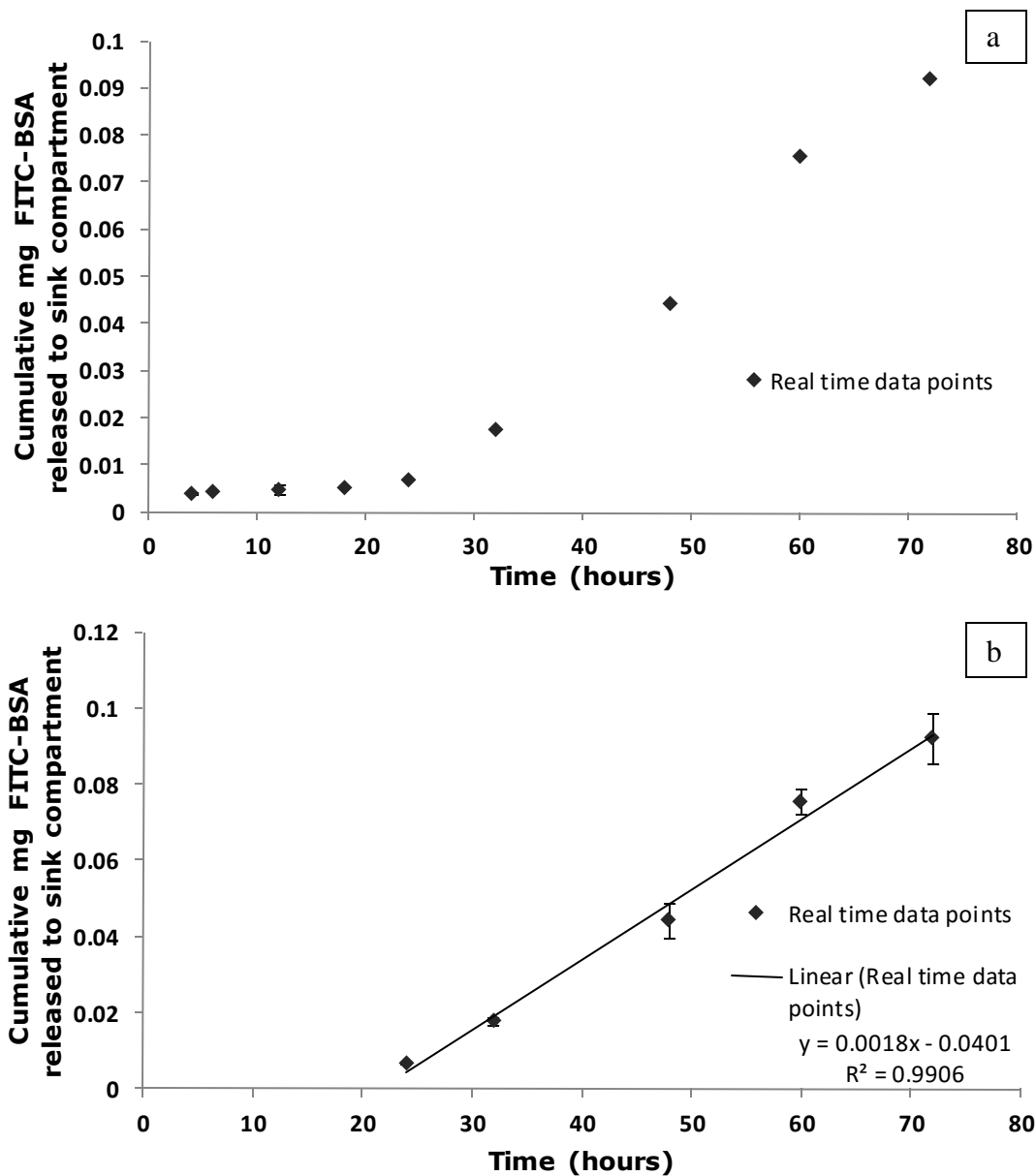


Figure 26: Determination of the diffusion coefficient of FITC-BSA in agarose hydrogels using membrane permeation model utilizing acellular scaffolds of 15×5×6.6 mm (Length × Width × Height) dimensions as gel membranes. Each time point was evaluated from 3 different scaffolds through which 500 µg/mL FITC-BSA diffused. a: Real time data points of amount of FITC-BSA measured in the sink compartments at the relevant time points. b: Linear regression for the same set of data after 24 hours, from which the diffusion coefficient of FITC-BSA in in 1% agarose is evaluated to be $5.20 \times 10^{-7} \text{ cm}^2/\text{s}$.

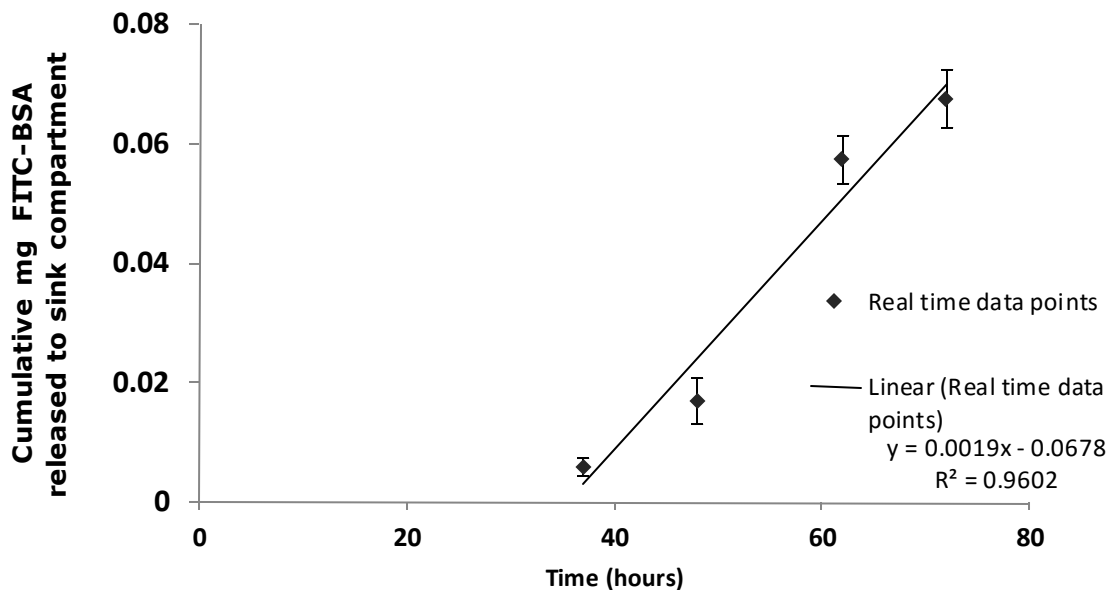


Figure 27: Determination of the diffusion coefficient of FITC-BSA in 2% agarose hydrogels using membrane permeation model utilizing acellular scaffolds of 15×5×6.6 mm (Length × Width × Height) dimensions as gel membranes. Each time point was evaluated from 3 different scaffolds through which 500 µg/mL FITC-BSA diffused. Linear regression for real time data points of FITC-BSA diffusion in 2% agarose after 36 hours, from which the diffusion coefficient is evaluated to be $3.24 \times 10^{-7} \text{ cm}^2/\text{s}$.

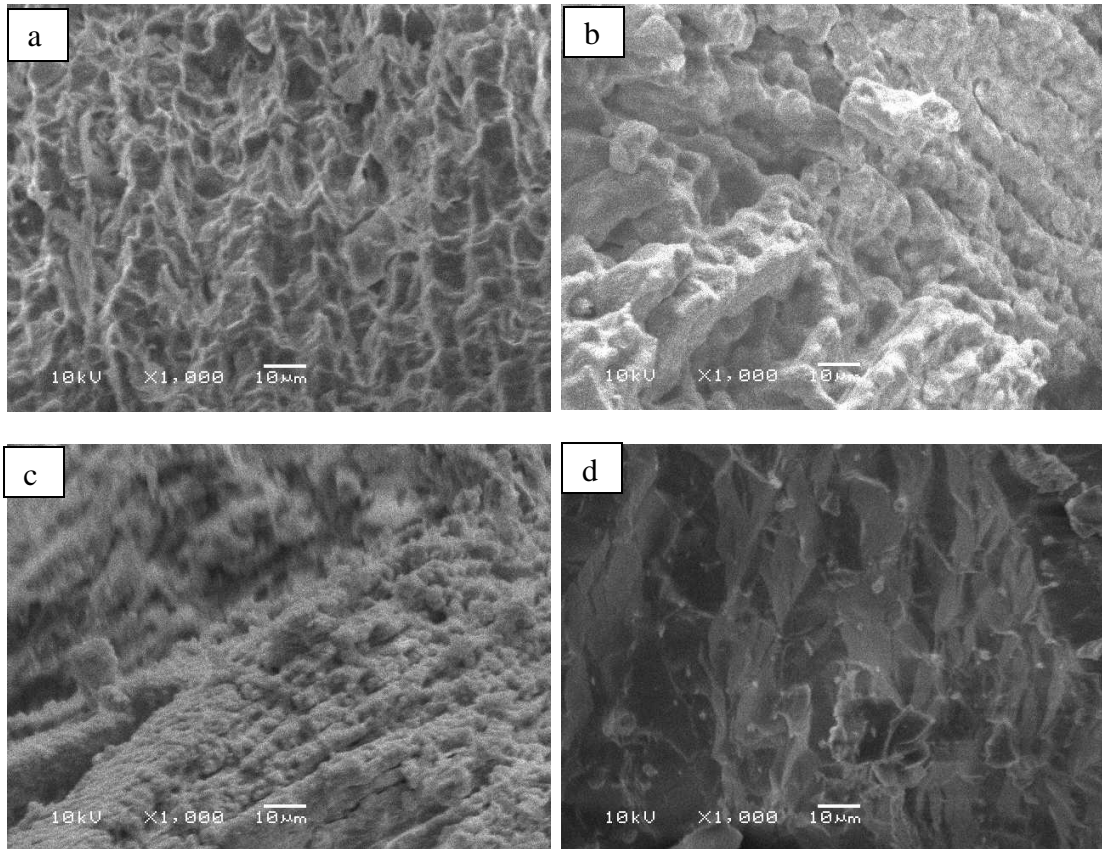


Figure 28: Cryo scanning electron micrographs of a: 1% agarose, b: 2% agarose, c: 1% agarose-1% gelatin & d: 1 day hydrated 1% agarose-1% gelatin as viewed under JEOL JSM-6060LV scanning electron micrograph under cryogenic conditions.

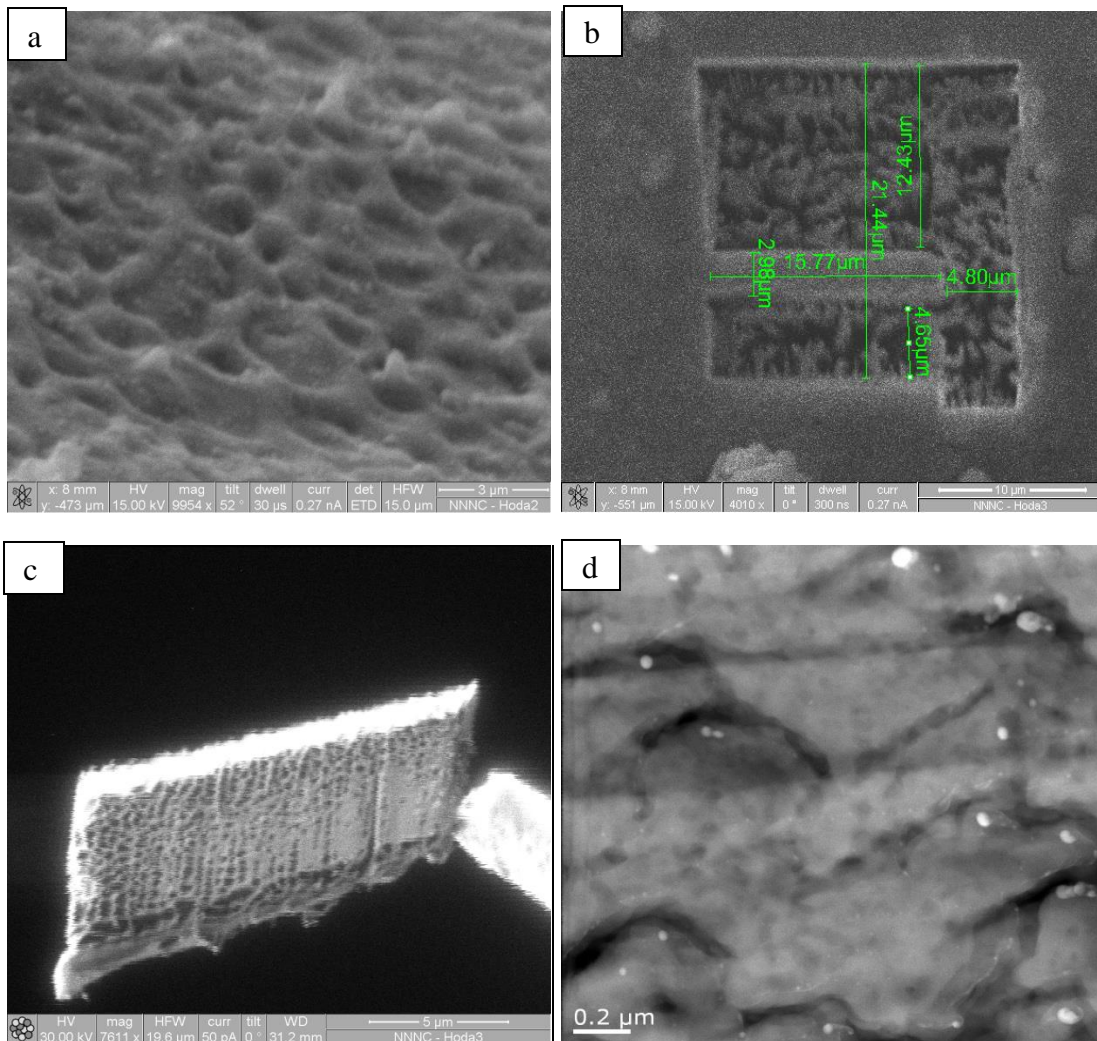


Figure 29: Cryo scanning electron micrographs of a: 1% agarose-1% gelatin, b: region in hydrogel cut using focused ion beam and c: thinned section following focused ion beam thinning viewed under scanning electron micrograph under cryogenic conditions & d: thin hydrogel section as viewed under transmission electron microscope.

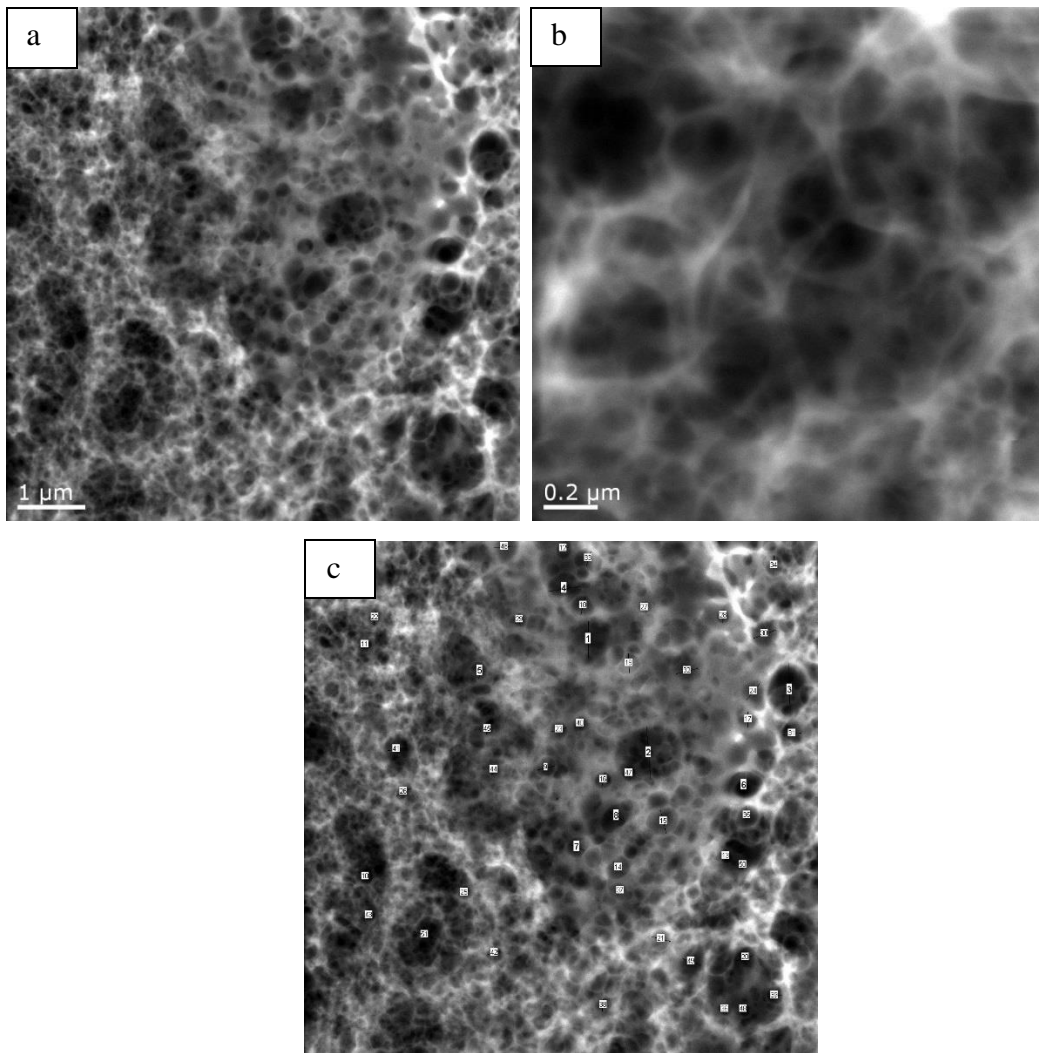


Figure 30: Transmission electron micrographs of a: 1% agarose following ultra-thin sectioning viewed under TEM, b: higher magnification, c: annotated pores from which the average pore size is calculated to be 273 ± 141 nm.

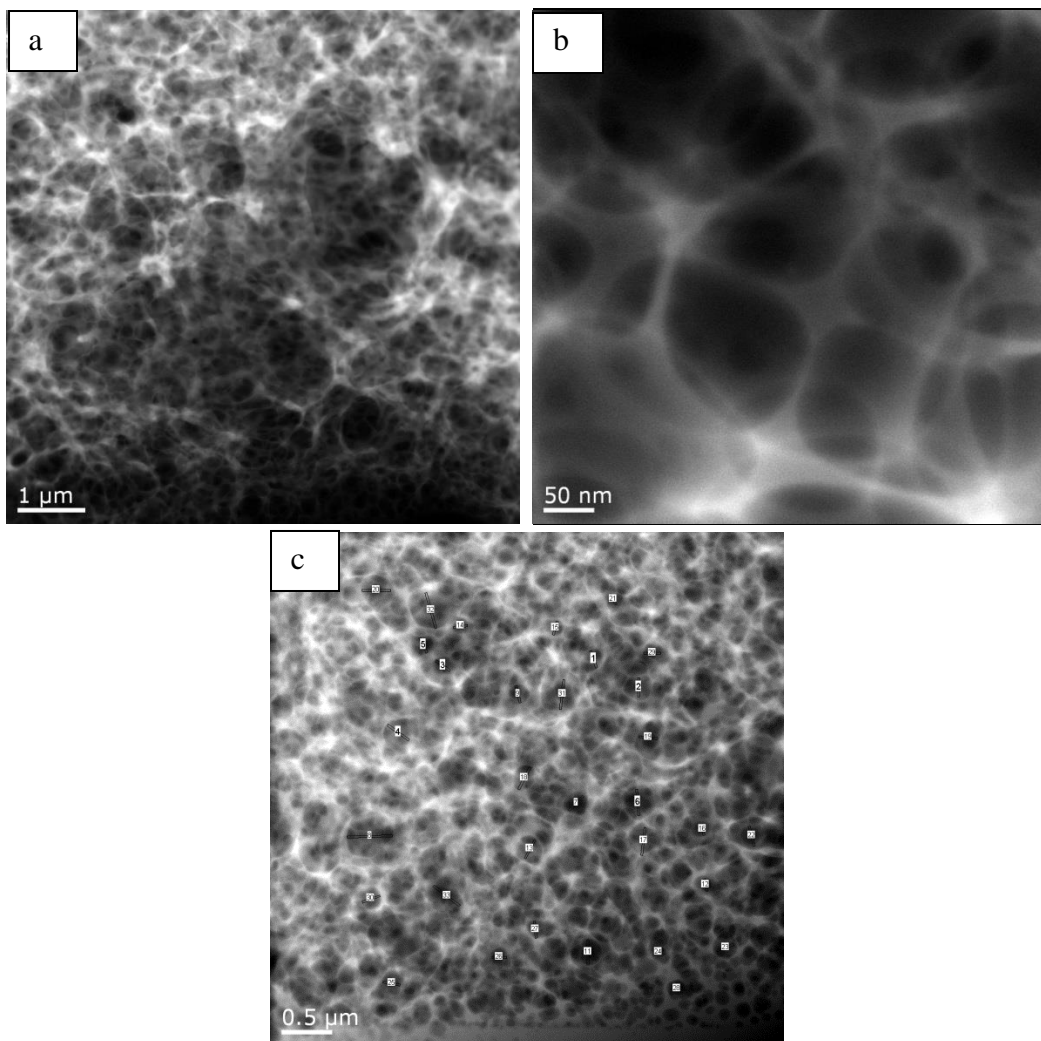


Figure 31: Transmission electron micrographs of a: 1% agarose-1% gelatin following ultra-thin sectioning viewed under TEM, b: higher magnification, c: annotated pores from which the average pore size is calculated to be 198 ± 8 nm.

3.4.4. Effect of nature of diffusing species

To further investigate the ability of the model to follow the diffusion of different species, different molecular weight polysaccharides were allowed to diffuse across 1% agarose. Diffusion profiles of dextran 4400 and 65000 in 1% agarose slices at different time points are shown in Figure 32 & Figure 34 respectively. To compare the diffusion profiles of TRITC Dextran 4400 & 65000, Figure 36 shows diffusion profiles of each diffusing species at day 1 and their correspondent phase decay fitted curves.

Figure 33 & Figure 35 show temporal monitoring of polysaccharides concentrations in the source and sink compartments following dextran 4400 and 65000 diffusion respectively. An increase in the amount of the dextran received in the sink compartments was observed as a function of time. This was more prominent with dextran 4400 as shown in Figure 35. The dextran concentrations in the source compartments were not following a specific pattern. A drop in the source concentration was observed after day 1 and thereafter the concentration was kept constant (Figure 33). In case of Dextran 4400, an extra time point measurement was performed at 13.5 hours. There was no replenishment of the source/sink compartments between 13.5 & 24 hours. A drop in the dextran 4400 concentration in the source compartment was observed from 13.5 hours to 24 hours and thereafter the concentration of the sink was relatively kept constant (Figure 35).

3.5. Discussion

3.5.1. Model validation

Randomly selected 20 μm -thick slices from different positions of homogeneously dispersed particular concentration FITC-BSA in 1% agarose scaffold showed similar fluorescence intensity responses for each specific concentration suggesting the validity of the quantification method to measure protein concentrations and subsequently construct diffusion profiles. This feature was further validated over different diffusing species-hydrogels combinations investigated as shown in appendix I.

Correlating the distance of the scaffold with higher fluorescence intensity of FITC-BSA ($\sim 1\text{ mm}$) to that quantitatively measured from the diffusion gradient profile suggests that model of diffusion and the quantification methods can be used to follow temporal proteins gradients.

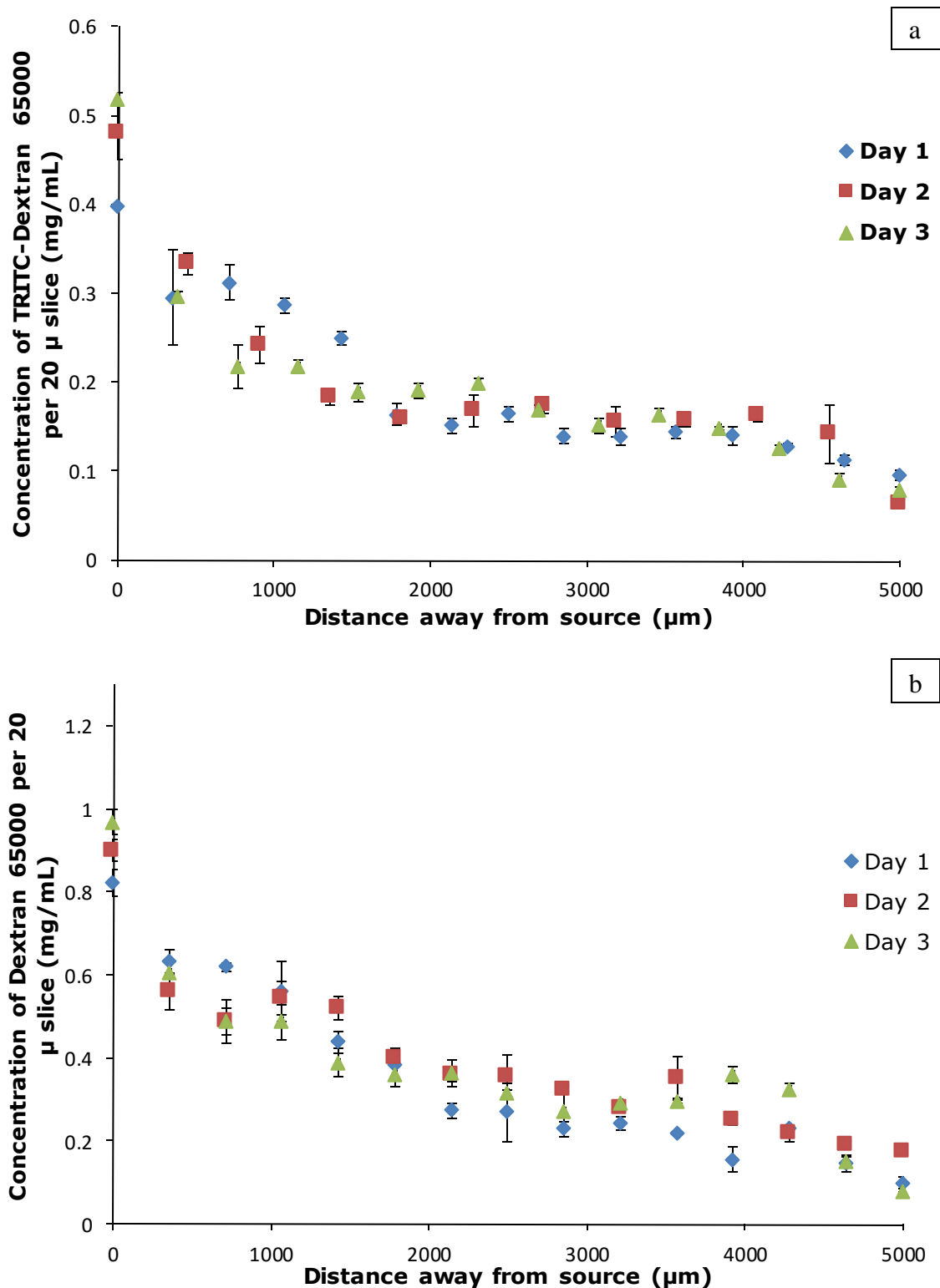


Figure 32: Diffusion pattern of TRITC-Dextran 65000 across 1% agarose hydrogel scaffolds of 15×5×6.6 mm (Length × Width × Height) dimensions. Each time point was evaluated from triplicate scaffolds through which a: 0.5 mg/mL or b: 1 mg/mL FITC-BSA diffused over days 1, 2 & 3.

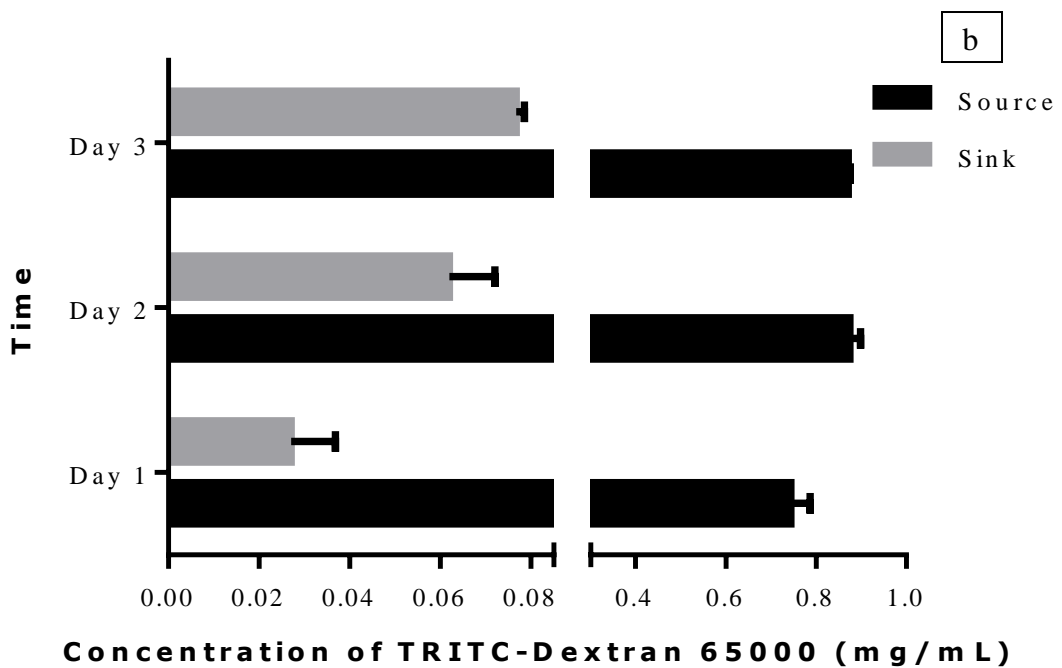
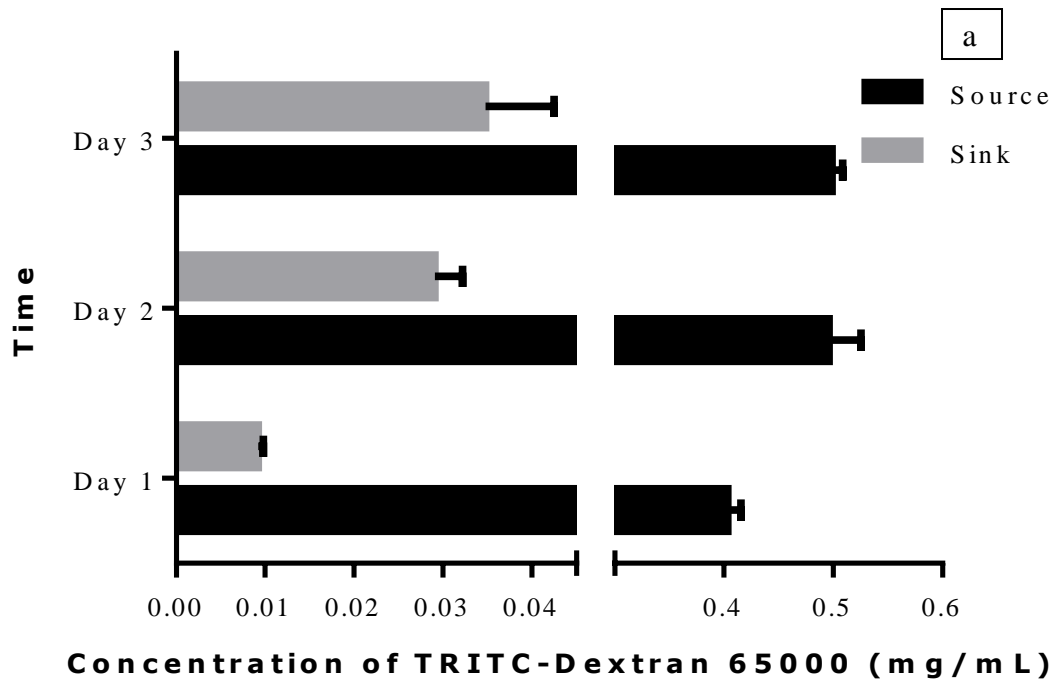


Figure 33: Monitoring TRITC-Dextran 65000 concentrations (mg/mL) in source and sink compartments next to 1% agarose hydrogel scaffold in the compartmentalized diffusion chamber following diffusion of a: 0.5 mg/mL & b: 1 mg/mL TRITC-Dextran 65000 at different time points.

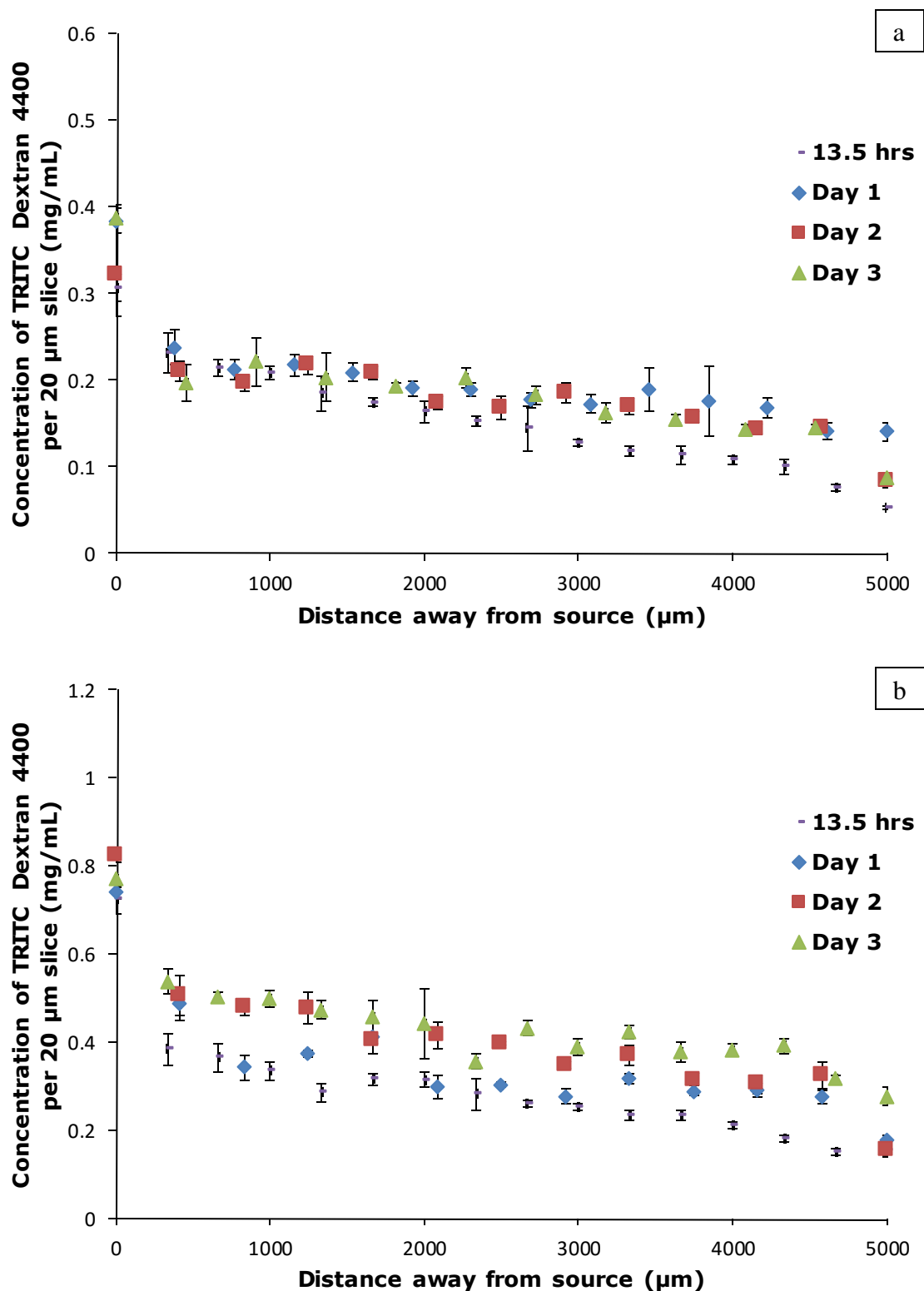


Figure 34: Diffusion pattern of TRITC-Dextran 4400 across 1% agarose hydrogel scaffolds of 15×5×6.6 mm (Length × Width × Height) dimensions. Each time point was evaluated from triplicate scaffolds through which a: 0.5 mg/mL or b: 1 mg/mL FITC-BSA diffused over 13.5 hours & days 1, 2 & 3.

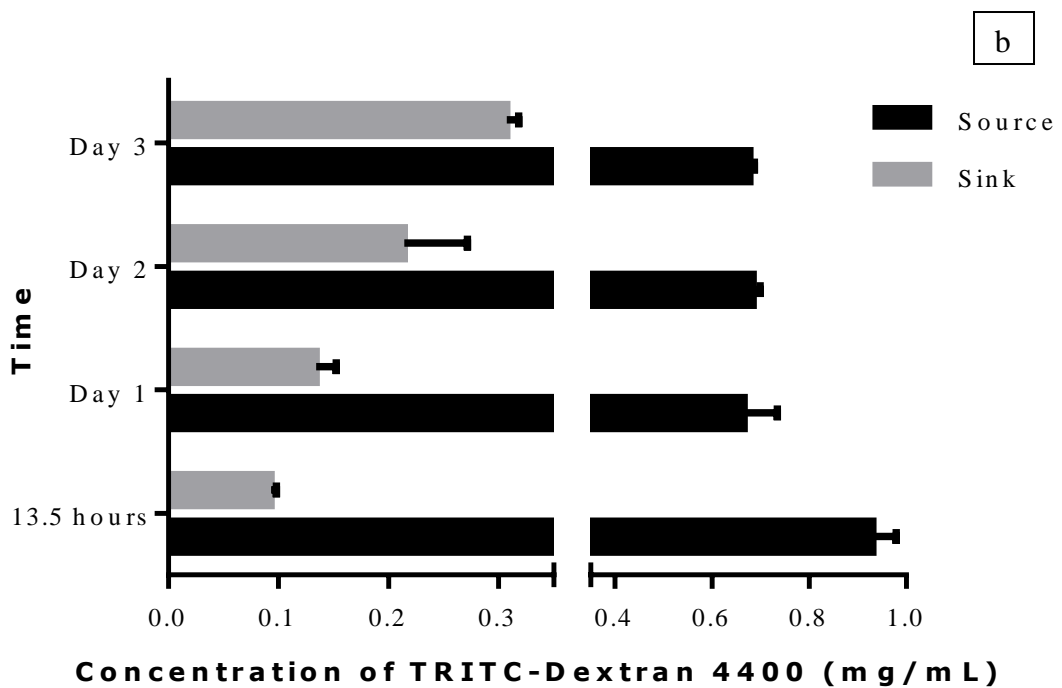
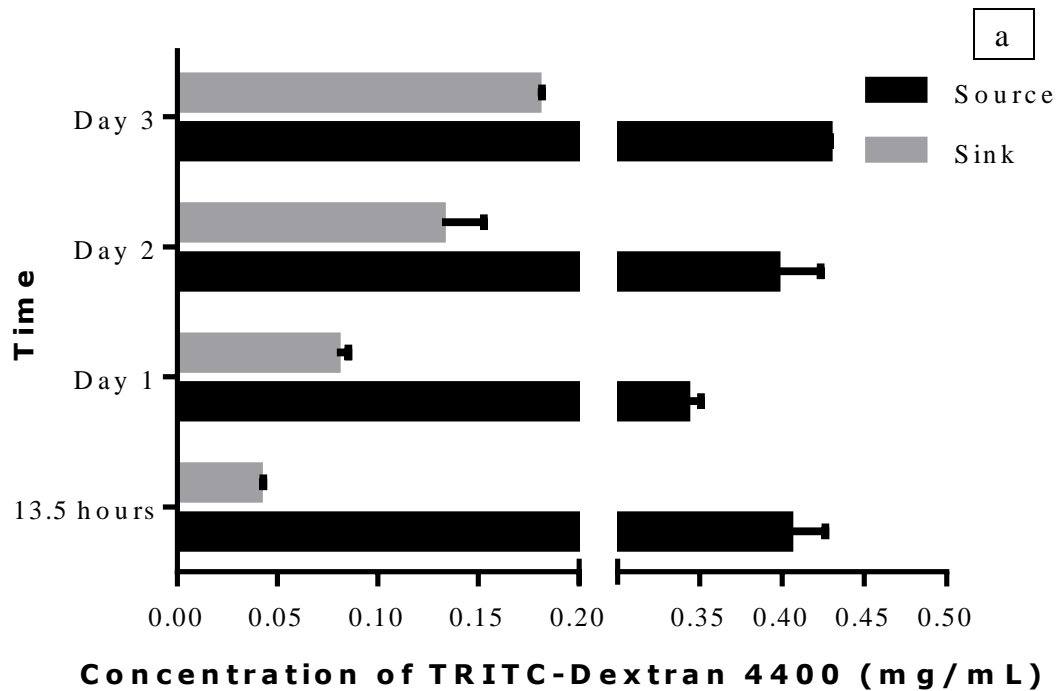


Figure 35: Monitoring TRITC-Dextran 4400 concentrations (mg/mL) in source and sink compartments next to 1% agarose hydrogel scaffold in the compartmentalized diffusion chamber following diffusion of a: 0.5 mg/mL & b: 1 mg/mL TRITC-Dextran 4400 at different time points.

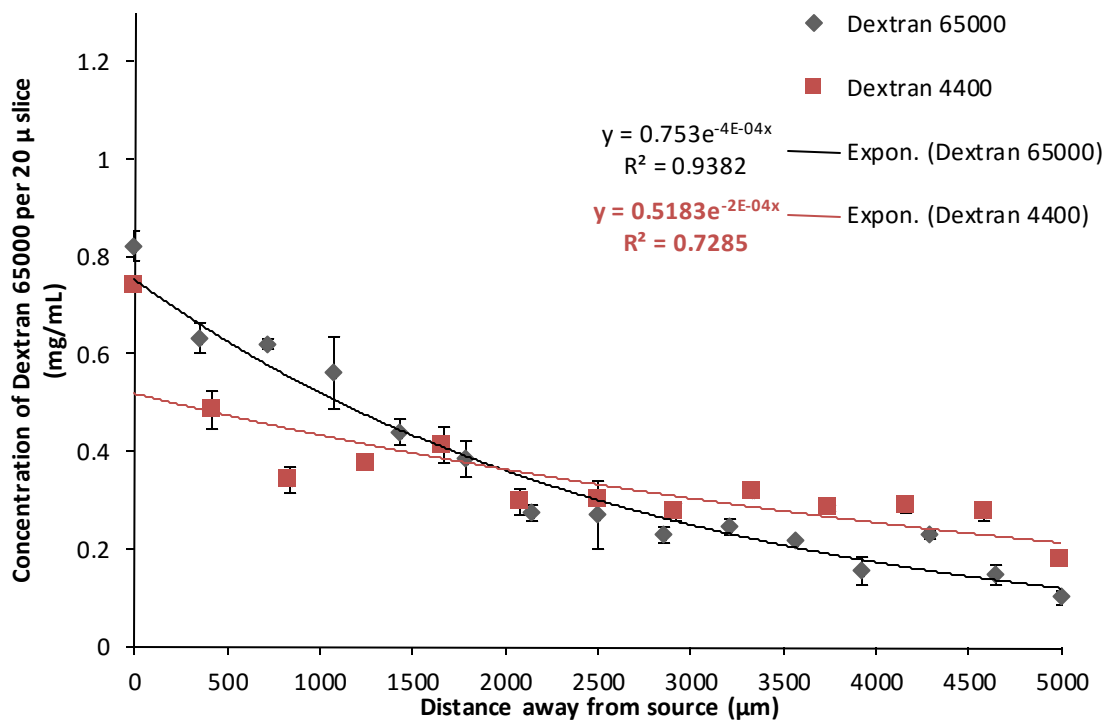


Figure 36: Diffusion pattern of TRITC-Dextran 65000 vs TRITC-Dextran 4400 across 1% agarose hydrogel scaffolds of 15×5×6.6 mm (Length × Width × Height) dimensions at day 1.

The observed large mesh size in the microscopic images of hydrogel sections sliced parallel to the direction of FITC-BSA was a cryosectioning ice crystals artefact [131]. To prevent cryosectioning artefacts, hydrogel scaffolds were supposed to be dehydrated in a concentrated sucrose solution prior to the freezing step. This step was neglected to avoid the dilution of the soluble fluorescent signals and the disturbance of the developed diffusion patterns.

The capability of the diffusion model to discriminate between different molecular weight species was investigated through comparison of diffusion profiles of fluorescein and FITC-BSA. A comparison of the equilibrated diffusion profile of fluorescein (Mwt= 332.31) at 16 hours to that steep gradient of FITC-BSA (Mwt= 66.5 kDa) at 14.5 hours shows that the model was capable of discriminating between different diffusing species based on their molecular weights. A similar finding was previously observed comparing the diffusion profile of sodium fluorescein to that of larger molecular weights dextrans in 1% agarose yet in different diffusion assembly [127].

FITC-BSA diffusion profile across 1% agarose scaffolds exhibited a gradient profile on day one that was maintained over days 2 & 3 by the frequent change of the source and sink compartments every 24 hours as stated in Table 4. These fresh supplements of the source/sink were capable of maintaining the gradients developed on day 1 via continuous withdrawal of the FITC-BSA towards the low concentration sink compartment. The achievement of linear stable gradients across hydrogel membrane in a compartmental diffusion chamber is directly correlated to the accomplishment of a steady state described by Fick's second law [61, 122]. This happens when the difference between the high and low concentration compartments is maintained below 1%. Simple calculations can be done to determine the appropriate time at which source/sink compartments are required to be replenished to guarantee achievement of stable linear gradients. Details of calculations can be found in Cao & Shoichet [61]. From which, and knowing that the membrane width is 5 mm and the diffusion coefficient was calculated to be $5.20 \times 10^{-7} \text{ cm}^2/\text{s}$, the time can be calculated to be 9.7 hours. The stability and the linearity of the developed gradient were not necessary to be achieved in the current study as the main objective was to validate the compartmental model to study gradients and maintain them by source/sink manipulation.

The common drawbacks reported for the usage of fluorescent labelled molecules to study their diffusivities were the difficulty of the labelling technique used and the

potential effect of the fluorescent label on the properties of the diffusing species [132]. In the current study, ready-made fluorescent labelled BSA were utilized to overcome the difficulty of the labelling technique. In order to investigate the effect of the fluorescent tag on the diffusive properties of the diffusing species, different labels can be used to compare the obtained diffusivities to determine whether the label results in different profile [133]. From this perspective, double opposing diffusion of the same molecular weight compound BSA yet with different fluorescent tag should result in identical profiles unless the model/quantitative method is compromised by the fluorescent tag. This was not the case with the double opposing diffusion of TRITC/FITC-BSA from different sides of the hydrogel membrane. Mirror image diffusion profiles were observed at days 1 & 3. Once again, the replenishment of both compartments at each determined time points was capable of trend's maintenance. However, an observed increase in the TRITC & FITC-BSA fluorescence intensities at each hydrogel slice's position. Continuous monitoring of the source and the sink compartments reflected similar changes in the two compartments for TRITC & FITC-BSA concentrations. Once more, this confirms the reliability of the model/quantification method for following the diffusion pattern of different molecules irrespective of the fluorescent tag used. Developmental biology models usually rely on opposing gradients of competing morphogens that determine the tissue fate. An example demonstrating the role of opposing morphogen gradients is gradients of BMP and nodal TGF- β that induce molecular mechanisms organizing the uncommitted cells of zebrafish into a well-developed embryo [46]. From this perspective, the compartmental diffusion chamber can be employed to generate opposing gradients of morphogens for developmental biology and regenerative medicine applications.

3.5.2. Effect of hydrogel composition on diffusivity

Comparing the diffusion profiles of 0.5 & 1 mg/mL FITC-BSA across 1% agarose scaffolds did not show a difference in the generated trend. This case was as well observed for different diffusing species/hydrogel combinations as shown in Figure 22, Figures 23, Figure 32 & Figure 34. This suggests that the trend of the developed gradient is independent of the initial source compartment concentration. This finding was as well previously reported [127].

Table 5 & Figure 14 reflect better fit using exponential decay curve rather than linear fit as decided by higher correlation coefficients of exponential decay kinetics. A similar

finding was previously reported for the diffusion of BSA across agarose matrices and following the diffusion profile using a refractive index method. There was an observed exponential decrease of the refractive index with an increase of the diffusion distance [134]. The model could be adjusted to achieve linear kinetics, if needed, by adjustment of the rate of change of source and sink compartments as explained in 3.5.1.

The diffusion behaviour of diffusing molecules in hydrogels as described earlier by Lieleg and Ribbeck is modulated by size and interaction filtering strategies [135]. Size filtration strategy describes the potential of hydrogels with specific molecular size cut-off to geometrically restrict the diffusion of particles above this mesh size. On the other hand, the interaction filtering strategy explains that molecules engaged in strong binding interactions with the hydrogel get trapped in the matrix irrelevant of their size [135].

Agarose is a linear polymer consisting of alternating D-galactose and 3, 6-anhydro-L-galactose units. Hydrogels formed from agarose are weakly ionic, bearing negative charges due to the infrequent substitution with pyruvate and sulphate ions [136]. However, the ultra-low melting temperature agarose is composed frequently hydroxyethylated galactose residues so that the agarose fibres are almost neutral with low electroendosmosis value ≤ 0.05 and low sulphate content $\leq 0.10\%$. Agarose molecules in liquid state at high temperatures possess random coil structures. However, upon cooling, the agarose chains adopt helical bundles held together by noncovalent hydrogen bonds. Gelation at low temperature takes place when the fibre bundles become linked via additional hydrogen bonds [137]. The average pore size was reported to vary from 100-400 nm according to the concentration and type of agarose [138-140]. However, it has been mentioned elsewhere to vary up to 900 nm [141]. The estimated gel pore radius depends on the method of determination. Methods of pore size determination included lattice models of DNA gel electrophoresis [142], Ferguson plot methods [143], nuclear magnetic resonance (NMR) [141], atomic force microscopy (AFM) [140, 144] or electron microscopy [145]. Another method to be considered is hydrogel cryo-fracture coupled with transmission electron microscopy [146]. The gel pore radii estimated by NMR or AFM methods are expected to be relatively more accurate compared to electrophoretic methods which mainly depend on the accessible pores for the migrating DNA molecules [147]. However, the exact estimation of hydrogel mesh sizes remains difficult to achieve [135].

Gelatin type B is denatured collagen with RGD-like sequences that support cell proliferation and attachment [148] and it is known to have a pI of 4.7-5.2 [149]. Gelatin B possesses negative charge due to the deprotonation of carboxyl groups (COO^-) in the amino acid sequence comprising it [150]. Thus the gelatin/agarose hydrogel would still possess a negative charge. Physical gelatin hydrogels possess hydrogen bonding gelation mechanism which is usually thermo-reversible and is obtained when the solutions are cooled. Chemical cross linking is required for production of irreversible hydrogels regardless of the temperature [151]. Gelatin has been added to various polymers to improve the mechanical or biological properties [152-154]. This could be done with or without cross linking [153]. Comparison of the pore size of cross linked to non-cross linked gelatin containing scaffolds showed no significant difference in the computed pore size. However, there was a significant reduction of the pore size with the increase in gelatin content [153]. Furthermore, the hydrogel network of agarose/gelatin is supposed to possess stronger network due to the presence of carboxyl groups in gelatin type B which interact with hydroxyl groups in agarose forming covalent ester bond [150].

Cryoscanning electron microscopy of hydrogel blocks (Figure 28) showed changes in the morphological features as a function of hydrogel concentration. However, they were not decisive about the pore size as the technique of sample of preparation under cryogenic condition guaranteed maintenance of water within the hydrogel sample as it is frozen-hydrated [155]. Hydration of gelatin/agarose hydrogels at 37 °C resulted in liquefaction of gelatin and plasticization of the hydrogel and accordingly, the change of the hydrogel morphology compared to the original 1% gelatin/agarose hydrogel. Figure 29 shows a trial to attain a thin section of the hydrogel under cryogenic condition using focused ion beam technique. This lamella (approximately 2 μm thick) was transferred to the transmission electron microscope under cryogenic conditions. Once more, the presence of frozen water in the hydrogel sample was denoted by the grey patches amongst the lighter gel matrix [120]. A shift in the methodology was done via the production of ultra-thin sections via cryoultramicrotomy. The ultra-thin sections produced were transferred to the electron microscope under ambient conditions. This should result in the evaporation of the water in the water filled pores and the pore structure was further evaluated. Dehydrated hydrogels resulted in straightforward interpretation owing to the high contrast between the gel material and void pores [120].

Results shown in Figure 30 & Figure 31 reflect average pore sizes of 273 ± 141 and 198 ± 8 nm for 1% agarose and 1% agarose-1% gelatin respectively. The median sizes were computed to be 235 and 170 nm respectively. Pore size of 2% agarose has been computed using variable methods that were summarized in Berk *et al.* to be ranging between 124 and 207 nm [156]. This could be attributed to the diffusion characteristics of the FITC-BSA across different concentrations of agarose hydrogels with or without gelatin. It was previously reported that the pore size of agarose hydrogels was inversely proportional to the gel concentrations [140]. Since the diffusion of solutes takes place in the liquid channels in the hydrogel matrix, an increase in the hydrogel concentration will result in a decrease in the mesh size, shrinkage of the space available for the diffusing solute and finally leading to an increase in the path length for diffusive transport [134].

Serum albumin is a widely used model globular protein to study protein localisation within particulate delivery systems and in cell culture or tissue engineering applications [157]. The net charge on the bovine serum albumin molecule at pH 7.2 should be negative as previously reported [158, 159]. This was further verified by the practical estimation of the zeta potential in 10 mM HEPES buffer at 37 °C shown in Table 12 which was -9.48 ± 2.50 . SDS-PAGE analysis of FITC-BSA released from gelatin microspheres shows one band that correlates with intact BSA indicating that the protein does not interact chemically with the gelatin matrix [160]. The hydrodynamic radius of FITC-BSA is computed via laser size diffraction principle at 37 °C to be 4.21 ± 0.46 nm in 10 mM HEPES buffer or 4.06 ± 0.32 nm in PBS as shown in Table 11. This matches with the hydrodynamic radius of FITC-BSA that has been previously reported to be 3.93 ± 0.20 in PBS at 25 °C [161]. This protein size is far below the minimum value reported for the agarose mesh size; 118.15 or 100 nm for 1% agarose or 1% agarose-1% gelatin hydrogels respectively (Figure 30 & Figure 31). This supports free migration through the negatively charged agarose and agarose/gelatin hydrogels based on the interaction filtering strategy and limits the diffusion to the size infiltration strategy described by Lieleg and Ribbeck [135].

The aforementioned characteristics were further confirmed by the practical estimation of the diffusion coefficients of FITC-BSA in 1% & 2% agarose using the model permeation method [61, 122]. These coefficients were computed to be 5.20×10^{-7} & 3.24×10^{-7} cm²/s for 1% and 2% agarose respectively. Saltzman reported a diffusion

coefficient of $6.4 \pm 0.4 \times 10^{-7}$ in PBS at 25 °C [161]. The diffusion coefficients of BSA in (3-0.5 wt. %) agarose matrices were reported to range from 4.98 to 8.21×10^{-7} cm²/s using a refractive index method [134]. Diffusion coefficients summarize all the contributing factors involved in the determination of how fast a specific species will diffuse through certain matrices. These diffusion coefficients confirm on the faster diffusion of FITC-BSA in less concentrated agarose matrices with larger pore sizes.

3.5.3. Effect of nature of diffusing species

Proteins and dextrans were commonly used in biological transport studies [156]. From this perspective and to show that the model was not restricted to follow protein diffusion across polysaccharides or proteins hydrogel matrices, the diffusion profiles of fluorescein (Mwt= 332.31) and different molecular weights Dextrans (4400 & 65000) were monitored. Diffusion profiles of different dextrans and continuous monitoring of their respective source/sink compartments reflect the capability of the model of temporal monitoring of slight changes in concentrations (Dextran 65000; Figure 32-Figure 33 & Dextran 4400; Figure 34-Figure 35).

Dextran is a group of hydrophilic polysaccharides with molecular chains consisting of anhydro-D-glucopyranose units linked by a -1,6-glycosidic bonds with different sizes and geometries. The net charge on the dextran is usually dependant on the conjugated fluorophore which is mostly anionic. However, rhodamine B, tetramethylrhodamine, and Texas Red® are zwitterionic and they result in neutral conjugates [162]. The diffusion coefficients and hydrodynamic radius of Dextran 4400 in PBS at 25 °C were computed to be $1.35 \pm 0.10 \times 10^{-6}$ cm²/s & 1.86 ± 0.15 nm respectively [163]. On the other hand, the diffusion coefficient of Dextran 74000 in agar membrane at 25 °C was $4.4 \pm 0.2 \times 10^{-7}$ cm²/s & the hydrodynamic radius in PBS at 25 °C was 5.71 ± 0.35 nm [164]. In a different research work, the diffusion coefficient for Dextran 69000 in collagen at 37 °C was 2.0×10^{-7} cm²/s and the hydrodynamic radius was reported to be 6 nm [165]. In a comparative study to detect the effect of molecular weight on the diffusivities of dextran, a Diclofop methyl-degrading biofilm was used and the computed diffusion coefficients of dextran 4000 and 70000 were estimated to be 3.1×10^{-8} and 1.1×10^{-8} cm²/s respectively [166]. These come in good agreement with the size infiltration strategy and suggest a faster diffusion of small molecular weight dextrans compared to larger counterparts. The current model utilized agarose as the diffusing membrane which possesses a slight negative charge. TRITC-Dextrans as neutral molecules can

accordingly pass freely across agarose networks and their diffusion will be dependent on their size characteristics. The presented compartmental diffusion model was able to confirm this finding by comparing the gradient profile of TRITC-Dextran 65000 at day 1 (exponential decay coefficient of determination $r^2=0.94$) to the relatively equilibrated diffusion profile of TRITC-Dextran 4400 (exponential decay coefficient of determination $r^2=0.73$).

3.6. Conclusions

The compartmental diffusion model presented in the current chapter was able to measure diffusion gradients of different diffusing species across three-dimensional agarose based hydrogel membranes. It accommodates a Source-Gel-Sink assembly that has been modified from a previous research work to generate and maintain gradients of bioactive molecules. Model validation demonstrated the capability of the model to distinguish between different types and size molecular weights species irrelevant of the fluorescent tag utilized. The role of hydrogel concentration and composition on the diffusion pattern of different species was studied. These findings revealed the potential of the model to be used for the generation and measurement of bioactive molecules gradients for tissue regeneration applications.

Chapter 4: Spatial and temporal control of protein release from microspheres/hydrogel composite scaffolds

4.1. Introduction

Intracellular delivery of functional proteins plays a significant role in various biological applications [167]. However, effective protein delivery has been a critical challenge in the biomedical research due to their critical physiochemical properties. The complex structure, high molecular weight, together with the potential for denaturation, and alteration of spatial characteristics represent a series of hurdles facing successful functional protein delivery [168]. Furthermore, the liability to proteolytic degradation, possession of short half-lives and rapid clearance complicate the formulation criteria to be addressed [169]. As a consequence, a successful protein formulation should maintain structural activity of functional protein during formulation, storage and delivery [170].

Polymeric-based particulate delivery systems are good candidates to deliver functional protein in light of the addressed problems. Various natural and synthetic polymers have been reported to effectively deliver proteins to the target sites and maintain the stability and integrity of incorporated therapeutic proteins [171]. In particular, they possess the ability to preserve the secondary and tertiary protein structures and prevent protein aggregation [169]. Biocompatibility and biodegradability come along other factors of considerations while formulating protein delivery system to maintain effectiveness while avoiding toxicity [172]. Another factor to be considered is the control of the release rate of the encapsulated proteins in a manner tailored to achieve the desired dose regimen [173].

Polyesters derived from lactic acid, glycolic acid and ϵ -caprolactone have acquired much interest in the field of tissue regeneration due to their biodegradable properties. PLGA polyesters are approved by the US Food and Drug Administration (FDA) for tissue engineering applications [174]. Biodegradability is achieved via hydrolysis and enzymatic degradation of lactic acid by lactate dehydrogenase with a control over the degradation process by changing the molar ratio of the lactic and glycolic acids comprising the PLGA polymer [175].

A range of particulate delivery systems including microspheres, microcapsules, nanoparticles, liposomes and micelles can be recruited for effective protein delivery based on the desired dose regimen. Biodegradable microspheres of size range 10-1000 μm have been reported to be prepared via different formulation technologies including spray drying, double emulsion and phase separation techniques [172].

The release of peptide macromolecules from hydrophobic polyesters occurs via diffusion through pores of the non crystalline region of the polymer with an observed slow release rate [172, 176]. An additional mechanism of protein release is the polyester degradation [172, 177]. To improve the release rate of proteins from polyesters, PLGA polymers have been blended with variable hydrophilic polymers to enhance the hydration of the polymeric matrix. Variable block co-polymers of polyesters with poly ethylene glycol (PEG) either di-block or tri-block were introduced as hydrophilic polymers for hydration enhancement [177, 178].

Polymeric PLGA microspheres with different protein release characteristics can be used as protein depots replacing the source compartment in the compartmental diffusion chamber introduced in chapter two. This should guarantee the maintenance of the structural integrity of the encapsulated proteins and overcome the burden of short protein half-lives. Understanding protein diffusion from polymeric microspheres to the surrounding matrix; scaffolds, can give an idea about the accurate design of the scaffold microarchitecture. In such a way, the exact placement of growth factors polymeric microspheres in 3D scaffolds can be achieved in high precision, nearby to cells to ensure the cell growth in three dimensions promoting the desired cell differentiation and deciding on the tissue fate.

4.2. Aims & objectives

4.2.1. Aim

The aim of the work presented in this chapter is to replace the source compartment in the Source-Gel-Sink compartmental diffusion model developed in chapter three with a layer of hydrogel with suspended depot protein loaded microparticles for optimum protein delivery.

4.2.2. Objectives

Research objectives addressed in this chapter included:

1. Fabrication of different compositions FITC-BSA loaded PLGA microspheres of tuneable protein release profiles.
2. Development of microspheres-hydrogel composite layered scaffolds.
3. Quantification of FITC-BSA gradients across the hydrogel membrane from different compositions microspheres in the microspheres-hydrogel layer.

4.3. Materials and methods

4.3.1. Fabrication of plain and protein loaded PLGA microspheres

Plain and FITC-BSA loaded microspheres were fabricated using a double emulsion technique followed by solvent evaporation [114]. Poly (vinyl alcohol) (PVA) (Mwt. 23000, 87-89% hydrolysed, Sigma-Aldrich) 0.3% w: v was prepared and the solution was filtered using a 0.2 μm pore size filter (Minisart, Sigma Aldrich, UK). 1g of PLGA 50:50 was dissolved in 6.67 mL dichloromethane DCM (HPLC grade, Sigma-Aldrich) in scintillation vials (Bn01 & Bn02). Batches with Triblock copolymer were prepared by addition of 6.67 mL DCM to 900 mg of PLGA 50:50 together with 100 mg Triblock copolymer (Bn03 & Bn04). 100 μL distilled water or 100 μL of 1% w: v FITC-BSA solution in distilled water were then added to the scintillation vial and homogenized at 4000 rpm for 2 minutes to produce the primary emulsion as a first step to produce blank (Bn01 & Bn03) or FITC-BSA loaded microspheres (Bn02 & Bn04) respectively. Detailed batch compositions are displayed in Table 7. The primary emulsion was then homogenized at 9000 rpm in 200 mL of the filtered PVA 0.3% solution for 2 minutes to give the secondary emulsion (w/o/w). For hardening of the formed double emulsion into solid microspheres, the mixture is stirred for 4 hours to allow the evaporation of the DCM. The microspheres were then collected after centrifugation of the mixture for 4 minutes at 300 rpm and a washing step using distilled water for another 4 minutes at 300 rpm. The collected microspheres were then freeze dried in ModulyoD freeze dryer (Thermo electron corporation, USA) for 24 hours prior to storage in fridge until used.

4.3.1.1. Characterization of PLGA microspheres

4.3.1.1.1. Size analysis

Laser diffraction was utilized to estimate the size distribution characteristics. For details, see section 2.2.3.2.1.

4.3.1.1.2. Microscopy

4.3.1.1.2.1. Scanning electron microscopy

See section 2.2.3.2.2.1.

4.3.1.1.2.2. Fluorescence microscopy

See section 2.2.3.2.2.2.

Table 7: Exact composition of batches formed using double emulsion/solvent evaporation method

Batch number	Composition
Bn01	PLGA (50:50)
Bn02	PLGA (50:50) with 1% FITC-BSA
Bn03	PLGA (50:50): Triblock copolymer (90:10)
Bn04	PLGA (50:50): Triblock copolymer (90:10) with 1% FITC-BSA

4.3.1.2. Estimation of protein encapsulation efficiency in protein loaded microspheres

The bicinchoninic Acid (BCA) assay was used to estimate the protein loading in the PLGA microspheres [116]. This assay provides a colorimetric estimate of peptide groups found within protein molecules using a standard spectrophotometer plate reader 562 nm. The BCA Protein Assay relies on reduction of Cu^{2+} to Cu^{1+} by protein in an alkaline medium followed by colorimetric detection of the Cu^{1+} by bicinchoninic acid. The protein loaded microspheres (10 mg) were dissolved in 750 μL DMSO and then a 2150 μL solution of 0.02% (w/v) SDS sodium dodecyl sulphate in 0.2 N NaOH sodium hydroxide was added to ensure the solubilisation of the polymer and the protein within a single phase. The samples were diluted appropriately in a solution of DMSO/SDS/NaOH and standard protein solutions were prepared. The absorbance at 562 nm was read after two hours of incubation at 37°C.

4.3.1.3. Protein release from PLGA microspheres

In vitro protein release from protein loaded microspheres was assessed in 3 mL PBS using 40 mg microspheres in 15 mL centrifugation tubes (Greiner, 188261). Microspheres were agitated using a labgent gyro twister (Germany) at 30 twists per minutes inside a temperature controlled incubator at 37°C for 35 days. Samples were drawn at different time intervals and fresh 3 mL PBS were added. The released protein was quantified using BCA assay explained in section 4.3.1.2.

4.3.2. Microspheres-hydrogel composite layered scaffolds

12.9 mg plain or FITC-BSA loaded PLGA microspheres with or without triblock copolymer prepared at 4.3.1 were mixed with 300 μL liquid gelatin/agarose hydrogel at 37°C. The microspheres/hydrogel mixture were cast next to one side of the solidified hydrogel compartment created in section 2.2.8 using a PTFE block of reduced width relative to the original PTFE block used to create the original 3 compartments model (Figure 12). The microspheres/hydrogel mixture was allowed to set at 4°C for 30 minutes and then the PTFE block was removed to leave a vertical bilayer of microspheres/hydrogel (2.5 mm width) on one side and plain hydrogel (5 mm width) on the other side.

4.3.2.1. Diffusion studies of FITC-BSA from microspheres-hydrogel composite layered scaffolds

The microspheres/hydrogel layer described in 2.2.8.3 replaced the source compartment described in. FITC-BSA loaded microspheres layer acted as the source for protein

diffusion. The sink compartment was composed of 500 μL added next to the plain hydrogel layer and was changed every 24 hours for 3 days.

4.3.2.2. Quantification of FITC-BSA diffusion gradients

Estimation of the released FITC-BSA concentration gradient across the plain 5 mm wide hydrogel layer was done as described in section 2.2.8.3.

4.3.2.3. Monitoring protein concentration in sink compartment

See section 2.2.8.4.

4.3.2.4. Imaging of microspheres-hydrogel composite layered scaffolds

Microspheres/hydrogel composite layered scaffold after 3 days of protein diffusion was directly frozen in O.C.T mounting media at -80°C and then sectioned upright at the rectangular 6.6×15 mm side of the scaffold using Leica CM 1100 cryostat at -20°C into 20 μm thick slices. Retrieved gel slices from the different layers; microspheres composite layer and from the plain hydrogel layer, were then viewed in bright field and under fluorescence microscopy image capturing using a Nikon stereomicroscope SMZ 1500 & Leica TCS SPE Confocal Macrocope for entire slice imaging.

Alternatively, microspheres/hydrogel composite layered scaffold after 3 days of protein diffusion was submerged in sucrose 15% w/v in PBS and then left overnight in sucrose 30% w/v. Scaffolds were then placed in O.C.T mounting media, frozen in liquid nitrogen cooled isopentane bath then stored at -80°C freezer. Scaffolds were subsequently sectioned parallel to the direction of protein diffusion using Leica CM 1100 cryostat at -20°C into 20 μm thick slices. Parallel sliced slices were composed of both layers; microspheres composite layer and plain hydrogel layer.

4.4. Results

4.4.1. Characterization of PLGA microspheres

Microspheres produced via the double emulsion method were subjected to size analysis based on laser diffraction using LS230 Beckmann Coulter and data of different batches is shown in Table 8. It shows the size distribution characteristics of variable compositions of PLGA microspheres in terms of the mean, median & mode size. Frequency size distributions of the produced microsphere batches are shown in Figure 37. The morphology and surface characteristics of the produced microspheres were revealed using scanning electron microscopy as shown in Figure 38. The size range of the produced microspheres ranged between 15 and 50 μm with slight variation according to batches' composition.

Bright field and fluorescence microscopy images of FITC-BSA encapsulated microspheres are shown in Figure 39. It shows encapsulation of the green fluorescence within the formed microspheres. The content and encapsulation efficiency of FITC-BSA in FITC-BSA loaded PLGA microspheres (Bn02 & Bn04) were estimated using Bicinchoninic acid assay as listed in Table 9. The cumulative amount of FITC-BSA released to PBS from Bn02 and Bn04 as a function of time is shown in Figure 40. To compare the release profiles of FITC-BSA from PLGA microspheres to 10% triblock PLGA microspheres, the % FITC-BSA released from Bn02 & Bn04 were plotted as a function of time as shown in Figure 41.

4.4.2. Development of layered hydrogel scaffolds

The protein source compartment introduced in chapter three was replaced by a microspheres-hydrogel composite layer adjacent to the hydrogel membrane of the compartmental diffusion model. Representative images of microspheres-hydrogel composite scaffold in the three compartmental diffusion chamber are shown in Figure 42. 300 μL of gelatin-agarose hydrogels with suspended 12.9 mg PLGA microspheres were cast next to the plain hydrogel layer of $15 \times 5 \times 6.6$ mm dimensions. The microspheres-hydrogel layer was opaque as compared to the plain hydrogel layer and it formed a layer of hydrogel of $15 \times 2.5 \times 6.6$ mm dimensions. The entire composite scaffold measured $15 \times 7.5 \times 6.6$ mm. Images under the fluorescence microscope (Figure 42) show a highly fluorescent microspheres-hydrogel layer at time zero as compared to non-fluorescent plain hydrogel layer.

Figure 43 shows a transverse section of the composite scaffold where the scaffold was sliced parallel to the base of the mould. A distinct top microspheres-hydrogel layer with an adjacent plain hydrogel layer was produced. Cryo SEM images displayed in Figure 44b show the embedment of PLGA microspheres in the hydrogel matrix without change in the hydrogel (Figure 44a) or the microspheres morphology.

Longitudinal slicing the scaffold at the microspheres-hydrogel layer is displayed in Figure 45. Fluorescence microscopy images shows green fluorescent dots representative of the FITC-BSA loaded microspheres.

4.4.3. Evaluation of FITC-BSA diffusion gradients

The diffusion gradient profiles of the released FITC-BSA from the different composition PLGA microspheres in the microspheres-hydrogel layer across the plain hydrogel layer are shown in Figure 46.

Table 8: Size distribution characteristics for representative samples of PLGA microspheres (Bn01-Bn04) as determined by laser diffraction using a LS230 Beckmann Coulter

Batch number	Composition	Mean	Median	Mode
		(μm)	(μm)	(μm)
Bn01	Plain PLGA 50:50	26	26	29
Bn02	1% BSA-PLGA 50:50	19	19	22
Bn03	Plain PLGA 50:50 with 10% Triblock	18	16	22
Bn04	1% BSA PLGA 50:50 with 10% Triblock	33	33	38

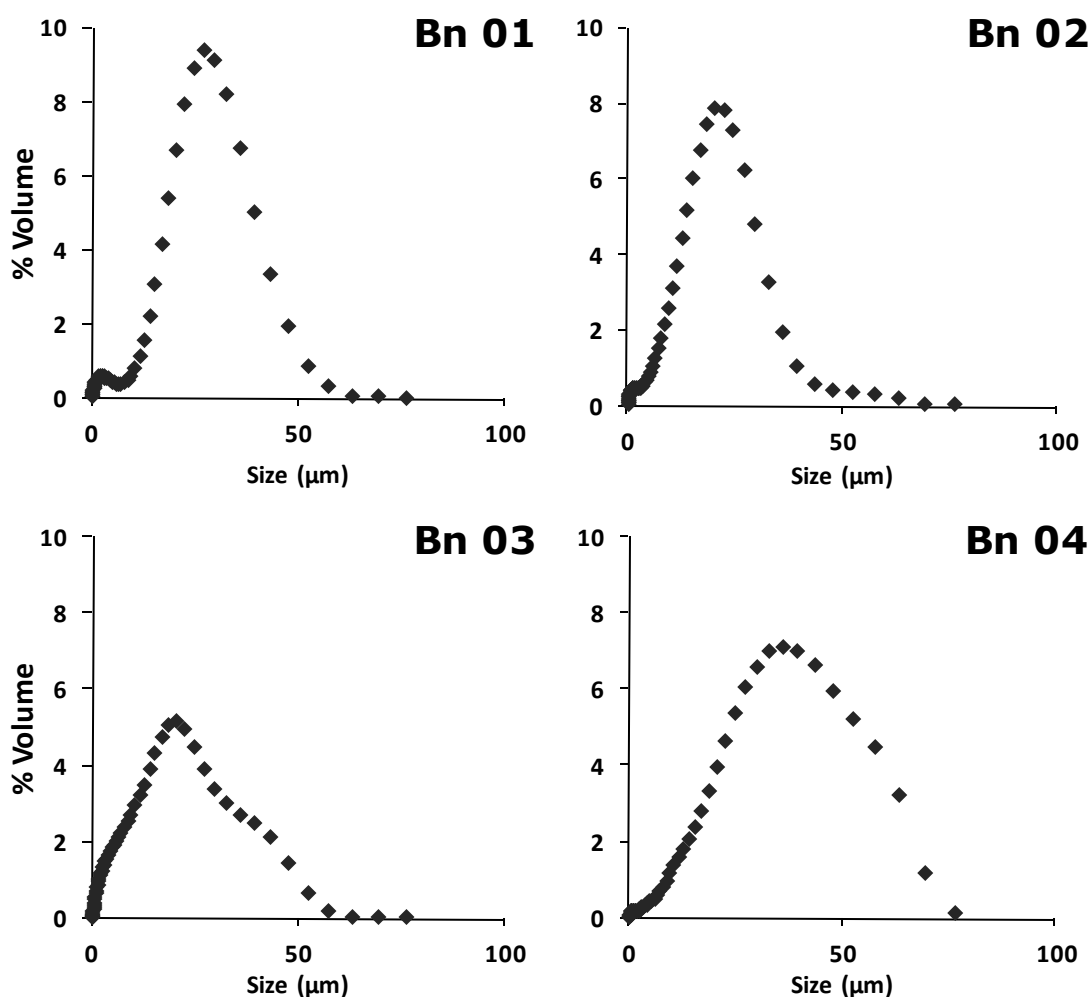


Figure 37: Size distribution (% volume) of microspheres prepared by double emulsion method. Plots show representative sample from each batch (Bn01-Bn04) PLGA 50:50 plain (Bn01), BSA loaded (Bn02), Plain with 10% Triblock (Bn03) or BSA loaded with 10% Triblock (Bn04)

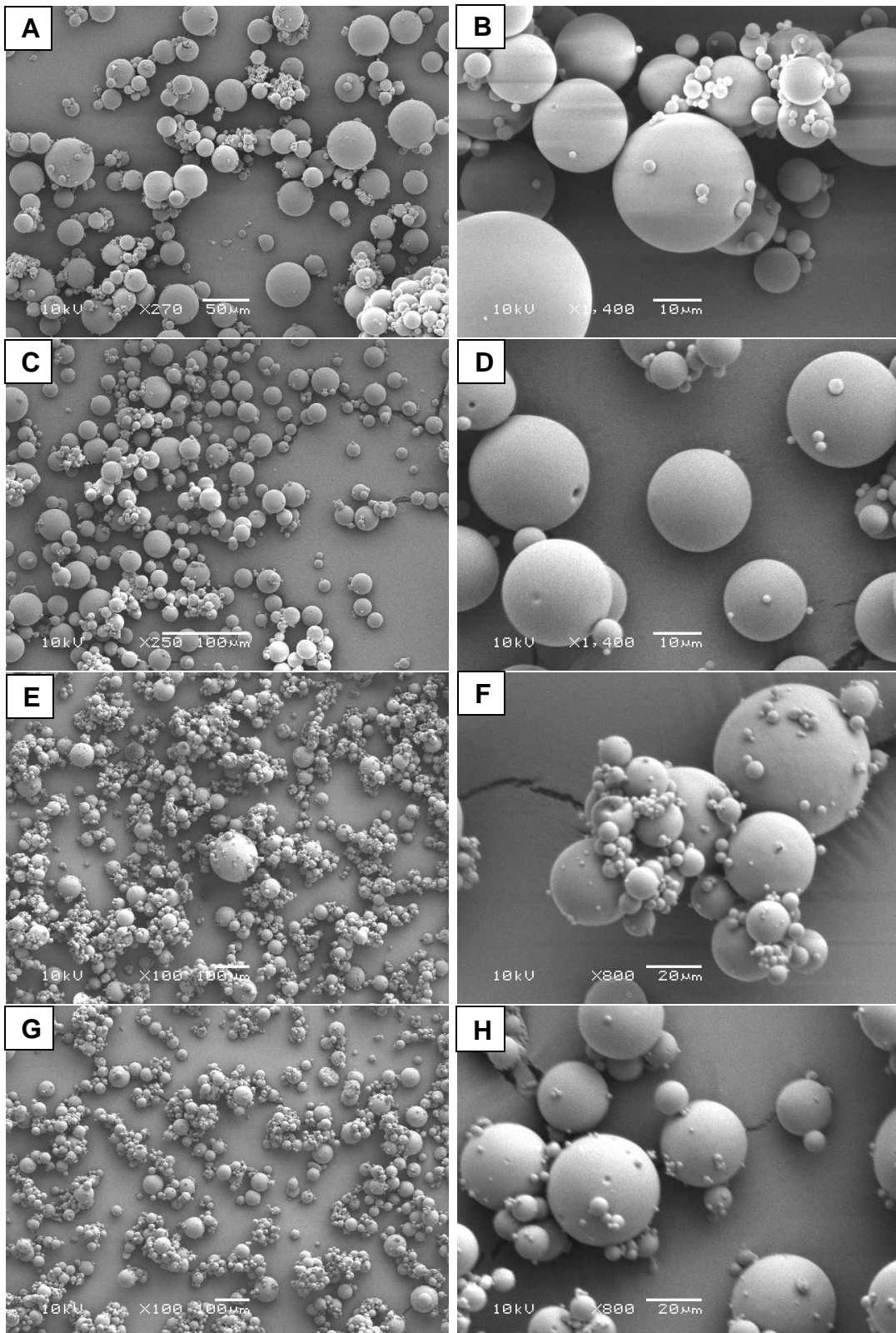


Figure 38: Scanning electron micrographs of PLGA 50:50 microspheres showing the size distribution of batches 1-4 over images A, C, E and G respectively and a close up to the microspheres' shape and surface characteristics over images B, D, F and H respectively.

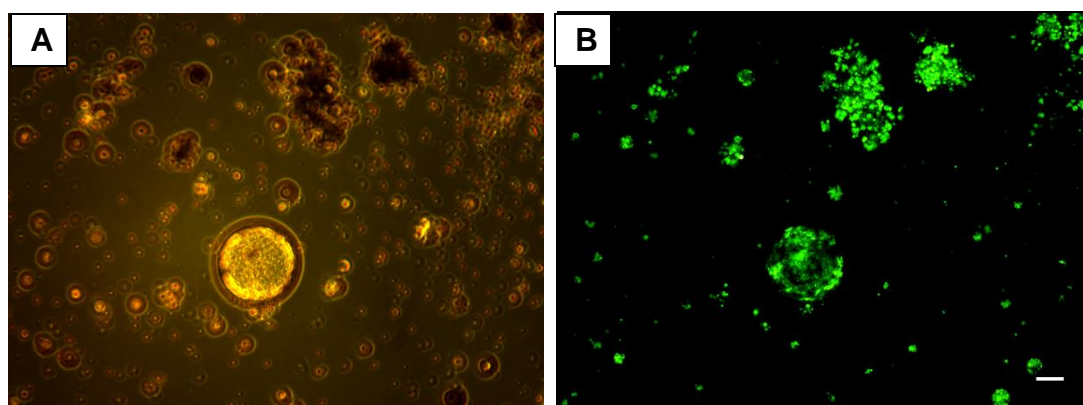


Figure 39: Bright field image (A) and fluorescence microscopy image (B) showing the entrapment of the fluorescent BSA inside the PLGA 50:50 microspheres (Bn02). Scale bar is 10 μm .

Table 9: Content and encapsulation efficiency of FITC-BSA in PLGA microspheres (Bn02 & Bn04) as determined by bicinchoninic acid assay, theoretical FITC-BSA content per 40 mg microspheres is 400 μg .

Batch	Actual BSA (μg) per 40 mg microspheres	% Encapsulation Efficiency
Bn02	122 ± 4	31 ± 1
Bn04	190 ± 12	48 ± 3

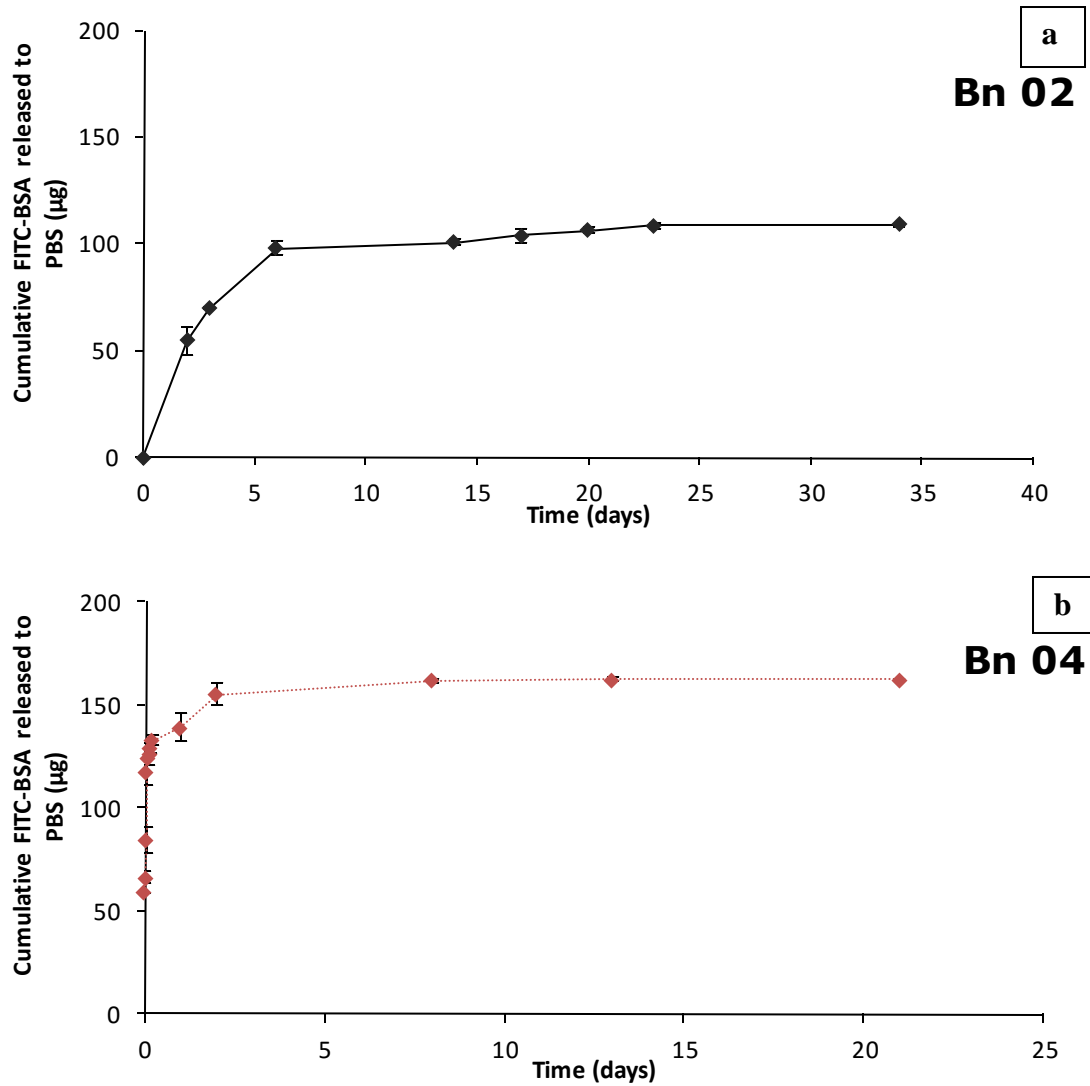


Figure 40: Release profiles of FITC-BSA (μg) in 3 mL Phosphate Buffer Saline from 40 mg Bn02 (a) or Bn04 (b) quantified using BCA assay kit and measuring absorbance at 562 nm using a TECAN infinite 200PRO multimode reader.

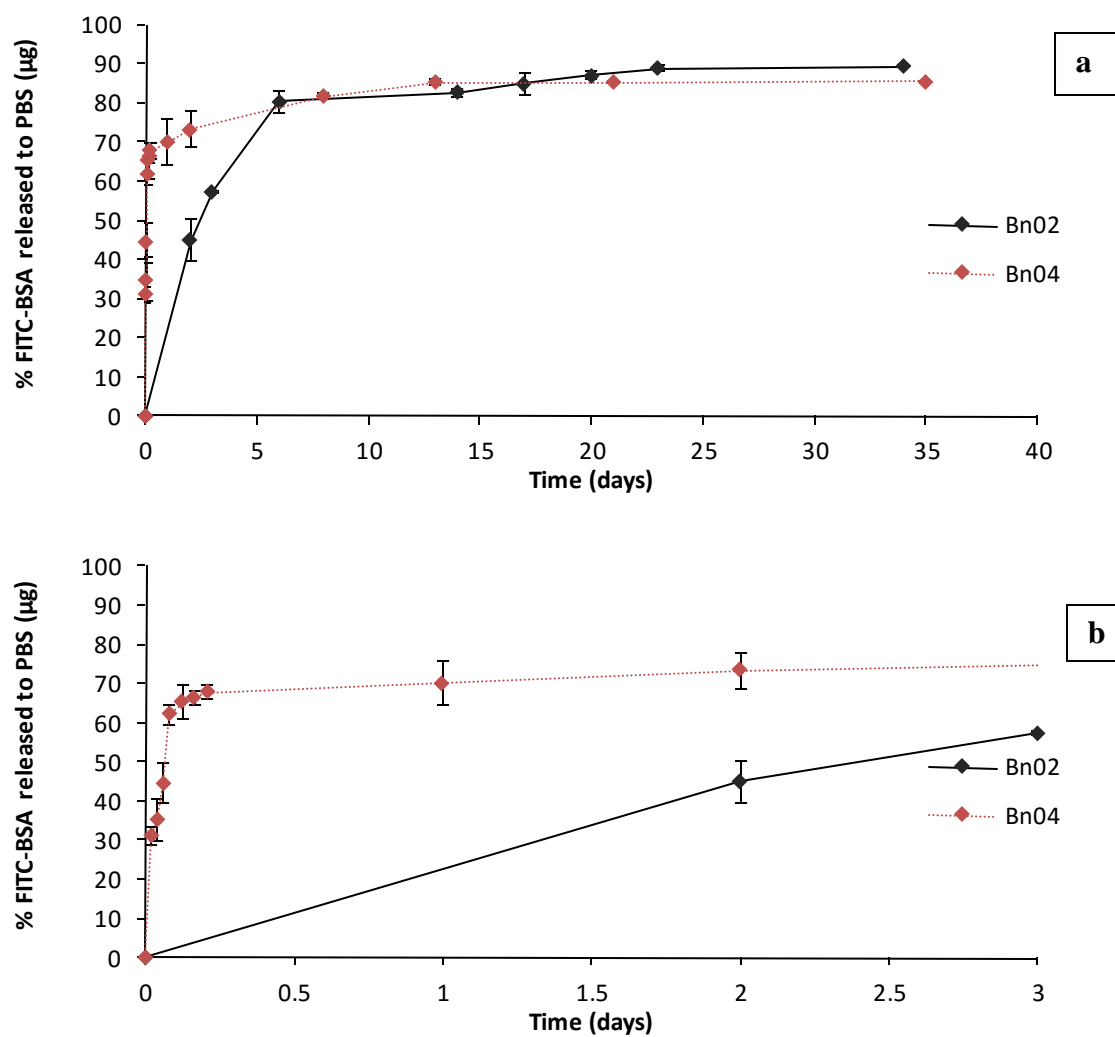


Figure 41: a: % FITC-BSA released in 3 mL Phosphate Buffer Saline from 40 mg Bn02 and Bn04 quantified using BCA assay kit and measuring absorbance at 562 nm using a TECAN infinite 200PRO multimode reader. b: close-up on data collected until day 3

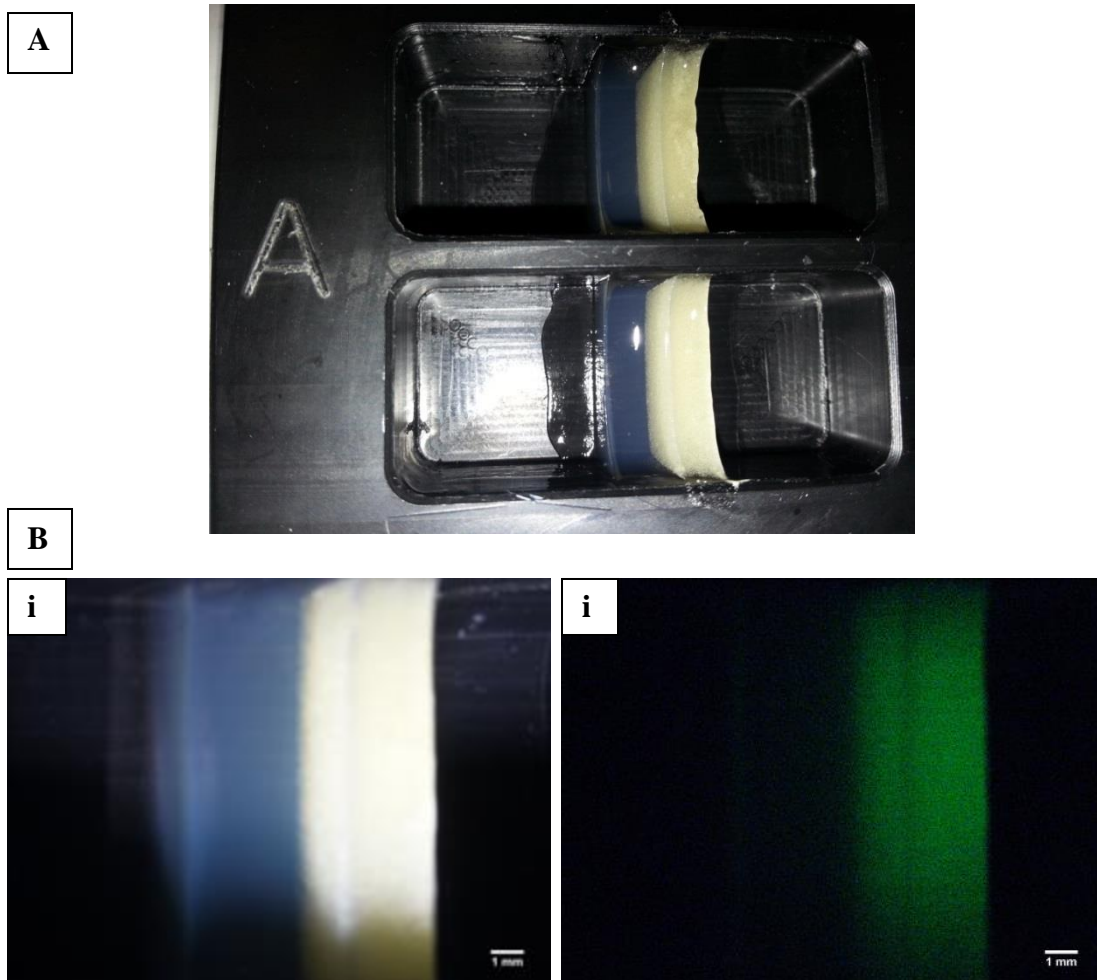


Figure 42: A. Representative image of microspheres-hydrogel composite scaffold in the three compartmental diffusion chamber. 300 μ L of gelatin-agarose hydrogels with suspended 12.9 mg PLGA (50:50) microspheres (Bn01-Bn04) ($15 \times 7.5 \times 6.6$ mm) were cast next to the plain hydrogel membrane ($15 \times 5 \times 6.6$ mm). B: Bn04 in GIA layered scaffolds on day 3 using Nikon SMZ1500 dissection microscope i: bright field & ii: green fluorescence channel.

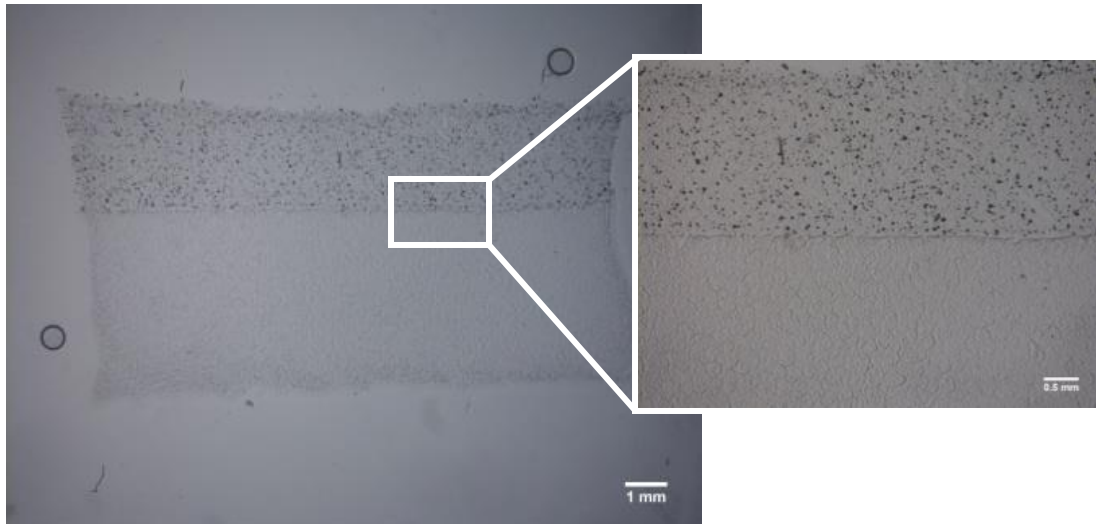


Figure 43: 20 μm thick transverse section of the microspheres-hydrogel composite scaffold showing the plain hydrogel layer adjacent to the microspheres hydrogel layer with 21.5 mg PLGA (50:50) microspheres viewed under Nikon SMZ1500 dissection microscope at different magnifications. Scaffolds were subject to sucrose dehydration steps prior to preservation in OCT, freezing at -80°C and sectioning using Leica CM1100 cryostat.

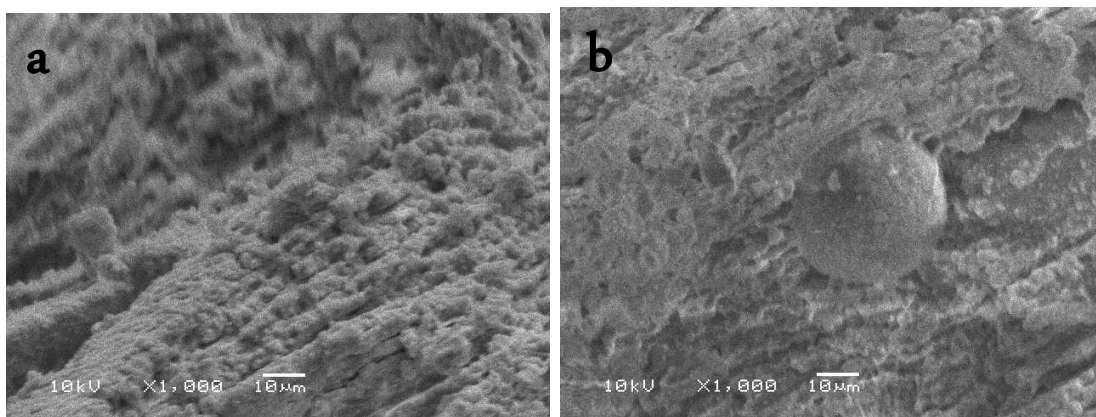


Figure 44: Scanning electron micrographs of the microspheres-hydrogel composite scaffold showing a: the plain hydrogel layer & b: the microspheres/hydrogel composite layer as viewed under Jeol JSM 6060LV.

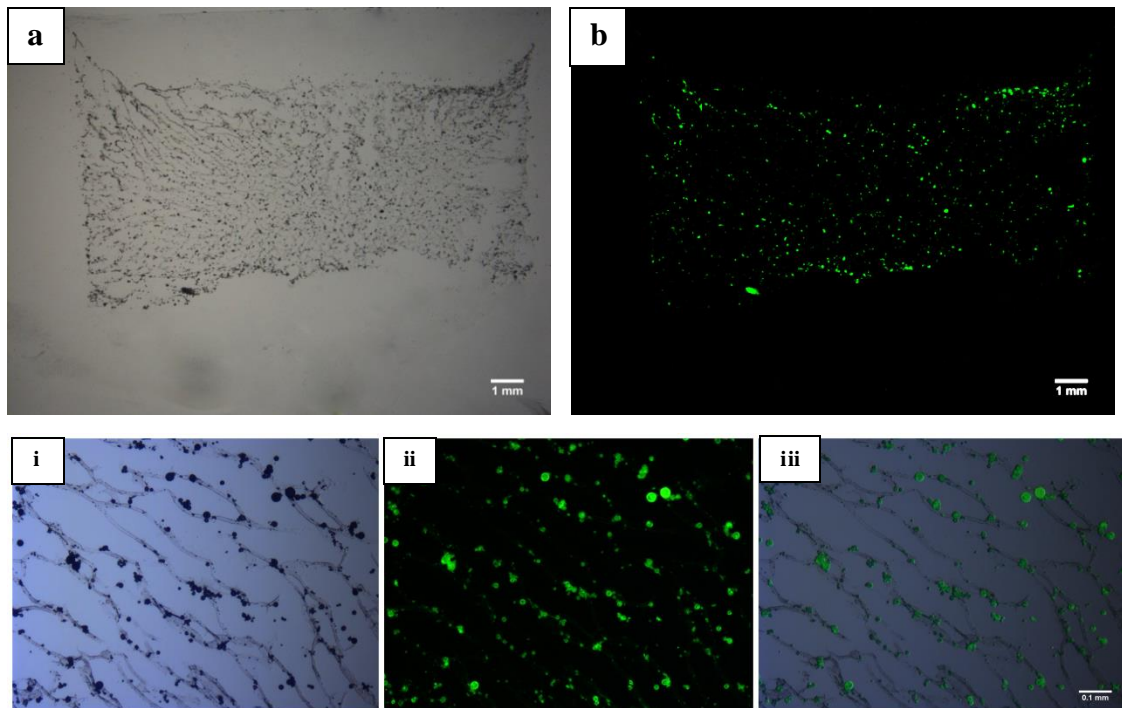


Figure 45: 20 μm thick longitudinal section of the microspheres-hydrogel composite scaffold showing the microspheres hydrogel layer with suspended 13.9 mg PLGA (50:50) microspheres (Bn04) viewed under Nikon SMZ1500 dissection microscope in a: bright field and b: fluorescent modes. Close up images at higher magnification are shown at the bottom row i: bright field, ii: fluorescence microscopy images & iii: an overlay of bright field and fluorescence channels. Scaffolds were directly preserved in OCT, frozen at $-80\text{ }^{\circ}\text{C}$ and then sectioned using Leica CM1100 cryostat.

The diffusion profile of FITC-BSA from triblock-PLGA microspheres scaffolds showed higher values of FITC-BSA concentrations at each hydrogel position as compared to equivalent profile from PLGA microspheres scaffolds at each time point. A steeper gradient was observed for triblock-PLGA microspheres containing scaffolds at each time point compared to plateau response from PLGA microspheres on day 1 (Figure 46A). Gradient of FITC-BSA released from Bn02 started to be observed on day 3 as shown in Figure 46B. Temporal monitoring of the sink compartment of different microspheres containing scaffolds is shown in Figure 47. An increase in the cumulative amount of FITC-BSA released to the sink compartment was observed at later time points for triblock-PLGA microspheres containing scaffolds compared to PLGA microspheres containing scaffolds.

4.5. Discussion

Plain and FITC-BSA loaded PLGA microspheres were prepared by a double emulsion/solvent evaporation method [179]. A water-in-oil-in-water (w/o/w) double emulsion technique was used for the encapsulation of hydrophilic drugs e.g. BSA, to improve the encapsulation efficiency of microspheres and to minimize their exposure to organic solvents during the manufacturing process and thus, minimize any loss of bioactivity [180]. The homogenization of FITC-BSA/DCM emulsions in the external water phase resulted in spherical particles with non-porous smooth surfaces [181]. Previous studies showed similar results for BSA loaded PLGA microspheres [182-184]. The selected homogenization speed of the secondary emulsion; 9000 rpm, should typically result in 10-20 μm microspheres. Comparable estimation of Bn02 mean microsphere size were computed by dynamic light scattering, image analysis of SEM images (Figure 38D) and fluorescence microscopy image (Figure 39b) with values of 19 ± 11 , 17 ± 7 & 19 ± 8 μm respectively. Smaller sizes of protein loaded PLGA microspheres compared to protein loaded microspheres containing triblock copolymer could be possibly attributed to lower affinity between PLGA and the hydrophilic BSA and better affinity was achieved by incorporating the hydrophilic triblock copolymer. The introduction of the hydrophilic PEG improved the hydrophilic property [185] resulting in relatively larger microspheres and higher encapsulation efficiency observed for Bn04.

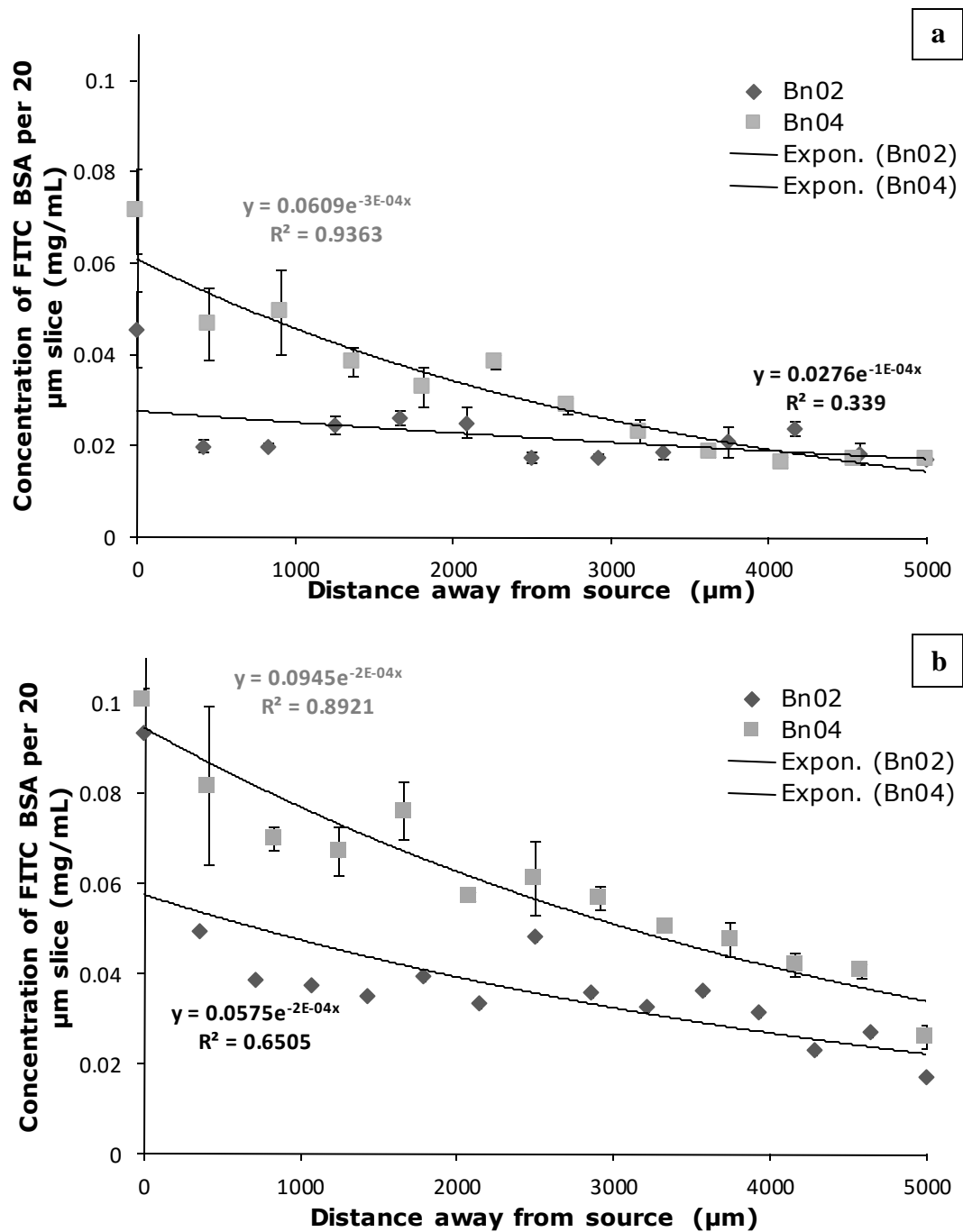


Figure 46: Diffusion gradient patterns of FITC-BSA released from FITC-BSA loaded microspheres in the microspheres-hydrogel layer to the plain 1% gelatin-1% agarose hydrogel layer on days a. 1 & b. 3.

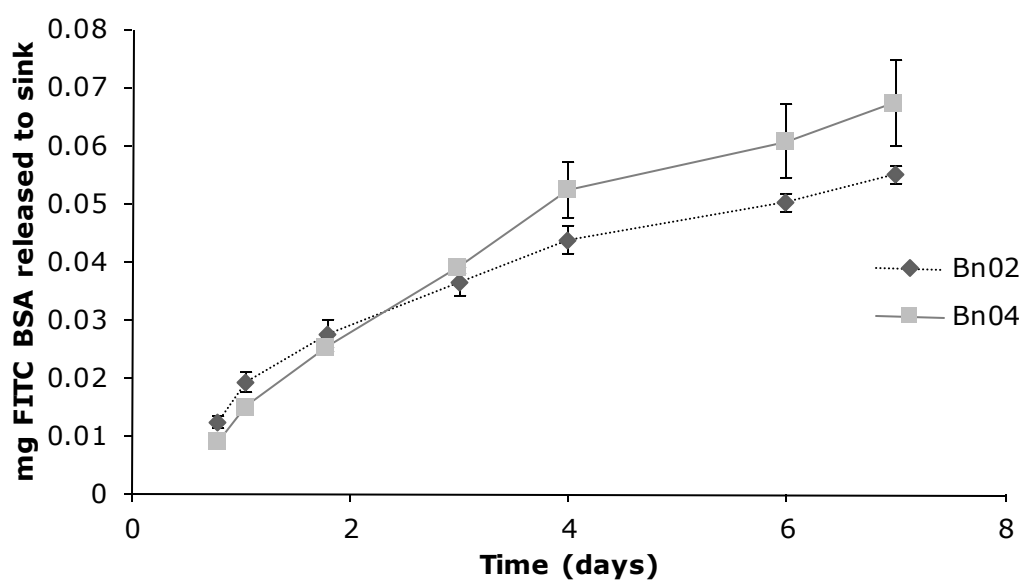


Figure 47: Cumulative amounts of FITC-BSA released to the sink compartment in the three compartmentalized diffusion chamber model following diffusion through 1% gelatin-1% agarose scaffolds of 15×5×6.6 mm (Length × Width × Height) dimensions.

Better encapsulation efficiency was observed upon incorporation of the hydrophilic PEG in the triblock backbone to the PLGA oil phase increasing the affinity to encapsulate BSA [185]. PEG-PLGA based particles showed higher entrapment efficiencies compared to plain PLGA particles in a previous study [186]. However, in another study, it was reported that the addition of PEG to the system may result in reduction of encapsulation efficiency for proteins due to steric interference of drug/protein-polymer interaction by the PEG chains [187]. Fluorescence microscopy images shown in Figure 39 revealed the incorporation of FITC-BSA inside microspheres was in pouches characteristic to the double emulsion method [188].

The microspheres showed an initial rapid release of protein deposited on the surface of the microspheres, followed by a slow and continuous release which corresponds to release of protein entrapped in the microspheres [182]. PLGA 50:50 generally exhibits faster degradation profiles compared to polymers with higher lactic acid percentages. The increase in the glycolic acid percentages in the polymer improves the hydrophilicity of the polymer, accelerates the polymer degradation and enhances the release of encapsulated hydrophilic drugs [177]. The increase in protein loading in triblock-containing microspheres compared to PLGA microspheres had an adjacent effect of increasing the surface embedded proteins and thus increasing burst release at earlier time points [114]. Higher release profiles were observed for Bn04 compared to Bn02 because of the incorporation of Triblock copolymer with the hydrophilic PEG portion. This resulted in increasing water uptake within the microspheres [189] and consequently the diffusion of BSA outside the microspheres, softening and plasticization of the microsphere matrix and ease of release of its protein content [185].

A microspheres-hydrogel composite layer cast next to the plain hydrogel membrane resulted in a double layered hydrogel membrane with a fine border (Figure 43) through which FITC-BSA diffused. This idea has been previously explored in relatively thinner PEG hydrogels where the diffusion of fluorescent labelled proteins; lysozyme, ovalbumin and BSA from PLGA microspheres was monitored [18]. However, the quantification method was dependant on microscopic fluorescence intensity measurements. Monitoring the sink compartments for protein showed continuous incremental increase of the protein concentrations in the sink compartment suggesting the efficiency of the model to drive protein release from the PLGA microspheres across a 3D hydrogel matrix in a gradient manner.

Spatial localization of the FITC-BSA PLGA depots next to the plain hydrogel membrane succeeded in developing of protein gradients across the 3D network. The diffusion profiles of FITC-BSA from different composition PLGA microspheres showed differential diffusion based on the initial release characteristics of the depot microspheres. Triblock containing microspheres showed higher FITC-BSA release at day 1 (~ 70% of the drug load) compared to FITC-BSA PLGA microspheres (~25% of the drug load). On day 3, the FITC-BSA released to PBS was increased to 55% of the initial drug load (Figure 41B). This theoretically indicates the availability of 7.9 μg FITC-BSA to diffuse on day 1 from Bn02 and the amount increases to 21.6 μg on day 3. This occurred in a kinetic release medium of liquid PBS and might not be the case in a static hydrogel system with the only driving force being a daily replenished sink.

Relatively smaller quantities of FITC-BSA were expected to be released from Bn02 to the plain hydrogel compartment and this did not establish a noticeable gradient (low exponential decay coefficient of determination $r^2= 0.339$ on day 1). The concentration gradient started to develop on day 3 when relatively higher amounts of FITC-BSA were expectedly released from the microspheres. This was observed by the relatively higher values of FITC-BSA at different positions as compared to day 1. Additionally, the coefficient of determination increased to be 0.6505 on day 3. On the other hand, the hydrophilic microspheres that contained triblock copolymer theoretically possessed 42.9 μg FITC-BSA available for diffusion on days 1 and 3. This resulted in more pronounced diffusion gradients on days 1 and 3 with coefficients of determination of the exponential decay 0.936 & 0.892 respectively. This shows that the temporal dynamics of the developed gradients were directly correlated to protein release from the localized protein depot microspheres [18].

4.6. Conclusions

The ability to replace the sink compartment with protein depots of polymeric-based particulate delivery system overcomes the challenges facing protein drug delivery and negates the need to replenish the source compartment at different time points. The ability to utilize tuneable release characteristics microspheres can be employed to provide temporal control on the developed protein concentration gradients. This can be further recruited to develop complex 3D scaffolds with tuneable time dynamics of bioactive molecules gradients essential in different biological applications.

Chapter 5: Intracellular transduction of proteins in three dimensional gradients system

5.1. Introduction

Several strategies of intracellular protein delivery have been thoroughly investigated to induce changes in cell behaviour [190-192], direct differentiation of somatic cell [193, 194] or stem cells [195]. The efficient intracellular protein delivery represents a major challenge in the process of drug discoveries and often requires continuous research to overcome the associated problems [196]. Challenges facing effective protein delivery include the ability to translocate the cell membrane and thereafter the potential of escaping entrapment inside vesicular structures to be accessible in the cytosol. Strategies of current protein delivery encompass mechanical delivery, carrier-based delivery and covalent protein modifications methods [197]. The delivery of active proteins and therapeutic agents via microinjection [195], liposomal [198], particulate delivery systems or viral vectors [199, 200] has been achieved. Variable reported shortcomings of such techniques included fluctuating delivery efficiency, protein modifications requirements, high cytotoxicity, and inevitable endosomal/lysosomal escape [197]. Mechanical/physical strategies such as microinjection and electroporation are invasive and of low-throughput requiring specialized equipment to puncture cell membranes [201].

On the other hand, the ability of various peptides; cell penetrating peptides (CPPs) to translocate the plasma membrane down to the cytosol has been reported [197, 202-204]. A broad range of synthetic and biological components has been delivered into cells using CPPs including enzymes, cytokines, hormones and cell-signalling proteins [197]. In this context, various oligocationic protein transduction domains; PTD derived from human immunodeficiency virus HIV or herpes simplex virus have been utilized to deliver macromolecules; peptides, proteins, oligonucleotides, siRNA and plasmid DNA [205, 206]. Alternatively, engineered CPPs were also utilized for cargo proteins delivery with enhanced cellular uptake and minimized degradation [190, 207].

Debates about the exact mechanism of cellular uptake of CPPs were more than once reported [190, 197, 208-210]. However, endocytosis-mediated uptake is assumed to be the main pathway through which CPPs are internalized within membranes [190-192], specifically, lipid raft-dependent micropinocytosis [210, 211]. The major limitations addressed to CPPs protein delivery mediated via endocytosis include the entrapment of the internalized cargo in the cytoplasm within endosomes. This hinders the release of the payload and exposes the trapped proteins to degradation in lysosome leading to ineffective protein delivery [191].

Eventually, this will require high starting concentration of CPPs to bypass entrapment inside endosomes [191, 212] and this could pose a toxic effect on cells.

To overcome this inefficiency in protein and macromolecules delivery, a recent study has introduced a new technology named glycosaminoglycan GAG enhanced transduction; GET [118]. The study proposed enhanced intercellular transduction upon coupling conventional CPPs with enhanced cell binding domains. This novel multi-domain protein is comprised of a membrane docking peptide to heparan sulphate glycosaminoglycans (GAGs) bound to the N-terminal of monomeric red fluorescent protein with an engineered poly-arginine PTD. Heparin is an intracellular polysaccharide while heparan sulphate (HS) is a proteoglycan commonly present on cell surfaces which also plays an important role in the extracellular matrix regulating a variety of biological processes [213]. For this reason, P21, a heparin-binding domain (HBD) that is comprised of a short 21 peptide residue (KRKKKGKGLGKKRDPCLRKYK) was used to enhance cell binding. Protease digestion of recombinant heparin-binding epidermal growth factor (HB-EGF) revealed that this 21-amino acid sequence in the amino-terminal region of the soluble HB-EGF is responsible for its binding to heparin [214]. The GAG-binding peptide was added to stimulate cell interaction and the PTD functions for high efficiency membrane transduction. This technology provides synergistic cell-targeting and cell-penetrating potentials and enables the delivery of therapeutic proteins to different cell-types. Functional quantities of variable protein cargos namely fluorescent proteins, transcription factors and enzymes were successfully delivered using this proposed technology with up to 16-fold increase in delivery compared to viral transgenesis achieved at their corresponding highest test doses [118].

Having demonstrated the enhanced 2D cellular transduction with GET technology in variable types of cells, we aim to deliver these novel proteins in a gradient manner using the compartmental diffusion model introduced in chapter three. The model was devoted to study the 3D gradient intracellular delivery of the novel GET proteins as an aim for gradient delivery of functional proteins.

5.2. Aims & objectives

5.2.1. Aim

The aim of the work presented in this chapter is to demonstrate the ability of the proposed diffusion model to follow gradient delivery of bioactive molecules in a cell laden hydrogel as a tool to direct cellular behaviour along the direction of protein gradient.

5.2.2. Objectives

Research objectives addressed in this chapter include:

1. Development of cell-laden hydrogels in a compartmentalized diffusion chamber.
2. Evaluation of the cellular viability and proliferation in the 3D hydrogel system
3. Development & evaluation of GET protein gradient across cell-laden hydrogels.

5.3. Materials and methods

5.3.1. GET proteins

GET protein synthesis was performed according to methodology described in section 2.2.4. Proteins concentrations were estimated using a BCA-based protein assay as explained in section 4.3.1.2 with absorbance measured at 595 nm using bovine serum albumin as a standard. The fluorescence of recombinant proteins was determined at excitation wave length of 584 nm and emission wave length 607 nm. Standards and samples were analysed using the TECAN infinite 200PRO multimode reader. Aliquots were stored at -80°C. Table 10 lists all the recombinant proteins produced via GET technology and their respective theoretical molecular weights and isoelectric points together with the original reporter fluorescent protein used. The resultant proteins are schematically presented in Figure 48.

5.3.1.1. Molecular weight

Proteins molecular weights were evaluated using SDS-PAGE using 10% Tris-Glycine mini protein gel. Details are described in section 2.2.4.1

5.3.1.2. Hydrodynamic radius & zeta potential

The hydrodynamic radii and the zeta potential of various different proteins were estimated using Zetasizer Nano ZS based on principles of dynamic light scattering (section 2.2.4.2) and doppler electrophoresis (section 2.2.4.3) respectively.

5.3.1.3. Diffusion coefficient across gelatin/agarose hydrogel

The diffusion coefficient of mRFP-1 and P21-mR-8R were estimated using model permeation method as detailed in section 2.2.8.7.4.

5.3.1.4. 2D intracellular transduction

NIH 3T3 mouse fibroblasts were maintained and cultured according to the general cell culture methodology described in section 2.2.1.1. To study the intracellular transduction in 2D, NIH 3T3 mouse fibroblasts were cultured on tissue culture plastics, different test proteins were added to the plated cells and the cellular transduction was evaluated as described in section 2.2.4.4.

5.3.2. Cellular viability and proliferation in 3D hydrogels

NIH 3T3 mouse fibroblasts viability and proliferation in gelatin/agarose system were evaluated according to methodology described in 2.2.7.

5.3.3. Compartmentalized diffusion

Acellular and cellular NIH 3T3 mouse fibroblasts scaffolds (section 2.2.1.4) agarose/gelatin hydrogels dispensed in culture medium were cast in the middle compartment of the compartmental diffusion chamber.

5.3.4. Evaluation of proteins diffusion gradients

Protein diffusion from the source compartment was followed as described in section 3.3.3 and diffusion gradients were evaluated as detailed in section 2.2.8.5.

5.3.5. Temporal imaging of scaffolds

See section 2.2.8.6.2.

5.3.6. 3D Intracellular transduction across cellular hydrogels

Cellular scaffolds, at pre-determined time points, were manually sliced perpendicular to the direction of the protein flow using sterile disposable blades (Personna 2-facet single edge blades, USA) into five parallel sections against glass microscope slides of 1 mm height to yield 1 mm thick slices. Each hydrogel slice was degraded by enzymatic digestion following a protocol modified from Ran Yu et al. [215]. Hydrogels were digested by addition of 10 μ L 10X agarase reaction buffer (New England Biolabs, USA) to each slice. The reaction mixture was heated at 50°C for 5 minutes and left to cool down to 44°C for 25 minutes using Thermobloc TD150 (FALC instruments, Italy). 2 μ L β -agarase I enzyme (New England Biolabs, USA) were added to each sample and the reaction mixtures were maintained for 1 hour at 44°C. Hoechst 33342 was added to the liquefied gel slices for 30 minutes to achieve final concentration (2.5 μ g/mL). Samples were then analysed using a MoFloTM DP (DAKO) Flow Cytometer according to experimental controls mentioned in section 2.2.9.

5.3.6.1. Statistical analysis

Statistical comparisons were carried out using the GraphPad Prism software package version 6. The statistical significance of the effects of diffusing species, the distance inside the scaffolds and their interaction on intracellular transduction at each time point was studied using two-way ANOVA followed by Dunnett's multiple comparisons test. Results were considered significant if $p < 0.01$.

Table 10: list of reporter fluorescent protein & recombinant proteins produced via GAG enhanced binding transduction technology, their amino acid sequences and their expected molecular weights & isoelectric points as calculated from [216]

Protein	Amino acid sequence	Theoretical Mwt	Theoretical pI
mRFP-1	MASSEDVIKEFMRFKVRMEGSVNGHEFEIEGEGEGRPYEGTQTAKLKVTKGGPLPFAWDILSPQFQYGSKAYVKHPADIPDYLKLSFPEGFKWERVMNFEDGGVVTVTQDSSLQDGEFIYKVKLRGTNFPSDGPVMQKKTMGWEASTERMYPEDGALKGEIKMRLKLLKDDGGHYDAEVKTTYMAKKPVQLPGAYKTDIKLDITSHNEDYTIVEQYERAEGRHSTGATSEFGRPGSTM	26574.97	5.66
P21-mR-8R	MKRKKKGKGLGKKRDPCLRKYKTSTMASSEDVIKEFMRFKVRMEGSVNGHEFEIEGEGEGRPYEGTQTAKLKVTKGGPLPFAWDILSPQFQYGSKAYVKHPADIPDYLKLSFPEGFKWERVMNFEDGGVVTVTQDSSLQDGEFIYKVKLRGTNFPSDGPVMQKKTMGWEASTERMYPEDGALKGEIKMRLKLLKDDGGHYDAEVKTTYMAKKPVQLPGAYKTDIKLDITSHNEDYTIVEQYERAEGRHSTGATSEFGRPGSTMRRRRRRRR	30743.07	9.59
mR-8R	MASSEDVIKEFMRFKVRMEGSVNGHEFEIEGEGEGRPYEGTQTAKLKVTKGGPLPFAWDILSPQFQYGSKAYVKHPADIPDYLKLSFPEGFKWERVMNFEDGGVVTVTQDSSLQDGEFIYKVKLRGTNFPSDGPVMQKKTMGWEASTERMYPEDGALKGEIKMRLKLLKDDGGHYDAEVKTTYMAKKPVQLPGAYKTDIKLDITSHNEDYTIVRRRRRRR	27824.47	8.81
P21-mR	MKRKKKGKGLGKKRDPCLRKYKTSTMASSEDVIKEFMRFKVRMEGSVNGHEFEIEGEGEGRPYEGTQTAKLKVTKGGPLPFAWDILSPQFQYGSKAYVKHPADIPDYLKLSFPEGFKWERVMNFEDGGVVTVTQDSSLQDGEFIYKVKLRGTNFPSDGPVMQKKTMGWEASTERMYPEDGALKGEIKMRLKLLKDDGGHYDAEVKTTYMAKKPVQLPGAYKTDIKLDITSHNEDYTIVEQYERAEGRHSTGATSEFGRPGSTM	29493.57	9.06
P21-mR-MyoD-8R	MKRKKKGKGLGKKRDPCLRKYKTSTMASSEDVIKEFMRFKVRMEGSVNGHEFEIEGEGEGRPYEGTQTAKLKVTKGGPLPFAWDILSPQFQYGSKAYVKHPADIPDYLKLSFPEGFKWERVMNFEDGGVVTVTQDSSLQDGEFIYKVKLRGTNFPSDGPVMQKKTMGWEASTERMYPEDGALKGEIKMRLKLLKDDGGHYDAEVKTTYMAKKPVQLPGAYKTDIKLDITSHNEDYTIVEQYERAEGRHSTGATSTMELLSPLRDVDLTAPDGLCSFATDDDFYDDPCFDSPDLRFFEDLDPRLMHV GALLKPEESHFPAAVHPAPGAREDEHVRAPSGHHQAGRCLLWACKACKRKT TNADRRKAATMRERRRLSKVNEAFETLKRCTSSNPQNRLPKVEILRN AIRYIEGLQALLRDQDAAPPAAAAFYAPGPLPPGRGGEHYSGSDASSPRSNCSGMMDYS GPPSGARRRNCYEGAYYNEAPSEPRPGKSAAVSSLDCLSSIVERISTESPAAPALLADVPSESPPRQEA AAPSEGESSGDPTQSPDAPQCPAGANPNPIYQVLEFGRPGSTMRRRRRRRR	65327.53	8.56

5.4. Results

5.4.1. GET proteins characterization

The theoretical molecular weights of GET proteins are listed in Table 9 according to the amino acid sequence of the different constituents of each protein [216]. Practical estimation of proteins molecular weights was done via acrylamide gel electrophoresis. Molecular weight of variable test proteins spanned around the core mRFP-1 which was almost 28 kDa (theoretically~26.6 kDa). Imaging of the gel showed a single band for the mRFP-1 while the other test proteins were split in double bands approximately at their expected theoretical molecular weights.

The hydrodynamic radii of different test proteins in different dispersants listed in Table 11 were estimated applying dynamic light scattering principles. Standard Divinyl benzene polymer microspheres, 0.057 μm diameter were used to validate the measurement method and the respective hydrodynamic radii were computed to be 25.65 ± 0.35 , 26.96 ± 0.18 or 27 ± 2 nm in HPLC water, 10 mM HEPES buffer or PBS respectively. Figure 50 shows representative histograms of the hydrodynamic radii of various proteins comprising the GET system as well as the reporter mRFP-1, FITC-BSA and the standard beads. The hydrodynamic radii of various test proteins ranged from 2.08 to 6.49 nm in HPLC water & 2.36 to 5.17 in 10 mM HEPES buffer (pH 7.2). Table 12 shows the zeta potential measured for each test protein in 10 mM HEPES buffer at 37 °C applying the Doppler electrophoresis principle. All test proteins exhibited slight negative charge at the test physiological pH of 10 mM HEPES buffer.

The diffusion coefficients of mRFP-1 & P21-mR-8R across gelatin/agarose hydrogels dispensed in DMEM culture medium were estimated using model permeation method. Linear fit of cumulative amount of proteins received in the sink compartments after achieving steady state after 24 hours for both test proteins (Supplementary figure 11 & Supplementary figure 12). Solving the regression equation for the slope and intercept from Equation 1 resulted in the diffusion coefficients to be 7.15×10^{-7} & 7.53×10^{-7} cm^2/s for mRFP-1 & P21-mR-8R respectively.

5.4.2. 2D intracellular transduction

The potential of the P21-mR-8R to efficiently transduce a monolayer of NIH 3T3 mouse fibroblasts was examined in comparison to the reporter mRFP-1 using flow cytometry as shown in Figure 51. This was coupled with fluorescence microscopy imaging of cells as a function of time (Figure 52). Comparing the fluorescence intensity in cells exposed

to P21-mR-8R to those exposed to mRFP-1 shows enhanced uptake of the fluorescence intensity into the cells at all time points. Cells exposed to the reporter mRFP-1 exhibited more or less similar fluorescence intensity to their equivalents exposed to plain culture medium. Meanwhile, there was an observed increase in the fluorescence intensity in cells exposed to P21-mR-8R as a function of time till 24 hours. This was succeeded by a decrease in the fluorescence intensity at 48 and 72 hours (Figure 51 & Figure 52). Thorough analysis revealed the presence of 2 populations of cells at the late time points; 48 & 72 hours as shown in the insert of Figure 51. Equally, exposing monolayer of NIH 3T3 mouse fibroblasts to the different protein moieties comprising the GET system as well as plain culture medium and the reporter mRFP-1 shows enhanced transduction in cells exposed to P21-mR-8R compared to other counterparts (Figure 53). This was confirmed by fluorescence microscopy at different time points as shown in Figure 53b.

5.4.3. Cellular viability and proliferation in 3D hydrogels

Cellular viability was assessed with a live/dead[®] cytotoxicity kit and ImageJ software was used to count the relative numbers of live (green) and dead (red) cells. A control monolayer of cells was evaluated for viability over 3 days and the viability was maintained constant around 100% viable cells (Figure 54). 3 different hydrogel systems namely 1% agarose, 2% agarose and 1% agarose-1% gelatin were used as 3D support systems for mouse fibroblasts. The cellular viabilities at day 1 were highest for 1% agarose and 1% agarose-1% gelatin of values 93 and 95% respectively. A relatively higher drop (~80%) in the viability of cells within 2% agarose was measured at day 1. Cellular viability dropped progressively at late time points for 1% & 2% agarose systems, yet moderately for 1% agarose-1% gelatin.

Cellular proliferation was assessed using Prestoblu[®] for the 3 different hydrogel systems over 3 days (Figure 55). Among the 3 hydrogel systems under investigation, Agarose/gelatin showed relatively higher cellular proliferation potentials especially on day 1. However, the cellular proliferation was reduced on successive time points. The cellular proliferation in agarose/gelatin system was furtherly examined using Cyquant[®] NF proliferation assay (Figure 56). Cellular proliferation in monolayer culture increased over time unlike the case for proliferation in 3D agarose/gelatin which slightly increased on day 1 and thereafter was kept constant.

5.4.4. Compartmental diffusion model

5.4.4.1. Temporal quantification of protein gradients

Calibration curves of increasing mRFP-1 concentrations in cellular and acellular scaffolds were established as shown in Figure 57. The presence of cells did not alter the fluorescence intensity responses of each specific protein concentration. Figure 58 shows temporal diffusion gradients of mRFP-1 across acellular and cellular agarose gelatin scaffolds. A steep mRFP-1 gradient developed in 6 hours, started to equilibrate at 24 hours and was totally equilibrated at 72 hours as denoted by the relatively low coefficient of determination $r^2 = 0.4051$. Similar patterns were observed for mRFP-1 diffusing across acellular and cellular scaffolds at each specific time point (Figure 58). At 72 hours, mRFP-1 diffusing across cellular scaffolds exhibited relatively equilibrated diffusion as denoted by low coefficient of determination of the exponential decay kinetics; $r^2 = 0.5028$. The diffusion of the GET protein; P21-mR-8R across acellular and cellular agarose/gelatin scaffold was followed (Figure 59). In contrast to mRFP-1, a steep gradient of P21-mR-8R was observed at 24 hours for acellular scaffolds. However, it started to equilibrate at 72 hours with coefficient of determination $r^2 = 0.5091$. On the other hand, the presence of mouse fibroblasts maintained the gradient observed at 72 hours as denoted by the relatively high coefficient of determination $r^2 = 0.8811$.

Temporal monitoring of protein concentrations in the source/sink compartments is shown in Figure 60. Lower quantities of proteins in the sink compartments were measured at 24 hours as compared to the relatively larger quantities of proteins in the source compartments. After 72 hours, an observed increase in the sink compartments concentrations was accompanied with a decrease in the source compartments concentrations.

5.4.4.2. Temporal imaging of protein gradients

Applying the selective washing protocol described in section 2.2.8.6.2, temporal monitoring of red fluorescence intensity entrapped inside the cells and not in the hydrogel matrix. Figure 61 shows progressive increase in the distance with dispersed positively transduced cells in scaffolds exposed to P21-mR-8R. The distance increased from 0.85 mm at 6 hours to 2.75 mm at 72 hours as measured in Figure 61. On the other hand, scaffolds exposed to mRFP-1 did not show any transduced cells at any time point assessed.

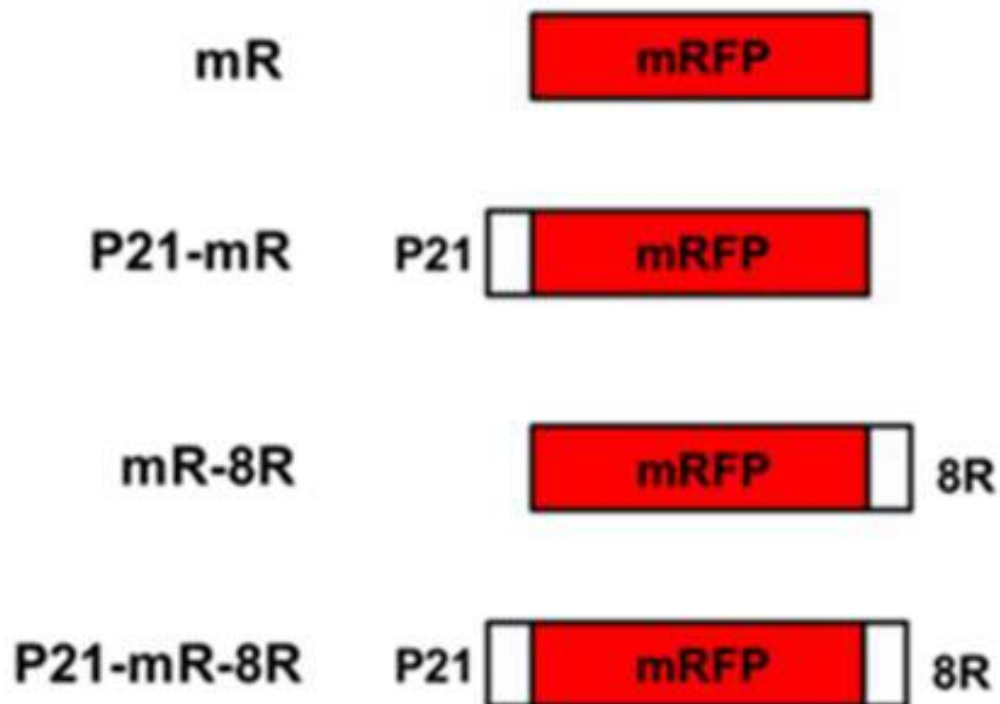


Figure 48: Schematic diagram of the test proteins; mRFP-1 is the reporter red fluorescent protein, mR-8R is the cell penetrating 8 arginine peptide linked to mRFP-1 while P21-mR is mRFP-1 with an N-terminal fusion of the P21 domain of heparin binding EGF (HB-EGF). P21-mR-8R is mRFP-1 with N-terminal fusion of P21 and C-terminal fusion of 8R. Reproduced from [118].

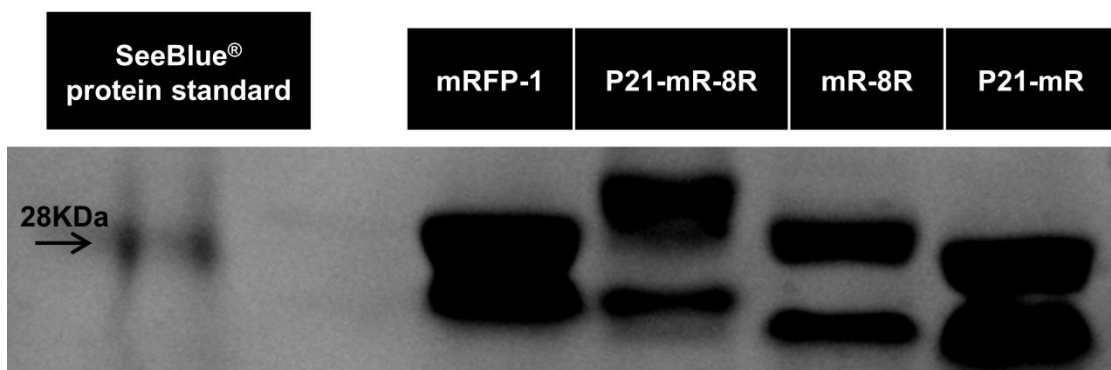


Figure 49: Determination of the protein molecular weight of mRFP-1, P21-mR-8R, mR-8R and P21-mR using SDS-PAGE using a SeeBlue® protein standard.

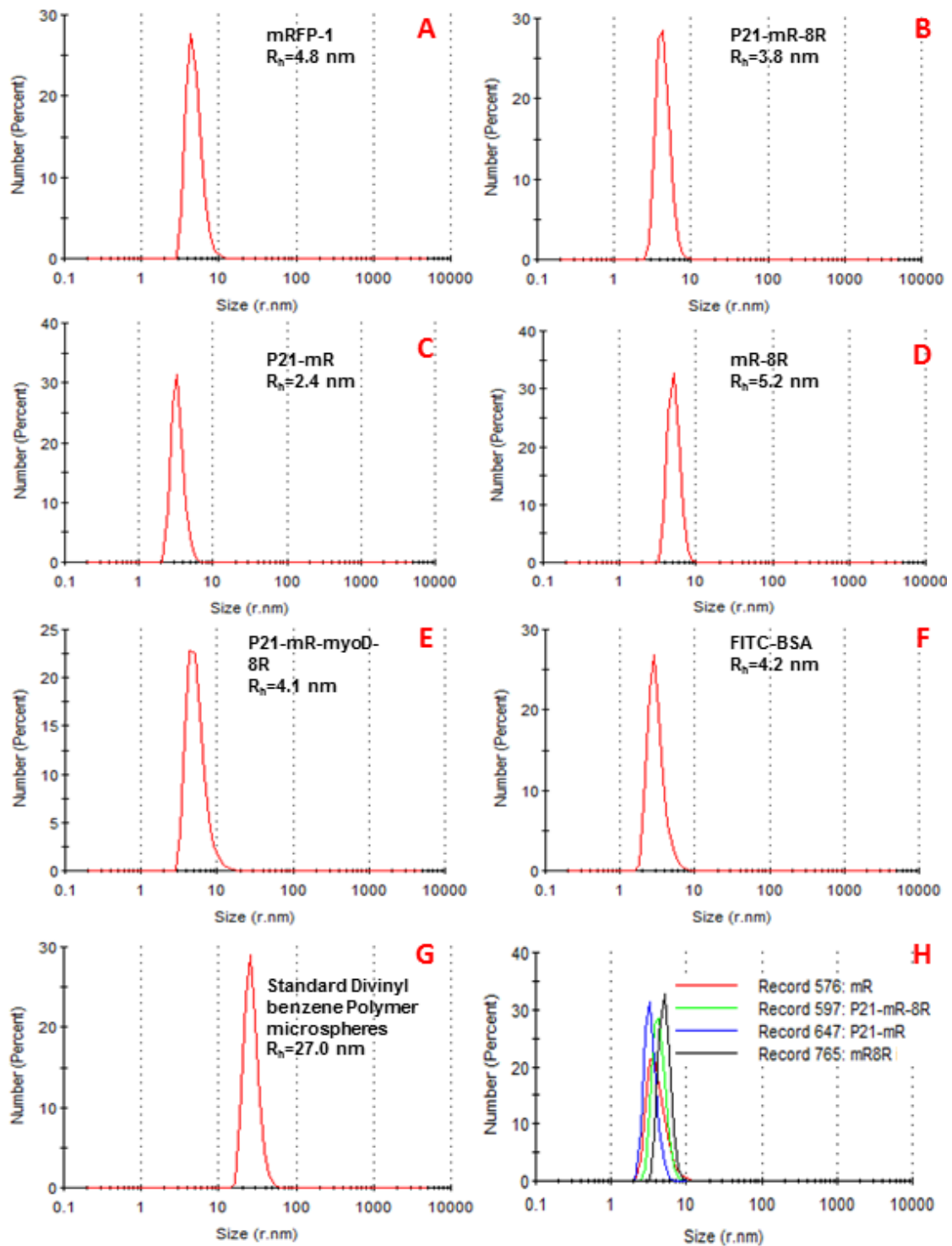


Figure 50: Determination of the hydrodynamic radii R_h (nm) of A: mRFP-1, B: P21-mR-8R, C: P21-mR, D: mR-8R, E: P21-mR-MyoD-8R, F: FITC-BSA, G: Standard Divinyl benzene Polymer microspheres & H: collective proteins in 10 mM HEPES buffer at 37 °C using Zeta sizer Nano ZS

Table 11: Determination of the hydrodynamic radius (nm) of various test samples in different dispersants using Zeta sizer Nano ZS at 37°C

Test samples	Hydrodynamic radius R_h (nm)		
	HPLC grade water pH 6.8	10 mM HEPES Buffer pH 7.2	PBS pH 7.4
Standard Divinyl benzene Polymer microspheres, 0.057 μ m diameter (Bangs Laboratories, Inc.)	25.7 \pm 0.4	27.0 \pm 0.2	27 \pm 2
mRFP-1	4 \pm 1	5 \pm 1	NA
P21-mR	4.6 \pm 0.6	2.4 \pm 0.5	NA
mR-8R	2.1 \pm 0.7	5.2 \pm 0.1	NA
P21-mR-8R	5.0 \pm 0.7	3.8 \pm 0.6	NA
P21-mR-MyoD-8R	7 \pm 2	4 \pm 1	NA
FITC-BSA	3.6 \pm 0.4	4.2 \pm 0.5	4.06 \pm 0.32

Table 12: Determination of the Zeta potential of various test samples in 10 mM HEPES buffer using Zeta sizer Nano ZS at 37°C

Test protein	HEPES Buffer (10 mM) pH 7.2
mRFP-1	-6.1 \pm 0.8
P21-mR	-9 \pm 2
mR-8R	-12 \pm 3
P21-mR-8R	-10 \pm 2
P21-mR-MyoD-8R	-8 \pm 2
FITC-BSA	-10 \pm 3

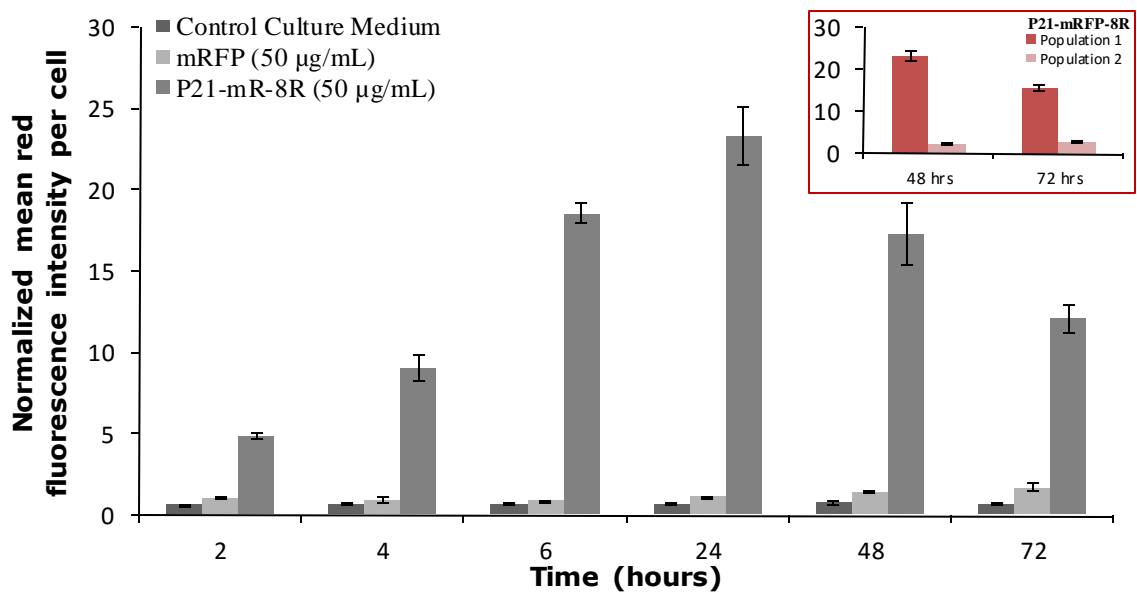


Figure 51: Intracellular transduction of P21-mR-8R versus mRFP-1 in NIH 3T3 mouse fibroblasts cultured in monolayer on tissue culture plastic. Mean fluorescence intensity inside cells was quantified using flow cytometric analysis using MoFlo™ DP (DAKO) Flow Cytometer. Data were normalized to the mean fluorescence intensity per monolayer of cells (1×10^6) exposed to 50 µg/mL mRFP-1 for 2 hours. Data are represented as the mean ($n=3$) \pm standard deviation.

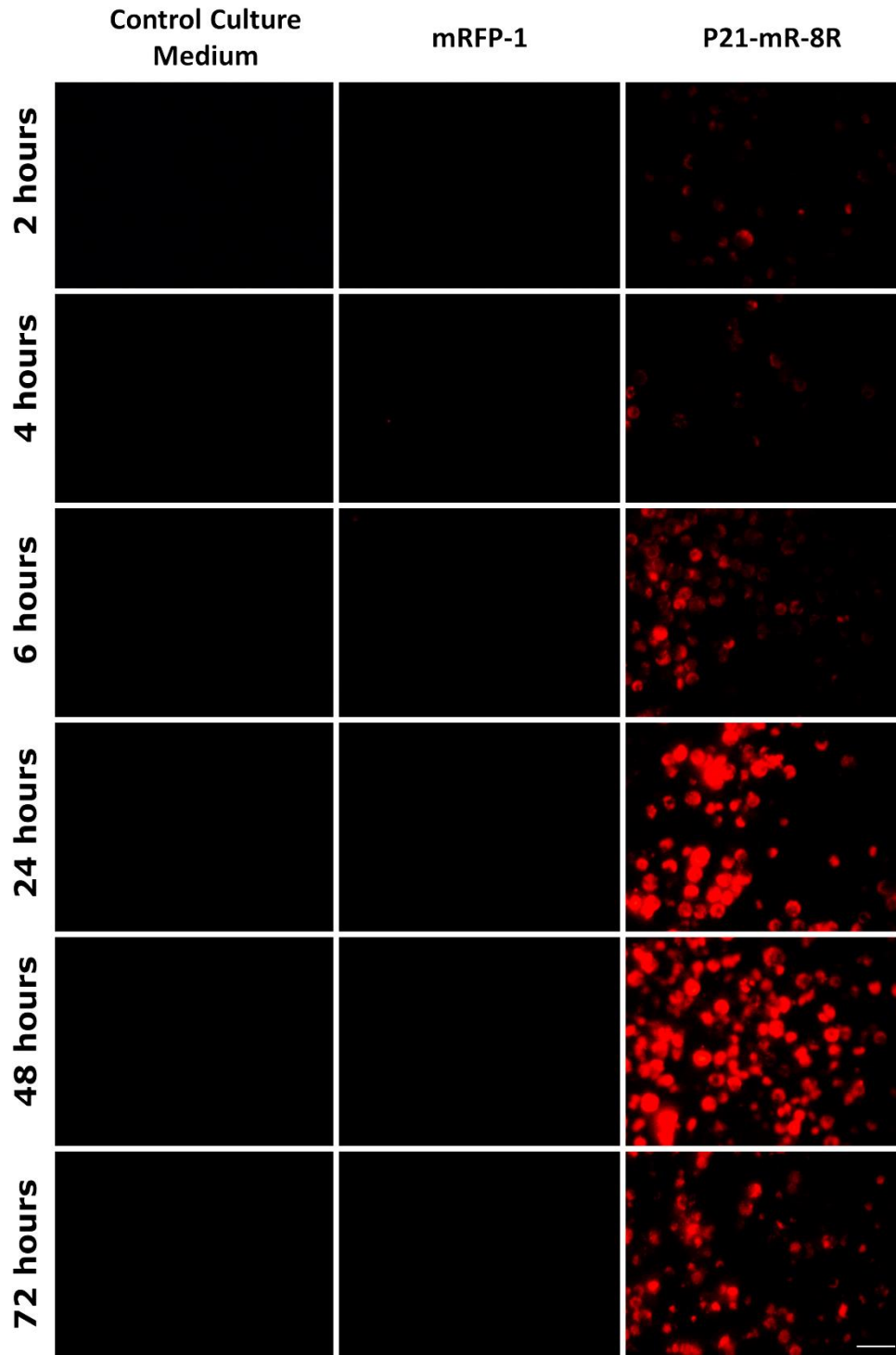


Figure 52: Fluorescence microscopy images of NIH 3T3 mouse fibroblasts exposed to culture medium or 50 $\mu\text{g}/\text{mL}$ mRFP-1 or P21-mR-8R at different time points imaged using Leica DM IRB microscope. Cells were detached using Trypsin-EDTA and the mean fluorescence intensity per cells was quantified using MoFlo™ DP (DAKO) Flow Cytometer and samples of cell solutions were subsequently imaged. Scale bar is 100 μm .

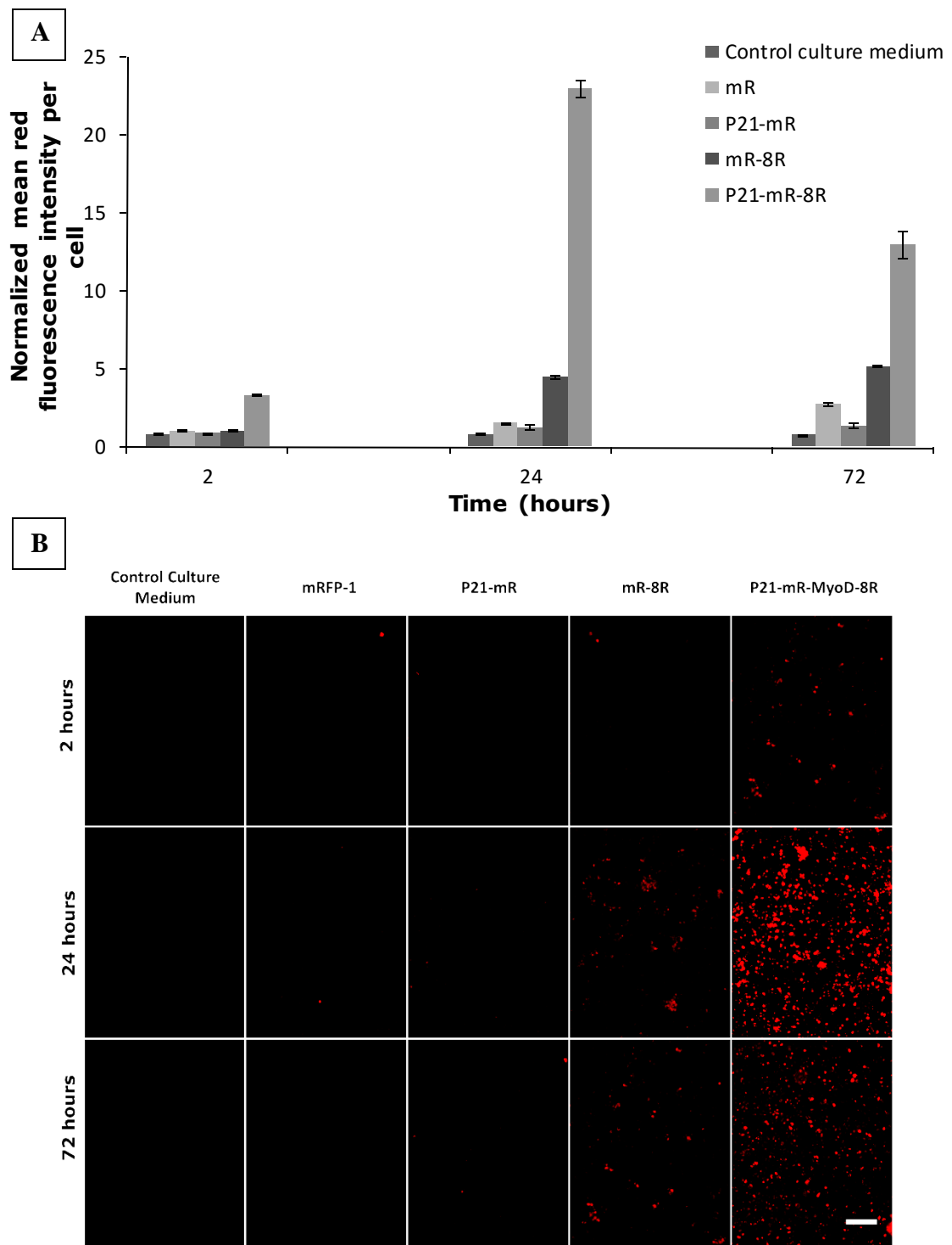


Figure 53: A: Intracellular transduction of P21-mR-8R versus mRFP-1, P21-mR & mR-8R in NIH 3T3 mouse fibroblasts cultured in monolayer on tissue culture plastic. Mean fluorescence intensity inside cells was quantified using flow cytometric analysis using MoFlo™ DP (DAKO) Flow Cytometer. Data were normalized to the mean fluorescence intensity per monolayer of cells (1×10^6) exposed to 50 $\mu\text{g}/\text{mL}$ mRFP-1 for 2 hours. Data are represented as the mean ($n=3$) \pm standard deviation. B: Fluorescence microscopy images of NIH 3T3 mouse fibroblasts exposed to culture medium or 50 $\mu\text{g}/\text{mL}$ mRFP-1, P21-mR, mR-8R or P21-mR-8R at different time points imaged using microscope.

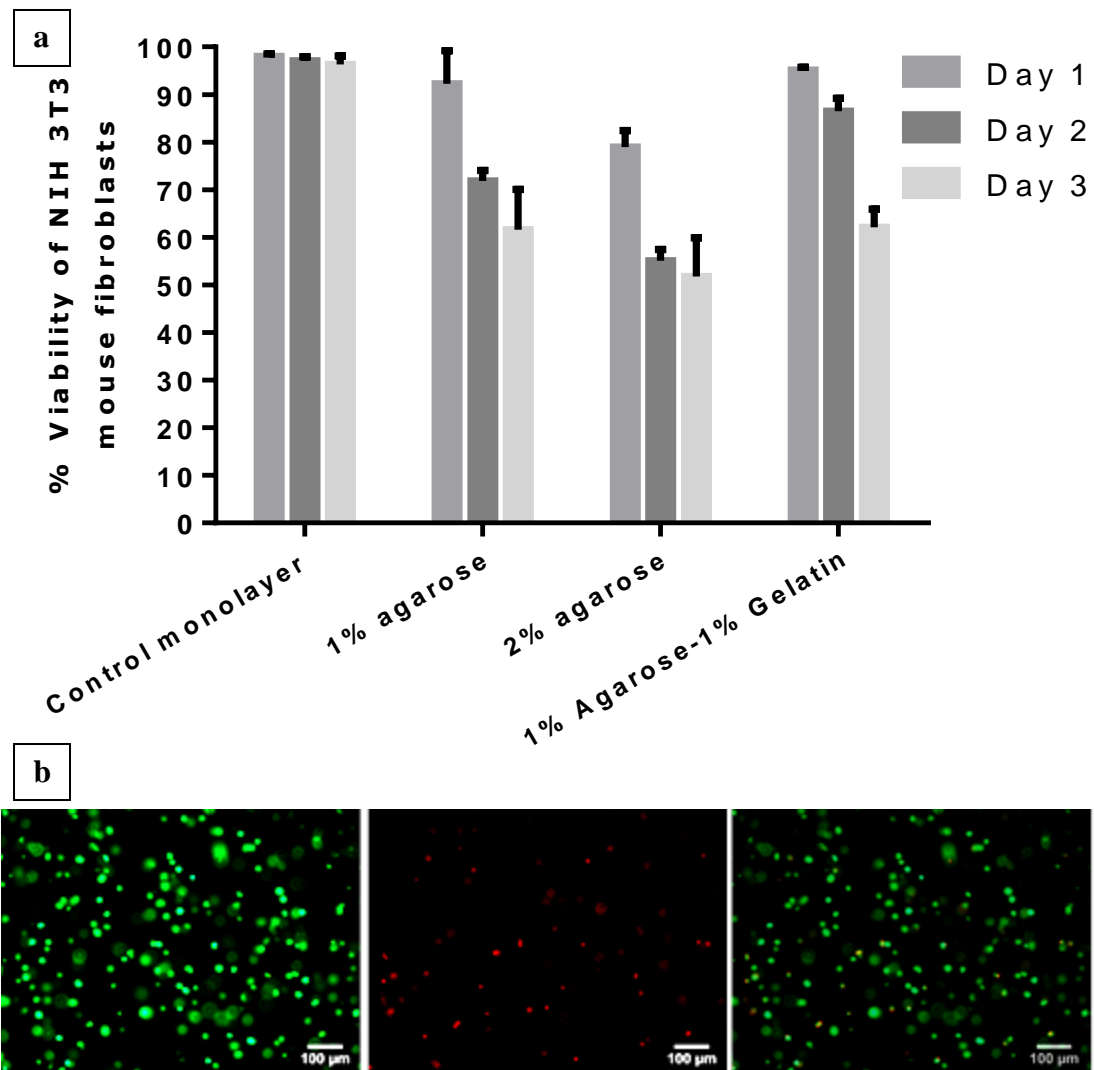


Figure 54: a: Viability of NIH 3T3 mouse fibroblasts cultured in monolayer on tissue culture plastic versus viability of cells encapsulated in 1% agarose, 2% agarose & 1% agarose-1% gelatin hydrogel at different time points using Live/Dead[®] Viability/Cytotoxicity Kit. b: representative images of viable (green), dead (red) cells and overlay of both for cells encapsulated in 1% agarose-1% gelatin hydrogel at day 3. Data is expressed as % of viable cells compared to total live and dead cells. Cells were counted using ImageJ software. Each data point is an average of 3 different samples and each sample was assessed from 3 different fields of views.

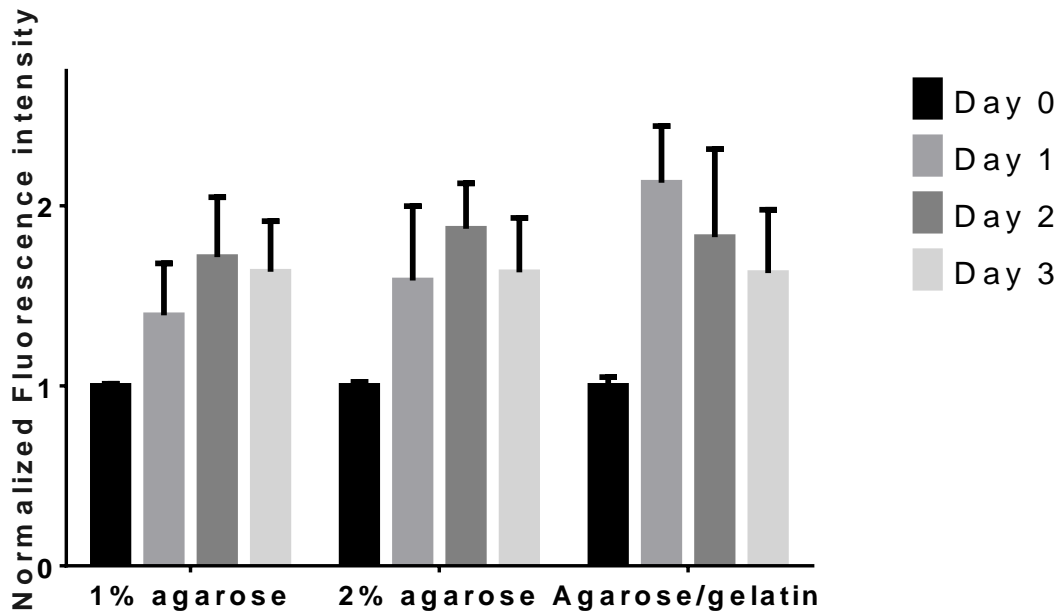


Figure 55: Metabolic activity of NIH 3T3 mouse fibroblasts cultured in monolayer on tissue culture plastic versus to results of cells encapsulated in 1% agarose, 2% agarose & 1% agarose-1% gelatin hydrogel at different time points using Prestoblu[®] proliferation assay. Data is normalized to the relevant fluorescence intensity of hydrogel systems at day zero. Each time point is an average of triplicate samples.

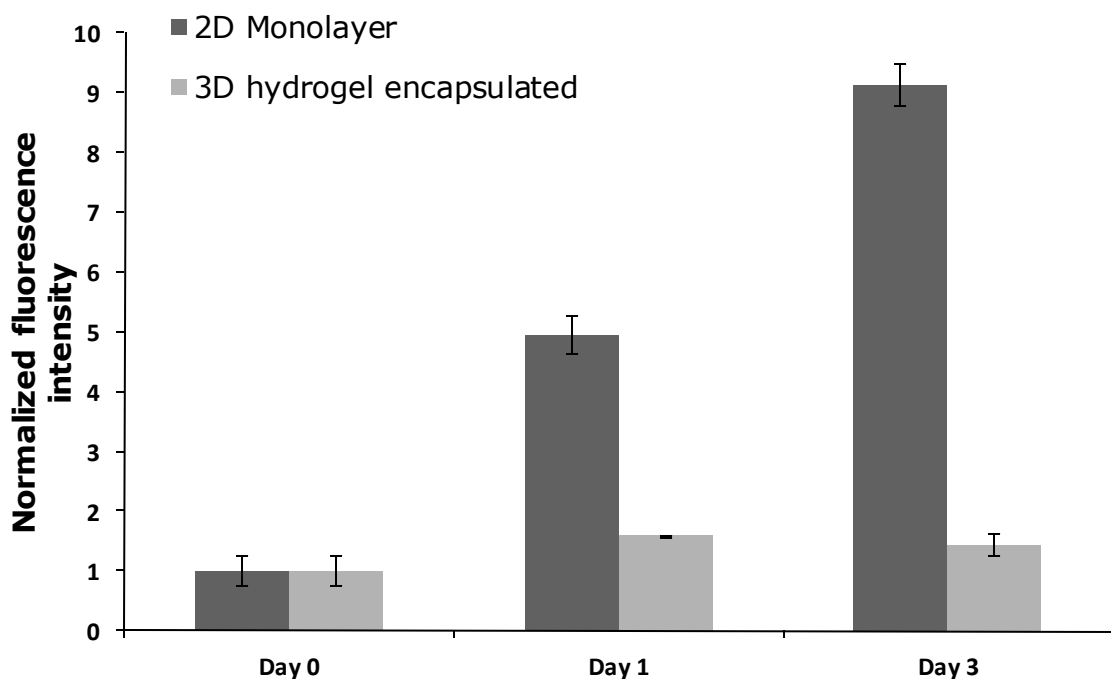


Figure 56: Proliferation assay of NIH 3T3 mouse fibroblasts cultured in monolayer on tissue culture plastic versus cells encapsulated in 1% agarose-1% gelatin hydrogel at different time points using CyQuant[®] NF proliferation assay. Data is normalized to the relevant fluorescence intensity at day zero. Each time point is an average of triplicate samples.

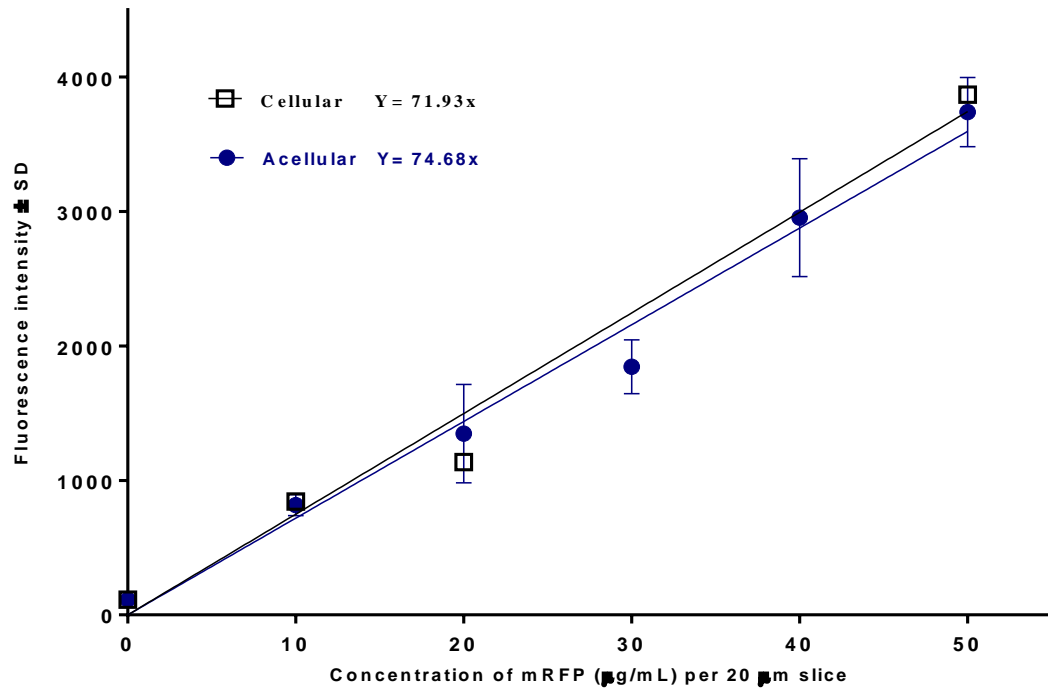


Figure 57: Calibration curve of mRFP-1 per 20 μm thick slices retrieved from cryosectioning of homogeneously dispersed increasing concentrations of mRFP-1 in cellular (2×10^6 NIH 3T3 mouse fibroblasts cells/mL) or acellular 1% agarose – 1% gelatin hydrogel scaffolds of 15×5×6.6 mm (Length × Width × Height) dimensions. Each concentration point was evaluated from 2 different scaffolds each with 8 different slices retrieved from random positions of the scaffold. Slices were dissolved in PBS and analysed for protein concentrations using a TECAN infinite 200PRO multimode reader (excitation: 584 nm; emission: 620 nm).

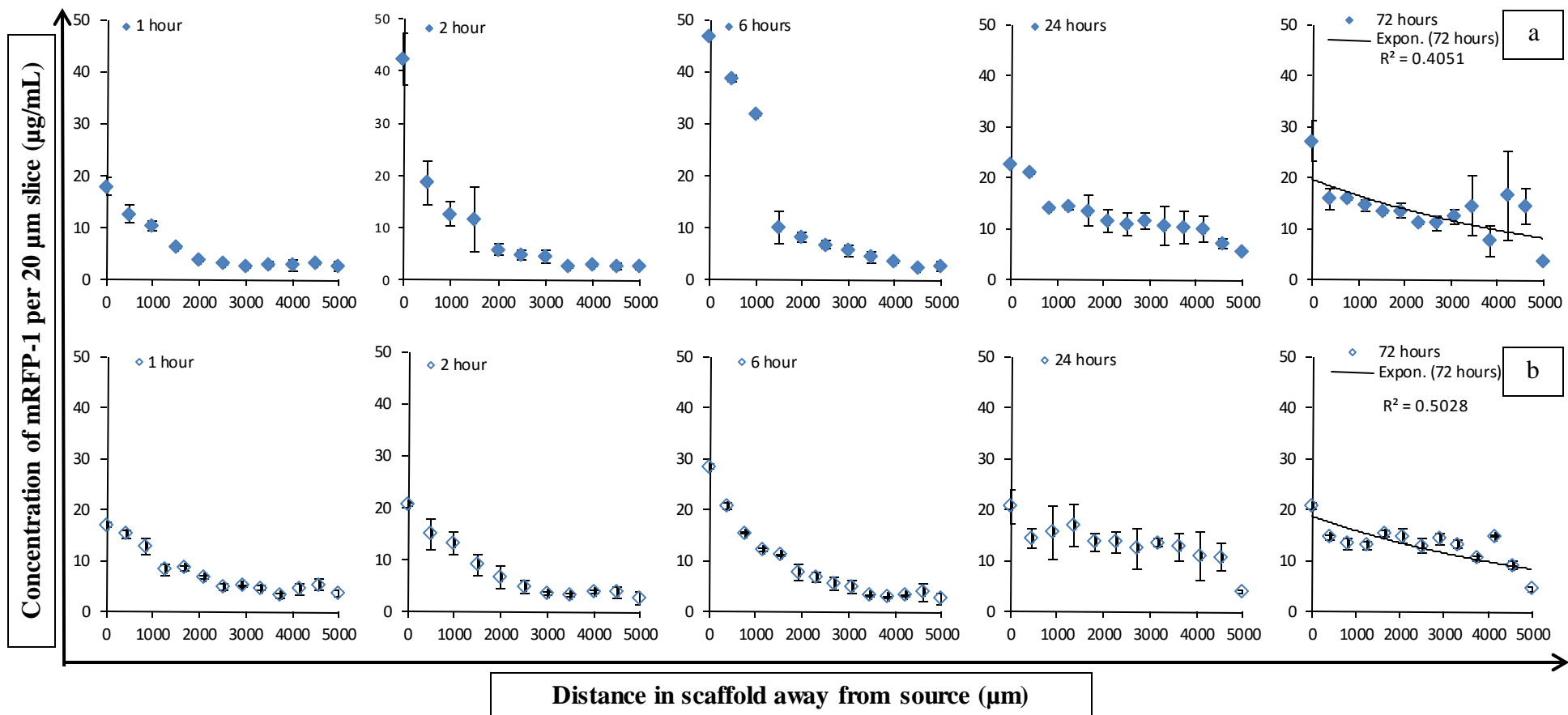


Figure 58: Diffusion gradients of 50 µg/mL mRFP-1 across (a) acellular and (b) cellular (NIH 3T3 mouse fibroblasts, $2 \times 10^6/\text{mL}$) 1% agarose-1% gelatin hydrogels at 1, 2, 6, 24 and 72 hours ($n=3$).

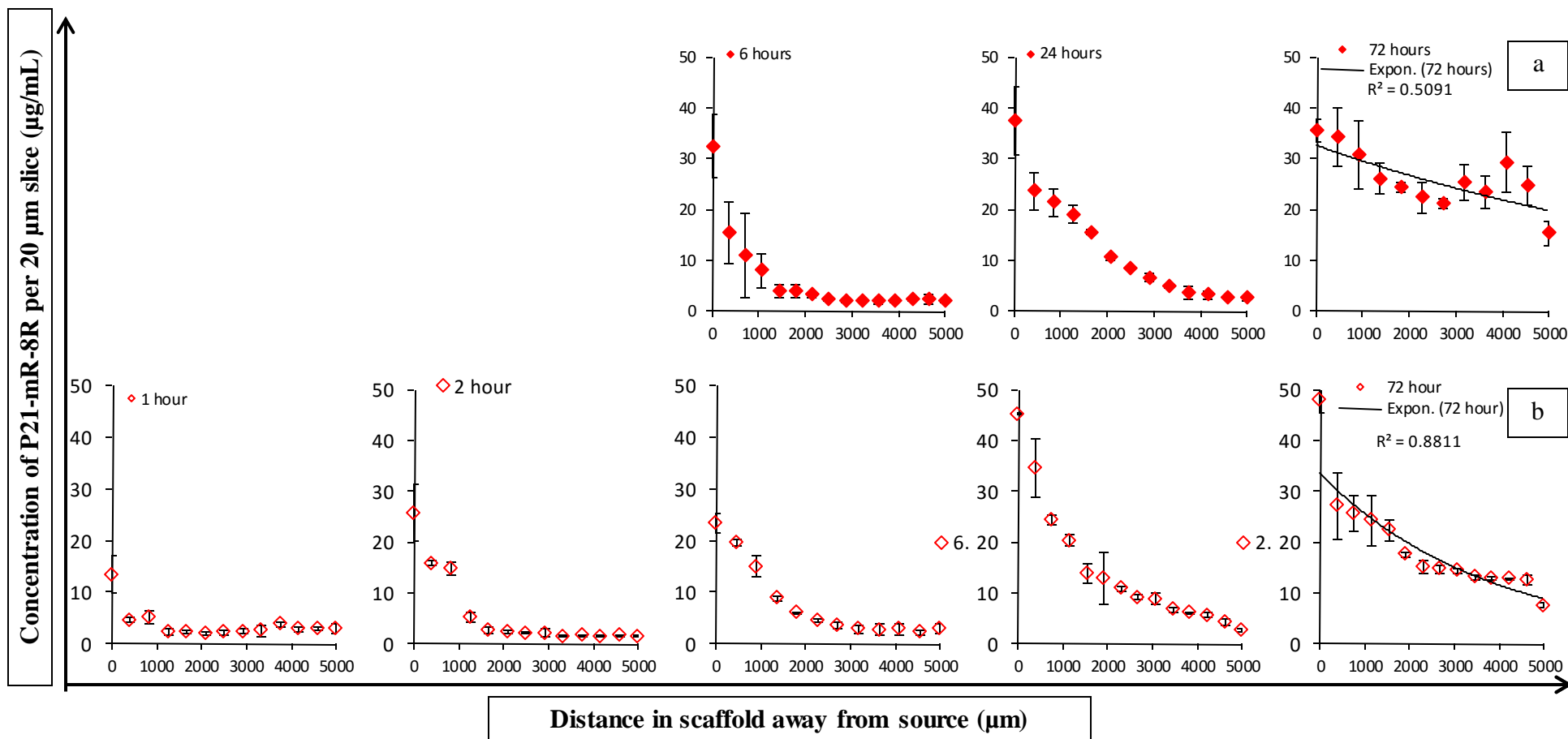


Figure 59: Diffusion gradients of 50 µg/mL P21-mR-8R across (a) acellular and (b) cellular (NIH 3T3 mouse fibroblasts, 2×10^6 /mL) 1% agarose-1% gelatin hydrogels at 1, 2, 6, 24 and 72 hours (n=3).

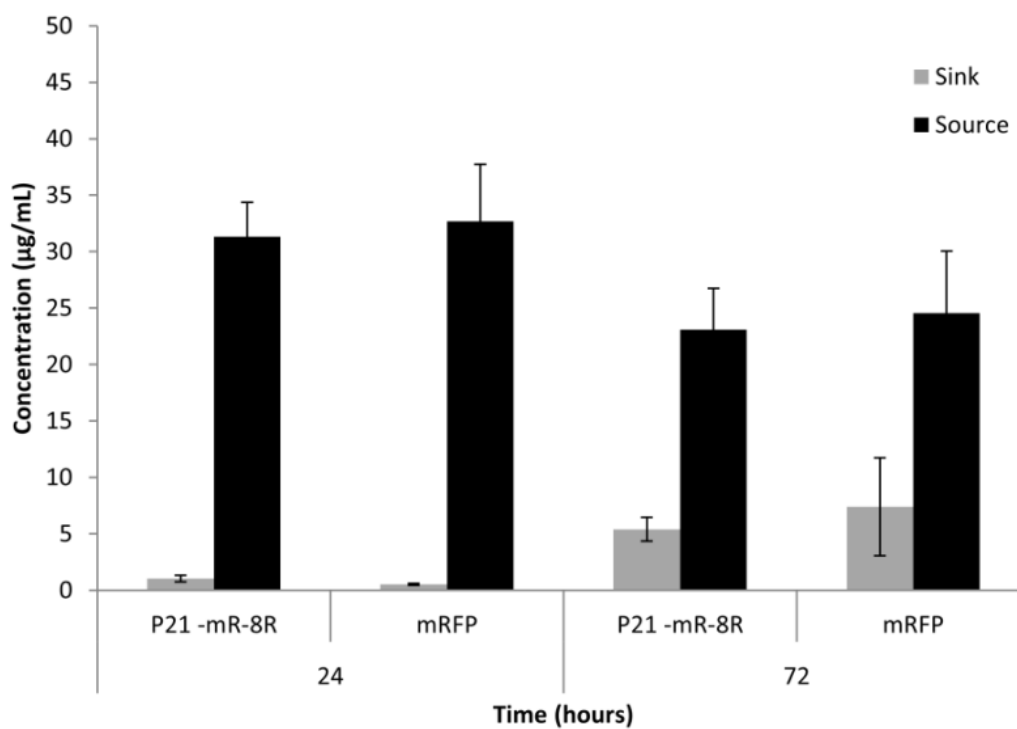


Figure 60: Concentration of proteins in the source and sink compartments next to cellular scaffolds (NIH 3T3 mouse fibroblasts; 2 M/mL) at 24 and 72 hours.

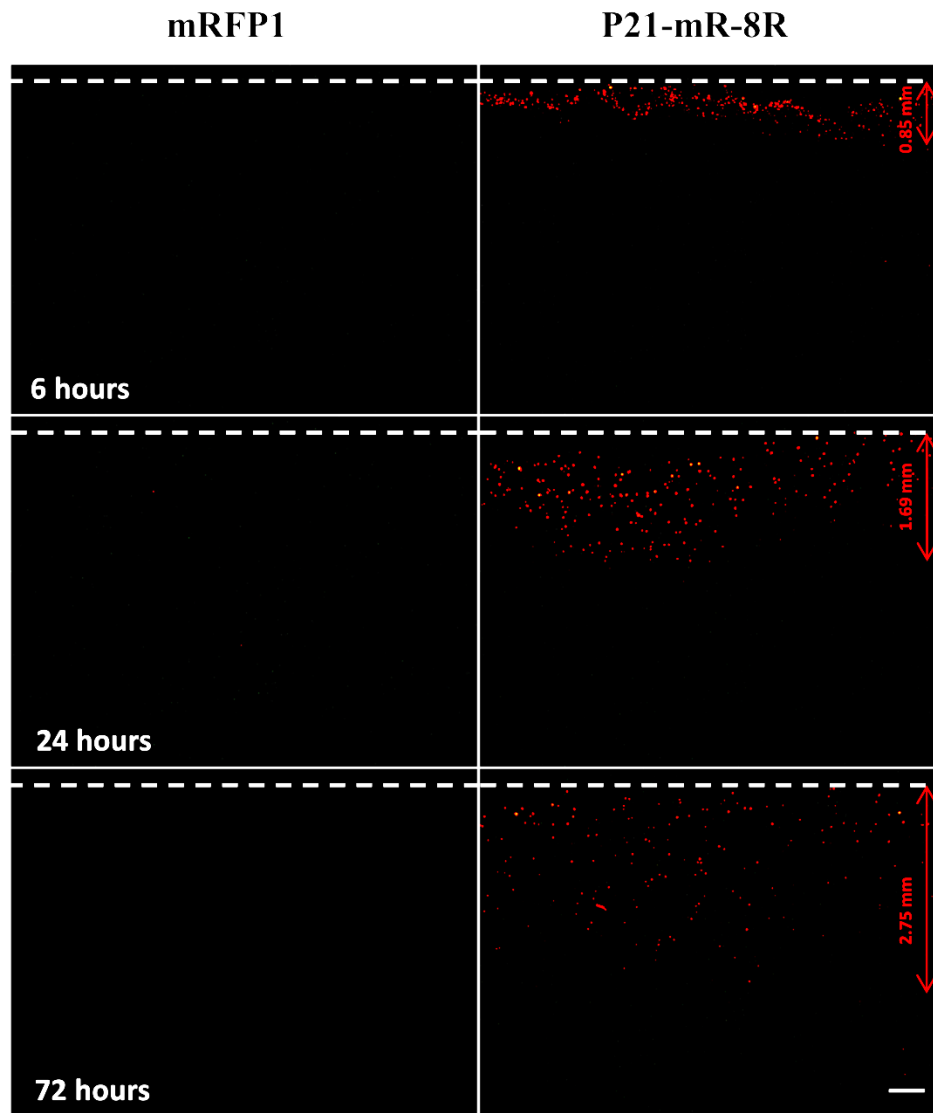


Figure 61: Fluorescence microscope images of cross sections of the cellular hydrogels sliced parallel to the direction of the protein flow: non-transducing mRFP-1 (left) and cell penetrating P21-mR-8R (right). Red dots represent transduced cells. Dashed lines represent the border between the hydrogel scaffold and the protein source (scale bar=0.5 mm).

5.4.5. Gradient intracellular transduction

In order to get a valid estimate of the amount of positively transduced cells as a function of distance inside the scaffolds, flow cytometry was employed. Controls of monolayer of NIH 3T3 mouse fibroblasts (duplicate) including non-labelled cells & cells exposed to mRFP-1 or P21-mR-8R for 1 day were initially assessed for their entrapped red fluorescence intensity using flow cytometry. These controls were treated with Hoechst 33342 to visualize the nucleus. The red and blue fluorescence intensities were accordingly monitored as shown in Figure 62. The upper right quadrants were used to evaluate the positively transduced cells where cells were labelled with red fluorescent proteins as well as the nuclei which were labelled with the blue fluorescent Hoechst 33342.

Applying the hydrogel digestion protocol described in 2.2.9, mouse fibroblasts were freely flowing in liquefied hydrogel slices. Fluorescence intensity in mouse fibroblasts retrieved from successive liquefied hydrogel slices as a function of distance away from source compartments were used to evaluate the gradient intracellular transduction of different test proteins. The percentages of gated cells in the upper right quadrants are displayed for each slice in different scaffolds (Figure 63). The percentages were low in slices comprising scaffolds exposed to culture medium and relatively higher for scaffolds exposed to mRFP-1 & P21-mR-8R respectively. The percent of gated cells were high for all slices of the scaffolds through which P21-mR-8R diffused at days 1 & 3. Hydrogel slices retrieved from scaffolds exposed to mRFP-1 exhibited gradual decrease of the percent of gated cells as a function of distance away from source on day 1. The trend was maintained at day 3, yet with higher percentages for all hydrogel slices. Figure 64 shows representative dot plot fluorescent responses of cells retrieved from hydrogel slices as a function of distance away from source compartments containing control culture medium, mRFP-1 or P21-mR-8R respectively. Levelled minimal red fluorescent intensities in slices comprising control scaffold were observed in the upper panel. The middle panel shows mRFP-1 scaffold with levelled red fluorescent intensities in the distant 4 slices and relatively higher red fluorescence intensity measured in cells comprising the first slice. The fluorescence intensities measured in cells retrieved from scaffolds where mRFP-1 diffused were comparable to their equivalents in scaffolds exposed to plain culture medium. On the other hands, scaffolds which were exposed to P21-mR-8R (lower panel) show gradient cellular uptake of the

red fluorescent protein across the hydrogel width. This was further confirmed by histograms of red fluorescence intensities as a function of distance away from source compartments displayed in Figure 65. The lower panel shows a gradual shift of the mean red fluorescence intensities towards lower values as a function of distance away from P21-mR-8R. In contrast, cells retrieved from different slices in the control scaffold or the mRFP-1 exhibited comparable fluorescence intensities with very slight shifts in the relevant histograms.

The effect of the diffusing species and the distance away from source compartments is shown in Figure 66. Cells retrieved from hydrogels through which mRFP-1 or blank culture medium diffused, display equal fluorescence intensities all over the scaffold width at different time points. On contrary, cells from scaffolds through which the P21-mR-8R diffused showed gradual decrease in fluorescence intensity as a function of distance. Significantly higher fluorescence values were measured for scaffolds exposed to P21-mR-8R as compared to those exposed to control culture medium or mRFP-1 at each slice position for each time point. The effects of diffusing species and the distance inside the scaffold and their interaction were highly significant ($p < 0.0001$) on the intracellular transduction as represented by the mean red fluorescence intensity per cell. Images of the liquefied hydrogel slices collected from scaffolds through which blank culture media, mRFP-1 or P21-mR-8R at day 1 and day 3 are shown in Figure 67 & Figure 68 respectively. Cells in the liquefied hydrogel slices through which blank culture media and mRFP-1 diffused did not show any red fluorescence signal. In contrast, scaffolds where mRFP-1 diffused showed minimal to negligible red fluorescence from cells. However, the liquefied hydrogel itself showed gradual decrease in the fluorescence intensity emerging from the hydrogel matrix as a function of distance on day 1 (Figure 67A) and relatively equal values of fluorescence intensity on day 3 (Figure 68A). Using ImageJ software, the brightness and contrast of the images were adjusted to remove the hydrogel background reading and limit the fluorescence within cells (higher values) as shown in Figure 67B & Figure 68B respectively.

In case of scaffolds through which P21-mR-8R diffused for 1 day, high red fluorescence intensity from cells was observed as well as background hydrogel for the first hydrogel slice with gradual decrease of the overall signal over subsequent slices. At day 3, the signals retrieved from cells in the first three slices were relatively higher than successive slices and the signal gradually decreased further in the scaffold away from the source.

Semi-quantitative fluorescence microscopy image analysis using ImageJ software (Figure 69) was performed on the crude images displayed in Figure 67A & Figure 68A. The mean red fluorescence shown in the upper panel was gradually decreasing as a function of distance on days 1 and 3 matching the trends shown earlier. The lower panel shows the relatively low variation of fluorescence signal for the mRFP-1 scaffold as compared to higher variation in case of P21-mR-8R at different time points. The standard deviation of the mean red fluorescence intensity for mRFP-1 was gradually decreasing as a function of distance away from source on day 1 and a plateau response of minimal variation was observed on day 3. This was unlike the gradual trend maintained on both time points for images following P21-mR-8R diffusion.

A collective comparison of the effect of all test proteins on the 3D intracellular transduction is shown in Figure 70 & Figure 71. The percentages of gated cells in the upper right quadrants are displayed for each slice in different test scaffolds (Figure 70). The percentages were high for all scaffolds through which different test proteins diffused on days 1 and 3 respectively. Similar to mRFP-1, minimal fluorescence uptake by the cells was observed following diffusion of the cell binding P21-mR. Meanwhile, the cell penetrating peptide mR-8R behaved similar to P21-mR-8R and maintained similar spatial trend showing gradual intracellular transduction as a function of distance. However, the gradual intracellular transduction following P21-mR-8R was significantly higher than the corresponding mR-8R transduction over 24 hours and 72 hours. This was furtherly confirmed by fluorescence microscopy of the red and blue fluorescent signals as a function of distance away from source proteins displayed in Figure 72 & Figure 73.

5.5. Discussion

5.5.1. 2D intracellular transduction

Green fluorescent proteins and their other coloured variants have been widely used as reporter proteins for tracking gene expression and protein localization in a variety of cell types [117, 217]. Campbell et al. introduced mRFP-1 as a colour variant permitting multicolour tracking of fusion proteins with a further advantage over green fluorescent proteins minimizing the eukaryotic cells autofluorescence at longer wave lengths [117].

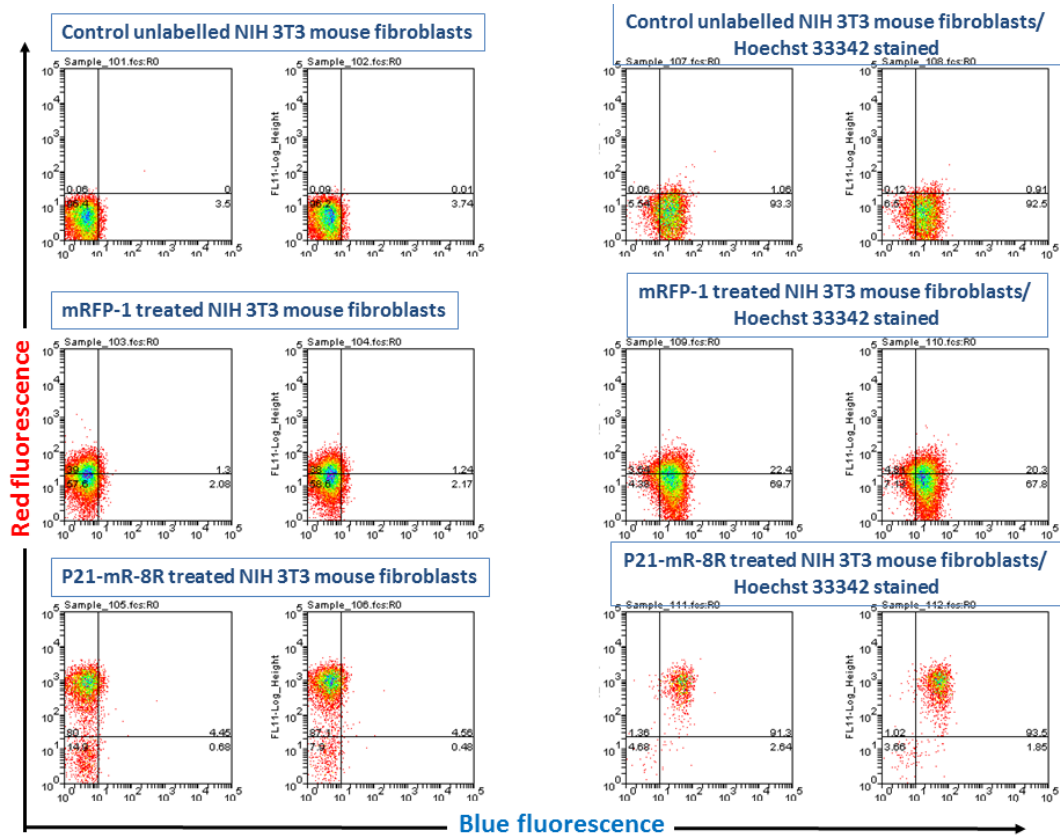


Figure 62: Flow cytometric analysis (dot plot) of monolayer of NIH 3T3 mouse fibroblasts cells exposed to 50 $\mu\text{g}/\text{mL}$ mRFP-1 or P21-mR-8R for 1 day with or without Hoechst 33342 staining.

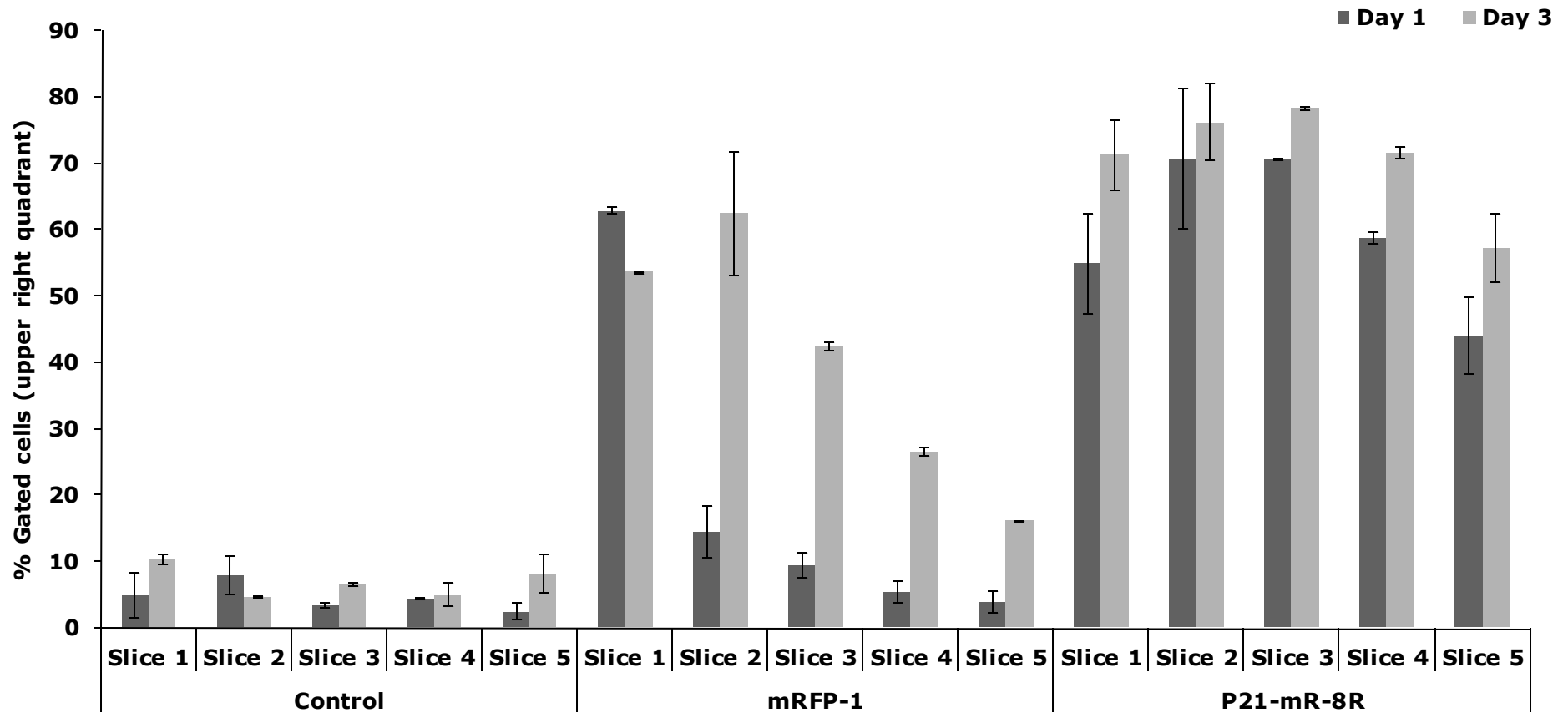


Figure 63: % Gated cells (upper right quadrant; double stained for red (mRFP-1) and blue (Hoechst 33342) fluorescence) from total cells examined per slice using flow cytometric analysis following diffusion of control culture media, non-transducing mRFP-1 and P21-mR-8R through cellular (NIH 3T3 mouse fibroblasts, 2×10^6 /mL) gelatin/agarose hydrogels at days 1 & 3. Data shown are representative of a single independent experiment and are represented as the mean ($n=2$) \pm standard deviation.

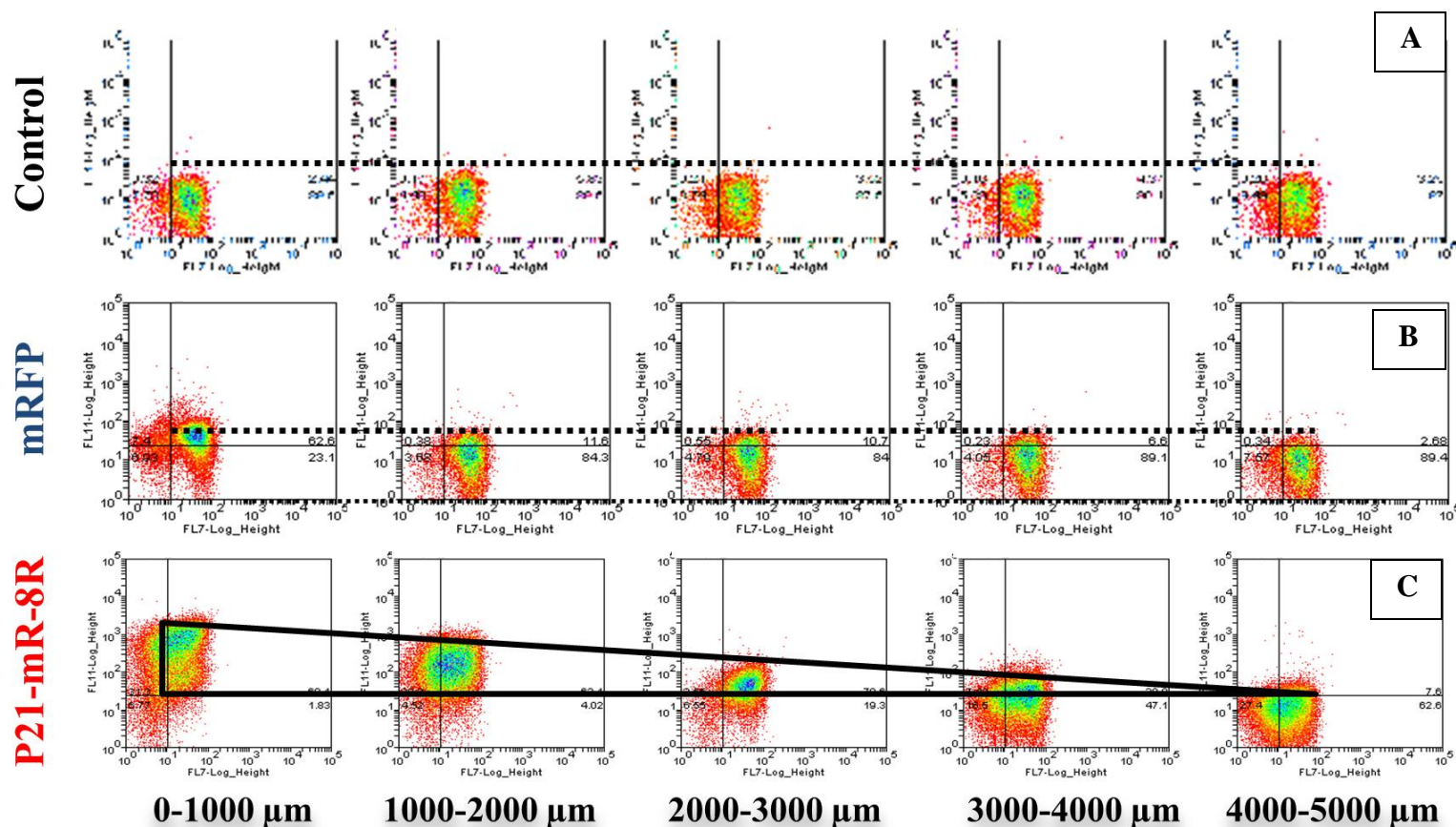


Figure 64: Flow cytometric analysis (dot plot) of cells retrieved from digested gel slices as a function of distance away from source protein following 1 day of protein diffusion. **A:** levelled minimal red fluorescent intensities (upper right quadrants) in slices comprising control scaffold (upper panel). **B:** mRFP-1 scaffold showing levelled fluorescent intensities for the last 4 slices with the first slice slightly higher. **C:** P21-mR-8R scaffold (lower panel) showing gradient cellular uptake of the red fluorescent protein across the hydrogel width. Dot plots shown are representative of a single set of scaffolds of a duplicate experiment.

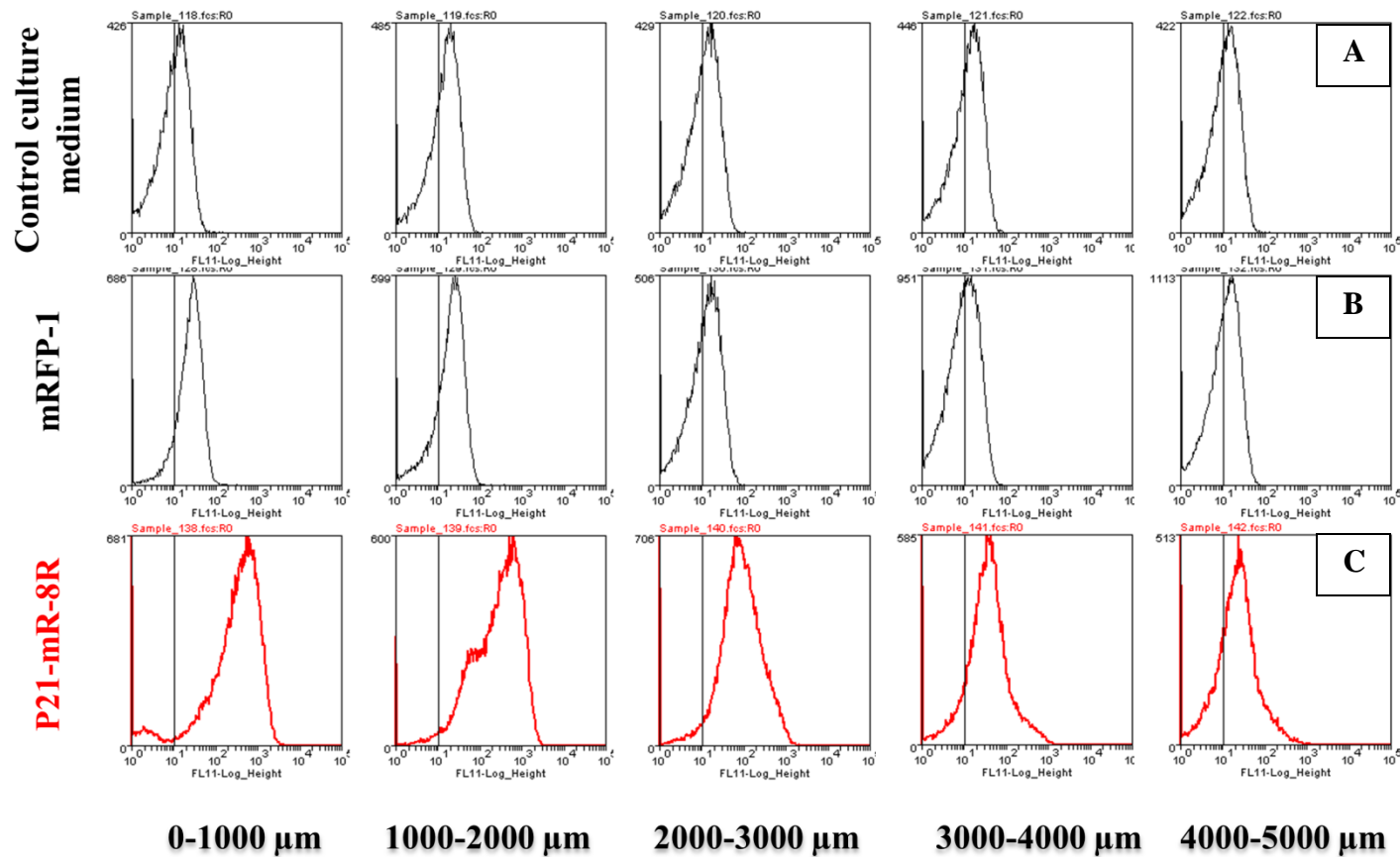


Figure 65: Flow cytometric analysis (histogram) of cells retrieved from digested gel slices as a function of distance away from source protein following 1 day of protein diffusion showing frequencies of number of gated cells in slices comprising A: control culture medium scaffold. B: mRFP-1 scaffold C: P21-mR-8R scaffold. Histograms shown are representative of a single set of scaffolds of a duplicate experiment.

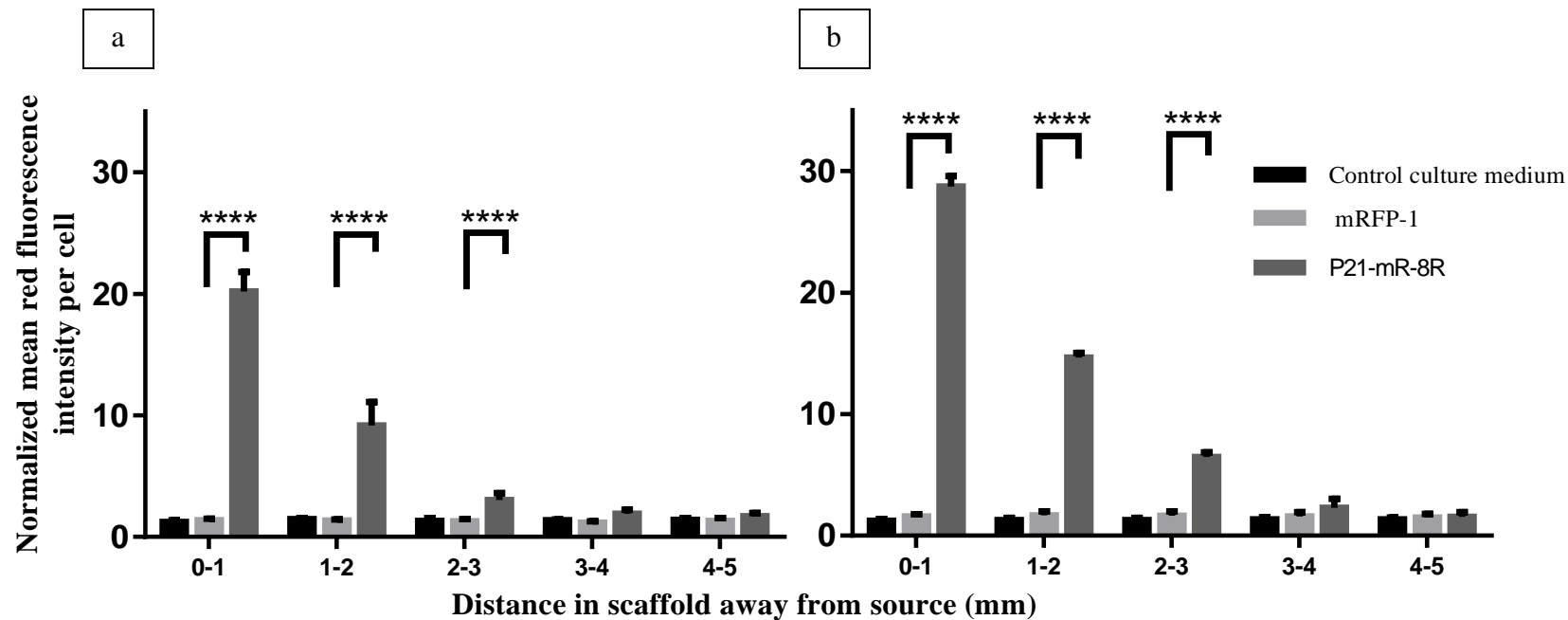


Figure 66: Intracellular fluorescent gradient profiles following control media, non-transducing mRFP-1 and P21-mR-8R diffusion through cellular (NIH 3T3 mouse fibroblasts, 2×10^6 /mL) gelatin/agarose hydrogels using flow cytometry analysis: (a) 24 hours and (b) 72 hours. Data were normalized to the mean fluorescence intensity per monolayer of cells (1×10^6) exposed to $50 \mu\text{g/mL}$ mRFP-1 for 24 hours. Data are represented as the mean of three independent experiments ($n=3$) \pm standard deviation.

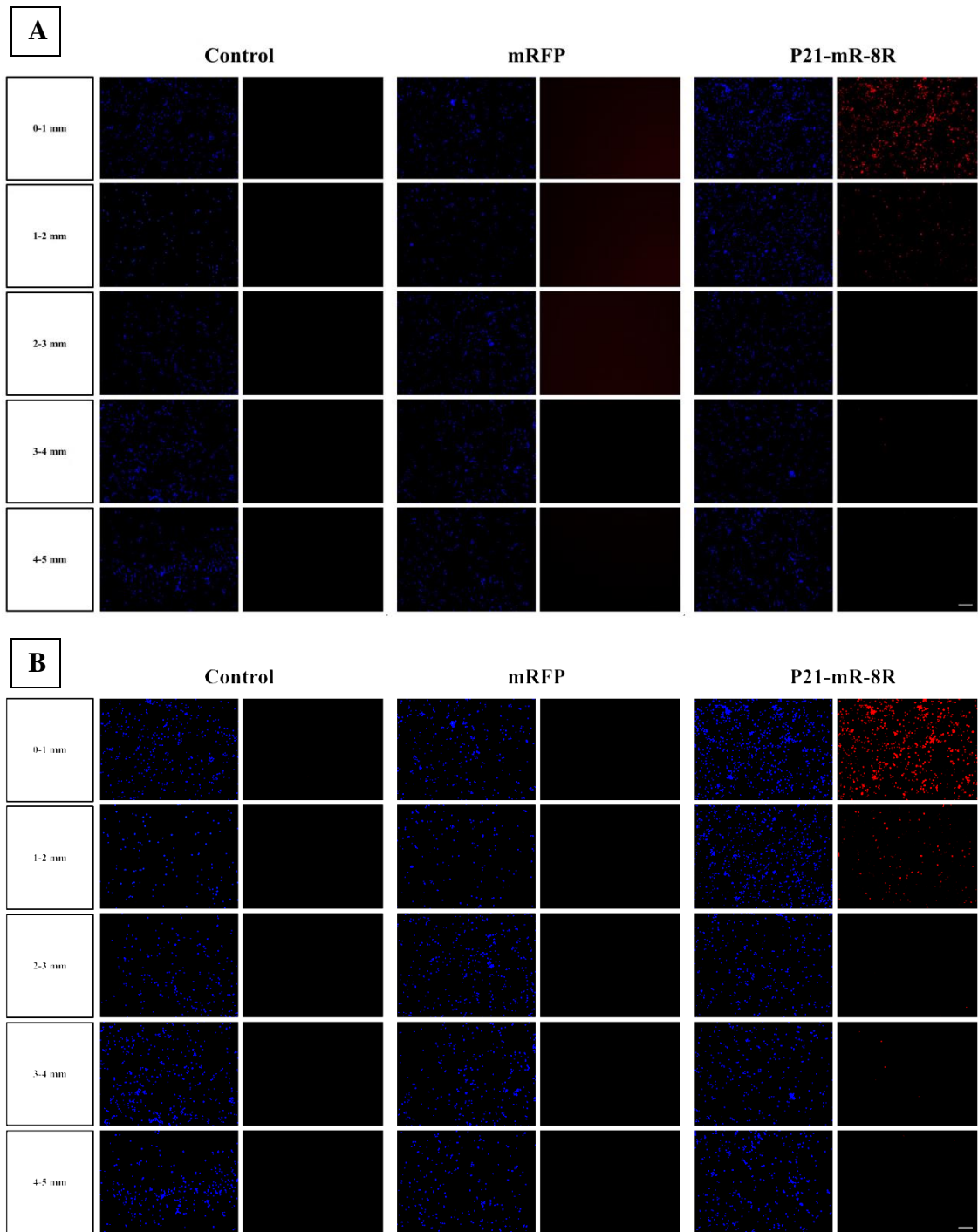


Figure 67: Representative fluorescence microscopy images of digested hydrogel slices retrieved from cellular scaffolds (NIH 3T3 mouse fibroblasts, $2 \times 10^6/\text{mL}$) exposed to media, mRFP-1 or P21-mR-8R respectively on day 1. Hoechst 33342; blue (left) and red fluorescent protein; red (right), scale bar = 100 μm . A: crude images & B: enhanced contrast images using ImageJ software.

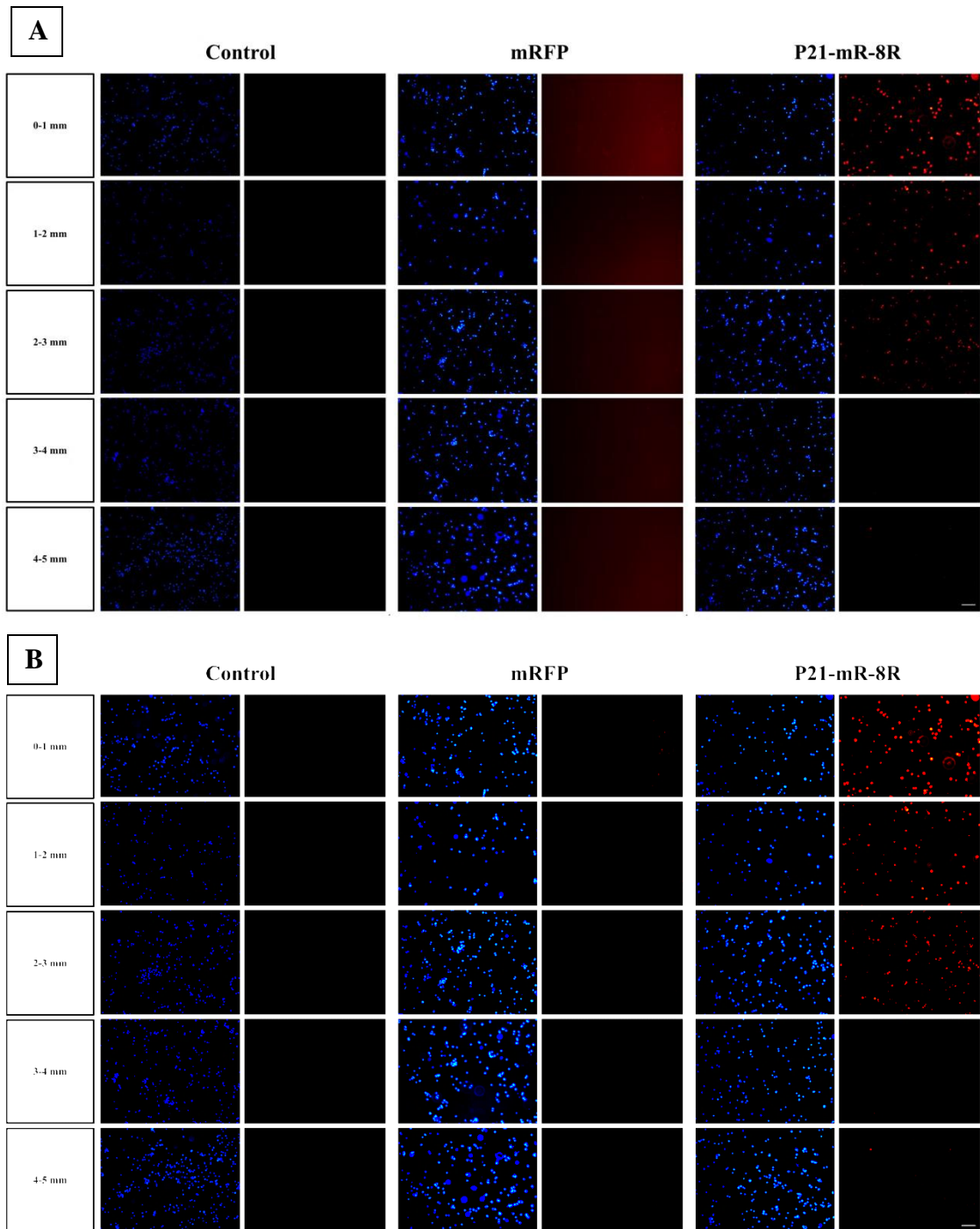


Figure 68: Representative fluorescence microscopy images of digested gel slices retrieved from cellular scaffolds (NIH 3T3 mouse fibroblasts, 2M/mL) exposed to media, mRFP-1 or P21-mR-8R respectively on day 3. Hoechst 33342; blue and red fluorescent protein; red, scale bar = 100 μ m. A: crude images & B: enhanced contrast images using ImageJ software.

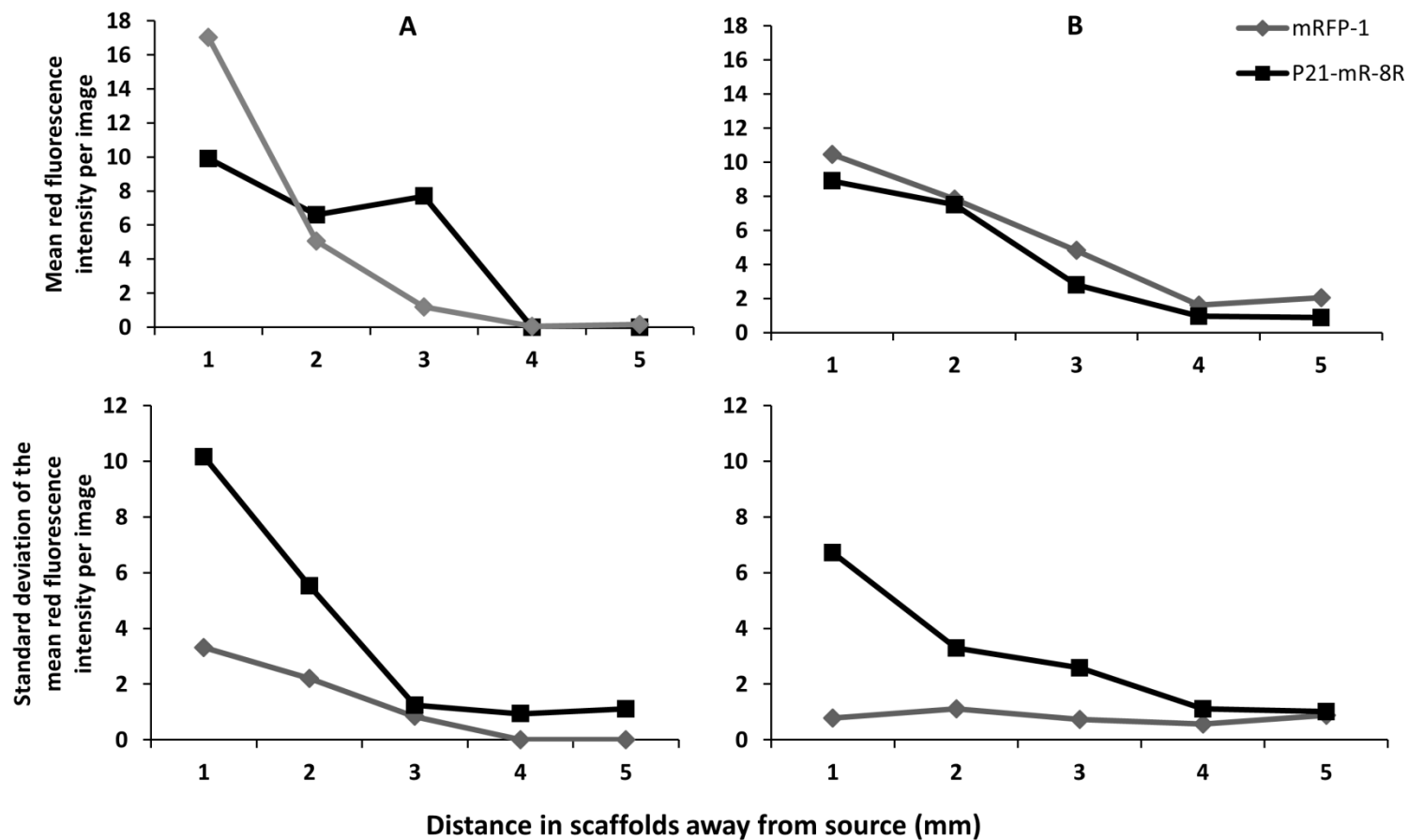


Figure 69: Image analysis of the fluorescence intensity of the liquefied gels retrieved as a function of distance away from source proteins using ImageJ software. Representative image analysis of liquefied hydrogels exposed to mRFP-1 or P21-mR-8R (50 $\mu\text{g}/\text{mL}$) for A: 24 hours or B: 72 hours showing the mean red fluorescence intensity per image (upper row) and the standard deviation of the mean red fluorescence intensity per image (lower row).

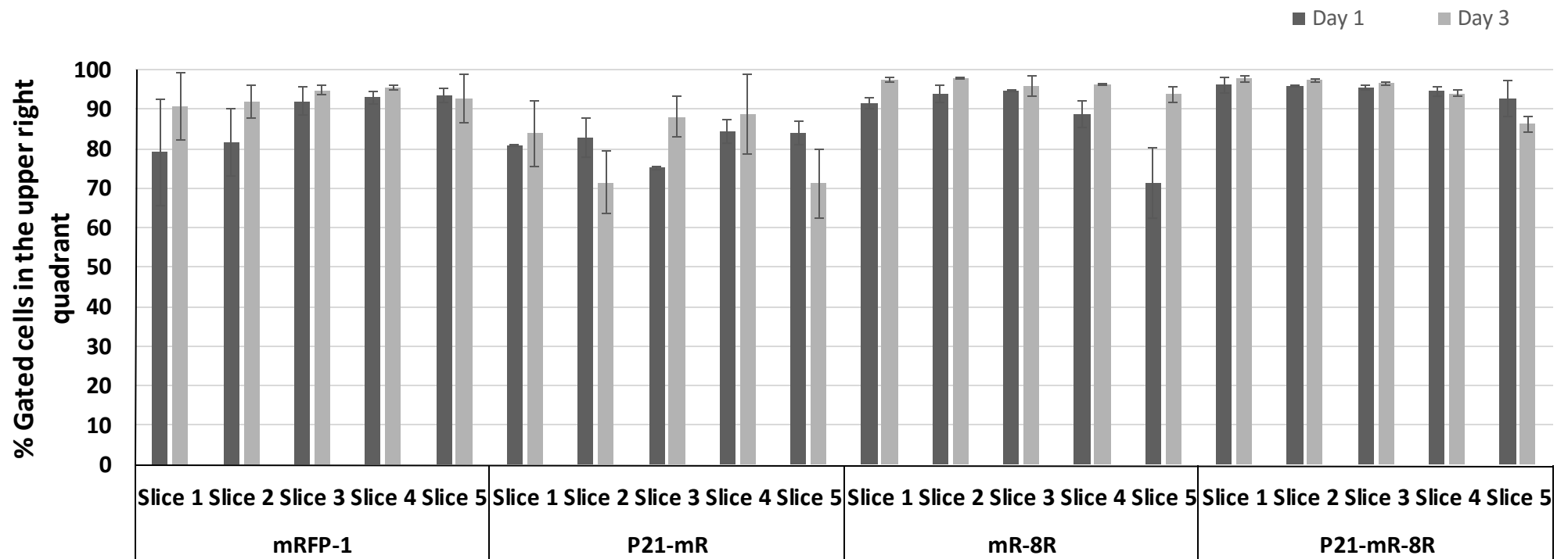


Figure 70: % Gated cells (upper right quadrant; double stained for red (mRFP-1) and blue (Hoechst 33342) fluorescence) from total cells examined per slice using flow cytometric analysis following diffusion of non-transducing mRFP-1, P21-mR, mR-8R and P21-mR-8R through cellular (NIH 3T3 mouse fibroblasts, 2×10^6 /mL) gelatin/agarose hydrogels at days 1 & 3. Data shown are representative of a single independent experiment and are represented as the mean ($n=2$) \pm standard deviation.

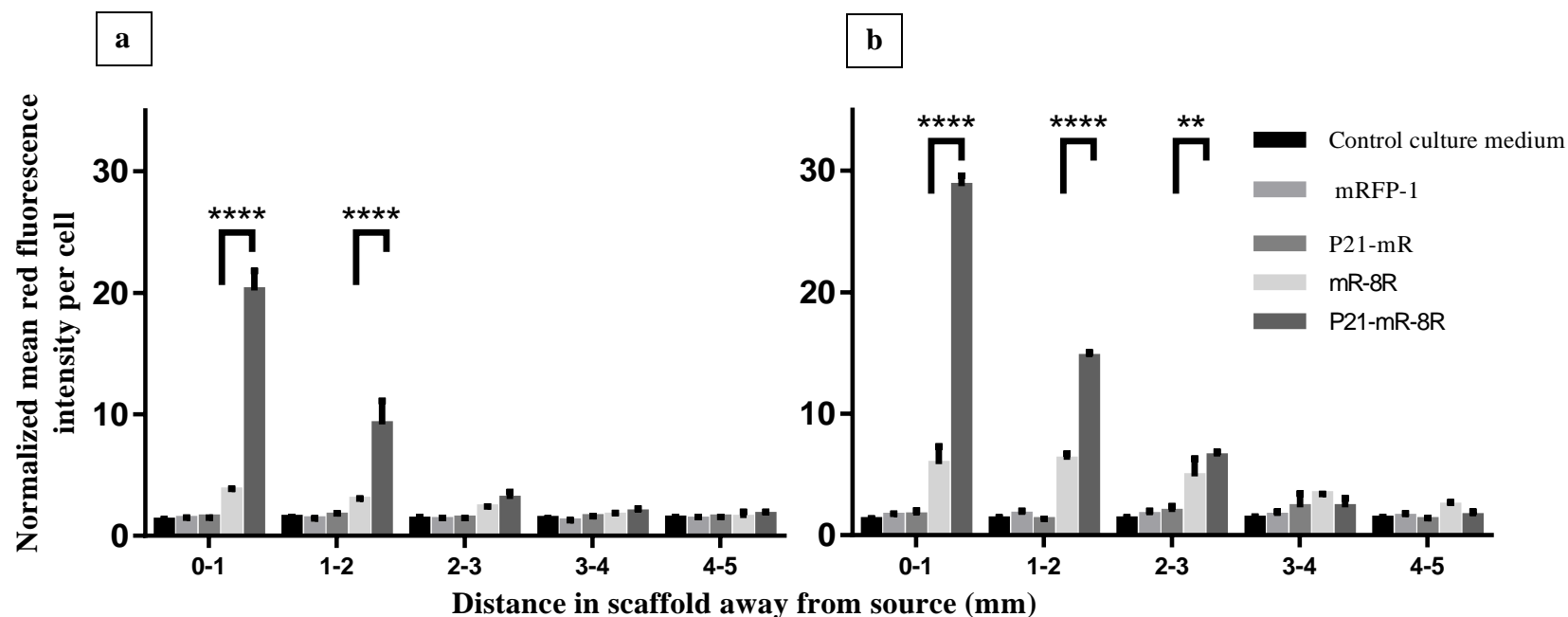


Figure 71: Intracellular fluorescent gradient profiles following control media, non-transducing mRFP-1, P21-mR, mR-8R and P21-mR-8R diffusion through cellular (NIH 3T3 mouse fibroblasts, 2×10^6 /mL) gelatin/agarose hydrogels using flow cytometry analysis: (a) 24 hours and (b) 72 hours. Data were normalized to the mean fluorescence intensity per monolayer of cells (1×10^6) exposed to $50 \mu\text{g/mL}$ mRFP-1 for 24 hours. Data are represented as the mean ($n=3$) \pm standard deviation.

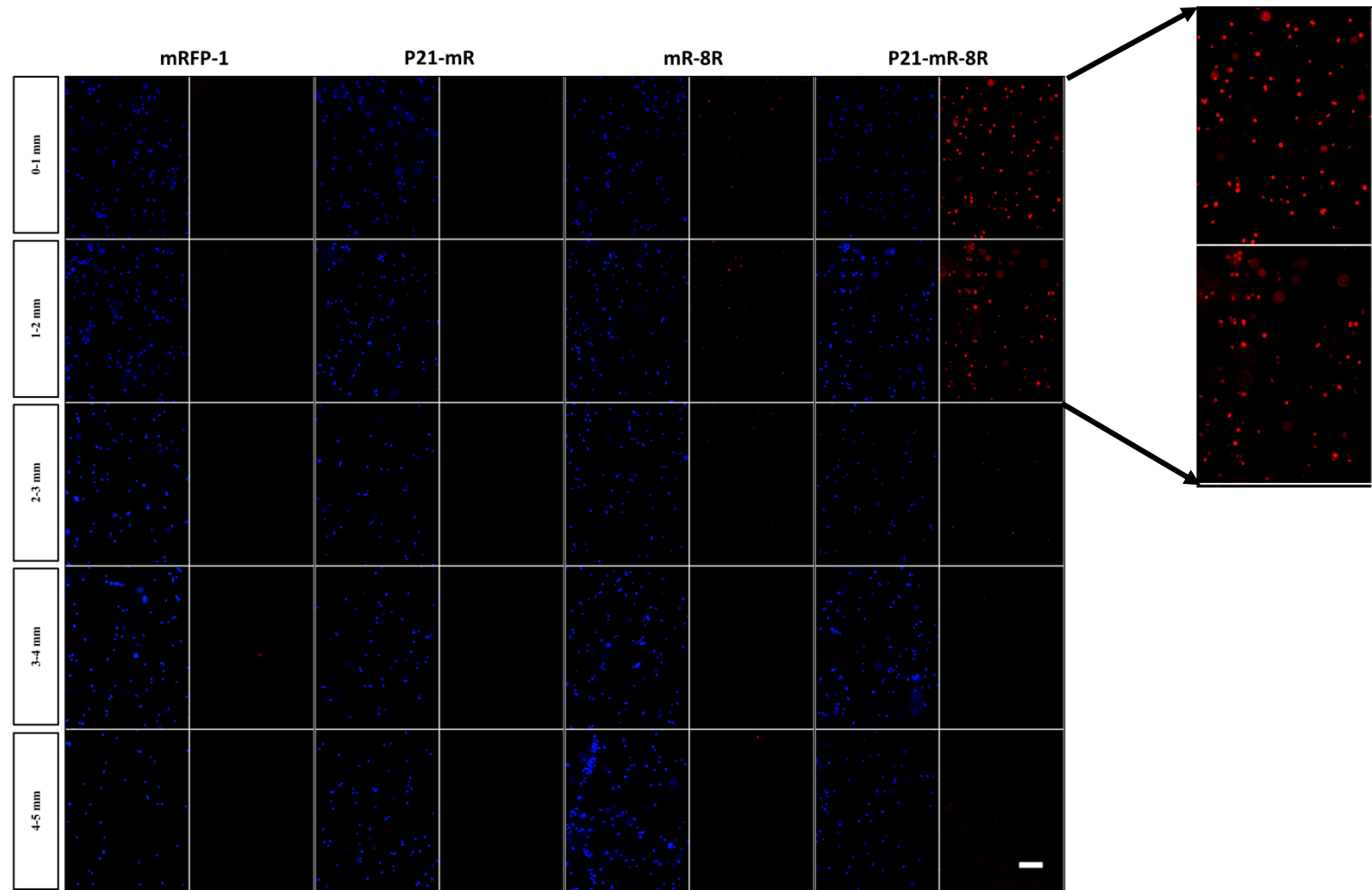


Figure 72: Representative fluorescence microscopy images of digested gel slices retrieved from cellular scaffolds (NIH 3T3 mouse fibroblasts, 2M/mL) exposed to media, mRFP-1, P21-mR, mR-8R or P21-mR-8R respectively on day 1. Hoechst 33342; blue and red fluorescent protein; red, scale bar = 100 μ m.

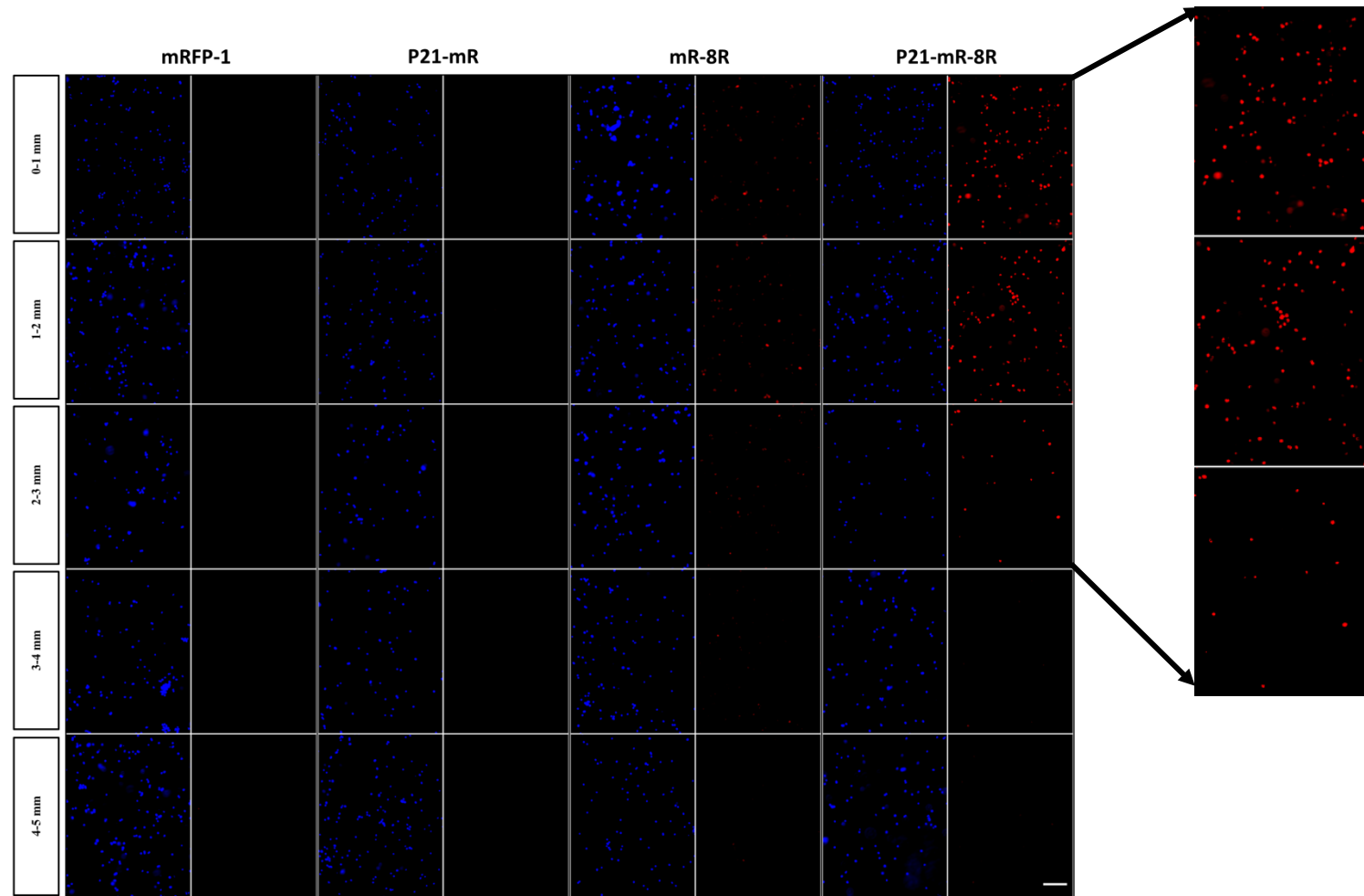


Figure 73: Representative fluorescence microscopy images of digested gel slices retrieved from cellular scaffolds (NIH 3T3 mouse fibroblasts, 2M/mL) exposed to media, mRFP-1, P21-mR, mR-8R or P21-mR-8R respectively on day 3. Hoechst 33342; blue and red fluorescent protein; red, scale bar = 100 μ m.

Comparing the effect of P21-mR-8R to that of the reporter red fluorescent protein on mouse fibroblasts revealed the transducing potential of P21-mR-8R at all test time points. The inclusion of both P21- and 8R resulted in synergistic enhancement of mouse fibroblasts transduction [118]. There was a trend of increasing transduction magnitude of P21-mR-8R with time until 24 hours and thereafter there was a drop in fluorescence intensity detected in cells at 48 and 72 hours. This was attributed to the presence of two cellular sub-populations at 48 & 72 hours corresponding to cell doubling and the presence of younger cells with smaller size [218]. Younger cells tend to incorporate smaller amounts of red fluorescent proteins and this may result in a shift in the mean fluorescence intensity per cells towards lower values.

P21-mediated transduction was more than six-orders of magnitude more efficient than mR-8R at 24 hours. However, this value was around two orders of magnitude at 72 hours. The enhanced transduction can be attributed to stimulation of cell binding interactions via P21. The enhanced cell surface binding permitted longer exposure periods of mouse fibroblasts to P21-mR-8R with efficient delivery of the reporter fluorescent protein cargo via the cell penetrating poly-arginine moieties. GAG binding was important for enhancing the lipid-bilayer translocation, yet, it has been mentioned that it is not essential for its existence [219].

5.5.2. Cellular health in 3D hydrogel systems

Mass transport and nutrient exchange limitations often result in cell necrosis in large 3D scaffolds. For this reason, it was important to study the effect of the hydrogel matrix and dimensions on the cellular viability and proliferation.

Agarose hydrogels are known for supporting encapsulation of cells with maintenance of the viability at low concentrations <0.3% w/v [220] while in high concentrations it could hinder the nutrients and waste transport especially in large dimensions scaffolds. Agarose as such does not support cellular attachment and often requires combinations with other hydrogels like collagen to provide attachment sites for anchorage-dependent cells. However, cells encapsulated in agarose hydrogels were still able to secrete their own ECM [221]. On the other hand, gelatin was added to improve cell attachment and proliferation in agarose matrices [148]. This could explain the superiority of gelatin containing scaffolds in maintaining higher fibroblasts viabilities. However, nutrient consumption from the external media resulted in decreased viability on day 2 in scaffolds dispensed in PBS similar to what was previously reported in 3D agarose

matrices [222]. On the other hand, systems prepared in DMEM showed better viability on day 2 that was reduced on day 3 due to consumption of nutrients from the external source and the hydrogel composition together with waste accumulation. Similar results were reported for AML-12 murine hepatocytes encapsulated within 1 cm thick 3% agarose slabs in a microfluidic channel system. The effect of PBS or culture medium flow on the overall viability as well as the viability as a function of distance away from channel was studied. The flow of culture medium across the agarose slab maintained 55% viability over day 3 as compared to 15% and 10% when PBS was allowed to flow or no fluid flow was allowed respectively. The distance away from channel was found to be significantly affecting the cell viability due to diffusion limitations within agarose matrix to cells embedded at larger distances from the microchannel [221].

Cellular proliferation in different hydrogel systems assessed using Prestoblu[®] confirmed the aforementioned results. The cellular proliferation was ceased or slightly dropped at later time points possibly because of the nutrients transport and waste removal limits. In order to measure protein diffusion without manipulation, the source/sink compartments were not changed over the 3-days experiment. This might have contributed to the reduced proliferation as a function of time as the nutrients in the culture medium comprising the sink compartment and the dispensing liquid of the test protein in the source compartment were not replenished.

Prestoblu[®] proliferation assay depends on the reducing power of living cells to the resazurin-based solution turning it to a highly fluorescent compound. This, accordingly, means that the test relies on the diffusive power of the non-fluorescent resazurin compound across the cell-laden hydrogel scaffold and the back diffusion of the fluorescent resazurin-reduced compound to be measured. Optimization of the incubation period of Prestoblu[®] reagent was performed and 6-hours incubation was selected to guarantee that the fluorescence was no longer changing. For this reason, the proliferative potential of mouse fibroblasts in the selected gelatin/agarose system was examined using a different proliferation assay. Cyquant[®] NF proliferation assay, which mainly depends on the DNA content, was used to assess the proliferation of cells within 3D gelatin/agarose in comparison to their proliferation in monolayer. The trend that was found using Prestoblu[®] assay was as well observed for Cyquant[®] NF proliferation assay suggesting the validity of the previous results.

5.5.3. Gradient 3D protein Delivery Gradient

The compartmental diffusion model introduced in chapter three was employed to study the gradient delivery of GET proteins. The presence of cells was investigated to decide whether it affected the fluorescence intensity measurements for protein loaded hydrogel slices and it did not alter the fluorescence responses of each specific protein concentration. This suggests that the cells exhibit no autofluorescence and that the cellular uptake during the preparation is kept negligible to minimal.

Unlike diffusion studies conducted in chapter 3, there was no continuous replenishment of source/sink compartments. The objective was to study the progressive diffusion of proteins with time and to assess the subsequent effects on cells. There was no point to pay more efforts to maintain a stable gradient via continuous change of source/sink compartments with fresh solutions. A seamless contact between the cell-laden hydrogel and the mould was achieved to ensure that there was no leakage between the source and sink. This was further confirmed by temporal monitoring of protein concentrations in the source and sink compartments. Continuous increase in sink protein concentrations accompanied with decrease in protein source concentrations with time suggests that the protein received in the sink compartment was diffusing through the hydrogel matrix. Furthermore, this suggests that the increase/decrease of the sink/source compartments was accompanied by an increase of the amounts of proteins within the hydrogel over time.

The diffusion profiles of mRFP-1 across cellular and acellular hydrogel scaffolds were comparable at each time point. This suggests that fluorescent signal detected was retrieved from the freely diffusible mRFP-1 in the hydrogel and with minimal contribution to cellular uptake. This finding was further confirmed by applying a washing protocol on cellular hydrogel scaffolds through which mRFP-1 diffused. The washing protocol that included immersion in aqueous PFA & sucrose solutions should remove any freely bound proteins in the hydrogel matrix and only fluorescent signals from transduced cells could be visible. No fluorescent signals were observed either from the hydrogel nor from the cells in scaffolds through which mRFP-1 diffused. On the other hand, the presence of cells in cellular scaffolds altered the temporal diffusion gradients observed in equivalent acellular scaffolds through which P21-mR-8R diffused. This suggests that the gradient observed was due to signals obtained from hydrogels and cells. Fluorescence microscopy images of scaffolds width following

diffusion of P21-mR-8R at different time points supported this finding. The width of the hydrogel bands with red fluorescence signals was increasing and was in good correlation with the characterization of the gradients measured by the fluorescence intensity of the sliced sections. This implies that the cells were positively transduced with the GET model protein. These findings suggest that the key factors regulating diffusion of mRFP-1 through gelatin/agarose hydrogels were governed by the size and interaction filtering strategies described earlier by Lieleg and Ribbeck [135] and not due to the presence of cells.

The reporter mRFP-1 has a theoretical molecular weight of 26.6 kDa and isoelectric point; pI of 5.66 based on the amino acid sequence comprising it [216]. These values were reported practically to be 32kDa and pI of 4.5 [117] implying that the protein will carry a net negative charge in agarose-gelatin hydrogel scaffold as the hydrogel was dispensed in culture medium adjusted to the physiological pH. On the other side, P21-mR-8R has a theoretical molecular weight of 30.7 kDa and pI of 9.59 [216] and this implies that the protein acquires a slight positive charge at pH 7.2. This could explain the relevant retardation of the diffusion of P21-mR-8R in comparison to that of the relatively similar molecular weight mRFP-1. P21-mR-8R was engaged in an ionic interaction with the negatively charged hydrogel resulting in relatively slower diffusion. Practically, the zeta potential measurements of both proteins were slightly negative with values of -6.05 ± 0.80 and -10.24 ± 2.00 for mRFP-1 and P21-mR-8R respectively. These values suggest free diffusion of both proteins across gelatin/agarose scaffolds without interaction with the slightly negative hydrogel. Finally, the hydrodynamic radii of both proteins in 10 mM HEPES buffer pH 7.2 were of comparable with values of 4.74 ± 0.97 & 3.76 ± 0.57 nm and were far below the cut off of the mesh size of agarose/gelatin hydrogel practically measured to be 198 ± 7.9 nm.

The expected similarity in the diffusivities of both proteins was further confirmed by the overall diffusion descriptive property namely diffusion coefficient [122]. Practical estimation of the proteins diffusion coefficients using membrane permeation model yielded values of 7.15×10^{-7} & 7.53×10^{-7} cm²/s for mRFP-1 & P21-mR-8R respectively. The values suggest relatively similar diffusion behaviour for both proteins in gelatin/agarose matrices with a slightly faster diffusion for P21-mR-8R.

These overall findings suggest that the cellular uptake of P21-mR-8R depleted the free diffusible protein and demonstrated that the cells themselves acted as sink that retained

the P21-mR-8R adding another factor that controls the diffusion pattern of GET proteins other than the size and interaction filtering strategies. Eventually, this was translated into temporal gradient delivery of GET proteins as a function of distance in cellular scaffolds.

5.5.4. 3D intracellular transduction

The concept of using fluorescence as a threshold for sorting minor subpopulations of cells using flow cytometry was previously reported [223]. In order to rely on the results of the flow cytometric analysis, cells within the liquefied hydrogels were further stained with nucleus stain; Hoechst 33342. This was essential for excluding any undigested hydrogel particles and to only include cellular events which were stained for Hoechst 33342 in the data analysis. Scaffolds through which control culture medium diffused showed minimal number of cells that were counted positively labelled with red fluorescence. This was attributed to the minimal fluorescent value assigned to set the gate between fluorescent and non-fluorescent cells. This gating reflected presence or absence of fluorescence with no impact on the magnitude of fluorescence. The majority of the events were present in the upper right quadrant over both time points and over all the distance points for scaffolds through which the transducing peptide mR-8R and the novel GET protein diffused. However, scaffolds through which mRFP-1 and P21-mR diffused exhibited high percentages of gated cells at all slices. This could possibly be attributed to the presence of the fluorescence protein at the surface of the cells and not being actually inside the cells.

Minimal red fluorescence signals were measured for cells exposed to either mRFP-1 or the culture medium with no significant difference. This implies minimal or no intracellular transduction power of mRFP-1. On contrast, P21-mR-8R showed a 20-fold increase in fluorescence intensity for cells in the first 1 mm next to source as compared to the mRFP-1 on day 1. This difference was amplified to 29-fold increase on day 3. Furthermore, cells encapsulated in scaffolds exposed to P21-mR-8R displayed gradual red fluorescence response on each time point. The overall gradient delivery was enhanced on day 3 as compared to that measured on day 1 as denoted by an increase in the magnitude of the fluorescent signals in all slices. This was different from the situation in monolayer culture which proliferated readily allowing the presence of multiple populations with different sizes and uptake potentials. Agarose based systems

support encapsulation with low proliferative capacities [220]. This allowed the accumulation of fluorescent signals in cells in all hydrogel slices on day 3.

The effect of protein moieties comprising the GET system on the 3D intracellular transduction was as well studied. The cell binding protein behaved like the non-transducing mRFP-1 with minimal levelled fluorescent intensities were detected from cells comprising slices of scaffolds exposed to P21-mR. The values were slightly higher than the mRFP-1 counterparts. This could be due to saturation of the GAG binding sites with the high concentration of test protein used without an efficient sink situation via cell penetration. On contrast, the synergistic combination of poly arginine cell penetrating peptide together with the cell membrane binding peptide; P21 using the GET technology showed significant intracellular transduction in a gradient fashion in comparison to mR-8R equivalents. Although this finding has been previously confirmed on variable kinds of cells in 2D [118], we aimed to prove the feasibility of gradient delivery of the model GET protein through three dimensional hydrogel networks with cells evenly dispersed within.

5.6. Conclusions

The 2D mouse fibroblasts intracellular transduction of the novel GET protein was demonstrated in comparison to its comprising proteins. This success was required to be demonstrated in the more practical 3D hydrogel relevant to the biological environment to which cells are exposed. The compartmental diffusion model with evenly dispersed mouse fibroblasts were used to investigate the 3D intracellular potential of the recently introduced GET protein; P21-mR-8R. The synergistic combination of cell penetrating peptide together with the cell binding peptide using the GET technology showed significant intracellular transduction in a gradient fashion as a function of distance away from source. This enhanced cellular uptake contributed to the factors regulating the diffusive characteristics of bioactive molecules together with the conventional size and interaction considerations. Combing the merits of the novel GET proteins and the compartmental diffusion model, gradient delivery of functional proteins produced via GET technology to cell-laden hydrogels can be achieved. This can be further dedicated to directing cellular response in a gradient manner and controlling tissue fate.

**Chapter 6: Induction of myogenic differentiation
using GAG-enhanced transduction proteins in
3D model**

6.1. Introduction

Muscular dystrophies are progressive myopathies with several genetic profiles and clinical manifestations. Currently, no treatment has been developed for muscular dystrophy due to the shortage of relevant human cellular models for drug screening purposes [224]. Mature skeletal cells are difficult to be expanded in *in-vitro* culture systems and on the other hand, the self-renewing stem cells become activated and differentiate hindering the development of disease-specific cellular models [225].

Skeletal muscle differentiation is governed by a family of four transcription factors known as myogenic regulatory factors (MRFs). MyoD and Myf5 are among the key transcription factors regulating myoblast proliferation and differentiation. However, their roles, during embryogenesis, are superfluous in identifying myogenic progenitors [226]. Growth and regeneration of skeletal muscle occur through satellite myogenic stem cells (SCs) that activate the expression of MRFs; MyoD and Myf5 and subsequently proliferate as myoblasts [227]. In muscle injury, inflammatory cells migrate to the site of injury to clear necrotic debris and induce an immune response that involves the secretion of cytokines; TNF α and IL-6 [228]. These factors activate local SCs to generate new muscle cells with the diagnostic expression of the paired-box transcription factor, Pax7 that in turn results in the expression of MyoD [229]. The muscle regenerative process following myogenesis is complemented with fibrosis and angiogenesis to recreate an environment for muscle growth appropriate for contractile functions [228].

MyoD and Myf5 target genes have been widely utilized in determination of the onset of differentiation. MyoD or Myf5 introduced into a MyoD/Myf5 double-null non-myogenic fibroblast cell line maintained in high serum resulted in their conversion to skeletal muscle. Microarray analysis and real-time PCR recognised differentially regulated genes, indicating equal transcriptional activity of MyoD and Myf5 in the proliferating cells with no unique gene targets. However, MyoD was superior in differentiation markers activation [227].

Strategies of myopathies treatment include genetic manipulation for myocytes regeneration or cell transplantation [230]. Exogenous expression of MyoD is, as well, employed to induce myogenic differentiation in multiple cell types including reprogramming of fibroblasts [230, 231]. Direct injection of β -galactosidase expressing retrovirus with the regulatory gene MyoD into myocardial infarction canine model

resulted in the conversion of cardiac fibroblasts into skeletal fast myosin heavy chain expressing cells[232]. Another study involved the in vivo transduction of adenovirus carrying MyoD into myocardial granulation rat tissues. Expression of myogenin and embryonic skeletal myosin heavy chain with multinucleated myotubes were observed one week following gene transfer [233].

Despite the promise offered by MRFs in treatment of different myopathies, the delivery of transcription factor remains a challenging burden to the process [234]. Low transfection efficiency was observed for gene transfer to infarcted tissues as compared to non-infarcted myocardium. Further concerns about immune responses [235] and higher doses were expressed [230]. An alternative safer strategy is to introduce transcription factors using protein transduction domains. Safety issues arise from permanent alteration of the genome upon gene transfection whilst the protein is degraded in cells upon transduction [236].

From these perspectives and confirming upon the aforementioned findings about the superiority of the novel high efficiency GET system over conventional CPPs [118], we aim at the efficient delivery of the transcription factor MyoD to clinically relevant human cells. Reprogramming cells into the myogenic lineage is studied following the gradient delivery of GET-MyoD in the proposed compartmentalized diffusion model. The efficient gradient delivery of functional proteins can be utilized in the development of complex multicellular organization characteristics of different tissue interfaces.

6.2. Aims & objectives

6.2.1. Aim

The aim of the work presented in this chapter is to recruit the validated diffusion model presented in previous chapters together with the GET technology to guide the myogenic differentiation along the direction of the GET transcription factor MyoD gradient.

6.2.2. Objectives

Research objectives addressed in this chapter included:

1. Development of different cell types of cell-laden hydrogels in compartmentalized diffusion chamber and evaluate their viabilities
2. Development & evaluation of GET-MyoD gradient across cell-laden hydrogels.
3. Evaluation of the gradient myogenic differentiation in 3D hydrogel system.

6.3. Materials and methods

6.3.1. GET protein synthesis

GET MyoD synthesis was performed according to methodology described in section 2.2.4.

6.3.2. 2D intracellular transduction

NIH 3T3 mouse fibroblasts, BJ6 human dermal fibroblasts or HEK 293T embryonic kidney cells were maintained and cultured according to the general cell culture methodology described in section 2.2.1.1, 2.2.1.2 & 2.2.1.3 respectively. To study the intracellular transduction in 2D, cells were cultured on tissue culture plastics, different test proteins were added to the plated cells and the cellular transduction was evaluated as described in section 2.2.4.4.

6.3.3. 2D myogenic differentiation

2D myogenic differentiation was measured following the exposure of BJ6 human dermal fibroblasts or HEK 293T cells to P21-mR-MyoD-8R as explained in section 2.2.10 using polymerase chain reaction.

6.3.4. Cellular viability and proliferation

Cellular viability and proliferation in gelatin/agarose system were evaluated according to methodology described in 2.2.7.

6.3.5. Cell-laden compartmentalized diffusion chamber

Different types of cells maintained as in section 2.2.1 were used to produce cell-laden hydrogels according to details in section 2.2.1.4. Compartmentalized diffusion model was then prepared as in 2.2.8 and diffusion of different test proteins from the source compartment was followed as described in 3.3.4.

6.3.6. Evaluation of temporal protein diffusion gradients

Protein diffusion gradients were evaluated at different time points as detailed in section 2.2.8.5.

6.3.7. Imaging of temporal protein diffusion gradients

See section 2.2.8.6.2

6.3.8. 3D Intracellular transduction across cellular hydrogels

The 3D intracellular transduction following gradient delivery of GET MyoD was monitored as a function of distance and time using flow cytometric analysis following

hydrogel enzymatic/heat digestion. Details of methodology employed are described in section 2.2.9.

6.3.9. 3D gradient myogenic differentiation across hydrogel scaffold

The myogenic differentiation in response to GET MyoD diffusion from the source compartment was measured as a function of distance was measured as explained in section 2.2.10 using polymerase chain reaction.

6.4. Results

6.4.1. NIH 3T3 mouse fibroblasts

The capability of P21-mR-MyoD-8R to transduce a monolayer of mouse fibroblasts was demonstrated in comparison to the non-transducing mRFP-1 as shown in Figure 74 and Figure 75. Comparing the fluorescence intensity in cells exposed to P21-mR-MyoD-8R to those exposed to mRFP-1 shows enhanced uptake of the fluorescence intensity into the cells at all time points. There was an observed increase in the fluorescence intensity in cells exposed to P21-mR-MyoD-8R as a function of time till 24 hours succeeded by a decrease in the fluorescence intensity at 48 and 72 hours. Thorough analysis, revealed the presence of 2 cell populations at the late time points; 48 & 72 hours as shown in the insert of Figure 74.

Figure 76 shows temporal diffusion gradients of P21-mR-MyoD-8R (100 $\mu\text{g}/\text{mL}$) across acellular and cellular (NIH 3T3 mouse fibroblasts) agarose/gelatin scaffolds cast in the compartmental diffusion chamber. Steeper gradients were observed in cellular scaffolds up to 72 hours as compared to equivalent acellular profiles. After 4 days, the diffusion profile of P21-mR-MyoD-8R across acellular scaffolds was relatively equilibrated while partially steep in cellular scaffolds. Figure 77 shows positively transduced cells in scaffold exposed to P21-mR-MyoD-8R at 72 hours.

6.4.2. BJ6 human dermal fibroblasts

The transduction potential of P21-mR-MyoD-8R was investigated in BJ6 human dermal fibroblasts. Figure 78 shows increasing fluorescence intensity up to 6 hours and then remained constant or slightly declined. Applying flow cytometry, the uptake of P21-mR-MyoD-8R (60 $\mu\text{g}/\text{mL}$) was significantly higher than 1-hour uptake of mRFP-1 at all-time points up to 72 hours, whilst, the uptake of mRFP-1 was significant as compared to the control only at 72 hours (Figure 79A). The ability of lower doses of P21-mR-MyoD-8R to transduce BJ6 dermal fibroblasts was investigated in Figure 79B. Similar fluorescence intensity responses were shown for 7.5 and 15 $\mu\text{g}/\text{mL}$ on day 1.

The response slightly increased on day 3 with the higher dose but was not significant from day 1 response neither from the lower concentration. Fluorescence microscope images (Figure 80) confirm on the aforementioned results in Figure 79B.

The viability of dermal fibroblast in large dimensions' agarose/gelatin hydrogels was assessed in comparison to control culture conditions up to 72 hours as shown in Figure 81. Comparable results were observed up to 48 hours, however, the viability dropped to 60% on day 3 for hydrogel encapsulated cells. The proliferation of human dermal fibroblasts in agarose/gelatin hydrogel was investigated as shown in Figure 82. There was no observed increase in proliferation neither for the monolayer nor for the hydrogel system and the normalized fluorescence was intensity relatively kept constant to the value observed at zero time.

The diffusion profiles of P21-mR-MyoD-8R (60 $\mu\text{g}/\text{mL}$) across 1% agarose/gelatin hydrogels with BJ6 dermal fibroblasts (1M/mL) are shown in Figure 83. The steepest gradient was observed at 6 hours and the concentrations across the cellular hydrogel were relatively equilibrated at days 1 and 3. Continuous monitoring of the concentrations of P21-mR-MyoD-8R in the source and sink compartments shown in Figure 84 revealed an increase in the protein content in the sink at 24 hours accompanied with decrease in protein concentration in source compartments.

The intracellular transduction of P21-mR-MyoD-8R (60 $\mu\text{g}/\text{mL}$) into hydrogel encapsulated BJ6 dermal fibroblasts as a function of distance in scaffold away from source protein is shown in Figure 85. Slightly higher uptake of P21-mR-MyoD-8R, as compared to mRFP-1, was observed in the first hydrogel slice at day 1 but not in distant slices. The gradient intracellular transduction profile of P21-mR-MyoD-8R was observed at day 3 and was of higher uptake of the protein into cells at each slice position as compared to the non-transducing mRFP-1.

The ability of P21-mR-MyoD-8R to induce myogenic transdifferentiation in BJ6 dermal fibroblasts in monolayer culture was investigated by following the myogenic differentiation markers; MyF-5 and MyoD on days 1-3 as shown in Figure 86. An increase in the expression of the myogenic differentiation markers in comparison to the house keeping gene β -actin was observed as a function of time with relatively higher expression for MyoD. The insert of the graph shows acceptable values of RNA extracted from different samples in term of quantities, purity and quality of RNA. A dose response curve (Figure 87) was established to investigate the myogenic response of monolayer

cultured BJ6 dermal fibroblasts towards 3-days exposure to increasing concentrations of P21-mR-MyoD-8R. An increase in the myogenic markers expression as a function of increasing concentrations of P21-mR-MyoD-8R was observed with markedly higher expression of MyoD over MyF-5. Cells exposed to control culture medium or mRFP-1 (30 µg/mL) did not show any increase in myogenic markers expression neither for MyF-5 nor MyoD. Table 13 shows the values of RNA extracted from different BJ6 dermal fibroblasts samples exposed to variable concentrations of test proteins. Trials to assess the 3D gradient myogenic differentiation of hydrogel encapsulated fibroblasts were unsuccessful due to failure to extract RNA from fibroblasts as a function of distance away from source proteins (Table 14).

6.4.3. Human embryonic kidney cells HEK 293T cell line

The proliferation of HEK 293T cells in agarose/gelatin system was assessed using CyQuant® NF proliferation assay as shown in Figure 87. Comparable results were shown for the profile of proliferation on day 1 for monolayer culture and 3D hydrogel encapsulated cells. However, on day 3 the proliferation in the hydrogel system was lower than its equivalent in monolayer culture.

The intracellular transduction of P21-mR-MyoD-8R (60 µg/mL) into hydrogel encapsulated HEK 293T cells as a function of distance in scaffold away from source protein is shown in Figure 89. Slightly higher uptake of P21-mR-MyoD-8R as compared to mRFP-1 was observed in all hydrogel slicea at day 1. Cells encapsulated in slice one of the scaffold exposed to P21-mR-MyoD-8R on day 1 was slightly higher to the relatively equal uptake observed in the distant four slices.

The gradient intracellular transduction profile of P21-mR-MyoD-8R was observed at day 3. However, the magnitude of the uptake in hydrogel encapsulated cells was not significantly higher than equivalent cells exposed to mRFP-1 at day 3. Figure 90 & Figure 91 show representative images of cells in liquified hydrogel slices after exposure to culture medium, mRFP-1 and P21-mR-MyoD-8R at days 1 and 3 respectively.

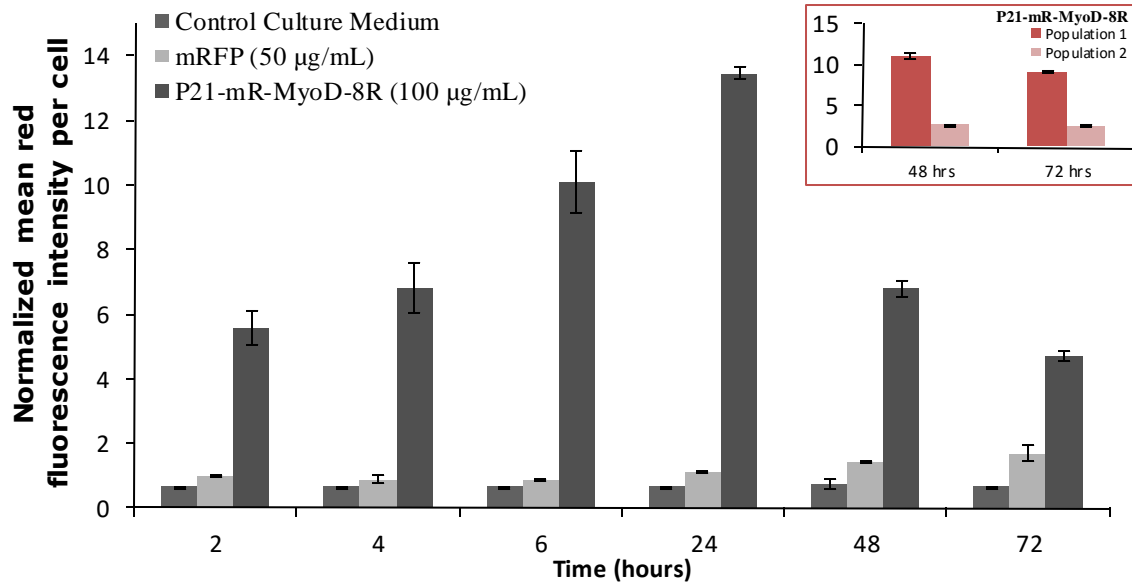


Figure 74: Intracellular transduction of P21-mR-MyoD-8R versus mRFP-1 in NIH 3T3 mouse fibroblasts cultured in monolayer on tissue culture plastic. Mean fluorescence intensity inside cells was quantified using flow cytometric analysis using MoFlo™ DP (DAKO) Flow Cytometer. Data were normalized to the mean fluorescence intensity per monolayer of cells (1×10^6) exposed to 50 µg/mL mRFP-1 for 2 hours. Data are represented as the mean ($n=3$) \pm standard deviation.

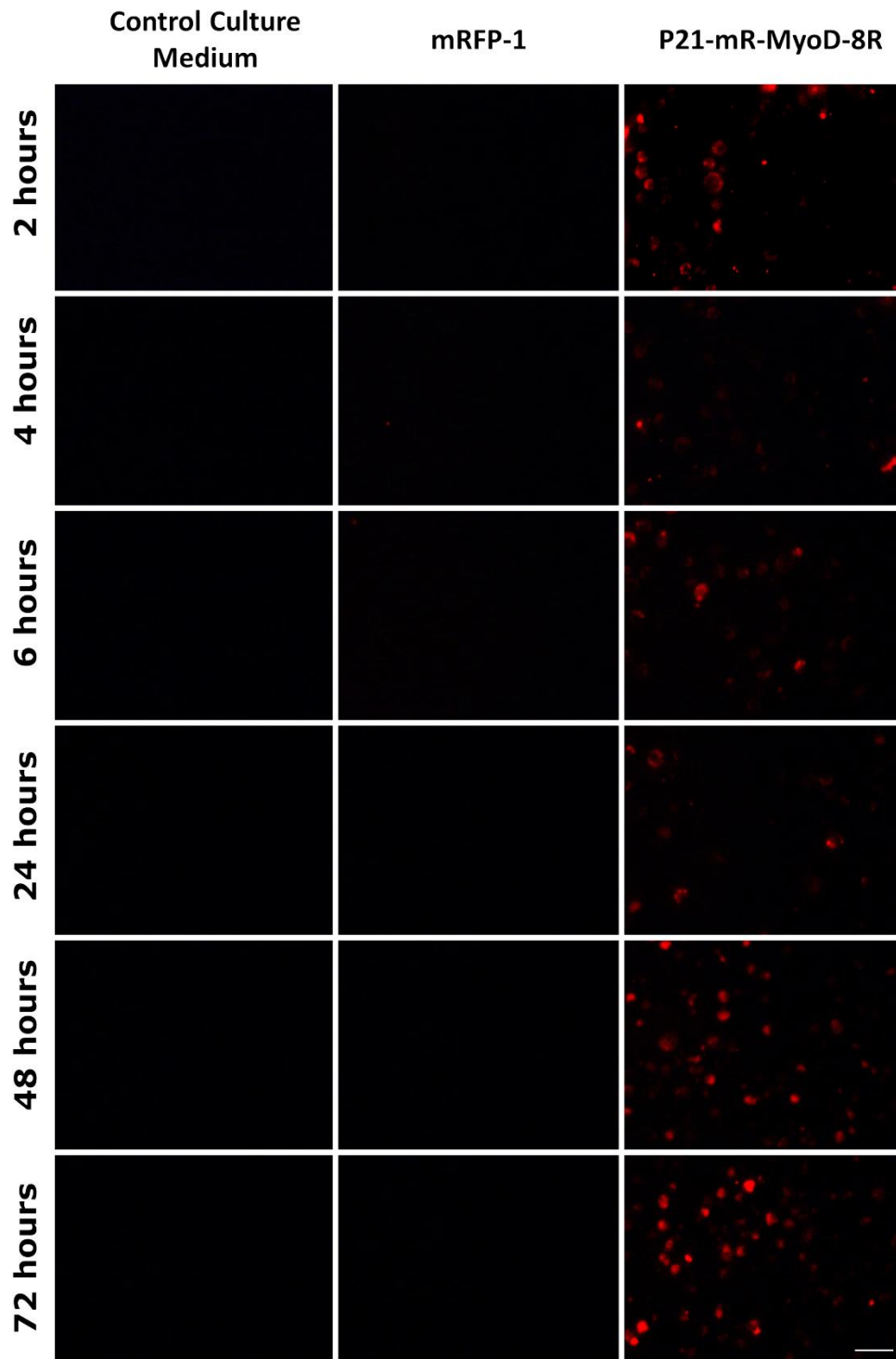


Figure 75: Fluorescence microscopy images of NIH 3T3 mouse fibroblasts exposed to culture medium or 50 $\mu\text{g}/\text{mL}$ mRFP-1 or 100 $\mu\text{g}/\text{mL}$ P21-mR-MyoD-8R at different time points imaged using Leica DM IRB microscope. Cells were detached using Trypsin-EDTA and the mean fluorescence intensity per cells was quantified using MoFlo™ DP (DAKO) Flow Cytometer and samples of cell solutions were subsequently imaged. Scale bar is 100 μm .

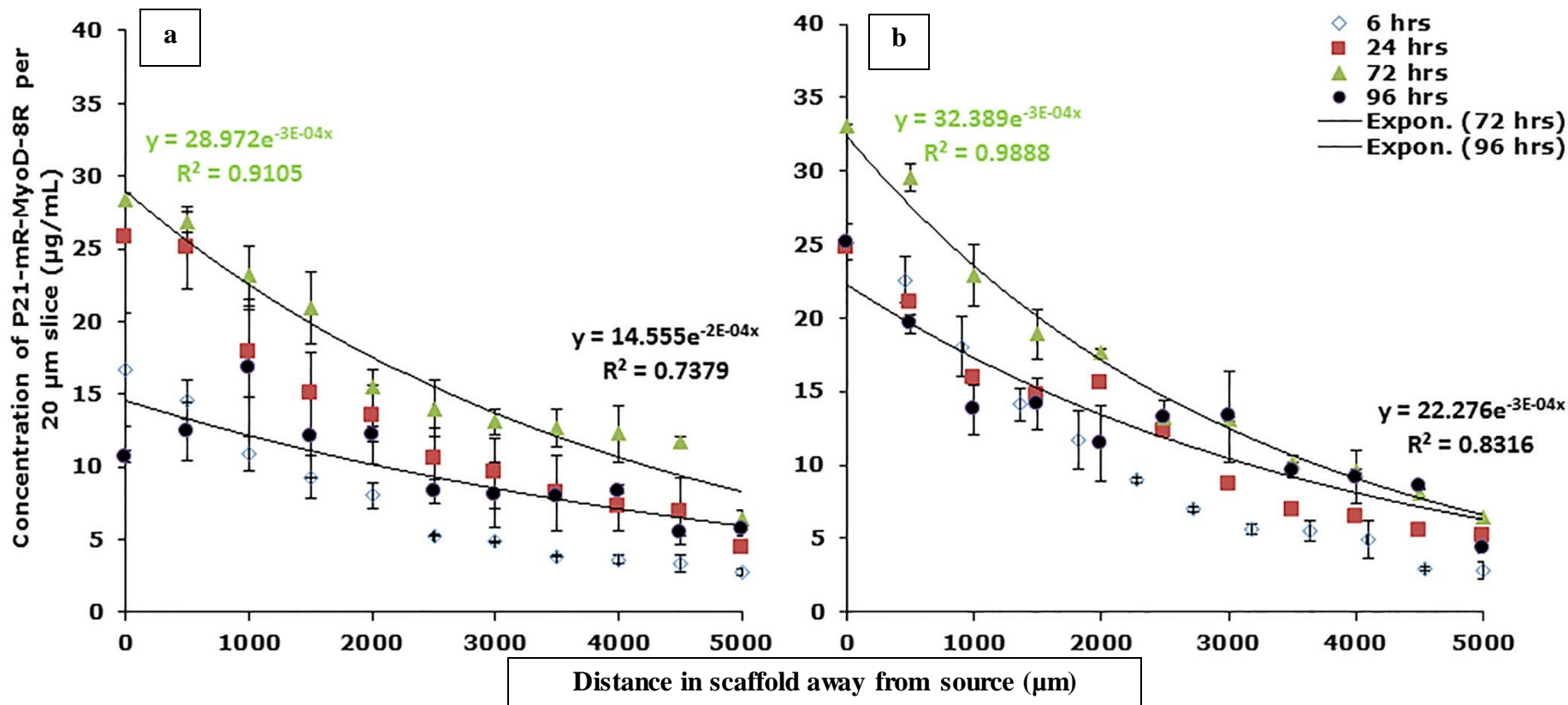


Figure 76: Diffusion gradients of 60 µg/mL P21-mR-MyoD-8R across (a) acellular and (b) cellular (NIH 3T3 mouse fibroblasts, 2×10^6 /mL) 1% agarose-1% gelatin hydrogels at 6, 24, 72 and 96 hours (n=3).

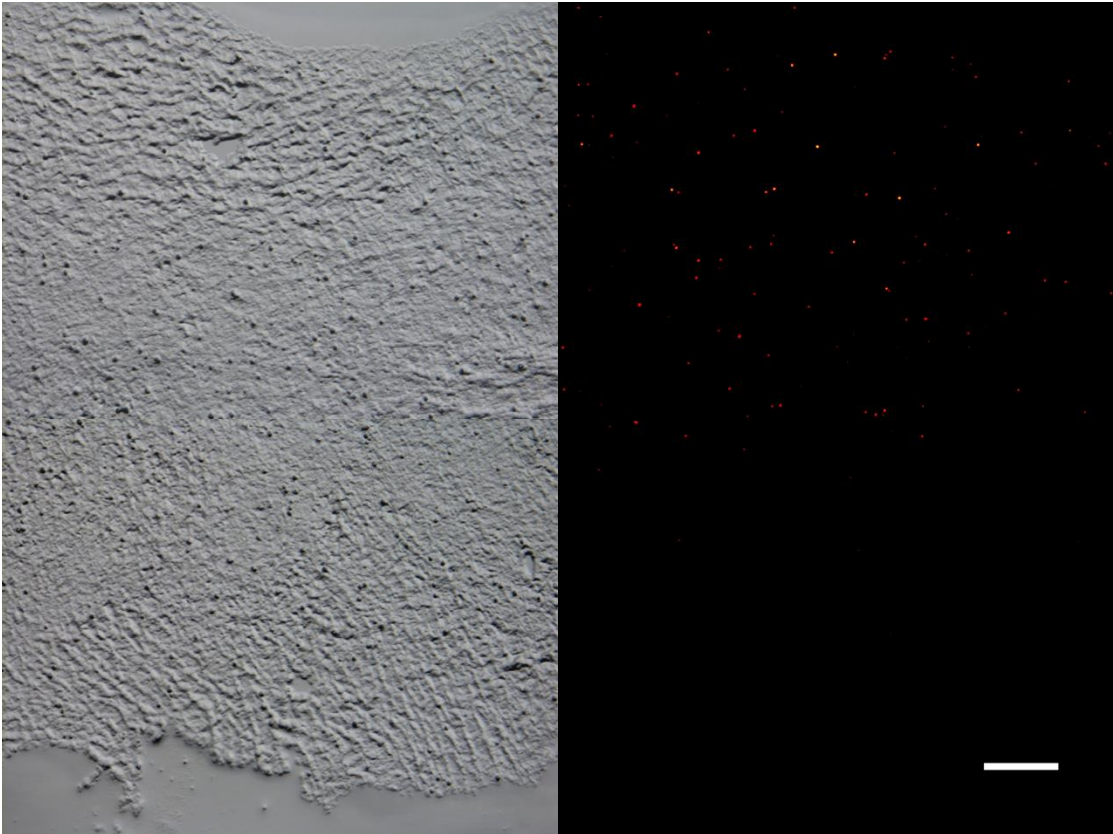


Figure 77: Bright and fluorescence microscopy images of cross sections of the cellular (NIH 3T3 mouse fibroblasts 2M/mL) hydrogels sliced parallel to the direction of the P21-mR-MyoD-8R at 72 hours. Red dots represent transduced cells (scale bar= 0.5 mm).

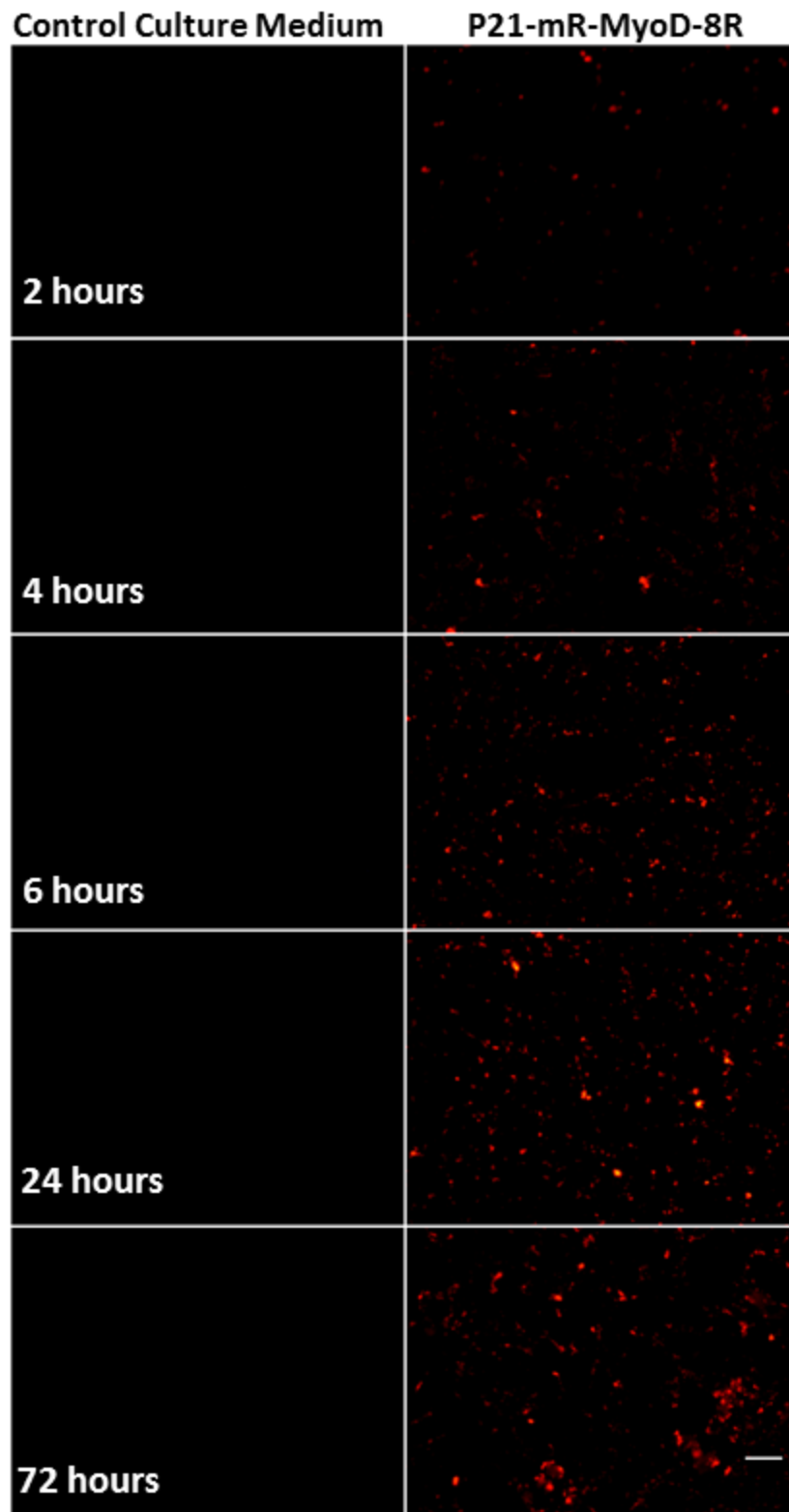


Figure 78: Fluorescence microscopy images of monolayer of 50,000 BJ6 dermal fibroblasts exposed to culture medium or 20 $\mu\text{g}/\text{mL}$ P21-mR-MyoD-8R at different time points imaged using Leica DM IRB microscope. Scale bar is 100 μm .

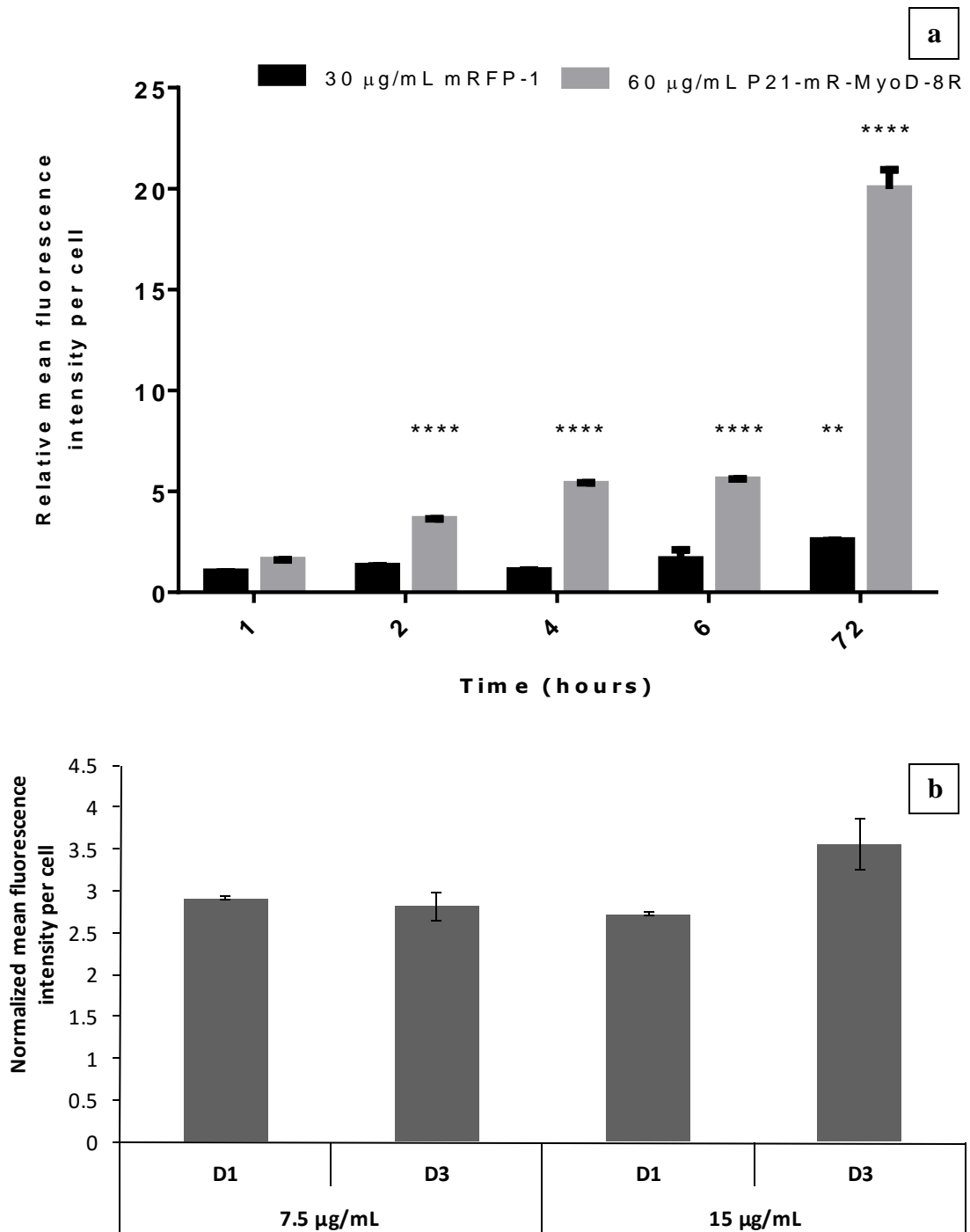


Figure 79: a: Intracellular transduction of P21-mR-MyoD-8R versus mRFP-1 in BJ6 dermal fibroblasts cultured in monolayer on tissue culture plastic. b: Intracellular transduction of lower doses of P21-mR-MyoD-8R in BJ6 dermal fibroblasts cultured in monolayer on tissue culture plastic. Mean fluorescence intensity inside cells was quantified using flow cytometric analysis using MoFlo™ DP (DAKO) Flow Cytometer. Data were normalized to the mean fluorescence intensity per monolayer of cells (0.5×10^6) exposed to 7.5 µg/mL mRFP-1 for 1 day. Data are represented as the mean ($n=3$) \pm standard deviation.

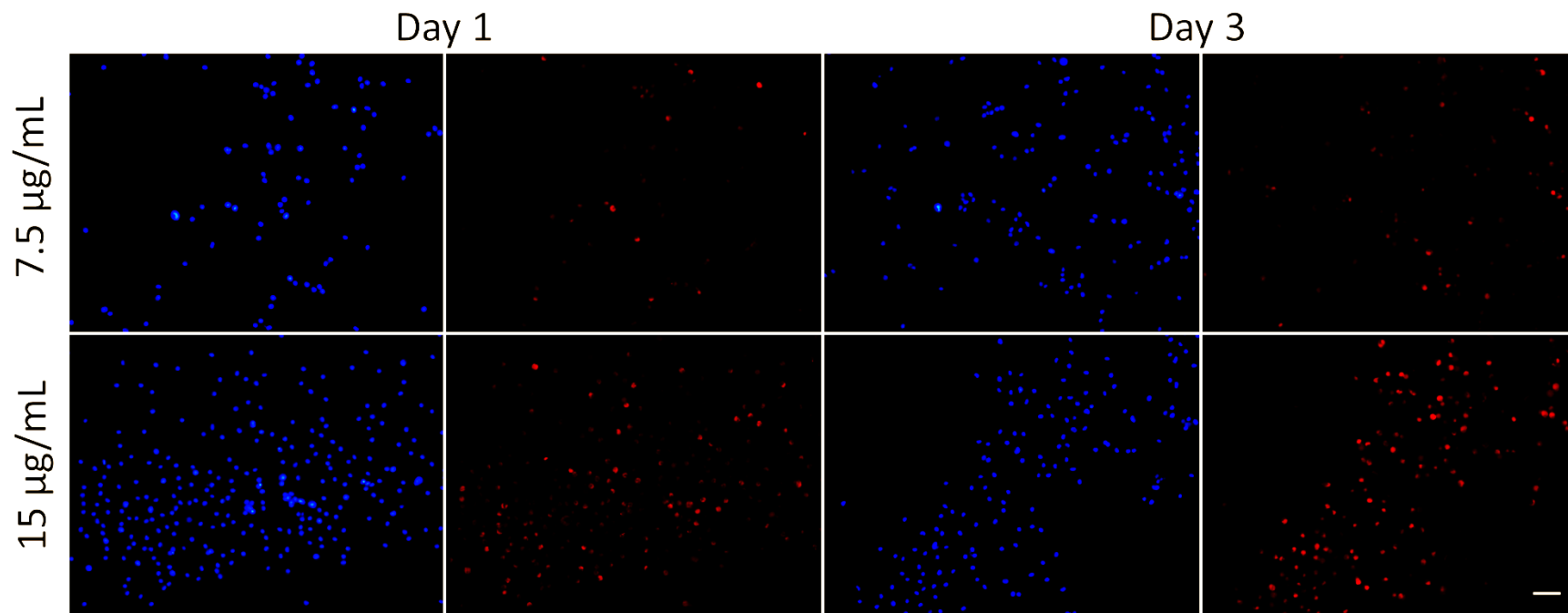


Figure 80: Fluorescence microscopy images of BJ6 dermal fibroblasts exposed to 7.5 µg/mL or 15 µg/mL P21-mR-MyoD-8R at different time points imaged using Leica DM IRB microscope. Cells were detached using Trypsin-EDTA and the mean fluorescence intensity per cells was quantified using MoFlo™ DP (DAKO) Flow Cytometer and samples of cell solutions were subsequently imaged. Scale bar is 100 µm.

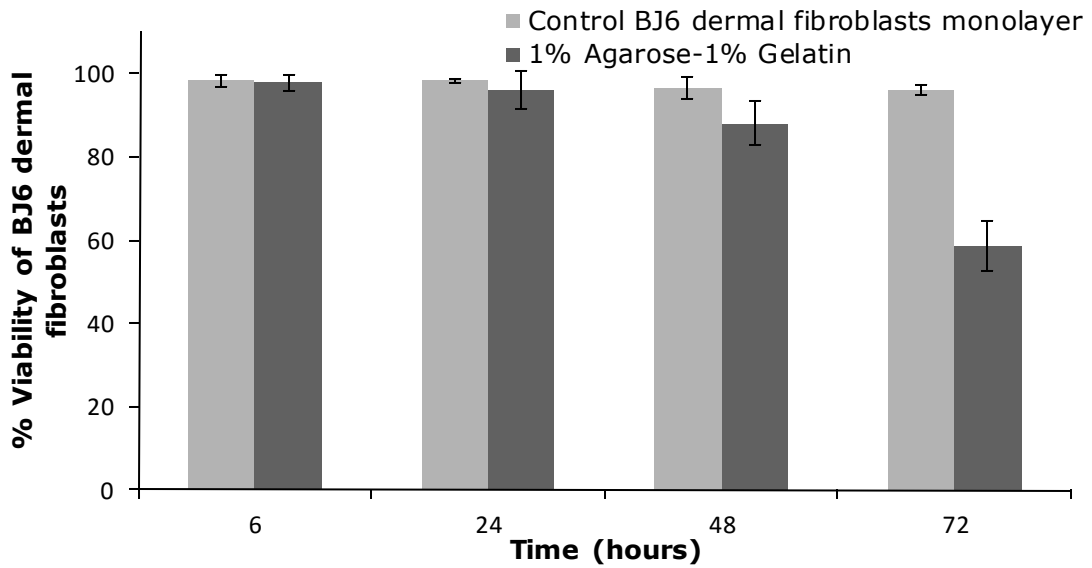


Figure 81: Viability of BJ6 dermal fibroblasts cultured in monolayer on tissue culture plastics versus viability in 1% agarose-1% gelatin hydrogel at different time points using Live/Dead[®] Viability/Cytotoxicity Kit. Data is expressed as % of viable cells compared to total live and dead cells. Cells were counted using ImageJ software. Each data point is an average of 3 different samples and each sample was assessed from 3 different fields of views.

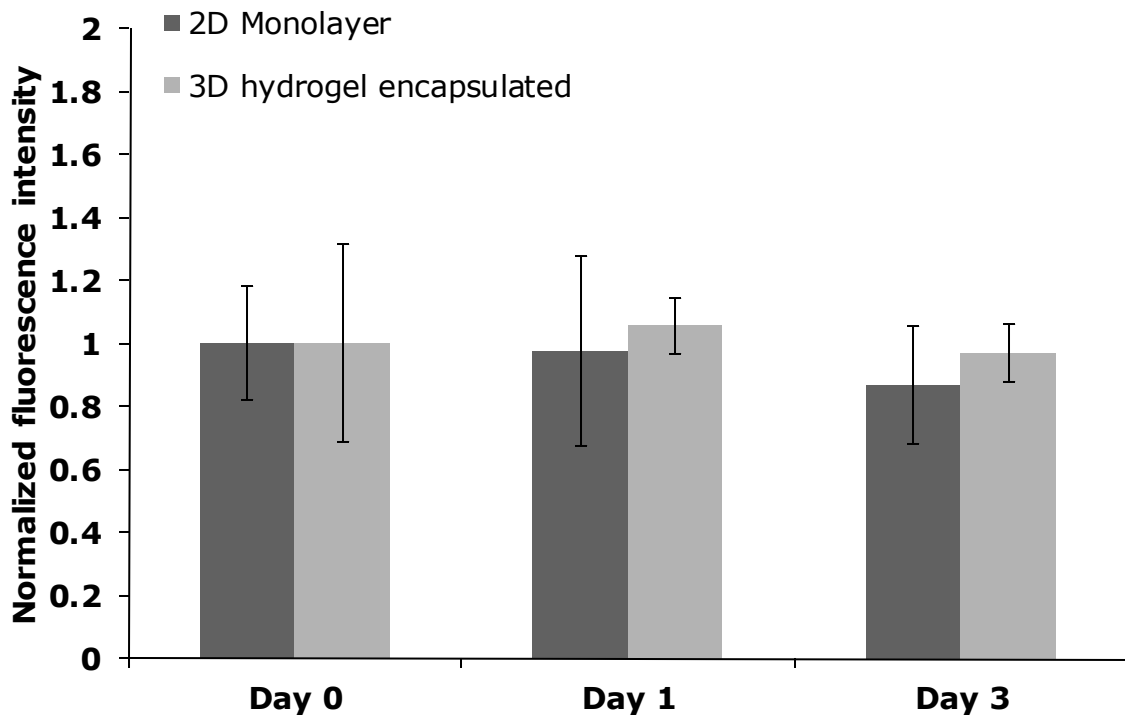


Figure 82: Proliferation assay of BJ6 human dermal fibroblasts cultured in monolayer on tissue culture plastic versus cells encapsulated in 1% agarose-1% gelatin hydrogel at different time points using CyQuant[®] NF proliferation assay. Data is normalized to the relevant fluorescence intensity at day zero. Each time point is an average of triplicate samples.

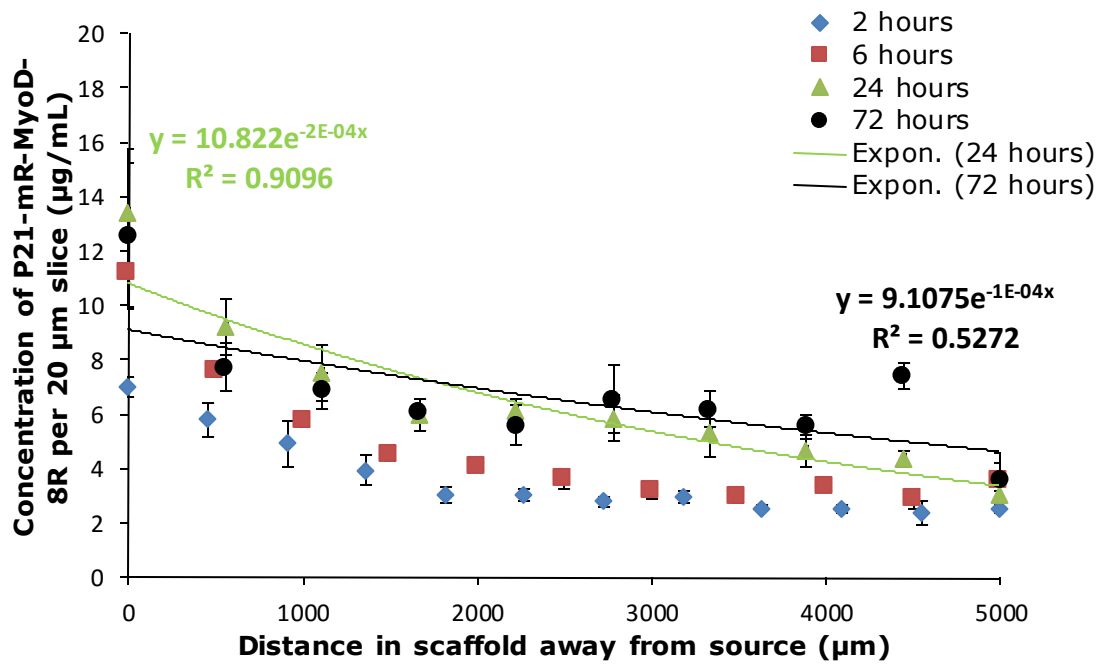


Figure 83: Diffusion gradients of 60 µg/mL P21-mR-MyoD-8R across cellular (BJ6 dermal fibroblasts, 1×10^6 /mL) 1% agarose-1% gelatin hydrogels at 2, 6, 24 and 72 hours (n=3).

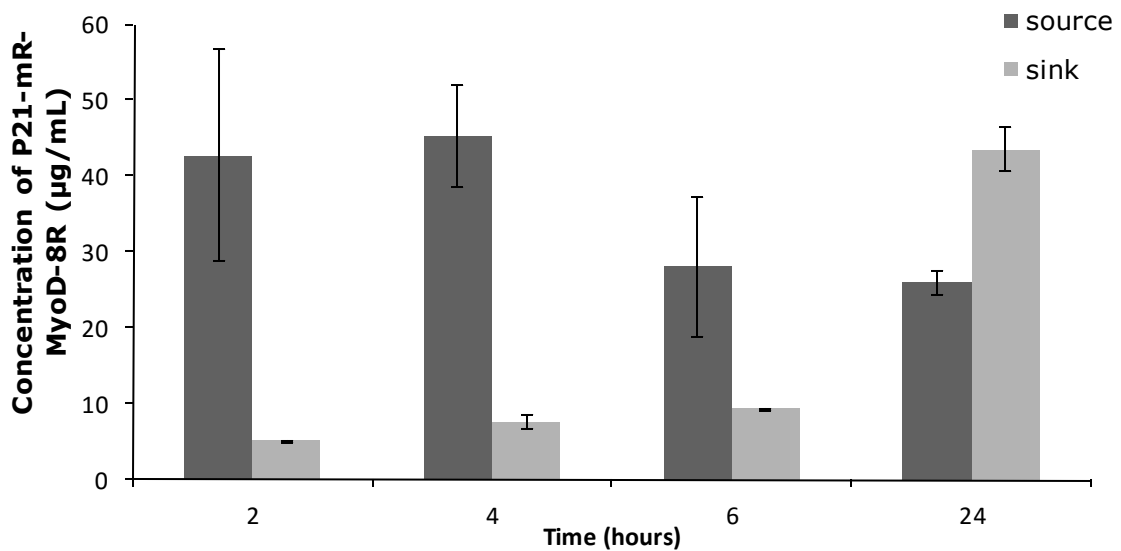


Figure 84: Concentration of P21-mR-MyoD-8R in the source and sink compartments next to cellular scaffolds (BJ6 dermal fibroblasts; 1 M/mL) at different time points.

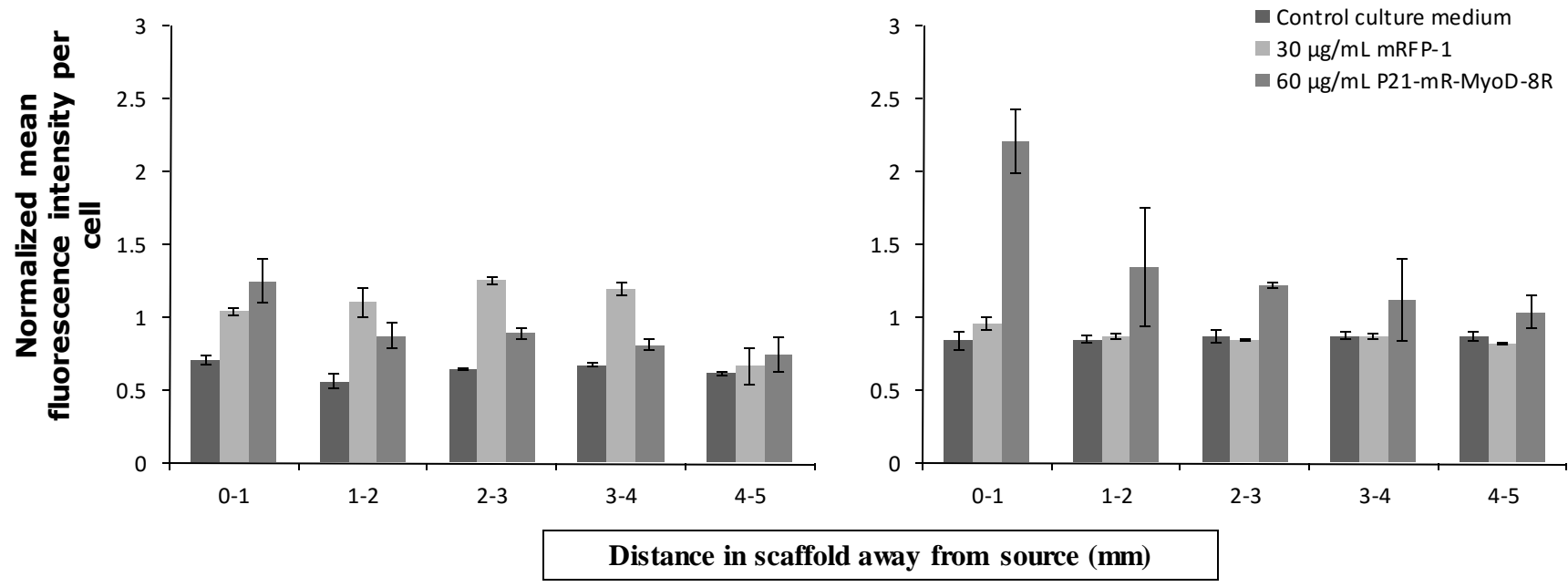


Figure 85: Intracellular fluorescent gradient profiles following diffusion of control culture medium, 30 µg/mL mRFP-1 and 60 µg/mL P21-mR-MyoD-8R diffusion through cellular (BJ6 dermal fibroblasts 1×10^6 /mL) gelatin/agarose hydrogels using flow cytometry analysis: (a) 24 hours and (b) 72 hours. Data were normalized to the mean fluorescence intensity per monolayer of cells (0.5×10^6) exposed to 30 µg/mL mRFP-1 for 24 hours. Data are represented as the mean ($n=3$) \pm standard deviation.

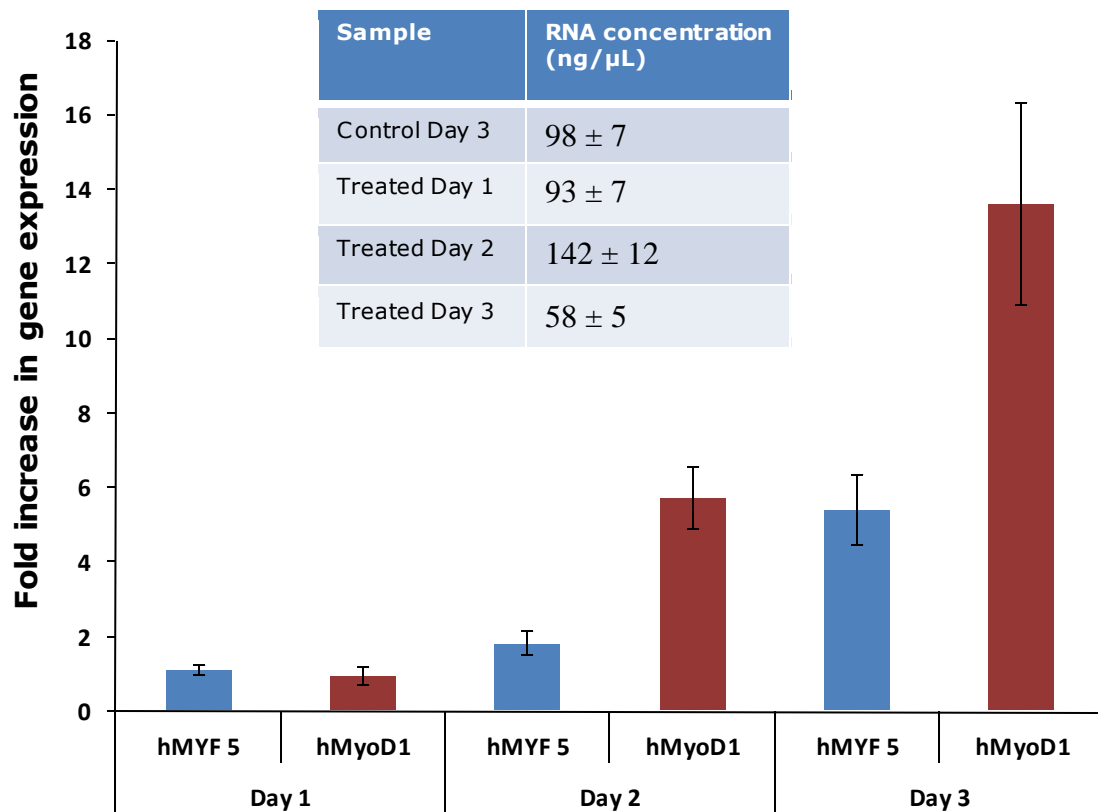


Figure 86: The effect of exposure of monolayer of BJ6 dermal fibroblasts 0.5 M cultured on tissue culture plastics to P21-mR-MyoD-8R (60 μ g/mL) at different time points. Myogenic differentiation is evaluated based on the fold increase in hMYF5 and hMyoD-1 gene expression compared to control untreated cells with the use of β -actin as the house keeping gene using real time quantitative PCR. Data is expressed as mean \pm SD. Table insert shows RNA concentrations (ng/ μ L) of test samples as quantified using NanoDrop[®] ND-1000 Spectrophotometer.

Table 13: List of RNA concentrations extracted from different monolayers of BJ6 dermal fibroblasts (0.5M) exposed to variable concentrations of P21-mR-MyoD-8R or 30 µg/mL mRFP-1 for 3 days. RNA was extracted using RNeasy spin columns and quantified using NanoDrop® ND-1000 Spectrophotometer. Data is expressed as mean (n=3) ± SD.

Sample	RNA concentration (ng/µL)	260/280	260/230
Control untreated monolayer of BJ6 dermal fibroblasts	171 ± 8	2.11 ± 0.01	2.0 ± 0.2
30 µg/mL mRFP-1	71 ± 5	2.05 ± 0.02	1.3 ± 0.7
5 µg/mL P21-mR-MyoD-8R	182 ± 12	2.13 ± 0.02	1.6 ± 0.3
20 µg/mL P21-mR-MyoD-8R	178 ± 25	2.13 ± 0.01	1.63 ± 0.09
60 µg/mL P21-mR-MyoD-8R	51 ± 6	2.15 ± 0.01	1.8 ± 0.2
90 µg/mL P21-mR-MyoD-8R	1 ± 2	3 ± 4	0
120 µg/mL P21-mR-MyoD-8R	2 ± 1	2 ± 1	0.02 ± 0.01
150 µg/mL P21-mR-MyoD-8R	2 ± 3	1.12 ± 0.53	0.02 ± 0.01

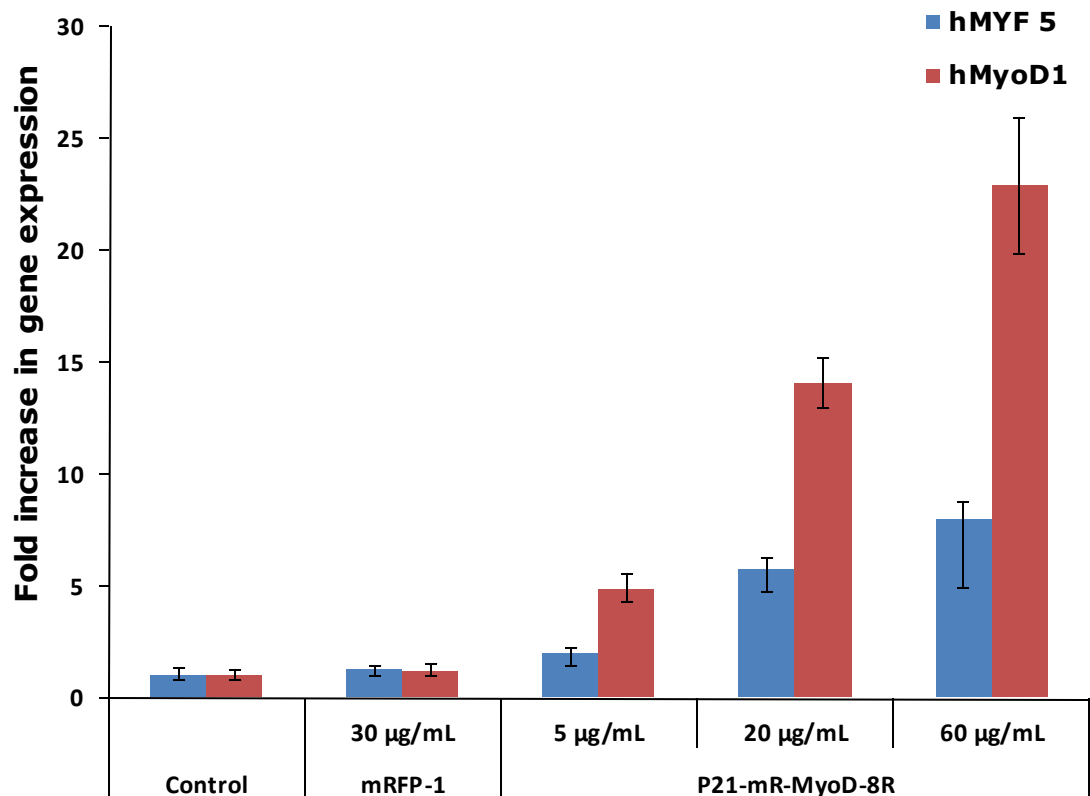


Figure 87: The effect of 3-days exposure of monolayer of BJ6 dermal fibroblasts 0.5 M cultured on tissue culture plastics to 30 µg/mL mRFP-1 or increasing concentrations of P21-mR-MyoD-8R. Myogenic differentiation is evaluated based on the fold increase in hMYF5 and hMyoD-1 gene expression compared to control untreated cells with the use of β -actin as the house keeping gene using real time quantitative PCR. Data is expressed as mean \pm SD.

Table 14: List of RNA concentrations extracted from BJ6 dermal fibroblasts loaded hydrogel slices (5×15×1 mm, 1M/mL) as a function of distance away from source of 60 µg/mL P21-mR-MyoD-8R or control culture media for 3 days. RNA was extracted using RNAeasy spin columns and quantified using NanoDrop® ND-1000 Spectrophotometer.

Sample	RNA concentration (ng/µL)	260/280	260/230
Control scaffold slice 1	2.3	3.21	0.18
Control scaffold slice 2	1.8	0.83	0.01
Control scaffold slice 3	0.7	0.7	0
P21-mR-MyoD-8R scaffold slice 1	2.1	1.92	0.03
P21-mR-MyoD-8R scaffold slice 2	2.6	1.28	0.15
P21-mR-MyoD-8R scaffold slice 3	1.1	0.63	0
P21-mR-MyoD-8R scaffold slice 4	0.2	0.14	0
P21-mR-MyoD-8R scaffold slice 5	1.7	1.79	0.03

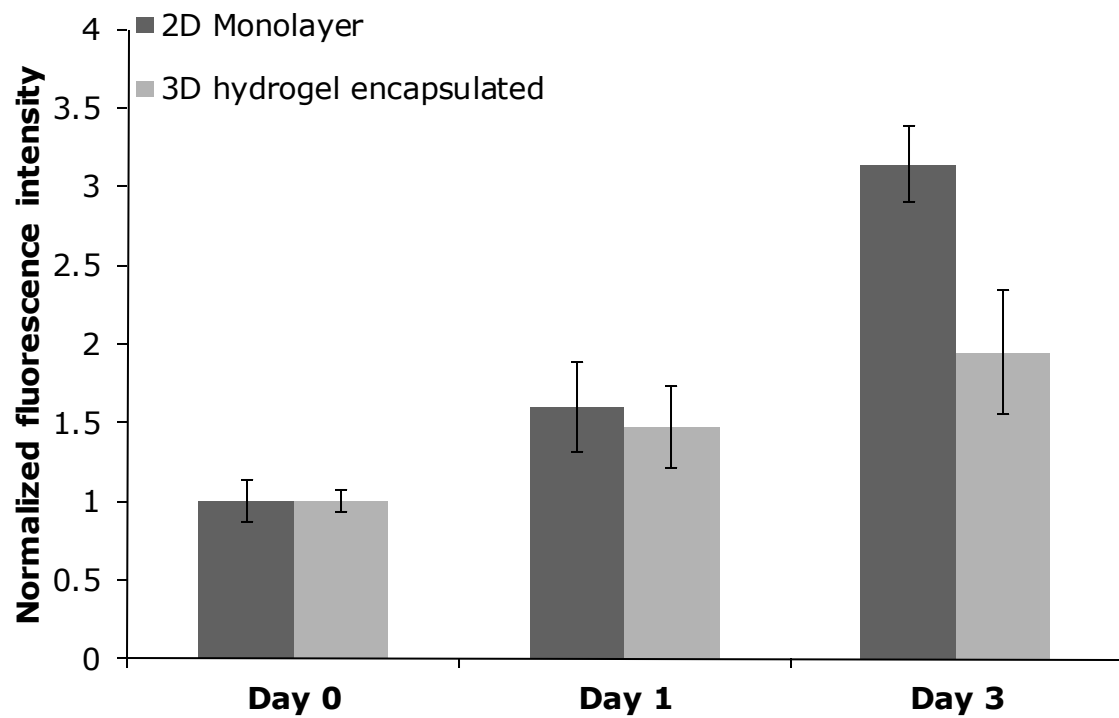


Figure 87: Proliferation assay of HEK 293T human embryonic stem cells cultured in monolayer on tissue culture plastic versus cells encapsulated in 1% agarose-1% gelatin hydrogel at different time points using CyQuant® NF proliferation assay. Data is normalized to the relevant fluorescence intensity at day zero. Each time point is an average of triplicate samples.

Myogenic differentiation of HEK 293T cells in monolayer culture was studied in response to 3 days exposure to increasing concentrations of P21-mR-MyoD-8R as shown in Figure 92. An increased response was observed up to exposure to P21-mR-MyoD-8R (10 µg/mL). The response was subsequently decreased as the concentration increased. The myogenic response was assessed in terms of MyoD gene expression in comparison to the expression of the house keeping gene; β -actin. MyF-5 gene was not expressed in any of the PCR samples tested for monolayer culture of HEK 293T cells exposed to P21-mR-MyoD-8R. Table 15 shows the values of RNA extracted from HEK 293T cells samples exposed to variable concentrations of test proteins.

3D myogenic differentiation of hydrogel encapsulated HEK 293T cells was assessed using PCR analysis of RNA extracted from HEK 293T cells as a function of distance away from source proteins (Table 16). Figure 93 shows the relative expression of MyoD as a function of distance away from P21-mR-MyoD-8R (60 µg/mL) or control culture medium. All slices retrieved from control scaffold that was exposed to plain culture medium showed similar negligible MyoD gene expression. On the other hand, HEK 293T cells encapsulated within hydrogel scaffold showed marked MyoD gene expression in all hydrogel slices irrelevant of distance away from source P21-mR-MyoD-8R. However, there was no gradient pattern in MyoD gene expression and relatively scattered values were computed at different positions in the scaffold.

6.5. Discussion

6.5.1. NIH 3T3 mouse fibroblasts

The 2D transduction of GET proteins previously proven in Dixon *et al.* [118] and in section 5.4.2 was furtherly confirmed upon the positive transduction of mouse fibroblasts with P21-mR-MyoD-8R. The decrease in fluorescence intensity on days 2 and 3 was attributed to the presence of two cellular sub-populations at 48 & 72 hours corresponding to cell doubling and the presence of younger cells with smaller size [218]. Recruiting the compartmental diffusion model in monitoring the gradient delivery of P21-mR-MyoD-8R across mouse fibroblasts loaded agarose/gelatin revealed similar results to the findings of chapter 5. The diffusion behaviour of different molecules in hydrogels is generally modulated by size and interaction filtering strategies [135]. The hydrodynamic radius of 4.07 ± 1.13 nm in 10 mM HEPES buffer and zeta potential of -8.10 ± 2.32 suggest free diffusion of P21-mR-MyoD-8R in negatively charged agarose/gelatin hydrogels with 198 ± 7.9 nm mesh size.

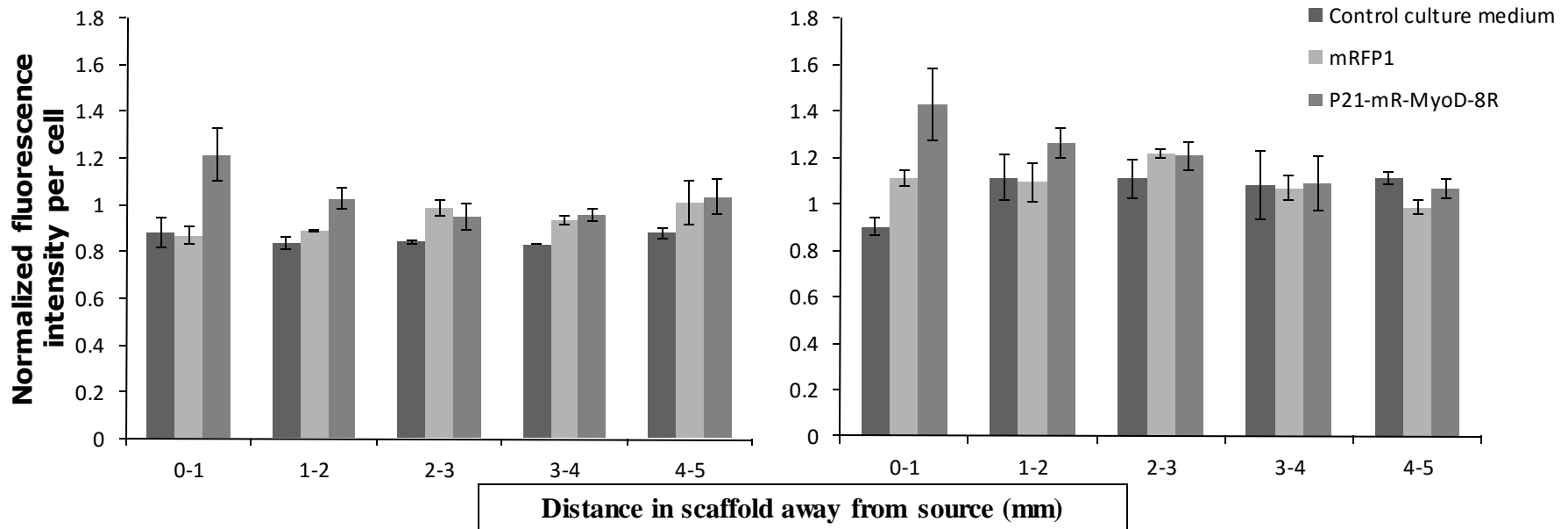


Figure 89: Intracellular fluorescent gradient profiles following diffusion of control culture medium, 30 $\mu\text{g}/\text{mL}$ mRFP-1 and 60 $\mu\text{g}/\text{mL}$ P21-mR-MyoD-8R diffusion through cellular (Human embryonic kidney cells HEK293T $2 \times 10^6/\text{mL}$) gelatin/agarose hydrogels using flow cytometry analysis: (a) 24 hours and (b) 72 hours. Data were normalized to the mean fluorescence intensity per monolayer of cells (1×10^6) exposed to 30 $\mu\text{g}/\text{mL}$ mRFP-1 for 24 hours. Data are represented as the mean ($n=3$) \pm standard deviation.

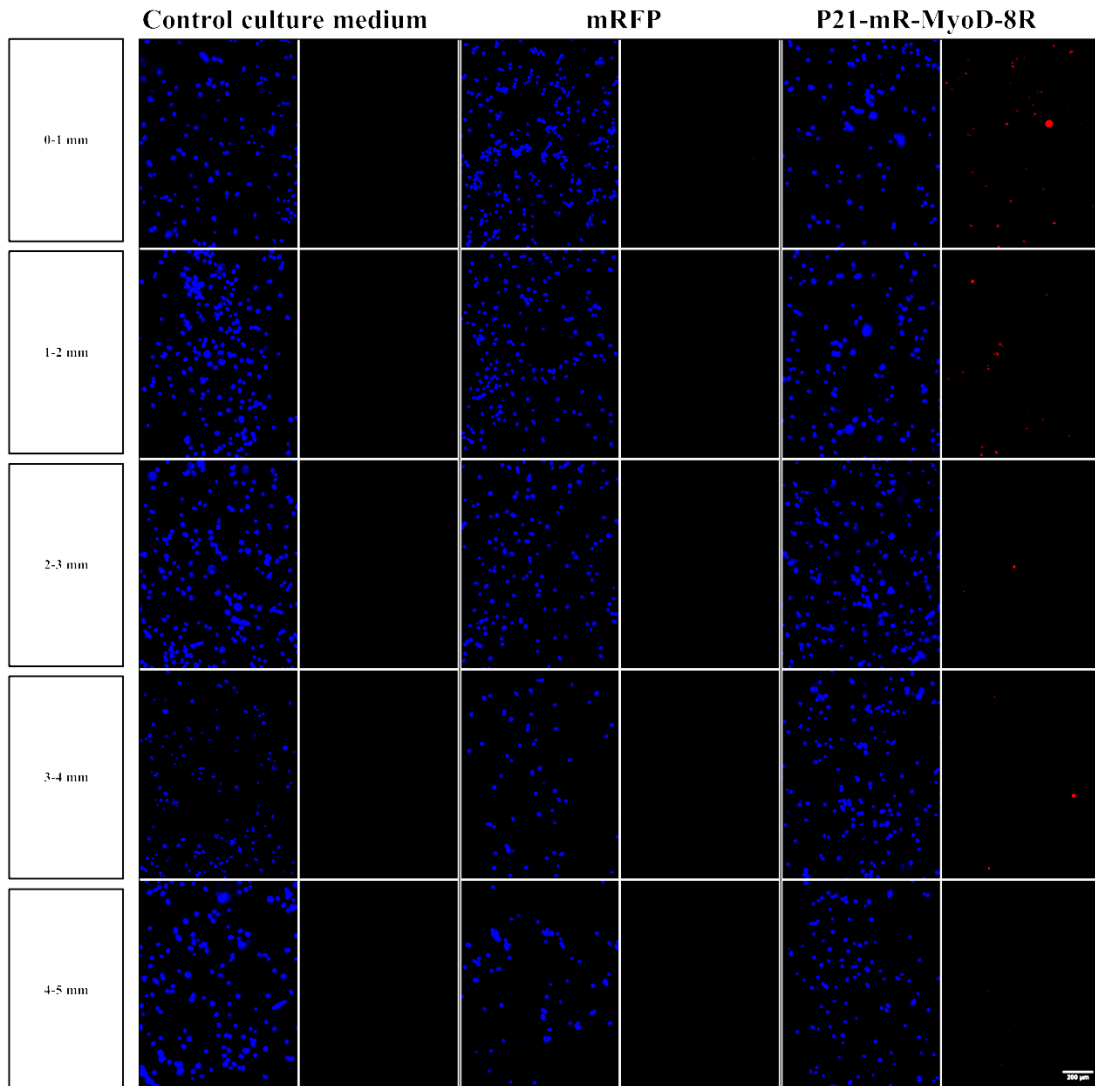


Figure 90: Representative fluorescence microscopy images of digested gel slices retrieved from cellular scaffolds (HEK293T human embryonic kidney cells, 2M/mL) exposed to control culture media, mRFP-1 or P21-mR-MyoD-8R respectively on day 1. Hoechst 33342; blue and red fluorescent protein; red, scale bar = 100 μ m.

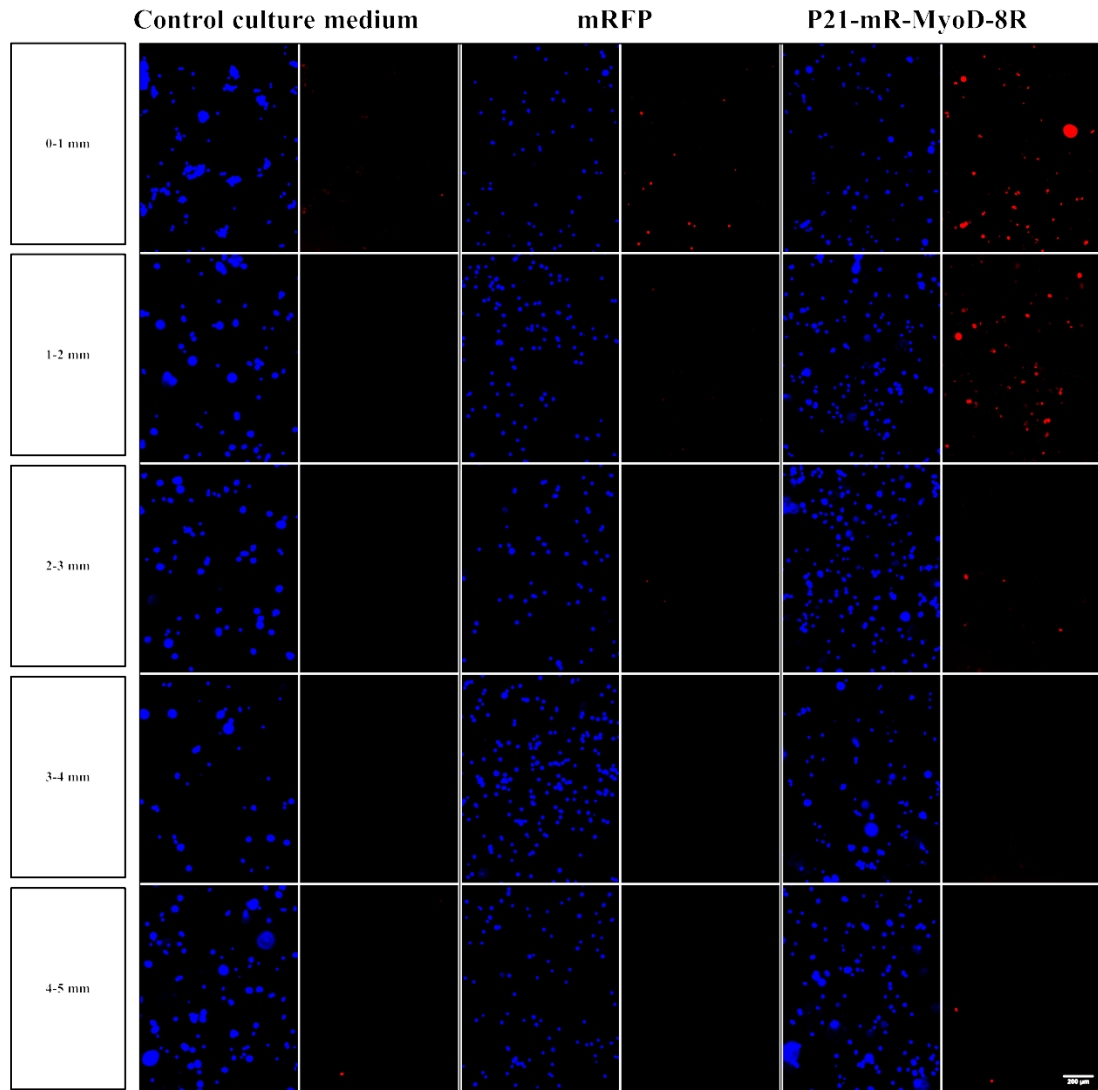


Figure 91: Representative fluorescence microscopy images of digested gel slices retrieved from cellular scaffolds (HEK293T human embryonic kidney cells, 2M/mL) exposed to control culture media, mRFP-1 or P21-mR-MyoD-8R respectively on day 3. Hoechst 33342; blue and red fluorescent protein; red, scale bar = 100 μ m.

Table 15: List of RNA concentrations extracted from different monolayers of HEK293T cells (1M) exposed to variable concentrations of P21-mR-MyoD-8R for 3 days. RNA was extracted using RNeasy spin columns and quantified using NanoDrop® ND-1000 Spectrophotometer. Data is expressed as mean (n=3) ± SD.

Sample	RNA concentration (ng/μL)	260/280	260/230
Control untreated monolayer of BJ6 dermal fibroblasts	519 ± 19	2.09 ± 0.01	1.8 ± 0.3
5 μg/mL P21-mR-MyoD-8R	307 ± 57	2.10 ± 0.02	1.1 ± 0.8
10 μg/mL P21-mR-MyoD-8R	384 ± 19	2.10 ± 0.02	1.12 ± 0.06
20 μg/mL P21-mR-MyoD-8R	290 ± 18	2.10 ± 0.02	1.5 ± 0.5
40 μg/mL P21-mR-MyoD-8R	348 ± 69	2.10 ± 0.02	1.3 ± 0.8
60 μg/mL P21-mR-MyoD-8R	341 ± 24	2.10 ± 0.01	2.04 ± 0.02

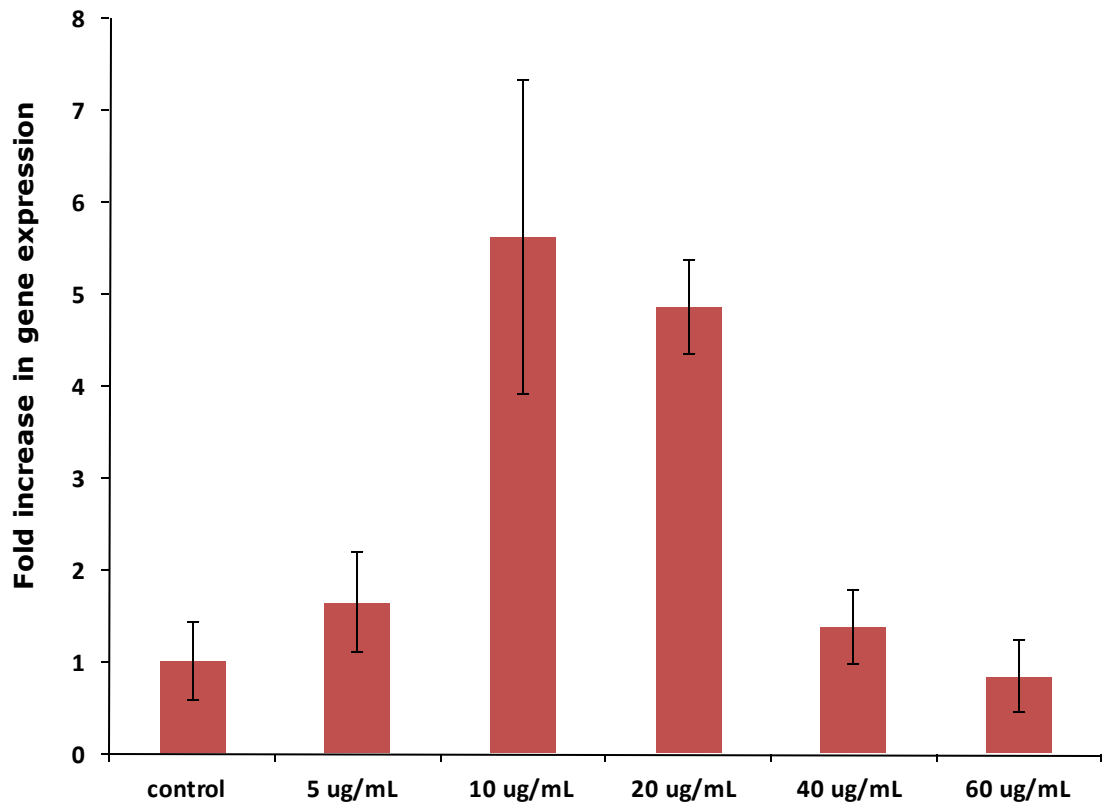


Figure 92: The effect of 3-days exposure of monolayer of Human embryonic kidney cells HEK293T (1 M) cultured on tissue culture plastics to increasing concentrations of P21-mR-MyoD-8R. Myogenic differentiation is evaluated based on the fold increase in hMyoD-1 gene expression compared to control untreated cells with the use of β -actin as the house keeping gene using real time quantitative PCR. Data is expressed as mean \pm SD

Table 16: List of RNA concentrations extracted from HEK293T loaded hydrogel slices (6.6×15×1 mm, 2M/mL) as a function of distance away from source of 60 µg/mL P21-mR-MyoD-8R or control culture media for 3 days. RNA was extracted using RNeasy spin columns and quantified using NanoDrop® ND-1000 Spectrophotometer. Data is expressed as mean (n=5 scaffolds) ± SD. Control scaffold is the average of 3 different slices retrieved from the same scaffold.

Sample	RNA concentration (ng/µL)	260/280	260/230
Control scaffold slice	35.35 ± 6.71	2.01 ± 0.05	1.15 ± 0.33
P21-mR-MyoD-8R scaffold slice 1	26.47 ± 16.01	1.93 ± 0.16	1.06 ± 0.46
P21-mR-MyoD-8R scaffold slice 2	38.76 ± 37.82	1.94 ± 0.17	0.66 ± 0.6
P21-mR-MyoD-8R scaffold slice 3	35.17 ± 14.63	2.01 ± 0.06	0.71 ± 0.73
P21-mR-MyoD-8R scaffold slice 4	40.12 ± 19.97	1.99 ± 0.12	0.61 ± 0.37
P21-mR-MyoD-8R scaffold slice 5	51.35 ± 27.05	2.05 ± 0.04	0.88 ± 0.65

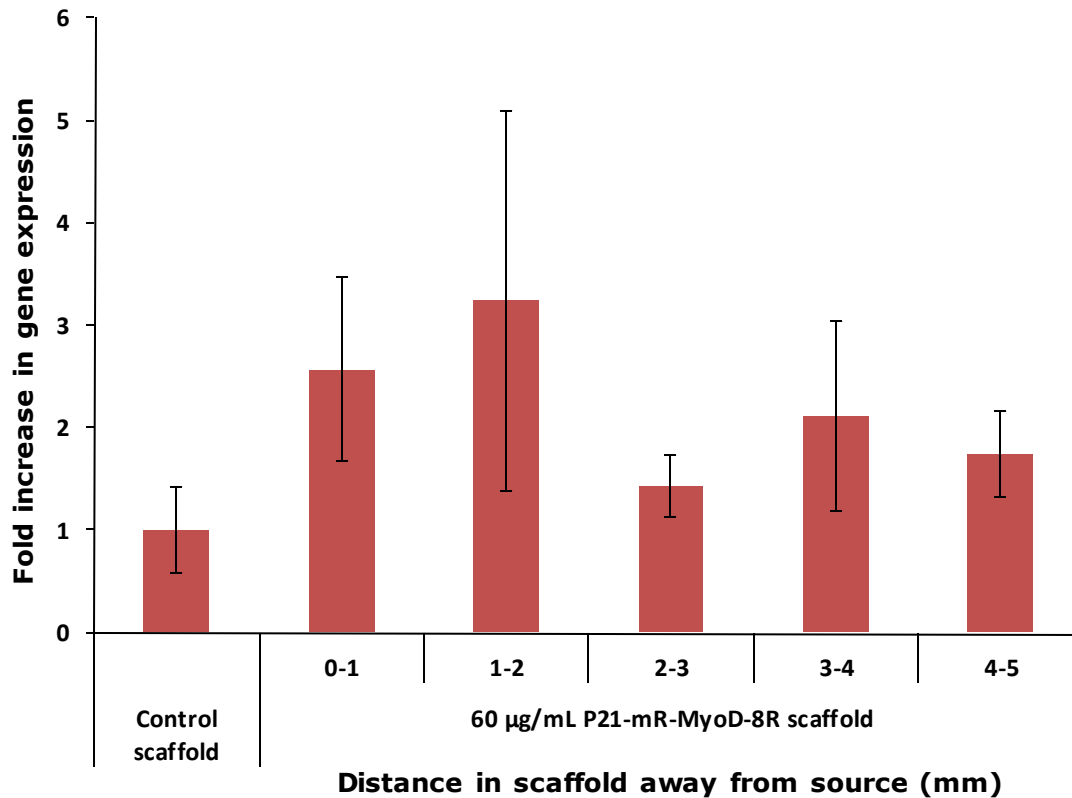


Figure 93: Relative myogenic gene expression as a function of distance away from source following diffusion of 60 $\mu\text{g}/\text{mL}$ P21-mR-MyoD-8R across cellular HEK293T (2 M/mL) 1% agarose-1% gelatin hydrogel scaffolds of 15 \times 5 \times 6.6 mm (Length \times Width \times Height) dimensions. Myogenic differentiation is evaluated based on the fold increase in hMyoD-1 gene expression compared to control cells recovered from 5 different slices of a scaffold through which control culture medium diffused with the use of β -actin as the house keeping gene using real time quantitative PCR. Data is expressed as mean (n=5) \pm SD.

However, the presence of cells, as previously proven, altered the temporal diffusion profiles of P21-mR-MyoD-8R across cellular scaffolds as compared to acellular ones. This was attributed to the gradient cellular uptake as a function of distance so that the cells acted as a sink that compelled the protein away from the source compartment and maintained steep gradient profiles up to 72 hours.

Determination of the diffusion coefficient of P21-mR-MyoD-8R in agarose/gelatin using model permeation model [61, 122, 123] revealed a value of $4.2 \times 10^{-7} \text{ cm}^2/\text{s}$. This value suggests slower diffusion across agarose/gelatin hydrogels compared to P21-mR-8R or mRFP-1 with values 7.53×10^{-7} & $7.15 \times 10^{-7} \text{ cm}^2/\text{s}$ respectively. The correlation between diffusion coefficients and molecular weight is described by Stokes–Einstein equation and there have been various models that predict diffusion coefficients as a function of the molecular weight [237]. This explains the lower value of diffusion coefficient of P21-mR-MyoD-8R (65.3 KDa) as compared P21-mR-8R (30.7 KDa) and mRFP-1 (26.5 KDa). This was further reflected on the diffusion profiles of P21-mR-MyoD-8R in cellular or acellular agarose/gelatin scaffolds. The gradient profile was maintained relatively steep up to 72 hours in acellular scaffolds (coefficient of determination of exponential curve decay, $r^2 = 0.9105$). Meanwhile, a relatively steeper gradient was observed in cellular scaffolds ($r^2 = 0.9888$). A later time point was introduced to study the expected continued diffusion. Higher coefficients of determination of exponential curve decay were observed at 4 days for both acellular and cellular scaffolds confirming the aforementioned findings.

6.5.2. BJ6 human dermal fibroblasts

Mouse fibroblasts were replaced, in the compartmental diffusion model, with human dermal fibroblasts as a step towards recruiting the model for developing clinically relevant scaffolds with multiple cell types upon the gradient delivery of GET proteins. The 2D intracellular transduction was efficient as previously proven in several cell types even with lower concentrations of P21-mR-MyoD-8R [118]. The next step was to prove the viability of human dermal fibroblasts in agarose/gelatin hydrogel. As explained in section 5.5.2, agarose/gelatin hydrogels dispensed in cell culture medium are capable of maintenance of the viability to an optimum value up to 3 days. However, nutrient consumption from the external media can result in decreased viability on later time points and this was previously reported in 3D agarose matrices [221, 222].

The diffusion gradient profile of P21-mR-MyoD-8R (60 $\mu\text{g}/\text{mL}$) across BJ6 dermal fibroblasts loaded agarose/gelatin hydrogels was equilibrated on day 3 with scattered concentrations around 7.5 $\mu\text{g}/\text{mL}$ at all hydrogel slices. On the other hand, the 3D gradient intracellular transduction profile demonstrated a steep gradient on day 3 as a function of distance. This could be possibly attributed to the accumulation of protein uptake in cells as there was no increase in proliferation of dermal fibroblasts in the hydrogel scaffold with time (Figure 82). Additionally, a concentration of P21-mR-MyoD-8R (7.5 $\mu\text{g}/\text{mL}$) was proven to sufficiently transduce dermal fibroblasts.

The ceased proliferation of human dermal fibroblasts in monolayer cultures and in 3D hydrogels could be explained by the limited space available for proliferation of relatively large cells with profound ECM secretion (rich in type I & type III collagen) [238] and the minimal change of culture medium to resemble diffusion studies. Dermal fibroblasts grow in flat and spindle-shape morphology in monolayer cultures. However, in 3D collagen hydrogels, fibroblasts possess elongated morphology with numerous dendrites and tend to proliferate slower than in 2D monolayer cultures [239]. These can consequently lead to detachment of the monolayer of cells or minimal transport of nutrients and waste within 3D matrix especially with high ECM secreted. Hydrogel stiffness together with decreased mesh size can result in decreased cell proliferation [240]. Another factor that could additionally contribute to the poor proliferation is the high passage number of the utilized cells [241, 242]. Finally, it has been reported that dermal fibroblasts in particular are very difficult to replicate in *in vivo* and *in vitro* environments as compared to other fibroblast types and they require higher FGF concentrations for replication [238].

The ability to induce myogenic transdifferentiation from human fibroblasts to cells expressing early myogenic markers was demonstrated. MyoD and Myf5 target genes were used to determine the onset of differentiation [227]. The expression of MRFs in monolayer cultures were demonstrated even at the lower concentrations expected to be available to cells in 3D systems. MyoD gene expression was remarkably higher than MyF-5 similar to results previously reported by Ishibashi *et al.* [227]. Exposure of dermal fibroblast to P21-mR-MyoD-8R concentrations (higher than 60 $\mu\text{g}/\text{mL}$) resulted in failure of RNA extraction and subsequent downstream PCR analysis. This could be justified by the toxicity of such doses to the sensitive high passage number dermal fibroblasts with limited proliferation capacity.

Despite the observed intracellular gradient of P21-mR-MyoD-8R across BJ6 dermal fibroblasts loaded agarose/gelatin hydrogels, trials to extract abundant amounts of RNA for downstream applications failed. This could be attributed to the limited proliferation and viability of dermal fibroblasts in agarose/gelatin scaffolds. Furthermore, the rationale behind using a cell loading density of 1 M/mL was to guarantee enough space for the elongated Human dermal fibroblasts to grow properly within agarose/gelatin matrix with elongated & multi-dendrites morphology reported to 3D systems [239]. This, together with limited viability and proliferation, can consequently result in lower amounts of viable cells per slice. In such way, one hydrogel slice would contain less than 100,000 cells which would subsequently mean lower availability of RNA to be extracted for downstream applications. Additionally, the process of extraction of RNA from polysaccharide-based hydrogels like agarose is often compromised by the presence of polysaccharides in the scaffold [243].

6.5.3. Human embryonic kidney cell line

The human dermal fibroblasts in cell-laden agarose/gelatin scaffolds were replaced by the robust HEK 293T cell line. This cell line is often used for gene transfection and expression experiments with almost 100% efficiency. Additionally, HEK 293T cells are employed in signal transduction and protein interaction upon viral vectors-based delivery [244]. HEK 293T cell line is known for availability of abundant RNA to be extracted following gene transfection studies [245, 246]. Furthermore, these cells can survive encapsulation within 3D hydrogels for longer periods of time with optimum viabilities [247, 248]. This should add to the potential success of RNA extraction from hydrogel encapsulated cells. This was practically proven using CyQuant® NF proliferation assay, in which HEK 293T cells proliferation within agarose/gelatin hydrogel was comparable to monolayer culture but was relatively lower on later time points. These results were superior to human dermal fibroblasts proliferation.

The gradient profile of P21-mR-MyoD-8R across HEK 293T loaded agarose/gelatin was not as steep as the equivalent profile in BJ6 dermal fibroblasts loaded hydrogels. Furthermore, the transduction was not significantly different from mRFP-1 treated scaffolds at distant hydrogel slices. This could be justified by the rapid proliferation of HEK 293T within the scaffold as a function of time that prevented the accumulation of red fluorescence signal inside cells together with slower diffusion of P21-mR-MyoD-8R across agarose/gelatin hydrogels ($D = 4.2 \times 10^{-7} \text{ cm}^2/\text{s}$).

Induction of myogenic differentiation of monolayer of HEK 293T cells upon transduction with P21-mR-MyoD-8R did not result in dose-related MRFs expression. The declined MyoD gene expression in response to higher doses could be attributed to altered gene profiling towards later differentiation stages or due to cell death upon exposure to higher doses. However, this assumption was not valid as the RNA extraction process revealed optimum concentrations & quality of the RNA extracted even at higher P21-mR-MyoD-8R concentrations. MyF-5 gene was not expressed in monolayer culture nor 3D hydrogel encapsulated cells. This could be justified by the potential of MyoD to rapidly induce myogenesis in dose-related action. In such way, higher doses can result in late myogenesis characteristic with no MyF-5 expression and reduced MyoD expression. MyoD is a MRF characteristic of early myogenesis that is highly expressed in early stages as compared to declined expression in the later phases of differentiation. Moreover, MyoD was found to be essential for MRF4 activation during the late differentiation of myoblasts, but not necessarily required for MyF-5 or myogenin gene expression [249].

In 3D matrix, the myogenic differentiation was confirmed to be higher than control scaffold at all hydrogel slices away from source protein. However, there was no pattern of gene expression to confirm the P21-mR-MyoD-8R gradient delivery. Once more, this could be due to altered gene expression in later differentiation stage that could be induced by higher doses of P21-mR-MyoD-8R available to HEK 293T cells especially at closer vicinity to source protein. Another explanation that could apply to distant hydrogel slices is the inefficient transduction of P21-mR-MyoD-8R with rapid proliferation and slow P21-mR-MyoD-8R diffusion.

6.6. Conclusions

The potential of the compartmental diffusion model in monitoring diffusion of functional proteins was demonstrated using a range of cell types. Each cell type possesses different proliferation characteristics that were reflected in the feasibility of utilization of the model in a continuously changed cellular environment. The diffusion characteristics of the biomolecules together with the cellular health and proliferation within the hydrogel system decided on the pattern of biological response recorded. From these perspectives, careful understanding of gene profiling in monolayer culture in response to bioactive molecules could be employed for proper choice of target genes of the temporal differentiation stage measured in the 3D matrices.

Chapter 7: General discussion & Future work

7.1. General discussion & conclusions

Biomimetic approaches employed in regenerative medicine applications aim at the replication of the native cellular microenvironment to restore compromised tissue/organ functions. This involves the reproduction of the structural complexity of the ECM including multiple cells interactions and physicochemical cues dictating cell fates. Chemical, physical and mechanical gradients in the cellular microenvironment are common cues that decide on the cellular behaviour and differentiation. From these perspectives, it is imperative to study cellular response towards *in vitro* gradients of chemical and mechanical cues for precise design of functional scaffolds.

7.1.1. Model validation

Different techniques were reported to generate and assess chemical gradients in cell culture systems or within 3D matrices [2, 11-18]. Molecular diffusion represents a simple and cost-effective method of generating chemical gradients with minimal shear stresses exerted on hydrogel encapsulated cells [95]. In the current thesis, we developed a compartmental diffusion model that is comprised of source-gel-sink compartment to study molecular diffusion of large molecules across hydrogel membrane. The model was previously presented in Cao *et al.*[61]. However, extra efforts were dedicated to guarantee seamless contact between the hydrogel system and the base of the diffusion chamber. This was to ensure diffusion of macromolecules only through the hydrogel membrane for accurate diffusion studies. Furthermore, the objective of our study was to evaluate the gradient delivery of biomolecules and their corresponding cellular responses. Consequently, different cell positioning was adopted. Homogenous dispersion of cells were used in our modified model rather than cells plated underneath agarose membrane presented in the original model [61].

A sacrificial quantification method was dedicated to evaluate the developed gradients as function of time and distance rather than a real time monitoring techniques that rely on microscopic quantitative evaluation of fluorescent or radiolabelled diffusing species [18, 97, 103]. Despite the advantages provided by such methods, accurate validated analysis software and effective fluorescent labelling without compromising the functionality of diffusing proteins are required. Chapter three was dedicated to validate the modified compartmental diffusion model/quantification protocol for generating and measurement of chemical gradients. The model was proven to be capable of

distinguishing between different molecular weight diffusing species as a function of time. The diffusion behaviour of diffusing molecules in hydrogels is modulated by size and interaction filtering strategies [135]. Consequently, effective models in generating and measuring chemical gradients should be able to distinguish between the fast and slow diffusion of small and large molecular weights species respectively. Furthermore, there was a good correlation between the quantitative analysis and the qualitative fluorescence microscopy images suggesting the validity of the quantification tool. Additionally, the model was not restricted to monitoring the diffusion of protein species. Large molecular weights polysaccharides were allowed to diffuse in the modified compartmental diffusion model. Finally, the effect of the fluorescent tag on the quantification process was studied. Double opposing diffusion of the same molecular weight compound, yet, with different fluorescent tags displayed mirror image diffusion profiles across the hydrogel width. This confirms the potential of the model/quantification protocol in creating and computing gradients of chemical compounds across 3D hydrogels irrelevant of the fluorescent tag employed. Furthermore, this demonstrates the potential application of recruiting the compartmental diffusion chamber in developing forward and reverse gradients for developmental biology models.

7.1.2. Localized release depots

Having demonstrated the efficiency of the diffusion model in achieving temporal chemical concentration gradients, fine tuning of source protein concentration, availability and functionality were crucial for effective protein delivery. The structural complexity, denaturation potential and alteration of spatial characteristics compromise protein functionality [168]. Furthermore, protein delivery is hampered by proteolytic degradation liability and proteins short half-lives [169]. As an approach to overcome such hurdles, we replaced the source compartment with localized protein depots of different protein release characteristics.

The incorporation of the triblock co-polymer resulted in enhanced the encapsulation efficiency and release kinetics of FITC-BSA. Possibly this resulted in increased water uptake within the microspheres [189] and back diffusion of FITC-BSA from the microspheres. Furthermore, it facilitated the softening & plasticization of the microsphere matrix and ease of release of its protein content [185]. In addition to protein protection, tuneable release characteristics microspheres resulted in temporal control

over the developed protein concentration gradients. This can be further recruited to develop complex 3D scaffolds with tuneable time dynamics of bioactive molecules gradients together with overcoming the burden of proteins short half-lives.

7.1.3. Gradient delivery of GET proteins

The high transduction efficiency of GET system in different cell types grown in monolayer cultures was established by Dixon *et al.* [118]. The enhanced transduction offered by the GET system overcomes the problems associated with endocytosis of CPPs. Endocytosis hinders the release of the functional proteins and exposes them to degradation [191] demanding high starting concentration of CPPs to bypass entrapment inside endosomes [191, 212] with possible toxic effect on cells.

The developed proteins were allowed to diffuse across cellular hydrogel membranes in the compartmentalized diffusion chamber. In comparison to the reporter mRFP-1, the cell binding (P21-mR) and the CPP (mR-8R), P21-mR-8R demonstrated synergistic enhanced transduction of both the cell binding domain and the cell penetrating domain. This was demonstrated in monolayer cultures and within 3D matrices. Gradient intracellular transduction of hydrogel encapsulated mouse fibroblasts with P21-mR-8R was demonstrated over 5 mm wide scaffolds. The effects of diffusing species and the distance inside the scaffold and their interaction were highly significant ($p < 0.0001$) on the intracellular transduction. The superiority of transduction with GET system over the conventional poly-arginine cell penetrating peptide suggests the system can be employed for delivery of functional proteins with lower doses and minimized toxicity. However, there is no guarantee of clear bypassing the endocytosis mediated uptake for the GET system [118]. The gradient delivery of P21-mR-8R confirmed that the cellular uptake adds up to the factors contributing to the diffusion behaviour of biologically active proteins other than the size and interaction filtering strategies described by Lieleg and Ribbeck [135].

7.1.4. Model application in induced myogenic differentiation

Combining the merits of the novel GET proteins and the compartmental diffusion model, gradient delivery of transcription factor MyoD to cell-laden hydrogels was investigated. We demonstrated the capability of encapsulation of different cell types. However, each cell type demonstrated different proliferation characteristics. Cell types exhibiting limited proliferative abilities within agarose/gelatin hydrogels allowed the accumulation of fluorescent signals within cells. This, concomitantly with slow

diffusion of MyoD, can result in enhanced uptake of the protein with a subsequent functionality. However, the limited proliferation and declined cell viability would not result in the target directed functionality. This was the case with dermal fibroblasts in which the gradient P21-mR-MyoD-8R delivery was demonstrated but not the anticipated gradient myogenic profile. Dermal fibroblasts are difficult to replicate in *in-vivo* and *in-vitro* environments [238]. On the other hand, HEK 293T cells survive encapsulation within 3D hydrogel matrices with optimum viabilities [247, 248]. The persistent proliferation together with slow diffusion of P21-mR-MyoD-8R did not result in steep gradient along the 5 mm wide hydrogel membrane.

Translating the developed subtle gradient uptake of P21-mR-MyoD-8R into gradient myogenic differentiation of the HEK 293T did not result in a distinct differentiation pattern. Despite the fact that all encapsulated cells demonstrated increased MyoD gene expression as compared to the control scaffolds, the response was irrespective of the distance away from P21-mR-MyoD-8R. Early myogenesis is characterized by high MyoD expression compared to decline in expression in the later phases of differentiation [249]. Consequently, the exposure to variable concentrations of P21-mR-MyoD-8R might have altered the MyoD gene expression profile at the selected time point. Careful selection of the target genes relevant to the differentiation stage would have assisted the proper monitoring of the gradient myogenic differentiation. It is advisable to monitor more than one gene to have better insights of the myogenic differentiation.

7.2. Future directions

The findings presented in this thesis reflected the validity of the modified diffusion model to generate and monitor diffusion gradients of biologically active proteins across cell-laden hydrogel systems. The model together with GET system could be recruited to direct cellular responses in a gradient manner with control over tissue fate. Polymeric microspheres with optimum release kinetics could be devoted to maintain structural and spatial stability of the encapsulated bioactive proteins. Furthermore, release depots could dictate the source protein concentrations without the need of continuous replenishment of the source compartment.

Agarose-based hydrogel systems support cell encapsulation and can be selectively devoted for chondrogenic/osteogenic differentiation characteristic of ligament/bone interface. Opposing 3D intracellular gradient delivery of functional GET proteins could

General discussion & future directions

be recruited for development of biomimetic scaffolds with the complex structure featuring tissue interfaces. Alternatively, other hydrogel systems with improved cellular viabilities and proliferation characteristics can be employed to recreate soft and vascularized tissue structures. The continuous change of the cellular environment in terms of cell number, degradation of the hydrogel system combined with the build-up of the inherent ECM need to be studied to contemplate the factors contributing to concentration gradient manipulation. Finally, careful choice of multiple differentiation markers corresponding to the continuous change of gene profiling with time together with immunohistochemistry could be devoted to study cellular responses towards the generated chemical gradients.

Chapter 8: References

1. Yamada, K.M. and E. Cukierman, *Modeling tissue morphogenesis and cancer in 3D*. Cell, 2007. **130**(4): p. 601-10.
2. Keenan, T.M. and A. Folch, *Biomolecular gradients in cell culture systems*. Lab Chip, 2008. **8**(1): p. 34-57.
3. Wolpert, L., *Positional information and the spatial pattern of cellular differentiation*. J Theor Biol, 1969. **25**(1): p. 1-47.
4. Turing, A.M., *The chemical basis of morphogenesis*. 1953. Bull Math Biol, 1990. **52**(1-2): p. 153-97; discussion 119-52.
5. Gierer, A. and H. Meinhardt, *A theory of biological pattern formation*. Kybernetik, 1972. **12**(1): p. 30-9.
6. Meinhardt, H. and A. Gierer, *Pattern formation by local self-activation and lateral inhibition*. Bioessays, 2000. **22**(8): p. 753-60.
7. Lander, A.D., *Morpheus unbound: reimagining the morphogen gradient*. Cell, 2007. **128**(2): p. 245-56.
8. Ferguson, E.L. and K.V. Anderson, *Decapentaplegic acts as a morphogen to organize dorsal-ventral pattern in the Drosophila embryo*. Cell, 1992. **71**(3): p. 451-61.
9. Driever, W. and C. Nusslein-Volhard, *The bicoid protein determines position in the Drosophila embryo in a concentration-dependent manner*. Cell, 1988. **54**(1): p. 95-104.
10. Godwin, J.W. and J.P. Brookes, *Regeneration, tissue injury and the immune response*. J Anat, 2006. **209**(4): p. 423-32.
11. Lüthmann, T. and H. Hall, *Cell Guidance by 3D-Gradients in Hydrogel Matrices: Importance for Biomedical Applications*. Materials, 2009. **2**(3): p. 1058-1083.
12. Sant, S., et al., *Biomimetic Gradient Hydrogels for Tissue Engineering*. Can J Chem Eng, 2010. **88**(6): p. 899-911.
13. Khademhosseini, A., et al., *Microscale technologies for tissue engineering and biology*. Proc Natl Acad Sci U S A, 2006. **103**(8): p. 2480-7.
14. Seidi, A., et al., *Gradient biomaterials for soft-to-hard interface tissue engineering*. Acta Biomater, 2011. **7**(4): p. 1441-51.

15. Singh, M., C. Berkland, and M.S. Detamore, *Strategies and applications for incorporating physical and chemical signal gradients in tissue engineering*. Tissue Eng Part B Rev, 2008. **14**(4): p. 341-66.
16. Wu, J., et al., *Gradient biomaterials and their influences on cell migration*. Interface Focus, 2012. **2**(3): p. 337-55.
17. Nguyen, E.H., M.P. Schwartz, and W.L. Murphy, *Biomimetic approaches to control soluble concentration gradients in biomaterials*. Macromol Biosci, 2011. **11**(4): p. 483-92.
18. Peret, B.J. and W.L. Murphy, *Controllable Soluble Protein Concentration Gradients in Hydrogel Networks*. Adv Funct Mater, 2008. **18**(21): p. 3410-3417.
19. Schonherr, E. and H.J. Hausser, *Extracellular matrix and cytokines: a functional unit*. Dev Immunol, 2000. **7**(2-4): p. 89-101.
20. Ghosh, K. and D.E. Ingber, *Micromechanical control of cell and tissue development: implications for tissue engineering*. Adv Drug Deliv Rev, 2007. **59**(13): p. 1306-18.
21. Discher, D.E., P. Janmey, and Y.L. Wang, *Tissue cells feel and respond to the stiffness of their substrate*. Science, 2005. **310**(5751): p. 1139-43.
22. Mikos, A.G., et al., *Engineering complex tissues*. Tissue Eng, 2006. **12**(12): p. 3307-39.
23. Phillips, J.E., et al., *Engineering graded tissue interfaces*. Proc Natl Acad Sci U S A, 2008. **105**(34): p. 12170-5.
24. Hall, S.J., *Basic biomechanics*. 2007: McGraw-Hill Boston, MA:.
25. Pope, A.J., et al., *Three-dimensional transmural organization of perimysial collagen in the heart*. Am J Physiol Heart Circ Physiol, 2008. **295**(3): p. H1243-H1252.
26. Vishwakarma, A., et al., *Stem Cell Biology and Tissue Engineering in Dental Sciences*. 2014: Academic Press.
27. Ali, S., et al., *The effect of Young's modulus on the neuronal differentiation of mouse embryonic stem cells*. Acta Biomater, 2015. **25**: p. 253-67.

28. Carter, D.R., M.C. Van Der Meulen, and G.S. Beaupre, *Mechanical factors in bone growth and development*. Bone, 1996. **18**(1 Suppl): p. 5S-10S.
29. Hove, J.R., et al., *Intracardiac fluid forces are an essential epigenetic factor for embryonic cardiogenesis*. Nature, 2003. **421**(6919): p. 172-7.
30. Moore, K.A., et al., *Control of embryonic lung branching morphogenesis by the Rho activator, cytotoxic necrotizing factor I*. J Surg Res, 2002. **104**(2): p. 95-100.
31. Inanlou, M.R., M. Baguma-Nibasheka, and B. Kablar, *The role of fetal breathing-like movements in lung organogenesis*. Histol Histopathol, 2005. **20**(4): p. 1261-6.
32. Chen, C.S., et al., *Geometric control of cell life and death*. Science, 1997. **276**(5317): p. 1425-8.
33. Nelson, C.M., et al., *Emergent patterns of growth controlled by multicellular form and mechanics*. Proc Natl Acad Sci U S A, 2005. **102**(33): p. 11594-9.
34. Gomez, E.W., et al., *Tissue geometry patterns epithelial-mesenchymal transition via intercellular mechanotransduction*. J Cell Biochem, 2010. **110**(1): p. 44-51.
35. Engler, A.J., et al., *Matrix elasticity directs stem cell lineage specification*. Cell, 2006. **126**(4): p. 677-89.
36. Jez, M., et al., *Concise review: the role of oxygen in hematopoietic stem cell physiology*. J Cell Physiol, 2015. **230**(9): p. 1999-2005.
37. Simon, M.C. and B. Keith, *The role of oxygen availability in embryonic development and stem cell function*. Nat Rev Mol Cell Biol, 2008. **9**(4): p. 285-96.
38. Genbacev, O., et al., *Regulation of human placental development by oxygen tension*. Science, 1997. **277**(5332): p. 1669-72.
39. Levesque, J.P. and I.G. Winkler, *Hierarchy of immature hematopoietic cells related to blood flow and niche*. Curr Opin Hematol, 2011. **18**(4): p. 220-5.
40. Nelson, C.M., *Geometric control of tissue morphogenesis*. Biochim Biophys Acta, 2009. **1793**(5): p. 903-10.
41. Crick, F., *Diffusion in embryogenesis*. Nature, 1970. **225**(5231): p. 420-2.

42. Makarenkova, H.P., et al., *Differential interactions of FGFs with heparan sulfate control gradient formation and branching morphogenesis*. *Sci Signal*, 2009. **2**(88): p. ra55.
43. Tickle, C. and H. Barker, *The Sonic hedgehog gradient in the developing limb*. *Wiley Interdiscip Rev Dev Biol*, 2013. **2**(2): p. 275-90.
44. Ericson, J., et al., *Pax6 controls progenitor cell identity and neuronal fate in response to graded Shh signaling*. *Cell*, 1997. **90**(1): p. 169-80.
45. Paves, H. and M. Saarma, *Neurotrophins as in vitro growth cone guidance molecules for embryonic sensory neurons*. *Cell and tissue research*, 1997. **290**(2): p. 285-297.
46. Xu, P.F., et al., *Construction of a vertebrate embryo from two opposing morphogen gradients*. *Science*, 2014. **344**(6179): p. 87-9.
47. Metzger, R.J. and M.A. Krasnow, *Genetic control of branching morphogenesis*. *Science*, 1999. **284**(5420): p. 1635-9.
48. Weaver, M., N.R. Dunn, and B.L. Hogan, *Bmp4 and Fgf10 play opposing roles during lung bud morphogenesis*. *Development*, 2000. **127**(12): p. 2695-704.
49. Hogan, B.L., et al., *Branching morphogenesis of the lung: new models for a classical problem*. *Cold Spring Harb Symp Quant Biol*, 1997. **62**: p. 249-56.
50. Caudron, M., et al., *Spatial coordination of spindle assembly by chromosome-mediated signaling gradients*. *Science*, 2005. **309**(5739): p. 1373-6.
51. Crock, P.A., et al., *Multiple pituitary hormone gradients from inferior petrosal sinus sampling in Cushing's disease*. *Acta Endocrinol (Copenh)*, 1988. **119**(1): p. 75-80.
52. Wang, F., *The signaling mechanisms underlying cell polarity and chemotaxis*. *Cold Spring Harb Perspect Biol*, 2009. **1**(4): p. a002980.
53. Firtel, R.A. and C.Y. Chung, *The molecular genetics of chemotaxis: sensing and responding to chemoattractant gradients*. *Bioessays*, 2000. **22**(7): p. 603-15.
54. Eccles, S.A., *Targeting key steps in metastatic tumour progression*. *Curr Opin Genet Dev*, 2005. **15**(1): p. 77-86.

55. Strieter, R.M., et al., *CXC chemokines in angiogenesis of cancer*. *Semin Cancer Biol*, 2004. **14**(3): p. 195-200.
56. Luppi, F., et al., *Interleukin-8 stimulates cell proliferation in non-small cell lung cancer through epidermal growth factor receptor transactivation*. *Lung Cancer*, 2007. **56**(1): p. 25-33.
57. Mortimer, D., et al., *Growth cone chemotaxis*. *Trends Neurosci*, 2008. **31**(2): p. 90-8.
58. Luster, A.D., *Chemotaxis: role in immune response*. eLS, 2001.
59. Lo, C.M., et al., *Cell movement is guided by the rigidity of the substrate*. *Biophys J*, 2000. **79**(1): p. 144-52.
60. Cukierman, E., R. Pankov, and K.M. Yamada, *Cell interactions with three-dimensional matrices*. *Curr Opin Cell Biol*, 2002. **14**(5): p. 633-9.
61. Cao, X. and M.S. Shoichet, *Defining the concentration gradient of nerve growth factor for guided neurite outgrowth*. *Neuroscience*, 2001. **103**(3): p. 831-40.
62. Aznavoorian, S., et al., *Integrin alphavbeta3 mediates chemotactic and haptotactic motility in human melanoma cells through different signaling pathways*. *J Biol Chem*, 1996. **271**(6): p. 3247-54.
63. Yang, H.Y., T.D. La, and R.R. Isseroff, *Utilizing custom-designed galvanotaxis chambers to study directional migration of prostate cells*. *J Vis Exp*, 2014(94).
64. Stocker, S., M. Hiery, and G. Marriott, *Phototactic migration of Dictyostelium cells is linked to a new type of gelsolin-related protein*. *Mol Biol Cell*, 1999. **10**(1): p. 161-78.
65. Lowe, B., *The role of Ca²⁺ in deflection-induced excitation of motile, mechanoresponsive balancer cilia in the ctenophore statocyst*. *J Exp Biol*, 1997. **200**(Pt 11): p. 1593-606.
66. Chada, S., et al., *Cytomechanics of neurite outgrowth from chick brain neurons*. *J Cell Sci*, 1997. **110** (Pt 10): p. 1179-86.

67. Vickerman, V., et al., *Design, fabrication and implementation of a novel multi-parameter control microfluidic platform for three-dimensional cell culture and real-time imaging*. Lab Chip, 2008. **8**(9): p. 1468-77.
68. Wang, X., et al., *Growth factor gradients via microsphere delivery in biopolymer scaffolds for osteochondral tissue engineering*. J Control Release, 2009. **134**(2): p. 81-90.
69. Ilkhanizadeh, S., A.I. Teixeira, and O. Hermanson, *Inkjet printing of macromolecules on hydrogels to steer neural stem cell differentiation*. Biomaterials, 2007. **28**(27): p. 3936-43.
70. He, J., et al., *Rapid generation of biologically relevant hydrogels containing long-range chemical gradients*. Adv Funct Mater, 2010. **20**(1): p. 131-137.
71. Moore, K., M. MacSween, and M. Shoichet, *Immobilized concentration gradients of neurotrophic factors guide neurite outgrowth of primary neurons in macroporous scaffolds*. Tissue Eng, 2006. **12**(2): p. 267-78.
72. Wong, J.Y., et al., *Directed movement of vascular smooth muscle cells on gradient-compliant hydrogels*. Langmuir, 2003. **19**(5): p. 1908-1913.
73. Nemir, S., H.N. Hayenga, and J.L. West, *PEGDA hydrogels with patterned elasticity: Novel tools for the study of cell response to substrate rigidity*. Biotechnol Bioeng, 2010. **105**(3): p. 636-44.
74. Park, J.Y., et al., *Simultaneous generation of chemical concentration and mechanical shear stress gradients using microfluidic osmotic flow comparable to interstitial flow*. Lab Chip, 2009. **9**(15): p. 2194-202.
75. Kloxin, A.M., J.A. Benton, and K.S. Anseth, *In situ elasticity modulation with dynamic substrates to direct cell phenotype*. Biomaterials, 2010. **31**(1): p. 1-8.
76. Marklein, R.A. and J.A. Burdick, *Spatially controlled hydrogel mechanics to modulate stem cell interactions*. Soft Matter, 2010. **6**(1): p. 136-143.
77. Li, N. and A. Folch, *Integration of topographical and biochemical cues by axons during growth on microfabricated 3-D substrates*. Exp Cell Res, 2005. **311**(2): p. 307-16.
78. Scholl, M., et al., *Ordered networks of rat hippocampal neurons attached to silicon oxide surfaces*. J Neurosci Methods, 2000. **104**(1): p. 65-75.

79. Loesberg, W.A., et al., *The threshold at which substrate nanogroove dimensions may influence fibroblast alignment and adhesion*. *Biomaterials*, 2007. **28**(27): p. 3944-51.
80. Miao, X. and D. Sun, *Graded/gradient porous biomaterials*. *Materials*, 2009. **3**(1): p. 26-47.
81. Al-Abboodi, A., et al., *In situ generation of tunable porosity gradients in hydrogel-based scaffolds for microfluidic cell culture*. *Adv Healthc Mater*, 2014. **3**(10): p. 1655-70.
82. Oh, S.H., et al., *In vitro and in vivo characteristics of PCL scaffolds with pore size gradient fabricated by a centrifugation method*. *Biomaterials*, 2007. **28**(9): p. 1664-71.
83. Bai, H., et al., *Biomimetic gradient scaffold from ice-templating for self-seeding of cells with capillary effect*. *Acta Biomater*, 2015. **20**: p. 113-9.
84. Du, F., et al., *Gradient nanofibrous chitosan/poly varepsilon-caprolactone scaffolds as extracellular microenvironments for vascular tissue engineering*. *Biomaterials*, 2012. **33**(3): p. 762-70.
85. Postma, M. and P.J. van Haastert, *Mathematics of experimentally generated chemoattractant gradients*, in *Chemotaxis*. 2009, Springer. p. 473-488.
86. Fok, S., et al., *Planar microfluidic chamber for generation of stable and steep chemoattractant gradients*. *Biophys J*, 2008. **95**(3): p. 1523-30.
87. Pellet-Many, C., *Chemotactic Migration of Endothelial Cells Towards VEGF-A165*. *Methods in molecular biology* (Clifton, N.J.), 2015. **1332**.
88. Zigmond, S.H., *Ability of polymorphonuclear leukocytes to orient in gradients of chemotactic factors*. *J Cell Biol*, 1977. **75**(2 Pt 1): p. 606-16.
89. Ma, S., et al., *Store-operated Ca(2)(+) entry mediated regulation of polarization in differentiated human neutrophil-like HL-60 cells under hypoxia*. *Mol Med Rep*, 2014. **9**(3): p. 819-24.
90. Zicha, D., G. Dunn, and G. Jones, *Analyzing chemotaxis using the Dunn direct-viewing chamber*. *Methods Mol Biol*, 1997. **75**: p. 449-57.
91. Chen, Y.B., et al., *Chemotactic Responses of Neural Stem Cells to SDF-1 alpha Correlate Closely with Their Differentiation Status*. *Journal of Molecular Neuroscience*, 2014. **54**(2): p. 219-233.

92. Jeon, N.L., et al., *Generation of solution and surface gradients using microfluidic systems*. Langmuir, 2000. **16**(22): p. 8311-8316.
93. van Duinen, V., et al., *Microfluidic 3D cell culture: from tools to tissue models*. Curr Opin Biotechnol, 2015. **35**: p. 118-26.
94. Zhou, B., et al., *Generation of tunable and pulsatile concentration gradients via microfluidic network*. Microfluidics and Nanofluidics, 2015. **18**(2): p. 175-184.
95. Kim, T., M. Pinelis, and M.M. Maharbiz, *Generating steep, shear-free gradients of small molecules for cell culture*. Biomed Microdevices, 2009. **11**(1): p. 65-73.
96. Chisti, Y., *Hydrodynamic damage to animal cells*. Crit Rev Biotechnol, 2001. **21**(2): p. 67-110.
97. Amadi, O.C., et al., *A low resistance microfluidic system for the creation of stable concentration gradients in a defined 3D microenvironment*. Biomed Microdevices, 2010. **12**(6): p. 1027-41.
98. Quake, S.R. and A. Scherer, *From micro- to nanofabrication with soft materials*. Science, 2000. **290**(5496): p. 1536-40.
99. Lii, J., et al., *Real-time microfluidic system for studying mammalian cells in 3D microenvironments*. Anal Chem, 2008. **80**(10): p. 3640-7.
100. Bischel, L.L., et al., *Tubeless microfluidic angiogenesis assay with three-dimensional endothelial-lined microvessels*. Biomaterials, 2013. **34**(5): p. 1471-7.
101. Yu, S.R., et al., *Fgf8 morphogen gradient forms by a source-sink mechanism with freely diffusing molecules*. Nature, 2009. **461**(7263): p. 533-6.
102. Suciati, T., et al., *Zonal release of proteins within tissue engineering scaffolds*. J Mater Sci Mater Med, 2006. **17**(11): p. 1049-56.
103. Guo, X., et al., *Creating 3D angiogenic growth factor gradients in fibrous constructs to guide fast angiogenesis*. Biomacromolecules, 2012. **13**(10): p. 3262-71.

104. Erisken, C., D.M. Kalyon, and H. Wang, *Functionally graded electrospun polycaprolactone and beta-tricalcium phosphate nanocomposites for tissue engineering applications*. *Biomaterials*, 2008. **29**(30): p. 4065-73.
105. Luhmann, T., et al., *The induction of cell alignment by covalently immobilized gradients of the 6th Ig-like domain of cell adhesion molecule L1 in 3D-fibrin matrices*. *Biomaterials*, 2009. **30**(27): p. 4503-12.
106. Oh, S.H., T.H. Kim, and J.H. Lee, *Creating growth factor gradients in three dimensional porous matrix by centrifugation and surface immobilization*. *Biomaterials*, 2011. **32**(32): p. 8254-60.
107. Dodla, M.C. and R.V. Bellamkonda, *Anisotropic scaffolds facilitate enhanced neurite extension in vitro*. *J Biomed Mater Res A*, 2006. **78**(2): p. 213-21.
108. Gunawan, R.C., et al., *Cell migration and polarity on microfabricated gradients of extracellular matrix proteins*. *Langmuir*, 2006. **22**(9): p. 4250-8.
109. Burdick, J.A., A. Khademhosseini, and R. Langer, *Fabrication of gradient hydrogels using a microfluidics/photopolymerization process*. *Langmuir*, 2004. **20**(13): p. 5153-6.
110. Kunze, A., et al., *Synergistic NGF/B27 gradients position synapses heterogeneously in 3D micropatterned neural cultures*. *PLoS One*, 2011. **6**(10): p. e26187.
111. Ali, H., et al., *Chemoattractant receptor cross-desensitization*. *J Biol Chem*, 1999. **274**(10): p. 6027-30.
112. Foxman, E.F., J.J. Campbell, and E.C. Butcher, *Multistep navigation and the combinatorial control of leukocyte chemotaxis*. *J Cell Biol*, 1997. **139**(5): p. 1349-60.
113. White, L.J., et al., *Accelerating protein release from microparticles for regenerative medicine applications*. *Mater Sci Eng C Mater Biol Appl*, 2013. **33**(5): p. 2578-83.
114. Yang, Y.Y., H.H. Chia, and T.S. Chung, *Effect of preparation temperature on the characteristics and release profiles of PLGA microspheres containing protein fabricated by double-emulsion solvent extraction/evaporation method*. *Journal of controlled release : official journal of the Controlled Release Society*, 2000. **69**(1): p. 81-96.

115. Smith, P.K., et al., *Measurement of protein using bicinchoninic acid*. Analytical biochemistry, 1985. **150**(1): p. 76-85.
116. Smith, P., et al., *Measurement of protein using bicinchoninic acid*. Analytical biochemistry, 1985. **150**(1): p. 76-85.
117. Campbell, R.E., et al., *A monomeric red fluorescent protein*. Proc Natl Acad Sci U S A, 2002. **99**(12): p. 7877-82.
118. Dixon, J.E., et al., *Highly efficient delivery of functional cargoes by the synergistic effect of GAG binding motifs and cell-penetrating peptides*. Proc Natl Acad Sci U S A, 2016.
119. Jachimska, B., M. Wasilewska, and Z. Adamczyk, *Characterization of globular protein solutions by dynamic light scattering, electrophoretic mobility, and viscosity measurements*. Langmuir, 2008. **24**(13): p. 6866-72.
120. Parmenter, C.D.J., et al., *Making the practically impossible 'merely difficult' – Cryogenic FIB Lift-out for 'damage free' soft matter imaging*. Microscopy Research and Technique, 2016. **Accepted**.
121. Walther, F., et al., *Stability of the hydrophilic behavior of oxygen plasma activated SU-8*. Journal of Micromechanics and Microengineering, 2007. **17**(3): p. 524-531.
122. Crank, J., *The mathematics of diffusion*. 1979: Oxford university press.
123. Goodhill, G.J., *Diffusion in axon guidance*. Eur J Neurosci, 1997. **9**(7): p. 1414-21.
124. Knapp, D.M., E.F. Helou, and R.T. Tranquillo, *A fibrin or collagen gel assay for tissue cell chemotaxis: assessment of fibroblast chemotaxis to GRGDSP*. Exp Cell Res, 1999. **247**(2): p. 543-53.
125. Pujic, Z., et al., *Assays for eukaryotic cell chemotaxis*. Comb Chem High Throughput Screen, 2009. **12**(6): p. 580-8.
126. Nelson, R.D., P.G. Quie, and R.L. Simmons, *Chemotaxis under agarose: a new and simple method for measuring chemotaxis and spontaneous migration of human polymorphonuclear leukocytes and monocytes*. J Immunol, 1975. **115**(6): p. 1650-6.

127. Uden, A.M., I. Hafstrom, and J. Palmblad, *Relation to chemotactic factor gradients to neutrophil migration and orientation under agarose*. *J Leukoc Biol*, 1986. **39**(1): p. 27-35.
128. Fisher, P.R., R. Merkl, and G. Gerisch, *Quantitative analysis of cell motility and chemotaxis in Dictyostelium discoideum by using an image processing system and a novel chemotaxis chamber providing stationary chemical gradients*. *J Cell Biol*, 1989. **108**(3): p. 973-84.
129. Yamamoto, M., K. Yanase, and Y. Tabata, *Generation of type I collagen gradient in polyacrylamide hydrogels by a simple diffusion-controlled hydrolysis of amide groups*. *Materials*, 2010. **3**(4): p. 2393-2404.
130. *National Center for Biotechnology Information. PubChem Compound Database; CID=16850, <https://pubchem.ncbi.nlm.nih.gov/compound/16850>*.
131. Peters, S.R., *A practical guide to frozen section technique*. 2010: Springer.
132. Yoshina-Ishii, C., et al., *Diffusive dynamics of vesicles tethered to a fluid supported bilayer by single-particle tracking*. *Langmuir*, 2006. **22**(13): p. 5682-9.
133. Johansson, B., et al., *Label-free measurements of the diffusivity of molecules in lipid membranes*. *Chemphyschem*, 2014. **15**(3): p. 486-91.
134. Liang, S., et al., *Protein diffusion in agarose hydrogel in situ measured by improved refractive index method*. *J Control Release*, 2006. **115**(2): p. 189-96.
135. Lieleg, O. and K. Ribbeck, *Biological hydrogels as selective diffusion barriers*. *Trends Cell Biol*, 2011. **21**(9): p. 543-51.
136. Hickson, T.G. and A. Polson, *Some physical characteristics of the agarose molecule*. *Biochim Biophys Acta*, 1968. **165**(1): p. 43-58.
137. Zeiger, R.S., et al., *Role of base composition in the electrophoresis of microbial and crab DNA in polyacrylamide gels*. *Nat New Biol*, 1972. **238**(81): p. 65-9.
138. Griess, G.A., et al., *The sieving of spheres during agarose gel electrophoresis: quantitation and modeling*. *Biopolymers*, 1989. **28**(8): p. 1475-84.
139. Holmes, D.L. and N.C. Stellwagen, *The electric field dependence of DNA mobilities in agarose gels: a reinvestigation*. *Electrophoresis*, 1990. **11**(1): p. 5-15.

140. Pernodet, N., M. Maaloum, and B. Tinland, *Pore size of agarose gels by atomic force microscopy*. Electrophoresis, 1997. **18**(1): p. 55-8.
141. Maaloum, M., N. Pernodet, and B. Tinland, *Agarose gel structure using atomic force microscopy: gel concentration and ionic strength effects*. Electrophoresis, 1998. **19**(10): p. 1606-10.
142. Slater, G.W., et al., *Quantitative analysis of the three regimes of DNA electrophoresis in agarose gels*. Biopolymers, 1988. **27**(3): p. 509-24.
143. Ferguson, K.A., *Starch-Gel Electrophoresis--Application to the Classification of Pituitary Proteins and Polypeptides*. Metabolism, 1964. **13**: p. SUPPL:985-1002.
144. Hecht, A.M., R. Duplessix, and E. Geissler, *Structural inhomogeneities in the range 2.5-2500. Å in polyacrylamide gels*. Macromolecules, 1985. **18**(11): p. 2167-2173.
145. Amsterdam, A., Z. Er-el, and S. Shaltiel, *Ultrastructure of beaded agarose*. Arch Biochem Biophys, 1975. **171**(2): p. 673-7.
146. Mitchell, G., et al., *Quantitative characterization of microscopic variations in the cross-link density of gels*. Macromolecules, 2002. **35**(4): p. 1336-1341.
147. Stellwagen, N.C., *Electrophoresis of DNA in agarose gels, polyacrylamide gels and in free solution*. Electrophoresis, 2009. **30 Suppl 1**: p. S188-95.
148. Bhat, S., A. Tripathi, and A. Kumar, *Supramacroporous chitosan-agarose-gelatin cryogels: in vitro characterization and in vivo assessment for cartilage tissue engineering*. J R Soc Interface, 2011. **8**(57): p. 540-54.
149. America, G.M.I.o., *Standard Methods for the Sampling and Testing of Gelatins*. Gelatins manufacturing Institute of America.
150. Saxena, A., et al., *Effect of agar-gelatin compositions on the release of salbutamol tablets*. Int J Pharm Investig, 2011. **1**(2): p. 93-8.
151. Hellio, D. and M. Djabourov. *Physically and chemically crosslinked gelatin gels*. in *Macromolecular Symposia*. 2006. Wiley Online Library.
152. Perez, R.A., H.W. Kim, and M.P. Ginebra, *Polymeric additives to enhance the functional properties of calcium phosphate cements*. J Tissue Eng, 2012. **3**(1): p. 2041731412439555.

153. Huang, Y., et al., *In vitro characterization of chitosan-gelatin scaffolds for tissue engineering*. Biomaterials, 2005. **26**(36): p. 7616-27.
154. Liu, Y. and M.B. Chan-Park, *Hydrogel based on interpenetrating polymer networks of dextran and gelatin for vascular tissue engineering*. Biomaterials, 2009. **30**(2): p. 196-207.
155. Hule, R.A., et al., *Correlations between structure, material properties and bioproperties in self-assembled beta-hairpin peptide hydrogels*. Faraday Discuss, 2008. **139**: p. 251-64; discussion 309-25, 419-20.
156. Pluen, A., et al., *Diffusion of macromolecules in agarose gels: comparison of linear and globular configurations*. Biophys J, 1999. **77**(1): p. 542-52.
157. Wischke, C. and H.H. Borchert, *Fluorescein isothiocyanate labelled bovine serum albumin (FITC-BSA) as a model protein drug: opportunities and drawbacks*. Pharmazie, 2006. **61**(9): p. 770-4.
158. Tanford, C. and J.G. Buzzell, *The Viscosity of Aqueous Solutions of Bovine Serum Albumin between pH 4.3 and 10.5*. The Journal of Physical Chemistry, 1956. **60**(2): p. 225-231.
159. Barbosa, L.R., et al., *The importance of protein-protein interactions on the pH-induced conformational changes of bovine serum albumin: a small-angle X-ray scattering study*. Biophys J, 2010. **98**(1): p. 147-57.
160. Rao, J.K., D.V. Ramesh, and K.P. Rao, *Controlled release systems for proteins based on gelatin microspheres*. J Biomater Sci Polym Ed, 1994. **6**(5): p. 391-8.
161. Saltzman, W.M., et al., *Antibody diffusion in human cervical mucus*. Biophys J, 1994. **66**(2 Pt 1): p. 508-15.
162. <https://www.thermofisher.com/order/catalog/product/P10361>. [cited 2015 04/10/2015].
163. Granath, K.A. and B.E. Kvist, *Molecular weight distribution analysis by gel chromatography on Sephadex*. J Chromatogr, 1967. **28**(1): p. 69-81.
164. Lebrun, L. and G.A. Junter, *Diffusion of sucrose and dextran through agar gel membranes*. Enzyme Microb Technol, 1993. **15**(12): p. 1057-62.
165. Ramanujan, S., et al., *Diffusion and convection in collagen gels: implications for transport in the tumor interstitium*. Biophys J, 2002. **83**(3): p. 1650-60.

166. Lawrence, J.R., G.M. Wolfaardt, and D.R. Korber, *Determination of diffusion coefficients in biofilms by confocal laser microscopy*. Appl Environ Microbiol, 1994. **60**(4): p. 1166-73.
167. Biswas, A., et al., *Endoprotease-mediated intracellular protein delivery using nanocapsules*. ACS Nano, 2011. **5**(2): p. 1385-94.
168. Jain, A., et al., *Peptide and protein delivery using new drug delivery systems*. Crit Rev Ther Drug Carrier Syst, 2013. **30**(4): p. 293-329.
169. Akash, M.S., K. Rehman, and S. Chen, *Polymeric-based particulate systems for delivery of therapeutic proteins*. Pharm Dev Technol, 2015: p. 1-12.
170. Wang, W., *Instability, stabilization, and formulation of liquid protein pharmaceuticals*. Int J Pharm, 1999. **185**(2): p. 129-88.
171. Oh, W.-K., O.S. Kwon, and J. Jang, *Conducting polymer nanomaterials for biomedical applications: Cellular interfacing and biosensing*. Polymer Reviews, 2013. **53**(3): p. 407-442.
172. Sinha, V.R. and A. Trehan, *Biodegradable microspheres for protein delivery*. J Control Release, 2003. **90**(3): p. 261-80.
173. Kirby, G.T., et al., *PLGA-based microparticles for the sustained release of BMP-2*. Polymers, 2011. **3**(1): p. 571-586.
174. Mi, F.L., et al., *Chitin/PLGA blend microspheres as a biodegradable drug delivery system: a new delivery system for protein*. Biomaterials, 2003. **24**(27): p. 5023-36.
175. Holy, C.E., et al., *In vitro degradation of a novel poly(lactide-co-glycolide) 75/25 foam*. Biomaterials, 1999. **20**(13): p. 1177-85.
176. Huatan, H., et al., *Preparation and characterization of poly(epsilon-caprolactone) polymer blends for the delivery of proteins*. Biomaterials, 1995. **16**(17): p. 1297-303.
177. Makadia, H.K. and S.J. Siegel, *Poly Lactic-co-Glycolic Acid (PLGA) as Biodegradable Controlled Drug Delivery Carrier*. Polymers (Basel), 2011. **3**(3): p. 1377-1397.

178. Lucke, A., et al., *Biodegradable poly(D,L-lactic acid)-poly(ethylene glycol)-monomethyl ether diblock copolymers: structures and surface properties relevant to their use as biomaterials*. *Biomaterials*, 2000. **21**(23): p. 2361-70.
179. Yang, Y.Y., H.H. Chia, and T.S. Chung, *Effect of preparation temperature on the characteristics and release profiles of PLGA microspheres containing protein fabricated by double-emulsion solvent extraction/evaporation method*. *J Control Release*, 2000. **69**(1): p. 81-96.
180. Yan, C.H., et al., *Characterization and morphological analysis of protein-loaded poly(lactide-co-glycolide) microparticles prepared by water-in-oil-in-water emulsion technique*. *Journal of Controlled Release*, 1994. **32**(3): p. 231-241.
181. Mahboubian, A., et al., *Preparation and In-vitro Evaluation of Controlled Release PLGA Microparticles Containing Triptoreline*. *Iranian Journal of Pharmaceutical Research*, 2010. **9**(4): p. 369-378.
182. Ravi, S., et al., *Development and characterization of polymeric microspheres for controlled release protein loaded drug delivery system*. *Indian journal of pharmaceutical sciences*, 2008. **70**(3): p. 303-9.
183. Kang, F. and J. Singh, *Effect of additives on the release of a model protein from PLGA microspheres*. *AAPS PharmSciTech*, 2001. **2**(4): p. 30.
184. Bozdag, S., et al., *In vitro evaluation and intra-articular administration of biodegradable microspheres containing naproxen sodium*. *Journal of microencapsulation*, 2001. **18**(4): p. 443-56.
185. Liu, Y., et al., *Investigation of polyDL-lactide-b-poly(ethylene glycol)-b-polyDL-lactide microspheres containing plasmid DNA*. *Chinese Journal of Polymer Science*, 2004. **22**(3): p. 205-214.
186. Patel, B., V. Gupta, and F. Ahsan, *PEG-PLGA based large porous particles for pulmonary delivery of a highly soluble drug, low molecular weight heparin*. *Journal of controlled release : official journal of the Controlled Release Society*, 2012. **162**(2): p. 310-20.
187. Makadia, H.K. and S.J. Siegel, *Poly Lactic-co-Glycolic Acid (PLGA) as Biodegradable Controlled Drug Delivery Carrier*. *Polymers*, 2011. **3**(3): p. 1377-1397.
188. Rosca, I.D., F. Watari, and M. Uo, *Microparticle formation and its mechanism in single and double emulsion solvent evaporation*. *Journal of controlled*

- release : official journal of the Controlled Release Society, 2004. **99**(2): p. 271-80.
189. Kissel, T., Y. Li, and F. Unger, *ABA-triblock copolymers from biodegradable polyester A-blocks and hydrophilic poly(ethylene oxide) B-blocks as a candidate for in situ forming hydrogel delivery systems for proteins*. *Advanced drug delivery reviews*, 2002. **54**(1): p. 99-134.
 190. Copolovici, D.M., et al., *Cell-penetrating peptides: design, synthesis, and applications*. *ACS Nano*, 2014. **8**(3): p. 1972-94.
 191. Torchilin, V., *Intracellular delivery of protein and peptide therapeutics*. *Drug Discov Today Technol*, 2008. **5**(2-3): p. e95-e103.
 192. Erazo-Oliveras, A., et al., *Protein delivery into live cells by incubation with an endosomolytic agent*. *Nat Methods*, 2014. **11**(8): p. 861-7.
 193. Dolgilevich, S., et al., *Transduction of TAT fusion proteins into osteoclasts and osteoblasts*. *Biochem Biophys Res Commun*, 2002. **299**(3): p. 505-9.
 194. Park, H.J., et al., *Nonviral delivery for reprogramming to pluripotency and differentiation*. *Arch Pharm Res*, 2014. **37**(1): p. 107-19.
 195. Wong, F.K., et al., *Microinjection of membrane-impermeable molecules into single neural stem cells in brain tissue*. *Nat Protoc*, 2014. **9**(5): p. 1170-82.
 196. Torres, A.G. and M.J. Gait, *Exploiting cell surface thiols to enhance cellular uptake*. *Trends Biotechnol*, 2012. **30**(4): p. 185-90.
 197. Fu, A., et al., *Promises and pitfalls of intracellular delivery of proteins*. *Bioconjug Chem*, 2014. **25**(9): p. 1602-8.
 198. Khatri, N., et al., *cRGD grafted liposomes containing inorganic nanoprecipitate complexed siRNA for intracellular delivery in cancer cells*. *J Control Release*, 2014. **182**: p. 45-57.
 199. Ieda, M., et al., *Direct reprogramming of fibroblasts into functional cardiomyocytes by defined factors*. *Cell*, 2010. **142**(3): p. 375-86.
 200. Vierbuchen, T., et al., *Direct conversion of fibroblasts to functional neurons by defined factors*. *Nature*, 2010. **463**(7284): p. 1035-41.

201. Choi, S.O., et al., *Intracellular protein delivery and gene transfection by electroporation using a microneedle electrode array*. *Small*, 2012. **8**(7): p. 1081-91.
202. Joliot, A. and A. Prochiantz, *Transduction peptides: from technology to physiology*. *Nat Cell Biol*, 2004. **6**(3): p. 189-96.
203. Frankel, A.D. and C.O. Pabo, *Cellular uptake of the tat protein from human immunodeficiency virus*. *Cell*, 1988. **55**(6): p. 1189-93.
204. Green, M. and P.M. Loewenstein, *Autonomous functional domains of chemically synthesized human immunodeficiency virus tat trans-activator protein*. *Cell*, 1988. **55**(6): p. 1179-88.
205. Drin, G., et al., *Studies on the internalization mechanism of cationic cell-penetrating peptides*. *J Biol Chem*, 2003. **278**(33): p. 31192-201.
206. Foerg, C. and H.P. Merkle, *On the biomedical promise of cell penetrating peptides: limits versus prospects*. *J Pharm Sci*, 2008. **97**(1): p. 144-62.
207. Varga, C.M., T.J. Wickham, and D.A. Lauffenburger, *Receptor-mediated targeting of gene delivery vectors: insights from molecular mechanisms for improved vehicle design*. *Biotechnol Bioeng*, 2000. **70**(6): p. 593-605.
208. Heitz, F., M.C. Morris, and G. Divita, *Twenty years of cell-penetrating peptides: from molecular mechanisms to therapeutics*. *Br J Pharmacol*, 2009. **157**(2): p. 195-206.
209. Nakase, I., et al., *Methodological and cellular aspects that govern the internalization mechanisms of arginine-rich cell-penetrating peptides*. *Adv Drug Deliv Rev*, 2008. **60**(4-5): p. 598-607.
210. Wadia, J.S., R.V. Stan, and S.F. Dowdy, *Transducible TAT-HA fusogenic peptide enhances escape of TAT-fusion proteins after lipid raft macropinocytosis*. *Nat Med*, 2004. **10**(3): p. 310-5.
211. Liu, N.Q., et al., *Human immunodeficiency virus type 1 enters brain microvascular endothelia by macropinocytosis dependent on lipid rafts and the mitogen-activated protein kinase signaling pathway*. *J Virol*, 2002. **76**(13): p. 6689-700.
212. Kim, D., et al., *Generation of human induced pluripotent stem cells by direct delivery of reprogramming proteins*. *Cell Stem Cell*, 2009. **4**(6): p. 472-6.

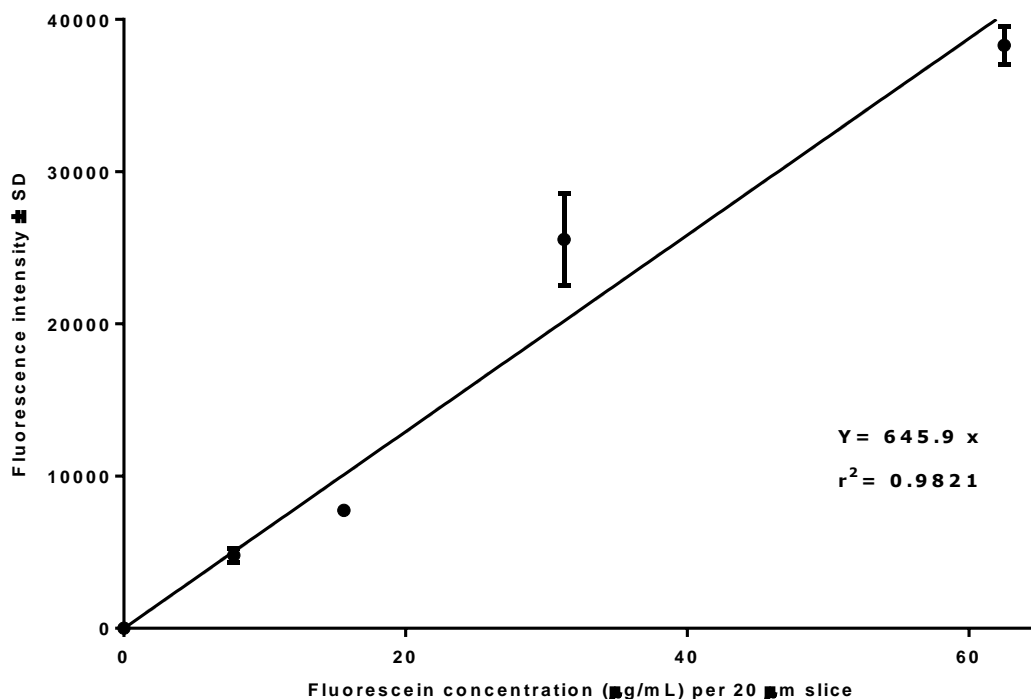
213. Munoz, E.M. and R.J. Linhardt, *Heparin-binding domains in vascular biology*. *Arterioscler Thromb Vasc Biol*, 2004. **24**(9): p. 1549-57.
214. Sakuma, T., et al., *CD9 antigen interacts with heparin-binding EGF-like growth factor through its heparin-binding domain*. *J Biochem*, 1997. **122**(2): p. 474-80.
215. Yu, R., J. Graf, and B.F. Smets, *An improved cell recovery method for iron oxidizing bacterial (IOB) enrichments*. *J Microbiol Methods*, 2008. **72**(3): p. 235-40.
216. LP., K. *Isoelectric Point Calculator*. . 2007-2013 27/11/2014; Available from: <http://isoelectric.ovh.org>
217. Tsien, R.Y., *The green fluorescent protein*. *Annu Rev Biochem*, 1998. **67**: p. 509-44.
218. Shields, R., et al., *Cell size, cell cycle and transition probability in mouse fibroblasts*. *Cell*, 1978. **15**(2): p. 469-74.
219. Gump, J.M., R.K. June, and S.F. Dowdy, *Revised role of glycosaminoglycans in TAT protein transduction domain-mediated cellular transduction*. *J Biol Chem*, 2010. **285**(2): p. 1500-7.
220. Ise, H., et al., *Analysis of cell viability and differential activity of mouse hepatocytes under 3D and 2D culture in agarose gel*. *Biotechnology Letters*, 1999. **21**(3): p. 209-213.
221. Ling, Y., et al., *A cell-laden microfluidic hydrogel*. *Lab Chip*, 2007. **7**(6): p. 756-62.
222. Song, Y.S., et al., *Engineered 3D tissue models for cell-laden microfluidic channels*. *Analytical and Bioanalytical Chemistry*, 2009. **395**(1): p. 185-193.
223. McCoy, J.P., Jr., et al., *Sorting minor subpopulations of cells: use of fluorescence as the triggering signal*. *Cytometry*, 1991. **12**(3): p. 268-74.
224. Ostrovidov, S., et al., *Stem Cell Differentiation Toward the Myogenic Lineage for Muscle Tissue Regeneration: A Focus on Muscular Dystrophy*. *Stem Cell Rev*, 2015.
225. Blau, H.M., C. Webster, and G.K. Pavlath, *Defective myoblasts identified in Duchenne muscular dystrophy*. *Proc Natl Acad Sci U S A*, 1983. **80**(15): p. 4856-60.

226. Rudnicki, M.A., et al., *MyoD or Myf-5 is required for the formation of skeletal muscle*. Cell, 1993. **75**(7): p. 1351-9.
227. Ishibashi, J., et al., *MyoD induces myogenic differentiation through cooperation of its NH₂- and COOH-terminal regions*. J Cell Biol, 2005. **171**(3): p. 471-82.
228. Juhas, M. and N. Bursac, *Engineering skeletal muscle repair*. Curr Opin Biotechnol, 2013. **24**(5): p. 880-6.
229. Charge, S.B. and M.A. Rudnicki, *Cellular and molecular regulation of muscle regeneration*. Physiol Rev, 2004. **84**(1): p. 209-38.
230. Leor, J., et al., *Gene transfer and cell transplant: an experimental approach to repair a 'broken heart'*. Cardiovasc Res, 1997. **35**(3): p. 431-41.
231. Weintraub, H., et al., *Activation of muscle-specific genes in pigment, nerve, fat, liver, and fibroblast cell lines by forced expression of MyoD*. Proc Natl Acad Sci U S A, 1989. **86**(14): p. 5434-8.
232. Prentice, H., et al. *TRANSFORMATION OF CARDIAC FIBROBLASTS INTO THE SKELETAL-MUSCLE PHENOTYPE BY INJECTION OF A MYOD-EXPRESSING RETROVIRUS INTO ISCHEMIC HEART*. in *Circulation*. 1993. AMER HEART ASSOC 7272 GREENVILLE AVENUE, DALLAS, TX 75231-4596.
233. Murry, C.E., et al., *Muscle differentiation during repair of myocardial necrosis in rats via gene transfer with MyoD*. J Clin Invest, 1996. **98**(10): p. 2209-17.
234. Lee, K., et al., *In vivo delivery of transcription factors with multifunctional oligonucleotides*. Nat Mater, 2015. **14**(7): p. 701-6.
235. Leor, J., et al., *Adenovirus-mediated gene transfer into infarcted myocardium: feasibility, timing, and location of expression*. J Mol Cell Cardiol, 1996. **28**(10): p. 2057-67.
236. Noda, T., et al., *Transduction of MyoD protein into myoblasts induces myogenic differentiation without addition of protein transduction domain*. Biochemical and biophysical research communications, 2009. **382**(2): p. 473-477.
237. Valencia, D.P. and F.J. González, *Understanding the linear correlation between diffusion coefficient and molecular weight. A model to estimate*

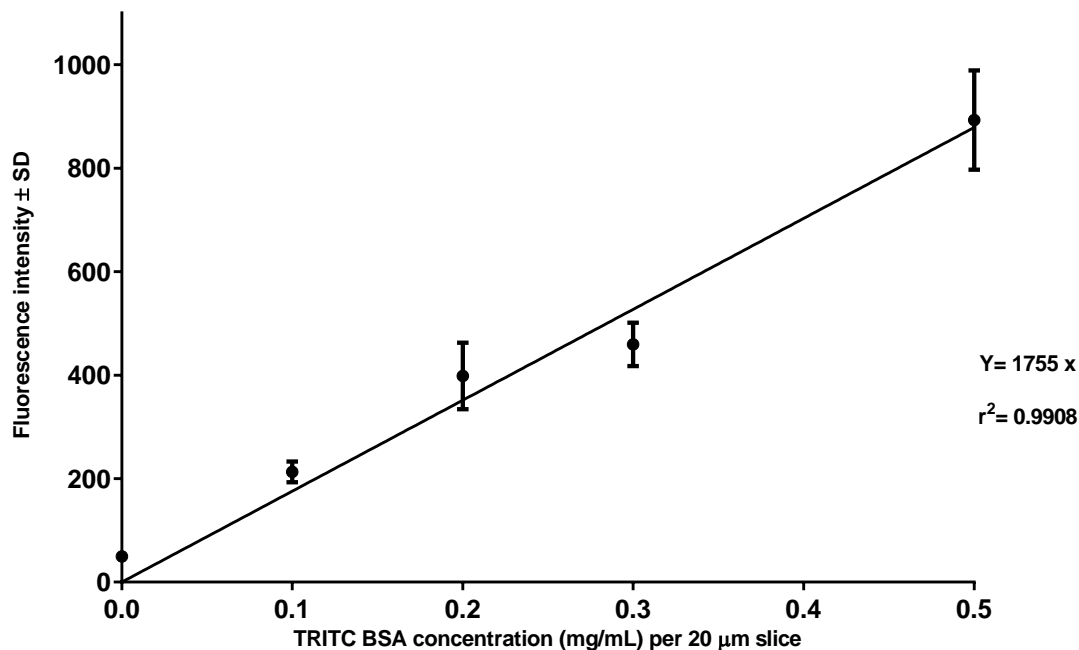
- diffusion coefficients in acetonitrile solutions*. *Electrochemistry Communications*, 2011. **13**(2): p. 129-132.
238. Alberts, B., et al., *Molecular Biology of the Cell*. New York: Garland Science; 2002. Classic textbook now in its 5th Edition, 2002.
239. Eckes, B., et al., *Downregulation of collagen synthesis in fibroblasts within three-dimensional collagen lattices involves transcriptional and posttranscriptional mechanisms*. *FEBS letters*, 1993. **318**(2): p. 129-133.
240. Gojgini, S., T. Tokatlian, and T. Segura, *Utilizing cell-matrix interactions to modulate gene transfer to stem cells inside hyaluronic acid hydrogels*. *Mol Pharm*, 2011. **8**(5): p. 1582-91.
241. Varani, J., et al., *Human skin in organ culture and human skin cells (keratinocytes and fibroblasts) in monolayer culture for assessment of chemically induced skin damage*. *Toxicol Pathol*, 2007. **35**(5): p. 693-701.
242. Mehrabani, D. and N. Manafi, *Role of cultured skin fibroblasts in aesthetic and plastic surgery*. *World J Plast Surg*, 2013. **2**(1): p. 2-5.
243. Wang, C., et al., *RNA extraction from polysaccharide-based cell-laden hydrogel scaffolds*. *Anal Biochem*, 2008. **380**(2): p. 333-4.
244. Lin, Y.C., et al., *Genome dynamics of the human embryonic kidney 293 lineage in response to cell biology manipulations*. *Nat Commun*, 2014. **5**: p. 4767.
245. Zagranichnaya, T.K., et al., *Gene expression profiles in HEK-293 cells with low or high store-operated calcium entry: can regulatory as well as regulated genes be identified?* *Physiol Genomics*, 2005. **21**(1): p. 14-33.
246. Donello, J.E., et al., *CLUSTERIN UPREGULATION BY BRIMONDINE*. *ARVO Annual Meeting Abstract Search and Program Planner*, 2003. **2003**: p. 2273.
247. Madl, C.M., et al., *Co-release of cells and polymeric nanoparticles from sacrificial microfibers enhances nonviral gene delivery inside 3D hydrogels*. *Tissue Eng Part C Methods*, 2014. **20**(10): p. 798-805.
248. Nguyen, K., P.N. Dang, and E. Alsberg, *Functionalized, biodegradable hydrogels for control over sustained and localized siRNA delivery to incorporated and surrounding cells*. *Acta Biomater*, 2013. **9**(1): p. 4487-95.

249. Muroya, S., et al., *Effect of phase limited inhibition of MyoD expression on the terminal differentiation of bovine myoblasts: no alteration of Myf5 or myogenin expression*. Dev Growth Differ, 2005. **47**(7): p. 483-92.
250. Lundkvist, A., et al., *Growth factor gradients in vascular patterning*. Novartis Foundation symposium, 2007. **283**: p. 194-201; discussion 201-6, 238-41.
251. Malone, E. and H. Lipson, *Fab@Home: the personal desktop fabricator kit*. Rapid Prototyping Journal, 2007. **13**(4): p. 245-255.
252. Enderlein, J., et al., *Art and artefacts of fluorescence correlation spectroscopy*. Current pharmaceutical biotechnology, 2004. **5**(2): p. 155-61.
253. Pluen, A., et al., *Diffusion of macromolecules in agarose gels: comparison of linear and globular configurations*. Biophysical journal, 1999. **77**(1): p. 542-52.
254. Chen, Y., et al., *Methods to measure the lateral diffusion of membrane lipids and proteins*. Methods, 2006. **39**(2): p. 147-53.
255. Liang, S., et al., *Protein diffusion in agarose hydrogel in situ measured by improved refractive index method*. Journal of controlled release : official journal of the Controlled Release Society, 2006. **115**(2): p. 189-96.

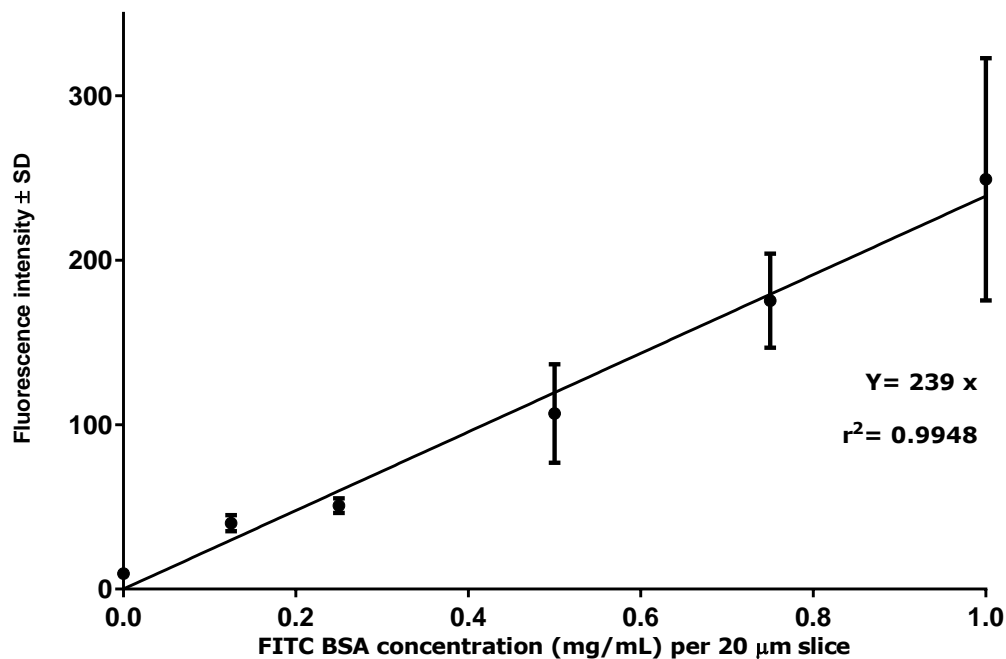
Appendix I: Supporting information



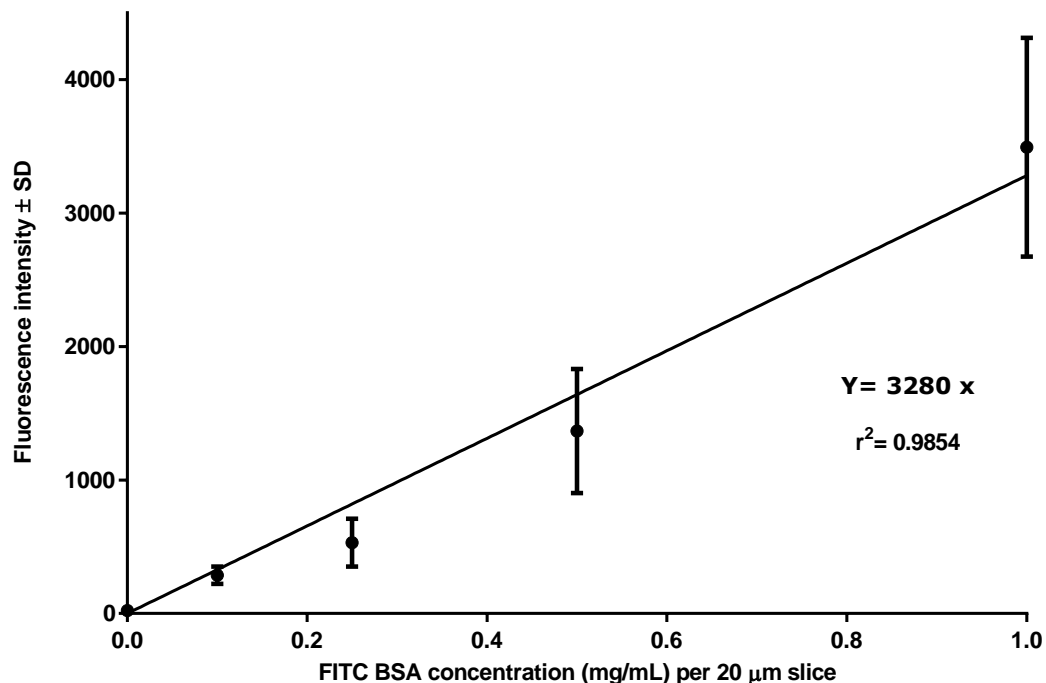
Supplementary figure 1: Calibration curve of Fluorescein per 20 μm thick slices retrieved from cryosectioning of homogeneously dispersed increasing concentrations of Fluorescein in 1% agarose hydrogel scaffolds of 15×5×6.6 mm (Length × Width × Height) dimensions. Each concentration point was evaluated from 2 different scaffolds each with 8 different slices retrieved from random positions of the scaffold. Slices were dissolved in PBS and analysed for protein concentrations using a TECAN infinite 200PRO multimode reader (excitation: 460 nm; emission: 515 nm).



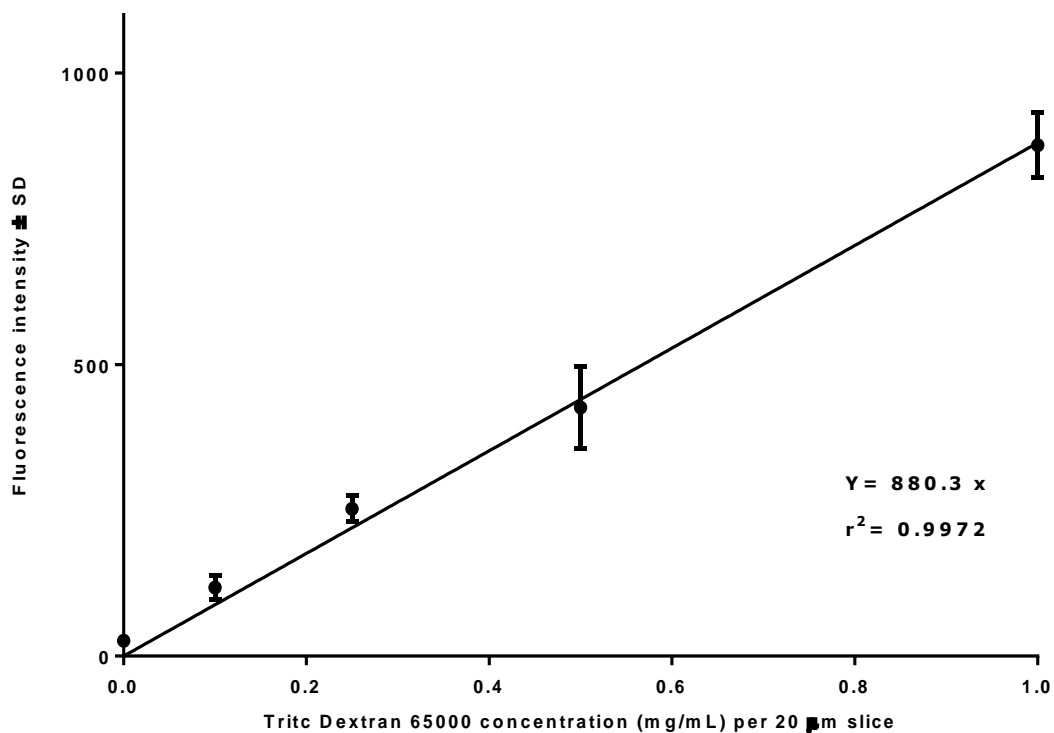
Supplementary figure 2: Calibration curve of TRITC-BSA per 20 μ m thick slices retrieved from cryosectioning of homogenously dispersed increasing concentrations of TRITC-BSA in 1% agarose hydrogel scaffolds of 15 \times 5 \times 6.6 mm (Length \times Width \times Height) dimensions. Each concentration point was evaluated from 2 different scaffolds each with 8 different slices retrieved from random positions of the scaffold. Slices were dissolved in PBS and analysed for protein concentrations using a TECAN infinite 200PRO multimode reader (excitation: 541 nm; emission: 572 nm).



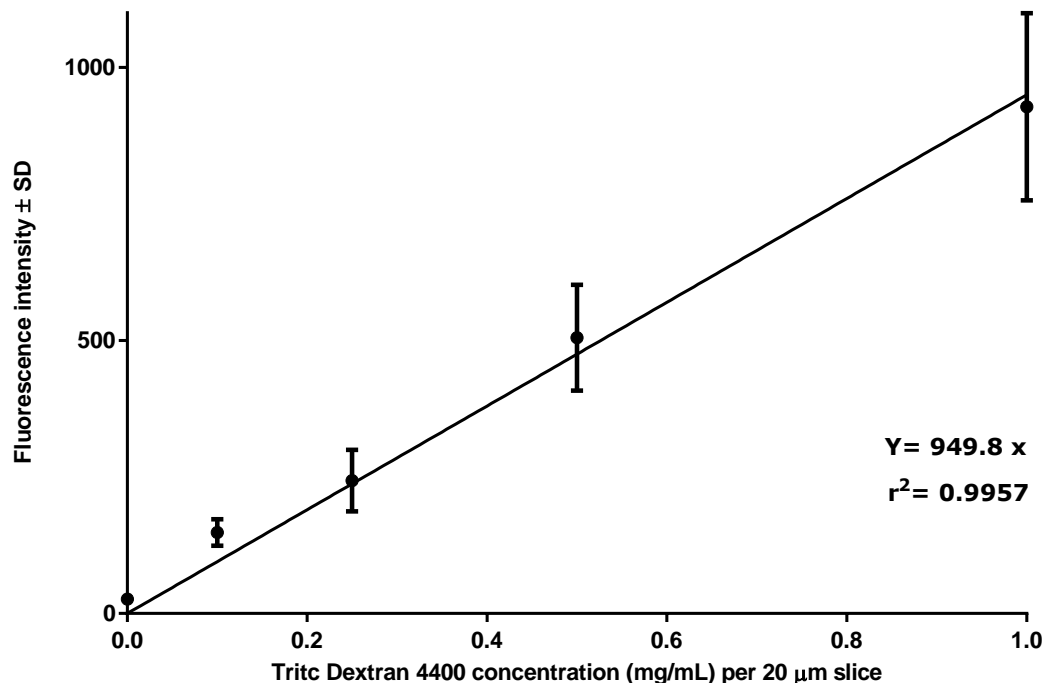
Supplementary figure 3: Calibration curve of FITC-BSA per 20 μm thick slices retrieved from cryosectioning of homogenously dispersed increasing concentrations of FITC-BSA in 2% agarose hydrogel scaffolds of 15×5×6.6 mm (Length × Width × Height) dimensions. Each concentration point was evaluated from 2 different scaffolds each with 8 different slices retrieved from random positions of the scaffold. Slices were dissolved in PBS and analysed for protein concentrations using a TECAN infinite 200PRO multimode reader (excitation: 490 nm; emission: 525 nm).



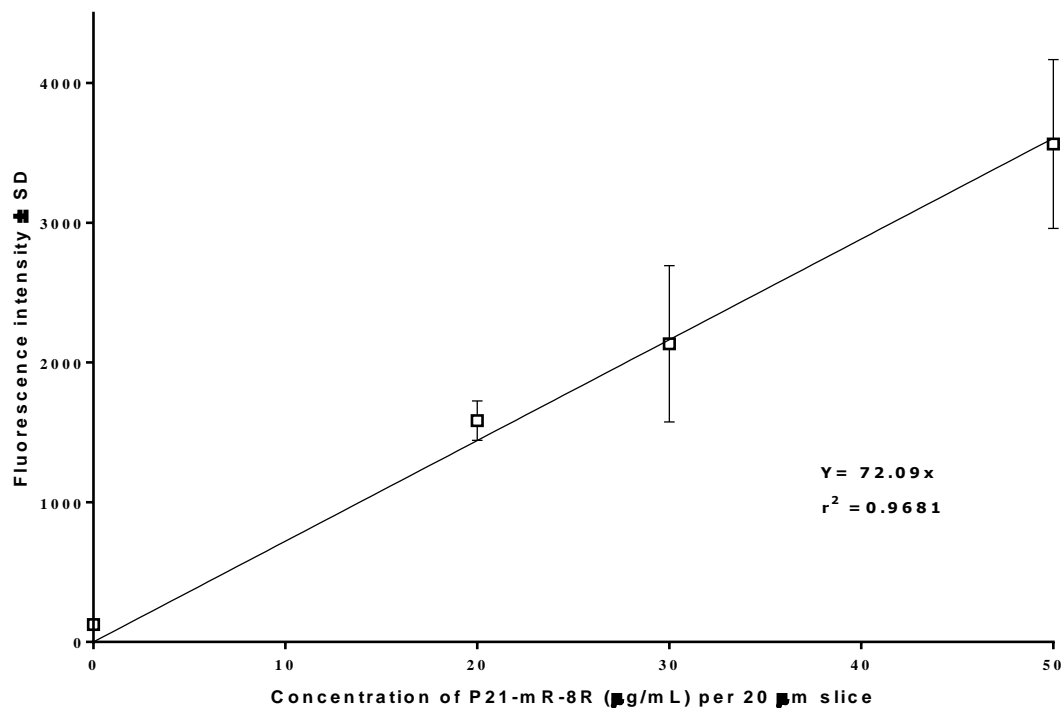
Supplementary figure 4: Calibration curve of FITC-BSA per 20 μ m thick slices retrieved from cryosectioning of homogeneously dispersed increasing concentrations of FITC-BSA in 1% agarose – 1% gelatin hydrogel scaffolds of 15 \times 5 \times 6.6 mm (Length \times Width \times Height) dimensions. Each concentration point was evaluated from 2 different scaffolds each with 8 different slices retrieved from random positions of the scaffold. Slices were dissolved in PBS and analysed for protein concentrations using a TECAN infinite 200PRO multimode reader (excitation: 490 nm; emission: 525 nm).



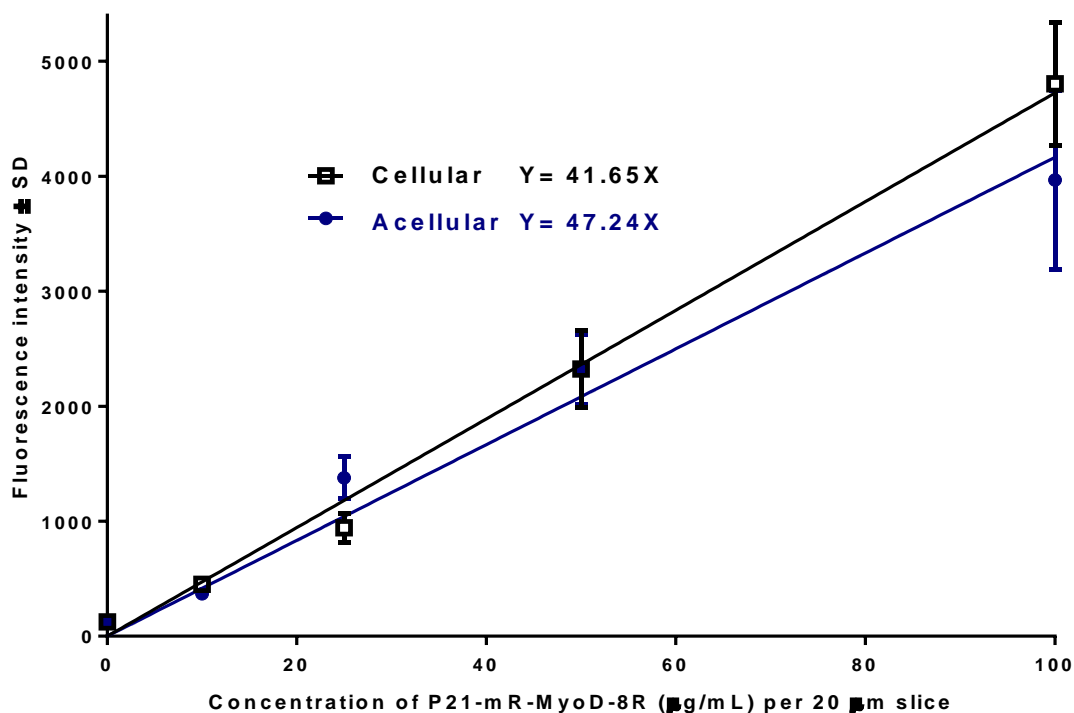
Supplementary figure 5: Calibration curve of TRITC-Dextran 65000 per 20 μ m thick slices retrieved from cryosectioning of homogenously dispersed increasing concentrations of TRITC-Dextran 65000 in 1% agarose hydrogel scaffolds of 15 \times 5 \times 6.6 mm (Length \times Width \times Height) dimensions. Each concentration point was evaluated from 2 different scaffolds each with 8 different slices retrieved from random positions of the scaffold. Slices were dissolved in PBS and analysed for protein concentrations using a TECAN infinite 200PRO multimode reader (excitation: 541 nm; emission: 572 nm).



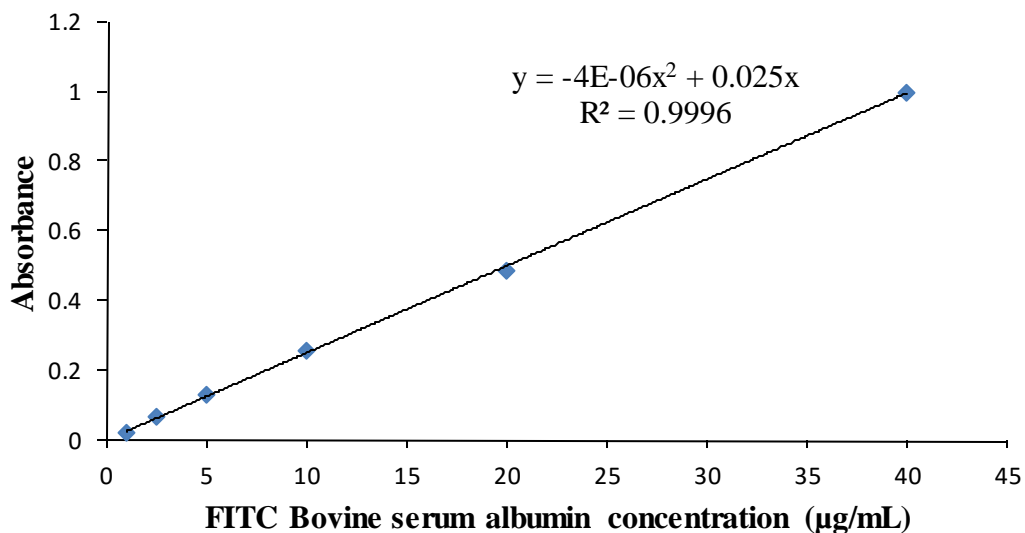
Supplementary figure 6: Calibration curve of TRITC-Dextran 4400 per 20 μm thick slices retrieved from cryosectioning of homogenously dispersed increasing concentrations of TRITC-Dextran 4400 in 1% agarose hydrogel scaffolds of 15×5×6.6 mm (Length × Width × Height) dimensions. Each concentration point was evaluated from 2 different scaffolds each with 8 different slices retrieved from random positions of the scaffold. Slices were dissolved in PBS and analysed for protein concentrations using a TECAN infinite 200PRO multimode reader (excitation: 541 nm; emission: 572 nm).



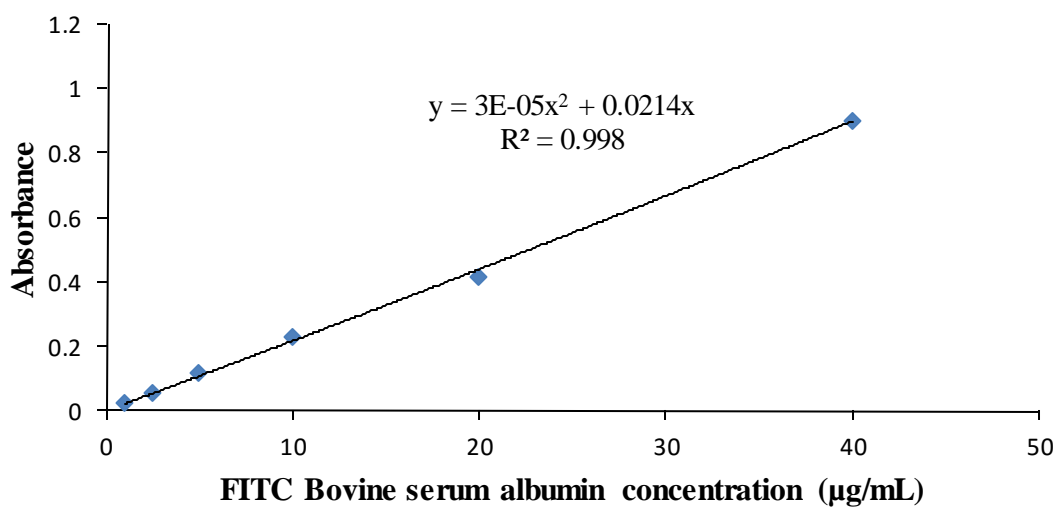
Supplementary figure 7: Calibration curve of P21-mR-8R per 20 μm thick slices retrieved from cryosectioning of homogenously dispersed increasing concentrations of P21-mR-8R in cellular (2×10^6 NIH 3T3 mouse fibroblasts cells/mL) 1% agarose – 1% gelatin hydrogel scaffolds of $15 \times 5 \times 6.6$ mm (Length \times Width \times Height) dimensions. Each concentration point was evaluated from 2 different scaffolds each with 8 different slices retrieved from random positions of the scaffold. Slices were dissolved in PBS and analysed for protein concentrations using a TECAN infinite 200PRO multimode reader (excitation: 584 nm; emission: 620 nm).



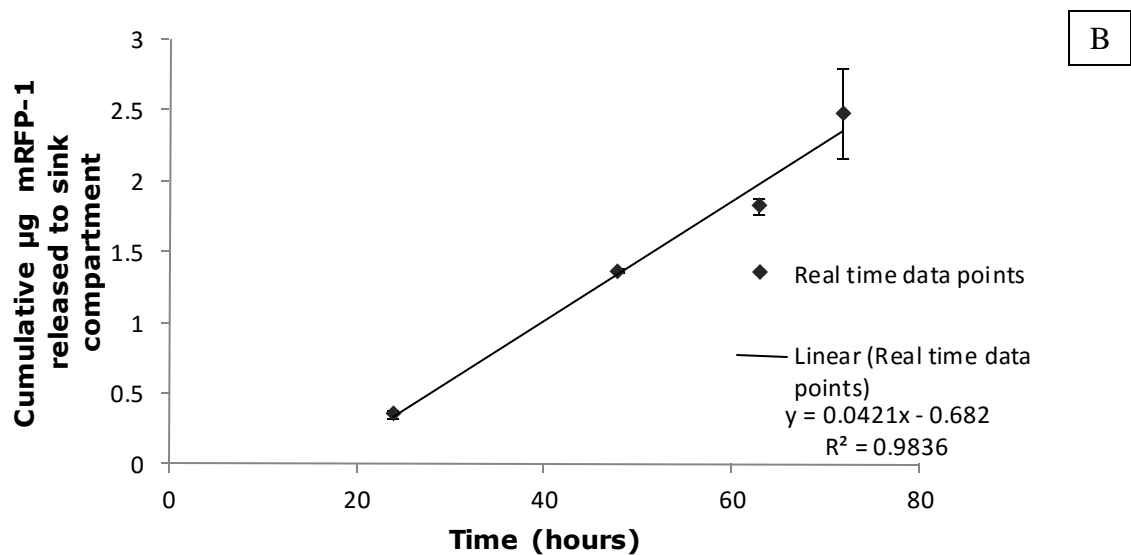
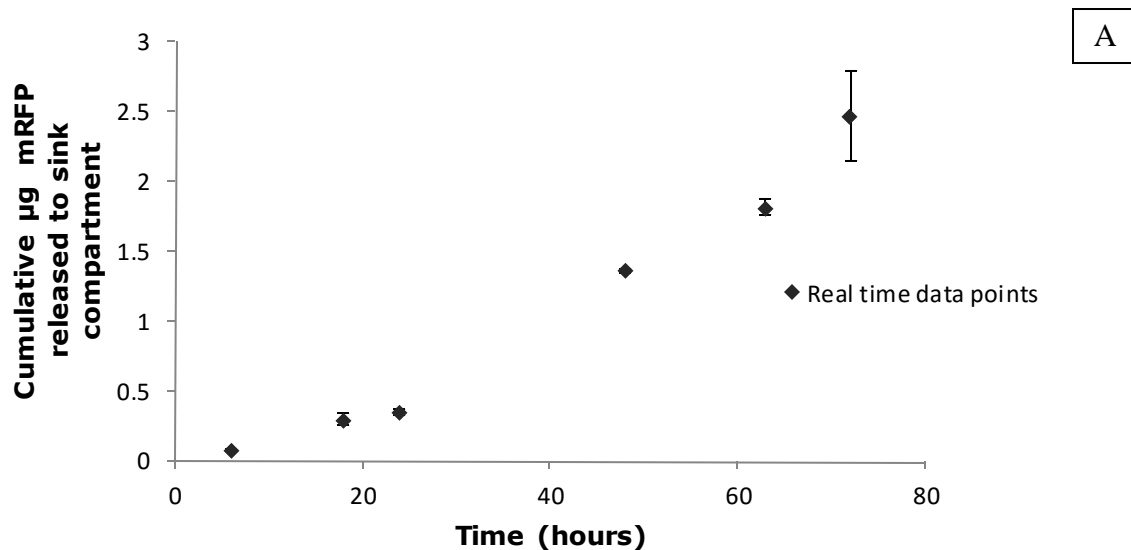
Supplementary figure 8: Calibration curve of P21-mR-MyoD-8R per 20 μm thick slices retrieved from cryosectioning of homogenously dispersed increasing concentrations of P21-mR-MyoD-8R in cellular (2×10^6 NIH 3T3 mouse fibroblasts cells/mL) or acellular 1% agarose – 1% gelatin hydrogel scaffolds of 15×5×6.6 mm (Length × Width × Height) dimensions. Each concentration point was evaluated from 2 different scaffolds each with 8 different slices retrieved from random positions of the scaffold. Slices were dissolved in PBS and analysed for protein concentrations using a TECAN infinite 200PRO multimode reader (excitation: 584 nm; emission: 620 nm).



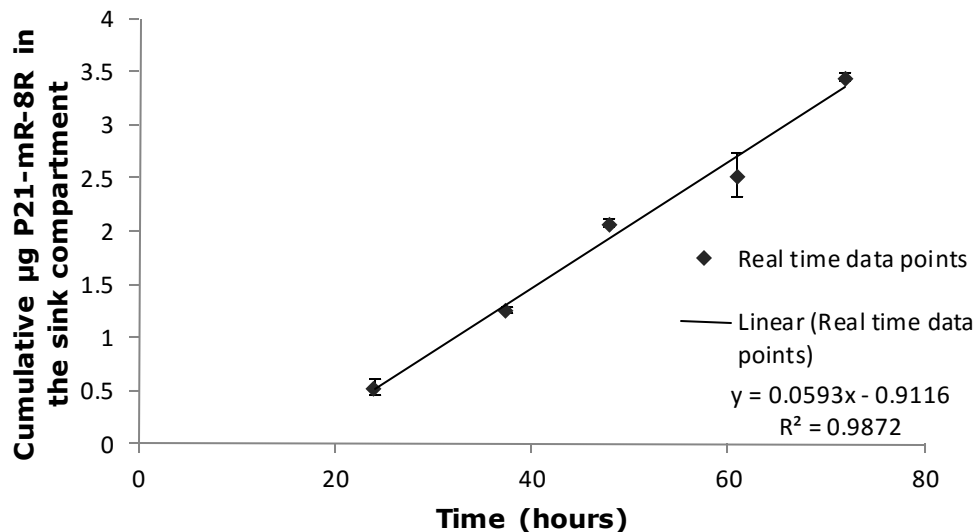
Supplementary figure 9: Calibration curve of the absorbance at 562 nm for different concentrations of FITC Bovine serum albumin using Bicinchoninic acid assay kit utilized for quantifying the % encapsulation efficiency of BSA in Bn02 & Bn04.



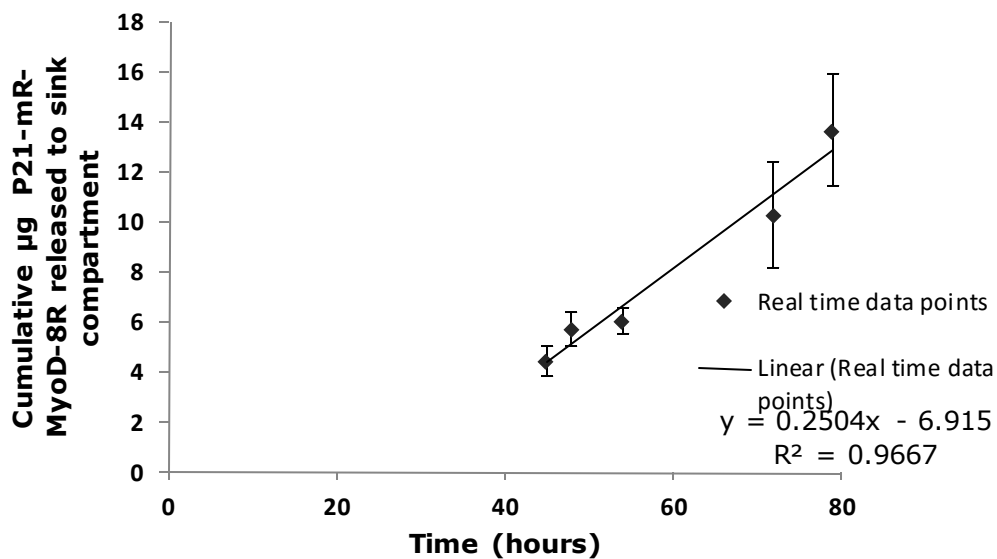
Supplementary figure 10: Calibration curve of the absorbance at 562 nm for different concentrations of FITC Bovine serum albumin using Bicinchoninic acid assay kit utilized for quantifying BSA released from PLGA 50:50 microspheres.



Supplementary figure 11: Determination of the diffusion coefficient of mRFP-1 in 1% agarose – 1% gelatin hydrogels using membrane permeation model utilizing acellular scaffolds of 15×5×6.6 mm (Length × Width × Height) dimensions as gel membranes. Each time point was evaluated from 3 different scaffolds through which 50 $\mu\text{g}/\text{mL}$ mRFP-1 diffused. A: Real time data points of amount of mRFP-1 measured in the sink compartments at the relevant time points. B: Linear regression for the same set of data after 24 hours, from which the diffusion coefficient of mRFP-1 in 1% agarose – 1% gelatin is evaluated to be $7.15 \times 10^{-7} \text{ cm}^2/\text{s}$.



Supplementary figure 12: Determination of the diffusion coefficient of P21-mR-8R in 1% agarose – 1% gelatin hydrogels using membrane permeation model utilizing acellular scaffolds of 15×5×6.6 mm (Length × Width × Height) dimensions as gel membranes. Each time point was evaluated from 3 different scaffolds through which 50 µg/mL P21-mR-8R diffused. Linear regression for real time data points after 24 hours, from which the diffusion coefficient of P21-mR-8R in 1% agarose – 1% gelatin is evaluated to be $7.53 \times 10^{-7} \text{ cm}^2/\text{s}$.



Supplementary figure 13: Determination of the diffusion coefficient of P21-mR-MyoD-8R in 1% agarose – 1% gelatin hydrogels using membrane permeation model utilizing acellular scaffolds of 15×5×6.6 mm (Length × Width × Height) dimensions as gel membranes. Each time point was evaluated from 3 different scaffolds through which 60 µg/mL P21-mR-MyoD-8R diffused. Linear regression for real time data points after 42 hours, from which the diffusion coefficient of P21-mR-8R in in 1% agarose – 1% gelatin is evaluated to be $4.2 \times 10^{-7} \text{ cm}^2/\text{s}$.

Appendix II: Validating the use of infinite[®] 200 pro microplate reader to measure diffusion gradients of protein drugs across hydrogel based scaffolds

I. Introduction

3D patterning techniques are being developed to achieve the clinical outcomes required from the complex arrangements of cells within extracellular matrices and chemical gradients [250]. The ultimate goal of these techniques is to accurately replicate the in vivo environment within a bulk construct. We aim to create an experimentally robust system in which we can create stable gradients using drug delivery technologies and expose cells to these gradients. Ultimately we would like to use 3D printing to create complex structures with multiple gradients. TECAN infinite 200PRO multimode reader offers an option of recording multiple readings inside the same well. Here, we investigated the use of the simple and accessible Infinite[®] 200 PRO microplate reader to study the diffusion pattern of fluorescent labelled proteins across transparent hydrogel matrices. The device software has a feature capable of recording multiple readings inside the same well and hence proposing scanning capabilities.

II. Methods

i. Design and fabrication of hydrogel constructs

a. 3D printed hydrogel constructs

The Fab@Home solid freeform fabrication platform (Model 2) [251] was used to produce 3D constructs in a layer-by-layer fashion by extrusion of hydrogels through tapered dispense tips (catalogue number TTNx where x is the tip gauge, Adhesive Dispensing, Milton Keynes, UK). Materials were sealed into 10 mL Luer lock syringe barrels (catalogue number 7100LL1NPK, Adhesive Dispensing, Milton Keynes, UK) by the use of SmoothFlow[™] pistons (catalogue number 5111PE-B, Nordson EFD, Westlake, OH, USA). These pistons were then depressed to deposit material at a computer-controlled rate utilizing the FabStudio (v2.0.1) and Fab Interpreter software suite designed for the Fab@Home platform. This software package controlled the motion of the syringe tips in 2D and of the build stage in the third dimension in order to achieve positional, as well as rate, control of deposition. Barium Alginate (BaCl₂ 0.2%: Sodium alginate 2%, 1:2), Calcium Alginate (CaCl₂ 0.25%: sodium alginate 2%, 1:2), 1.5 and 2% Agarose donut shaped hydrogel constructs were 3D printed using blue tapered tips (22G~0.4 mm). Supplementary table 1 shows printing parameters applied. The final volume of the hydrogel construct was 3 mL positioned centrally in 6 tissue culture treated well plate as shown in Supplementary figure 14.

b. Moulded/Punched hydrogel constructs

1 mL or 0.5 ml hot molten 1-2% w/v Agarose hydrogel were cast in 12 or 24-well plate respectively to form solid matrix. Biopsy punches of 8 mm diameter were then used against Acetal place holder to accurately create central compartment in each construct so that single central compartment model were created in 12 or 24-well plate respectively. Hydrogel constructs possessed dimension of 22 or 16 mm outer diameter and 8 mm diameter inner compartment and 2 mm height for the 12 and 24-well plate respectively. Supplementary figure 15 shows a diagram illustrating the dimension of hydrogel construct in 12-well plate.

ii. Measurement of protein concentrations

TECAN infinite 200PRO multimode reader was used to measure changes in fluorescence intensity in different zones at different time points. Multiple points read out 15×15 points filled circle for each hydrogel construct. In order to make analysis easier, multiple points were assigned in consecutive zones. Points at similar distance inside the circular lay out were represented as a particular zone as function of distance from the proposed central compartment as shown in Supplementary figure 16 so that each zone reading represents an average reading for all points lying at this zone. The following equation illustrates that zone spacing is affected by the well plate used, analysis border margin inside well and lay out picked as zone spacing is calculated by.

$$\text{Zone spacing} = (D - 2b)/(n - 1)$$

Where **D** is the diameter of well, **b** is the border at which plate reader starts to read multiple points inside well and n is the number of points read across the diameter of the well.

iii. Method Validation

a. Multiple reads per well for dispersed fluorescent labelled proteins in moulded hydrogels

60 µL of 0.6, 1.2 and 1.8 mg/mL FITC-BSA or of 50, 75 and 150 µg/mL P21-mR-8R were dispersed in 0.5 mL of 1-2% w/v agarose solutions and then moulded inside 24-well plate. Plates were left to cool down and then left in the incubator at 37 °C for 2 hours to equilibrate and then multiple points per well were recorded as previously stated at both 15×15 and 5×5 circle filled patterns. The effect of settling time (time to move from point to another to record reading) was studied as well by applying different settling times of 150 ms and 450 ms.

b. Multiple reads per well for dispersed fluorescent proteins in aqueous solutions

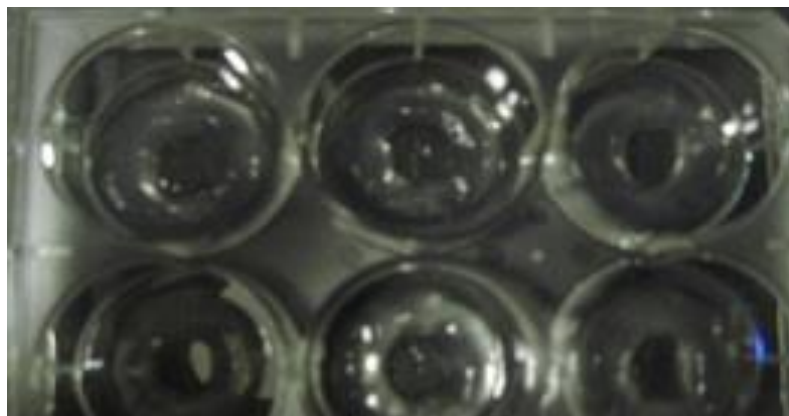
180 μL of 0.6, 1.2 and 1.8 mg/mL FITC-BSA or of 50, 75 and 150 $\mu\text{g/mL}$ P21-mR-8R aqueous solutions were placed inside 24-well plate. Multiple points per well were recorded at 15×15 circle filled pattern at different settling times of 150 ms and 450 ms.

c. Multiple reads per well for fluorescent dye: Rhodamine B aqueous solutions

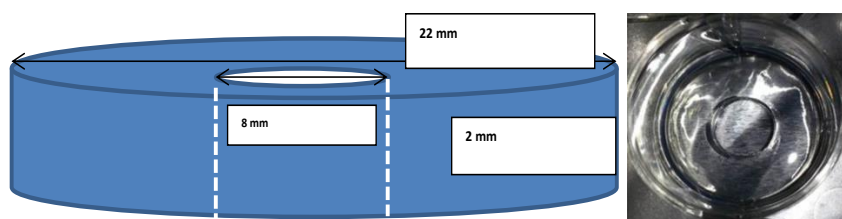
180 μL six replicates of 1 $\mu\text{g/mL}$ Rhodamine B red fluorescent dye aqueous solution were placed inside 24-well plate. Multiple points per well were recorded as previously stated at 15×15 circle filled pattern at different settling times of 150 ms.

Supplementary table 1: Printing parameters applied to fabricate hydrogel constructs

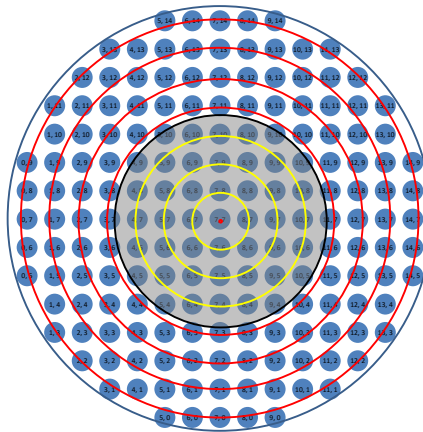
Parameter	Value
Deposition Rate	0.003 mm/mm
Path speed	10 mm/s
Path width	0.4 mm
Path height	0.4 mm
Push out time	0.03 s



Supplementary figure 14: 3D printed Barium Alginate donut shaped hydrogel constructs in 6 well tissue culture treated plate.



Supplementary figure 15: Dimensions for Moulded/Punched hydrogel construct in 12-well plate.

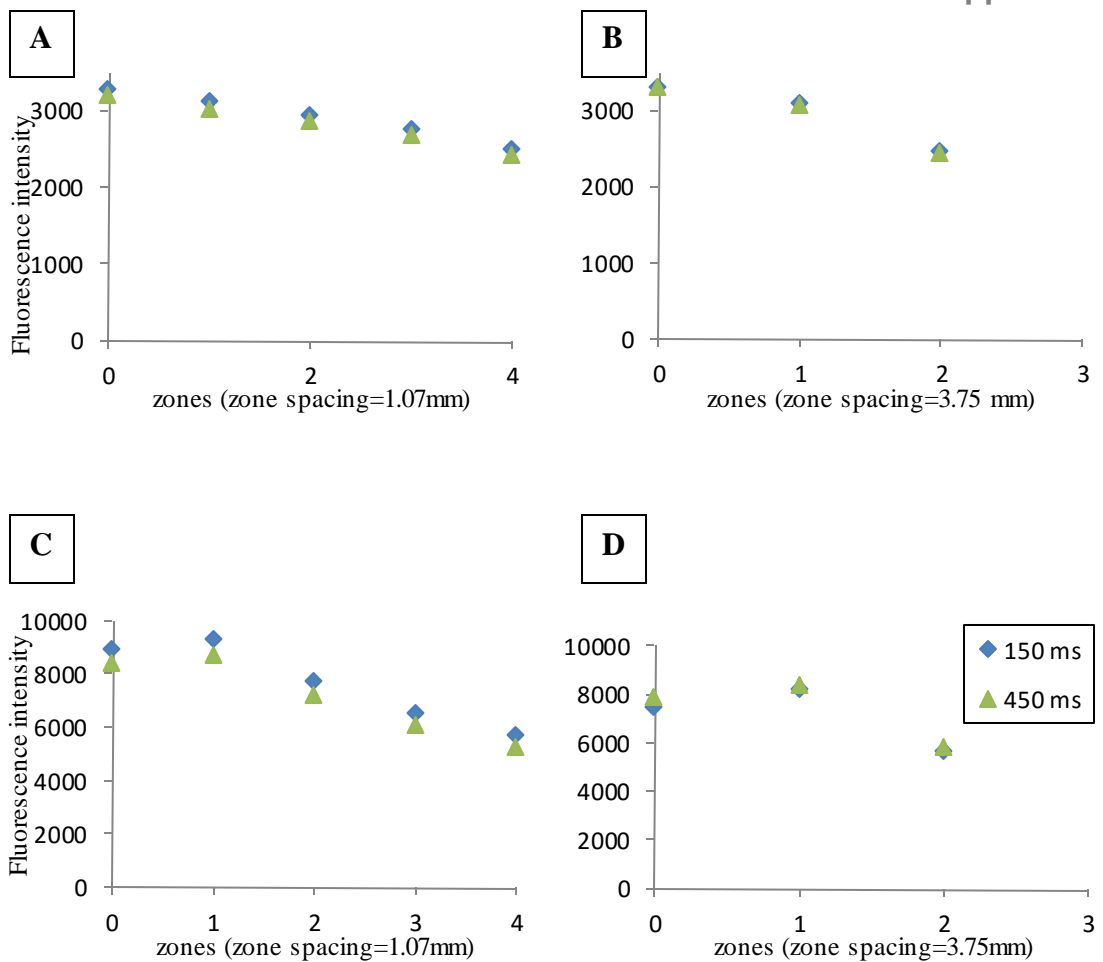


Supplementary figure 16: Multiple points 15 times 15 circle filled lay out in 12 well plate; blue dots: points read, black circle: central compartment margin, yellow circles: central compartment reading summed up as zone zero, red zones; zones inside the hydrogel construct with zone spacing = 1.5 mm

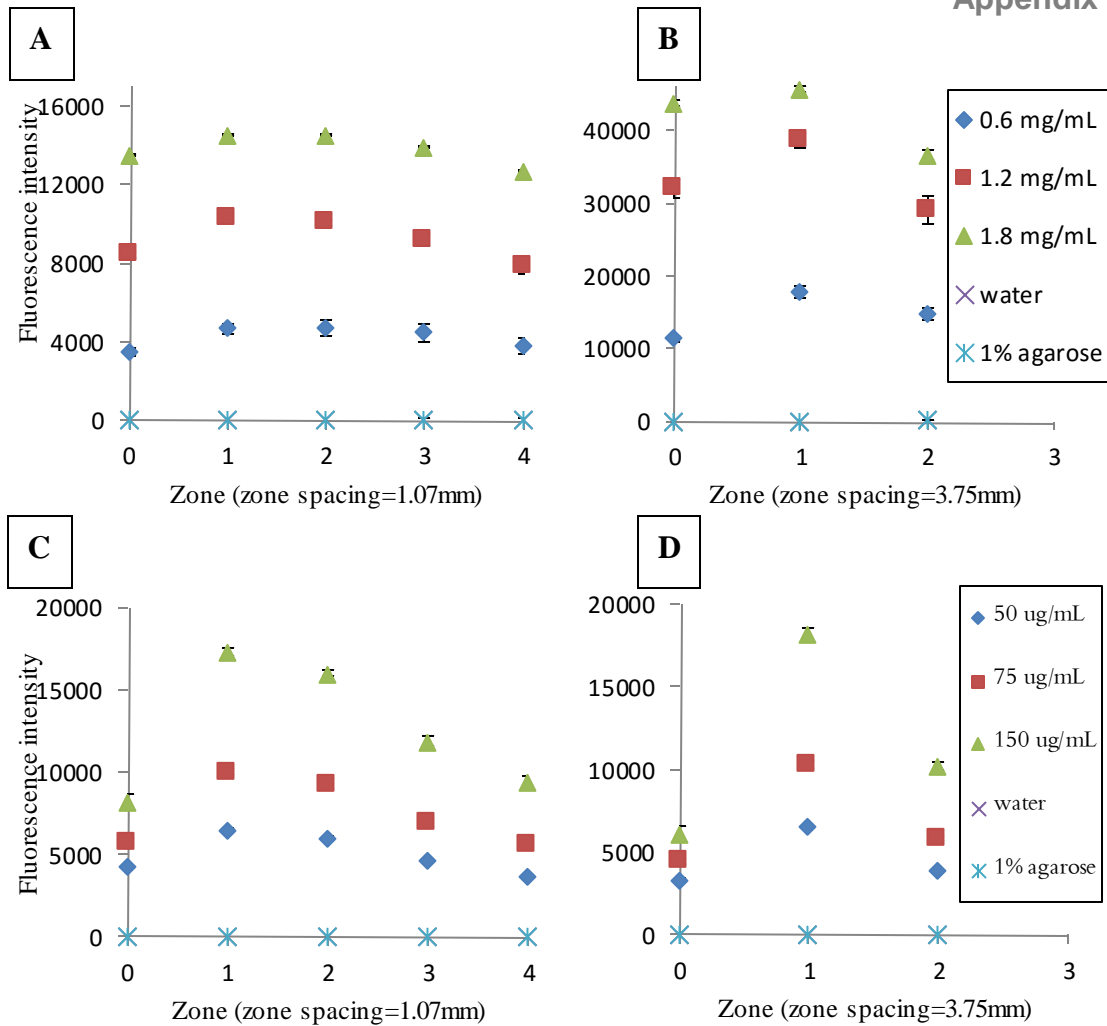
III. Results & discussion

Moulding/punching hydrogels represents a simple re-producible way to fabricate constructs of thermoresponsive gels to observe diffusion pattern of source protein throughout the construct. Casting yielded constructs of 2 ± 0.2 mm height. The dimensions of the constructs were reproducible throughout all constructs fabricated using the aforementioned method. The reproducibility of the construct dimensions was important to guarantee minimal variation due to construct design and attribute all variations to the analytical method employed.

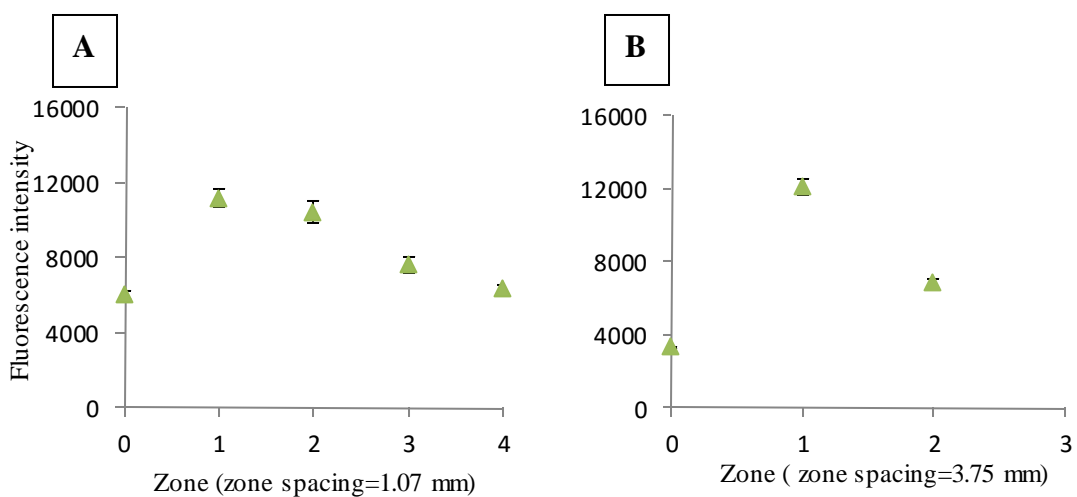
Studying the effect of settling time on the sensitivity of reading of homogenous dispersions of protein in agarose (Supplementary figure 17) reflected that it did not affect measurements. Delaying reading acquisition extra 300 ms did not result in difference in the reading precision that could be vandalized upon rapid movement of the reading probe. Similarly, number of points in the multiple points pattern and hence zone spacing did not affect the readings (Supplementary figure 17). However, aqueous solutions of FITC-BSA displayed higher fluorescence intensity readings in the 5×5 circle filled pattern (Supplementary figure 18B) compared to narrower zone spacing 15×15 circle filled pattern (Supplementary figure 18A). This might be due to change in the plate reader measurement set up to acquire less number of points in the 5×5 circle filled pattern resulting in magnification of the signal as the number of points decreases and the distance between them increases.



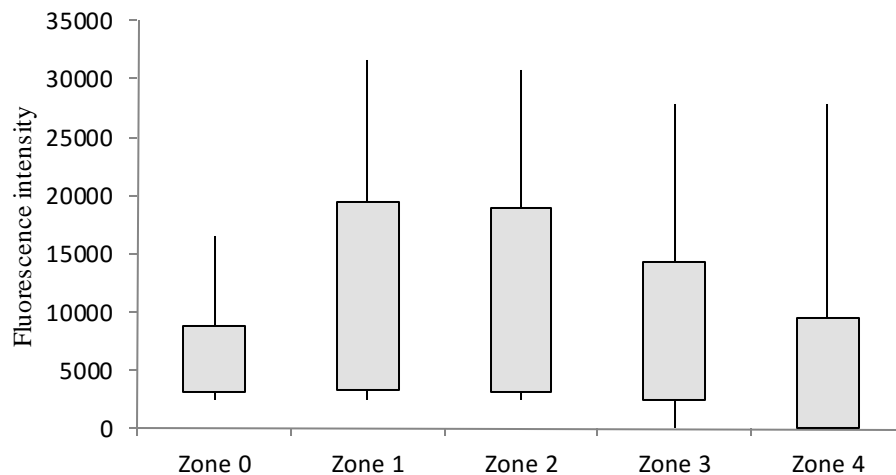
Supplementary figure 17: The effect of settling time on the fluorescence intensity reading of A: 1.8 mg/mL FITC-BSA dispersed in 1% Agarose using 15×15 circle filled pattern or B: 5×5 circle filled pattern and C: 150 µg/mL P21-mR-8R dispersed in 1% Agarose using 15×15 circle filled pattern or D: 5×5 circle filled pattern



Supplementary figure 18: Multiple points per well fluorescence intensity reading of A: FITC-BSA aqueous solution using 15x15 multiple points layout or B: 5x5 multiple points layout and C: P21-mR-8R aqueous solution using 15x15 multiple points layout or D: 5x5 multiple points layout.



Supplementary figure 19: Multiple points per well fluorescence intensity reading of 180 µL of 1 µg/mL Rhodamine B aqueous solution (Average of six replicates) A: 15x15 circle filled pattern or B: 5x5 circle filled pattern



Supplementary figure 20: Box and Whisker plot of multiple points per well fluorescence intensity reading of 180 μL of 1 $\mu\text{g}/\text{mL}$ Rhodamine B aqueous solution (single sample) using 15 \times 15 circle filled pattern. (The bottom and top of the box are the first and third quartiles and the ends of the whiskers represent the minimum and maximum of the data recorded per zone)

Yet, this was not the case with P21-mR-8R aqueous solutions (Supplementary figure 18C and D) and agarose dispersions (Supplementary figure 17C and D) or even FITC-BSA agarose dispersions (Supplementary figure 17A and B), eventually leading to unexplained device readings and proposing unreliability of measurements.

Moreover, uneven readings of different distance points were observed despite the use of homogenous solutions of proteins which should give relatively equal values for all points. Similarly, performing the experiment on Rhodamine B aqueous solution below its saturated solubility (Supplementary figure 19) gave uneven readings throughout all zones. High intra-zonal variations were observed in Supplementary figure 20. The rationale behind the use of Rhodamine B solution was the fear that the device was incapable of discriminating between signals of multiple points per well due to over saturation of large molecular weight moieties [252]. This anticipation was no longer valid after having similar results with small molecular weight compound below its saturation solubility. Further, high standard deviations between points comprising certain zones were computed and an overall % standard deviation between the 177 points comprising the whole well was calculated to be 96.72%.

IV. Conclusion

The inability of the device to read variable points in homogenous solutions equally, suggests that the method would not be suitable for multiple point analysis. Variable sensitivities of fluorescence intensity readings from aqueous to gel matrices as well as potential artefact readings from adjacent points in multiple points pattern further support this conclusion. Despite how promising was it to find a feature in an accessible device capable of measuring different distance points in scaffolds, method validation revealed insensitivity and irreproducibility of the multiple points per well measurements. For multiple points per well analysis, the Infinite[®] 200 Pro microplate reader, or generally a multimode reader, might not be the ideal choice.

Multimode readers are primarily designed to read a sum-signal of one whole well and the use of the 'multiple reads per well' feature can improve the well-to-well uniformity and reproducibility when measuring signals that are not homogeneously distributed. But for scanning applications that require high inner-well resolution, the performance of the plate reader will be limited. A dedicated scanning device of a pixel resolution of 10 μm ; laser scanning cytometer, microscope or a microarray scanner that can also be used with microplate might be better suited.

Appendix III: Fluorescence recovery after photobleaching (FRAP)

Determination of FITC-BSA diffusion coefficient in 4% w: v agarose gel

(1-4% w/v) Agarose, Type IX-A (A2576-5G, Sigma-Aldrich) hydrogels; plain and 0.4 mg% w/v FITC-BSA loaded, were prepared ready for investigation under Leica TCS-SP2 confocal microscope mounted on a Leica DM-LFS upright microscope. The aim was to detect FITC-BSA diffusion coefficient using FRAP [253].

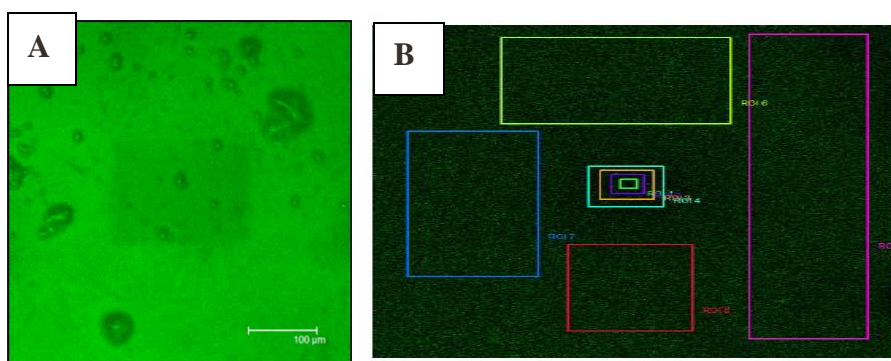
The confocal microscope is equipped with 3 lasers and for these studies the argon ion laser emitting light of 488 nm was used to study the FITC fluorescence. The TCS-SP2 confocal is equipped with a dispersive spectrophotometric detection system that permits the acquisition of up to three definable bands of the emission spectrum concurrently. Images of the various samples were acquired by illumination using the 488 nm argon laser and acquisition of the transmitted light, the reflected light (of wavelengths between 485 and 495 nm), and fluorescence between 510 nm and 550 nm, and between 550 nm and 600 nm. A 10x dry objective was used providing a maximum image dimension of 1 mm by 1 mm.

An assessment of the diffusion of the fluorescently-tagged protein through the gel was made by performing FRAP (fluorescence recovery after photobleaching): Here, a small region of the 0.4 mg% w: v BSA dispersed in 4% w: v agarose gel was repeatedly imaged with the illuminating laser power turned to maximum with the aim to bleach the fluorescence of the probes in this region. After approximately 20 seconds of bleaching, the laser power was returned to normal and the field of view widened. Images of the central bleached area were recorded for the subsequent few minutes. In this way, the measure of the average intensity inside the bleached area with reference to the surrounding non-bleached area reflected the amount of photobleached probes remaining. An increase in the fluorescence seen inside this area is due to the diffusion of non-bleached probes into the region, from which an approximation of the diffusivity of the protein/probe can be made. This is an approximation as the thickness of the photobleached area was not characterized and diffusion in this system occurs in 3 dimensions. Diffusion coefficient of FITC-BSA in 4% agarose gel was then calculated using the following equation.

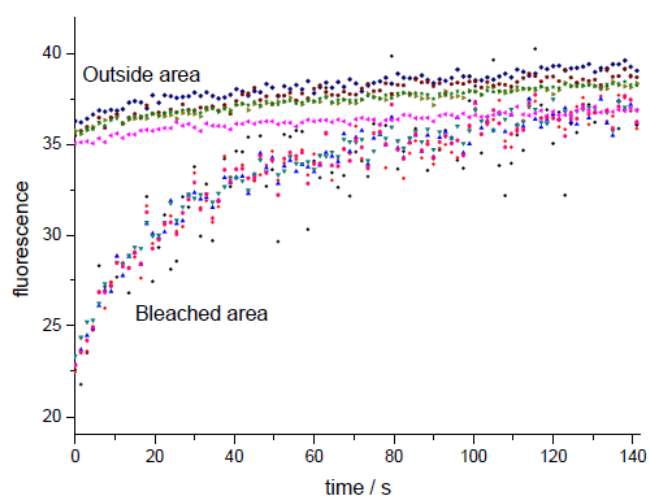
$$D = \frac{r_0^2 \gamma}{4\tau_{1/2}}$$

Where r_0 is the $1/e^2$ radius of the Gaussian profile laser beam used for both photobleaching and measuring fluorescence, and γ is a parameter that depends on the extent of photobleaching, varying slowly from 1.0 to about 1.2 [254].

FITC-BSA fluorescence is observed in Supplementary figure 21A and the areas adjacent to the bleached area, used as references to the intrinsic fluorescence are shown in Supplementary figure 21B. Recovery of fluorescence in the bleached area with comparison to intrinsic fluorescence of the reference adjacent areas which were not bleached can be clearly observed in Supplementary figure 22. The time, $\tau_{1/2}$, required to reach 50% of complete recovery, can be deduced from Supplementary figure 22 to be 20 s. The diffusion coefficient is calculated to be 10^{-8} cm²/sec. The value is comparable to values of protein diffusion over different concentrations of agarose gel using improved refractive index method [255] and to values measured in agarose gels using FRAP system [253].



Supplementary figure 21: Fluorescence bleaching of selected area in 4% agarose gel (A) and illustrated area of measurements of bleached area and adjacent non-bleached areas as references (B)



Supplementary figure 22: FITC-BSA Fluorescence recovery in the bleached area in 4% agarose gel compared to non-bleached adjacent areas.